

Europium sorption experiments with muscovite, orthoclase, and quartz: Modeling of surface complexation and reactive transport

Von der
Fakultät Architektur, Bauingenieurwesen und Umweltwissenschaften
der Technischen Universität Carolo-Wilhelmina
zu Braunschweig

zur Erlangung des Grades einer
Doktorin der Naturwissenschaften (Dr. rer. nat.)
genehmigte

Dissertation

von
Susan Marina Britz
geboren am 28.10.1983
aus Berlin

Eingereicht am: 17. Januar 2018

Disputation am: 06. April 2018

Berichterstatter: Prof. Dr. W. Durner
Prof. Dr. D. Zachmann

2018

Von der Fakultät Architektur, Bauingenieurwesen und Umweltwissenschaften
der Technischen Universität Carolo-Wilhelmina zu Braunschweig
zur Erlangung des Grades
einer Doktorin der Naturwissenschaften (Dr. rer. nat.)

genehmigte Dissertation

Eingereicht am: 17. Januar 2018

Disputation am: 06. April 2018

Berichterstatter/in: Prof. Dr. W. Durner
Prof. Dr. D. Zachmann

Abstract

For long-term safety analysis of a potential radioactive waste disposal site it is, amongst others, a prerequisite to understand and characterize transport and retardation processes of relevant radionuclides in order to be able to adequately describe hypothetical release scenarios and assess the barrier capacity of the contaminant providing rock zone but also of the geological formation and the overburden. To mechanistically simulate migration processes of radionuclides or chemical homologues a sound understanding of solid-solution interface reactions is necessary to determine the influence of the geochemical environment on sorption (adsorption, absorption, cation exchange), precipitation, speciation, and dissolution processes. For long-term safety assessments of nuclear waste disposal sites the behaviour of activation and fission products as well as radionuclides from decay chains are of major interest. The trivalent lanthanide europium(III) is a chemical homologue for trivalent actinides such as curium(III) and americium(III) which are products of neutron capture reactions in nuclear reactors.

In the field of safety assessments for a potential radioactive waste repository there is still a need for sound data concerning the interaction of minerals with the surrounding solution even for presumingly well known surfaces such as quartz, muscovite, and orthoclase. Up to now only some studies have taken the comprehensive approach to study the interaction and interrelation of surface charge, surface complexation, and transport processes for trivalent lanthanides and actinides for orthoclase, muscovite, and quartz; and so far only very few studies tried to describe all processes under varying geochemical conditions with one set of mineral-specific parameters. The advantage of one parameter set for a range of geochemical conditions in contrast to one set for each individual geochemical environment is the reduction of the amount of mineral-specific parameter sets necessary to predict transport processes of potentially hazardous pollutants under varying geochemical conditions.

A vast amount of titration, batch, and column experiments were carried out and evaluated with mechanistic thermodynamic sorption models to derive so-called

surface complexation parameters of Eu that were subsequently used to simulate Eu reactive transport under varying experimental boundary conditions with reactive transport models. It could be shown that the chosen approach to simulate different geochemical conditions with one surface complexation parameter set (derived from batch experiments) yielded adequate predictions of Eu transport under laboratory and close to nature conditions for the quartz systems; for orthoclase Eu transport under the influence of complexing ligands was satisfyingly represented. Generally, the simulation of column experiments involving orthoclase and muscovite was more challenging and revealed that more precise data but also knowledge are needed to adequately describe retardation and transport processes of the trivalent lanthanide.

This study contributed to fill the gap of sorption and transport data of Eu and, thus, relevant trivalent radionuclides for ubiquitously present minerals. Expertise in the development of reactive transport models was gained and results offered valuable insight into the transport behaviour of trivalent lanthanides and actinides. Knowledge regarding the transferability of surface complexation parameters from mineral titration and Eu batch experiments to reactive transport models as well as their influence on the performance of these transport models was achieved. Furthermore, results highlighted open questions and the need for further research in the field of solid-solution interface science.

Acknowledgements

I believe scientific achievements in any field of science have always been an accomplishment of many rather than one scientist. Five years of research have contributed to this thesis and therefore many people were involved that supported, encouraged, and helped to finish this work.

I am very grateful to my supervisors Prof. Dr. W. Durner (Technical University Carolo-Wilhelmina zu Braunschweig, Institute of Geoecology) and Prof. Dr. D. Zachmann (Technical University Carolo-Wilhelmina zu Braunschweig) who provided me with guidance and mentorship, contributed fruitful discussions, and who have always offered an open door for advises and support.

I want to express my deep and dearest gratitude to Dr. Ulrich Noseck (GRS gGmbH) who has always supported me over the years, provided scientific guidance, offered open, constructive, and solution-orientated critique and advice. During challenging, gooey times, he provided encouragement and help. Thanks for your time, your help, your understanding, and of course your strong nerves and endurance.

Furthermore, I would like to thank Dr. Jörg Mönig (GRS gGmbH) and Dr. Jens Wolf (GRS gGmbH). They encouraged me over the last years always offering support and advice. A million thanks go to my dear colleges Julian Fricke (GRS gGmbH), Anne Gehrke (GRS gGmbH), Dr. Judith Flügge (GRS gGmbH), and Sebastian Herr for their support, friendship, and countless discussions. I am fortunate to have been working with you.

I am happy to have worked together with colleges of different departments and institutes. Therefore, many thanks for advises, scientific discussions, and support as well as memorable social evenings go to Prof. Dr. Vinzenz Brendler (HZDR, IRE), Dr. Madlen Stockmann (HZDR, IRE), Dr. Frank Bok (HZDR, IRE), Dr. Constanze Richter (UIT Dresden), as well as the entire WEIMAR team. I would also like to thank all involved colleges from the Helmholtz-Zentrum Dresden-Rossendorf (IRE) who contributed their time to provide valuable data for the research project in general.

It was a pleasure to work together with Dr. Johannes Lützenkirchen (KIT, INE). With his patient support, constructive critique, many discussions, and continuous help he enabled me to develop an initial understanding of electrochemical processes at solid-solution interfaces.

I am also thankful to Dr. Sascha Iden (Technical University Carolo-Wilhelmina zu Braunschweig) with whom I worked together during the last two years of my work. Thanks a lot for your time, for pleasant and helpful discussions, and your scientific know-how.

I have also successfully worked together with Peter Hardy (Technical University Carolo-Wilhelmina zu Braunschweig, iBMB) who made REM-analysis possible for this research project in the first place. Many thanks also go to my master and bachelor students Charlotte Glassneck, Julian Fricke, Alexander Schulze, Lennart Steinbrecher, Jaqueline Haller-Jans, and Marc Wendisch. It was a pleasure to have worked with you. I would also like to thank the laboratory staff of the GRS gGmbH in Braunschweig. Without sound and trustworthy analyses none of this work would have been possible.

I owe my greatest gratitude to my friends and family. As always they supported me, shared successes and achievements with me, listened to my needs and concerns. Thank you so much for believing in me and supporting me over the past years. Arndt, no words express how much I owe you. Thank you so much.

Contents

Abstract	3
Acknowledgements	5
List of Figures	11
List of Tables	17
List of PHREEQC input file code blocks	19
List of Abbreviations	21
List of Symbols	27
Introduction	35
1.1 Relevance of the study	35
1.2 Objectives of the thesis	41
1.3 Outline	42
Mineral surface charge properties: Experiments and inverse modeling	45
2.1 Introduction	46
2.2 Theoretical background	47
2.2.1 Electrostatic interface models: Brief overview of theory	47
2.2.2 1-pK vs. 2-pK approach: Surface protolysis reactions	52
2.2.3 Points of zero charge	57
2.2.4 Specific surface area after Brunauer, Emmett, Teller (1938) . .	60
2.2.5 Determination of the surface site density	63
2.3 Material	66
2.3.1 Muscovite	67
2.3.2 Orthoclase	74

2.3.3	Quartz	75
2.4	Methods	76
2.4.1	Experimental approach	77
2.4.2	Data processing of relative titration data	79
2.4.3	Application of PHREEQC and UCODE: Surface charge model development, parameter optimization, model limitations . . .	79
2.4.4	Thermodynamic database	87
2.5	Results and discussion	87
2.5.1	Experimental results	88
2.5.2	Modeling results	97
2.6	Summary	113
Europium surface complexation: Experiments and inverse modeling		115
3.1	Introduction	116
3.1.1	Europium speciation	117
3.1.2	Europium conditional cation exchange selectivity coefficients .	120
3.2	Material and Methods	125
3.2.1	Experimental set-up	126
3.2.2	Estimation of Eu surface complexation constants with PHREEQC	126
3.2.3	Thermodynamic database	134
3.3	Results and discussion	135
3.3.1	Quartz	135
3.3.2	Orthoclase	145
3.3.3	Exclusion of muscovite from further modeling studies	150
3.4	Summary	153
Europium transport: Experiments and simulation		157
4.1	Introduction	158
4.2	Material and methods	161
4.2.1	Experimental set-up of column experiments	161
4.2.2	Data processing of breakthrough curves	165
4.2.3	Determination of retardation factors	165
4.2.4	Transport parameter determination with CXTFIT	166
4.2.5	PHREEQC 1D reactive transport	167
4.2.6	Thermodynamic database	170

4.3	Results and discussion of Br and Eu transport experiments	170
4.3.1	Quartz	170
4.3.2	Orthoclase	180
4.3.3	Muscovite	183
4.3.4	Synthetic sediment	187
4.4	Results and discussion of 1D reactive transport simulations	190
4.4.1	Transport parameter determination from Br breakthrough curves	191
4.4.2	1D reactive Eu transport simulations	196
4.5	Summary and first conclusions	207
Main conclusions and future perspectives		211
Bibliography		219
Appendix A - Materials, methods, and additional information		235
A.1	Further information on the experimental procedure of titration experiments and reference pH values	235
A.1.1	Mass titration	235
A.1.2	Electrolyte titration	235
A.1.3	Potentiometric acid-base titration	236
A.1.4	Isoelectric point	236
A.2	Tools, equipment, and techniques used for the characterization of muscovite, orthoclase and quartz	237
A.2.1	Specific surface area	238
A.2.2	Particle size separation	238
A.2.3	SEM, EDX measurements	239
A.2.4	Additional information on muscovite XRD measurements . . .	239
A.3	Tools, equipment, and techniques used for mineral titration experiments of muscovite, orthoclase, and quartz	240
A.3.1	Correction of pH measurements in high IS conditions	241
A.3.2	Determination of pH uncertainties after DIN 19268 (2007) . .	243
A.3.3	Uncertainty of surface charge measurements	243
A.4	Processing of relative raw data from potentiometric acid-base titration experiments to absolute values	243
A.4.1	Orthoclase: Linear relationship	243
A.4.2	Muscovite: Third order polynomial	244

A.5	Goodness of fit (UCODE)	245
A.6	Additional information on surface charge models	246
A.6.1	Orthoclase surface charge models	246
A.6.2	Muscovite surface charge models and cation exchange	247
A.7	Tools, equipment, and techniques used for batch experiments of muscovite, orthoclase and quartz	250
A.8	Estimation of Eu measurement uncertainties	251
A.9	Data processing of quartz batch measurements and supplementary information on quartz SCMs	251
A.10	Data processing of orthoclase batch measurements and supplementary information on orthoclase SCMs	252
A.11	Data processing of muscovite batch measurements	253
A.12	Tools, equipment, and techniques used for the experimental set-up of transport experiments	253
A.12.1	Preconditioning of mineral samples for column experiments	255
A.12.2	Specification of the artificial groundwater after Klinge et al. (2002)	257
A.12.3	Equations for the evaluation of transport data and determination of transport parameters	257
Appendix B - Supplementary data		261
B.1	Characterization of muscovite, orthoclase and quartz	261
B.2	Comparison of potentiometric titration measurements of muscovite, orthoclase, and quartz	268
B.3	Supplementary data on Eu batch experiments	269
B.4	Supplementary data on Eu transport experiments	273

List of Figures

1.1	Stepwise approach of titration, batch, and column experiments to develop RTMs for the prediction of Eu reactive transport with SCPs based on surface charge and sorption measurements.	43
2.1	Schematic illustration of the basic Stern model (BSM) and the diffuse double layer model (DDLDM).	51
2.2	XRD analyses of muscovite: Comparision of pristine and preconditioned mineral samples.	68
2.3	XRD analyses of muscovite: Comparision between pristine samples, diethyleneglycol preparation, and preconditioned muscovite.	69
2.4	SEM analysis of preconditioned and pristine muscovite.	70
2.5	EDX analyses (area scan) of orthoclase.	75
2.6	XRD analysis of orthoclase.	76
2.7	Flowchart of PHREEQC application in combination with UCODE for universal parameter estimation after Britz (2011).	81
2.8	Experimental mass (A) and electrolyte (B) titration data of quartz. .	89
2.9	Continuous potentiometric acid-base titration of quartz.	91
2.10	Mass (A) and electrolyte titration (B) measurements of orthoclase. .	92
2.11	Continuous potentiometric acid-base titration measurements of orthoclase.	93
2.12	Comparison of surface charge data from this study and literature data of feldspar minerals.	94
2.13	Experimental mass (A) and electrolyte (B) titration results of muscovite.	95
2.14	Comparison of surface charge data from this study and literature data of clay minerals.	97
2.15	DDLDM and BSM fit and simulation results of Bolt (1957) experimental titration data in the range of $IS = 10 \text{ mM} - 400 \text{ mM}$	98

2.16	Surface charge model results (DDLm) of absolute orthoclase titration data and simulations of surface potential development.	106
2.17	BSM results of absolute orthoclase acid-base titration data and zeta-potentials using SCPs from Table 2.4.	108
2.18	DDLm results of absolute muscovite acid-base titration data and zeta-potentials using SCPs from Table 2.4.	111
2.19	BSM results of absolute muscovite acid-base titration data and zeta-potentials using SCPs from Table 2.4.	112
3.1	Europium speciation under atmospheric influence (A) and in equilibrium with muscovite (B), orthoclase (C), quartz (D).	119
3.2	Scatter plots of raw and converted experimental batch data of quartz, orthoclase, and muscovite.	128
3.3	Results of Eu batch experiments with quartz.	136
3.4	1-pK DDLm results: Model was calibrated with experimental quartz batch data.	139
3.5	1-pK DDLm results including a hypothetical exchange site: Model was calibrated with experimental quartz data [%Eu(III) immobilized] and a hypothetical Na-Eu cation exchange reaction on the silica surface.	140
3.6	Contributions of Eu mono- and bidentate surface complexes in combination with a hypothetical Na-Eu exchange reaction on quartz of 1-pK DDLms.	141
3.7	Results of Eu batch experiments with quartz and fitted noEDLM results including mono-, bi-, and mono- combined with bi-dentate surface complexes.	142
3.8	Batch data of quartz with Eu and 1-pK BSM results using mono-, bi-, and mono- combined with bidentate surface complexes.	144
3.9	Results of Eu batch experiments with orthoclase.	146
3.10	DDLm and noEDLM results of orthoclase Eu batch data.	147
3.11	BSM results of orthoclase Eu batch experiments.	149
3.12	Results of Eu batch experiments with orthoclase, quartz, and muscovite.	152
4.1	Experimental set-up of column experiments.	163
4.2	Results of quartz column experiments Q-i and Q-ii: 10 mmol L ⁻¹ NaClO ₄ at pH _{ini} = 3.5 and pH _{ini} = 5.6.	172

4.3	Quartz column experiment Q-iii (5 mmol L ⁻¹ Na ₂ SO ₄) and Q-iv (50 mmol L ⁻¹ Na ₂ SO ₄) at pH _{ini} ≈ 5.5.	174
4.4	Eu retardation and pH development of quartz column Q-iv: 50 mmol L ⁻¹ Na ₂ SO ₄ , pH _{ini} = 5.5.	175
4.5	Sulphate (SO ₄ ²⁻) ligand influence on Eu transport processes in quartz columns, pH _{ini} = 5.6.	176
4.6	Influence of pore water velocity v [cm d ⁻¹] on Eu transport through quartz columns with 5 mmol L ⁻¹ Na ₂ SO ₄ background electrolyte at pH _{ini} = 5.6 (Q-iii, Q-vi).	177
4.7	Comparison of Eu transport through quartz columns using an artificial groundwater (Q-v) and 50 mmol L ⁻¹ Na ₂ SO ₄ background electrolyte (Q-iv), pH _{ini} = 5.5.	179
4.8	Eu transport through quartz and orthoclase columns using 10 mmol L ⁻¹ NaClO ₄ background electrolyte, pH _{ini} ≈ 3.5.	180
4.9	Eu transport through quartz and orthoclase columns using 50 mmol L ⁻¹ Na ₂ SO ₄ background electrolyte, pH _{ini} = 3.5 and 5.5.	182
4.10	Eu transport through quartz, orthoclase, and mica columns using 10 mmol L ⁻¹ NaClO ₄ background electrolyte, pH _{ini} ≈ 3.5.	183
4.11	Eu immobilization on quartz, orthoclase, and mica surfaces: Comparison of measured batch and column K_d values.	184
4.12	Eu transport through quartz, orthoclase, and mica columns using 10 mmol L ⁻¹ NaClO ₄ , 5 mmol L ⁻¹ Na ₂ SO ₄ , and an artificial groundwater as background electrolytes, pH _{ini} = 3.6 and 5.5.	185
4.13	Eu transport through quartz, orthoclase, and mica columns using 10 mmol L ⁻¹ NaClO ₄ and 5 mmol L ⁻¹ Na ₂ SO ₄ background electrolyte, pH _{ini} ≈ 5.5.	187
4.14	Eu transport through quartz, orthoclase, muscovite, and synthetic sediment columns using 10 mmol L ⁻¹ NaClO ₄ background electrolyte, pH _{ini} ≈ 3.5.	188
4.15	Eu transport through quartz, muscovite, and synthetic sediment columns using the artificial groundwater as a background electrolyte (Tab. A.1), pH _{ini} = 5.5 and the inert NaClO ₄ background electrolyte, pH = 3.6.	189
4.16	Experimental Br BTCs and fitted BTCs of Q-iii and Q-vi.	195

4.17	Reactive transport simulations of Eu through quartz columns, $\text{pH}_{ini} \approx 5.5$ (Q-ii - Q-v).	200
4.18	Reactive transport simulations of Eu through orthoclase columns (FS-ii): Comparison between experimental Eu transport data (BTC), Br BTCs, and pH development with predictions.	202
4.19	Eu DDLM transport simulations of column experiment FS-iii: Comparison between experimental and predicted Eu BTCs and pH development.	205
4.20	Eu BSM transport simulations of column experiment FS-iii: Comparison between experimental and predicted Eu BTCs and pH development.	206
4.21	Eu noEDLM transport simulations of column experiment FS-iii: Comparison between experimental and predicted Eu BTCs and pH development.	207
A.22	Δ_{pH} vs. NaClO_4 concentration $[\text{mol kgw}^{-1}]$ after Schwabe (1967) and Hagemann et al. (2014).	242
A.23	Shift of relative muscovite titration data in relation to pH_{IEP} with $\Delta\sigma = 0.005 \text{ C m}^{-2}$.	244
B.24	EDX analysis of muscovite (preconditioned sample).	263
B.25	Comparison of SEM analysis of muscovite, quartz, orthoclase.	263
B.26	Example of BET isotherm for SSA determination after Brunauer et al. (1938).	264
B.27	Zeta-potential measurements of muscovite and orthoclase.	268
B.28	Comparison of relative titration data of muscovite, orthoclase, and quartz.	268
B.29	Batch data of orthoclase, muscovite, quartz vs. pH.	269
B.30	Comparison between batch experimental data of Eu, Am, Cm on quartz from literature and data collected in this study.	270
B.31	Batch sorption data of orthoclase.	271
B.32	noEDLM fitting results of orthoclase batch data.	271
B.33	DDLm fitting results of orthoclase batch data.	272
B.34	Pretests: Equilibration of muscovite and orthoclase columns for transport experiments (pretests) with $10 \text{ mmol L}^{-1} \text{ NaClO}_4$, pH 3.5 background electrolyte.	273
B.35	Technical drawing of PFA columns including PTFE frits, sealing ring, and bracket.	274

B.36 Eu speciation (10^{-5} mol L $^{-1}$ Eu) without atmospheric influence (T = 298 K) in 5 mmol L $^{-1}$ and 50 mmol L $^{-1}$ Na ₂ SO ₄	275
B.37 Eu speciation (10^{-5} mol L $^{-1}$ Eu) without atmospheric influence (T = 298 K) in artificial groundwater (App. Tab. A.1).	275
B.38 Comparison of Br and Eu transport through quartz columns: 50 mmol L $^{-1}$ Na ₂ SO ₄ , pH _{ini} = 5.6.	276
B.39 Br BTCs of orthoclase column experiments.	276
B.40 Br BTCs of muscovite column experiments.	277
B.41 Eu transport through orthoclase and synthetic sediment columns using 10 mmol L $^{-1}$ NaClO ₄ background electrolyte, pH _{ini} \approx 3.5.	278
B.42 Eu transport through synthetic sediment columns using the artificial groundwater after Klinge et al. (2002) as a background electrolyte, pH _{ini} = 5.5.	279
B.43 Illustration of ideal Br tracer BTC characterization by means of quartz column experiment Q-iii, pH _{ini} \approx 5.5, 5 mmol L $^{-1}$ Na ₂ SO ₄ background electrolyte.	280
B.44 Eu transport simulations of column experiment Q-i.	280
B.45 Eu transport simulations of column experiment Q-iii.	281
B.46 Eu transport simulations of column experiment Q-v.	282
B.47 Eu transport simulations (<i>SCP Q I bi+mono</i>) of column experiment Q-v: Influence of Al ³⁺ as a potential competing cation.	282
B.48 Eu transport simulations of column experiment FS-i: Comparison between experimental Br BTCs and predicted Eu BTCs.	283

List of Tables

2.1	Definitions of reference pH values and experimental measurements of this study.	58
2.2	Summary of BET analyses of muscovite, orthoclase, and quartz. . . .	72
2.3	Summary of optimized parameters, initial parameter values, and surface reactions of surface charge models and SCP sets of muscovite, quartz, and orthoclase for the DDLM and BSM in combination with the 1-pK and 2-pK approaches.	101
2.4	Summary of final surface charge models, SCPs, and UCODE goodness of fit of muscovite, quartz, and orthoclase DDLM and BSM approaches in combination with the 1-pK and 2-pK approaches.	103
3.1	Comparision of muscovite and illite CECs.	121
3.2	Summary of relevant cation exchange selectivity coefficients of mica minerals published in literature.	124
3.3	Pauling's bond valence parameters for Eu surface complexation reactions of mono-, bi-, and multi-dentate surface complexes (Si-OH, Al-OH).	133
3.4	Summary of final SCP sets including Eu surface complexation constants of quartz and orthoclase.	137
3.5	Comparison of quartz Eu SCPs from literature and final SCPs of this study.	145
4.1	Summary of quartz, orthoclase, muscovite, and synthetic sediment column experiments including geochemical conditions.	164
4.2	Summary of transport parameters of quartz, orthoclase, muscovite, and synthetic sediment column experiments.	193
4.3	Summary of K_d values calculated from experimental data and reactive transport simulations of quartz column experiments (Q-i – Q-v). . . .	197

4.4	Comparison of K_d values calculated from experiments and simulations of orthoclase transport experiments (FS-i – FS-iii).	203
A.1	Composition and specification of chemicals used for the artificial groundwater.	257
B.2	Comparison of supplier’s data and HF digestion analysis of muscovite, quartz, and orthoclase.	261
B.3	Summary of BET measuring conditions, error sources, and estimation of SSA_{BET} error ranges as provided in literature.	265

List of PHREEQC input file code blocks

2.1	Perchlorate (ClO_4^-) definition of the NaClO_4 background electrolyte for PHREEQC calculations. Abbreviations used as priorly introduced. # indicates comments.	84
3.1	Surface complexation reactions, co- and counter ion association coefficients, and charge distribution as used for electrostatic models and noEDLM approaches in PHREEQC SCMs and RTMs (Sec. 4.2.5). # indicates comments.	131
4.2	Competing surface complexation reaction for Al^{3+} on quartz (DDLm) (Kuan et al., 2004) as used in PHREEQC SCMs. S- refers to a mineral surface. # indicates comments.	168

List of Abbreviations

1D	one-dimensional
A	
A	Cation A
AAS	Atom Adsorption Spectroscopy
Al-OH	Aluminol surface functional group
alk	[eq kgw ⁻¹] Contribution of an anion to the alkalinity of a solution
ANDRA	Agence Nationale pour la Gestion des Déchets Radioactifs
app	Apparent
appl.	Application
aq	In solution (aqua)
B	
B	Cation B
BE	Background electrolyte
BET	Specific surface area determination after Brunauer et al. (1938)
bi	Bidentate
BSM	Basic Stern model
BTC	Breakthrough curve
C	
CA	Component additivity (approach)
CCM	Constant capacitance model
CD-MUSIC	Charge distribution multi site complexation (model approach)
cip	Common intersection point

COMPO		SEM back-scattering measurement mode
CPRZ		Containment providing rock zone
CXTFIT		Transport code (Toride et al., 1998) which is part of the free ware software package STANMOD (STudio of ANalytical MODels, Version 2.0, Simunek et al. (1999))
cr		crystalline
D, E		
DDLm		Diffuse double layer model
EDL		Electric double layer
EDX		Energy Dispersive X-ray spectroscopy
element_gfw	[g mol ⁻¹]	Keyword for molar mass as included in database for PHREEQC
EM		Electrostatic model
ESTRAL		Joint research project: Realitätsnahe Einbindung von Sorptionsprozessen in Transportprogramme für die Langzeitsicherheitsanalyse (Realistic implementation of sorption processes in transport codes for long-term safety analysis), grant numbers 02E10518, 02E11072A, funded by Federal Ministry of Economics and Energy (BMWi)
ET		Electrolyte titration
EX		Exchange reactions
EXAFS		Extended X-ray absorption fine structure
F, G		
FeOX		Iron oxides, iron hydroxides
FES		Frayed edge site
FS		Orthoclase (Kali Norflot 600)
G20 EAS extra		Quartz sample used in the present study
gfw	[g mol ⁻¹]	Gram formula weight
gfw_formula		Keyword for chemical formula as included in database for PHREEQC

gof	Goodness of fit
GC	Generalized composite (approach)
GRS gGmbH	Gesellschaft für Anlagen- und Reaktorsicherheit gGmbH

H

H_2O_{bi}	hydrolyzed bidentate Eu surface complex
$\text{H}_2\text{O}_{mono}$	hydrolyzed monodentate Eu surface complex
HF	Hydrofluoric acid
HLW	High level radioactive waste
HZDR	Helmholtz-Zentrum Dresden-Rossendorf e.V.

I

IAP	Ion activity product
iBMB	Institute of Building Material, Concrete Construction and Fire Protection of the Technical University of Braunschweig, Germany
ICDD	International Center for Diffraction Data (2005) for powder diffraction analysis
ICP MS	Inductively Coupled Plasma Mass Spectrometry
ICP OES	Inductively Coupled Plasma Optical Emission Spectrometry
ICSD	Inorganic Crystal Structure Database
ID	Identification
IEP	Isoelectric point
IHP	Inner Helmholtz plane
ILW	Intermediate level radioactive waste
IRE	Institute of Resource Ecology (HZDR)
IUPAC	International Union of Pure and Applied Chemistry

K, L

Kali Norflot 600	Orthoclase sample used in the present study
------------------	---

KIT-INE	Institute for Nuclear Waste Disposal (INE), Karlsruhe Institute of Technology (KIT), Ger- many
LLNL	Lawrence Livermore National Laboratory
LLW	Low level radioactive waste
M	
M	Muscovite (mica WG)
M ³⁺	Trivalent metal cation
Max	Maximum
Me	Metal ion
Mica WG	Muscovite sample used in the present study
Min	Minimum
Mono	Monodentate
MonoEu(OH) ₂	Monodentate Eu-hydroxo surface complex
MT	Mass titration
Musc	Muscovite (mica WG)
N, O	
NAGRA	National Cooperative for the Disposal of Ra- dioactive Waste
NEA	Nuclear Energy Agency
noEDLM	Non-electrostatic model
obs	Observations
OHP	Outer Helmholtz-plane
nphc	Net proton and hydroxide consumption
ortho	Orthoclase (Kali Norflot 600)
P	
Pc	Perchlorate as included in PHREEQC database
Pc ⁻	Perchlorate ion as included in PHREEQC database
PEST	Model-independent Parameter ESTimation and uncertainty analysis (Doherty, 2002)
PFA	Perfluoroalkoxy alkane polymer

PHREEQC		Geochemical speciation code (Parkhurst and Appelo, 2013)
pot		Potentiometric acid-base titration
ppm		Parts per million
ppzc		Pristine point of zero charge
PS		Planar sites
PSI		Paul Scherrer Institute
PTFE		Polytetrafluoroethylene
PV	$[V/V_0]$	Pore volume
pznpc		Point of zero net proton charge
pzc		Point of zero charge
pzse		Point of zero salt effect
Q, R		
Q		Quartz (G20 EAS extra)
Ref.		Literature reference
RES ³ T		Rossendorf Expert System for Surface and Sorption Thermodynamics (Brendler et al., 2003), www.hzdr.de/res3t
RH		Relative humidity
RN		Radionuclide
RTM		Reactive transport model (PHREEQC)
S		
s		Solid
S-		Surface
SCM		Surface complexation model
SCP		Surface complexation parameter, SCPs comprise Eu surface complexation constants, protolysis constants, SSD, SSA, co-/counter-ion associations, capacitances, and cation exchange selectivity coefficients
SCP M		ID for SCPs and SCM of muscovite
SCP O		ID for SCPs and SCM of orthoclase
SCP Q		ID for SCPs and SCM of quartz
SD		Spatial distribution
SEM		Scanning Electron Microscopy

SEM ²	Research project: Rare Earth Elements Metallurgy - Advanced methods for optimized extraction and beneficiation by ion-adsorption clays (project period June 2015 - March 2018)
SFG	Surface functional group
SHC	Surface hydroxyl configuration
S-OH	Surface functional group
Si-OH	Silanol surface functional group
SynSed	Synthetic sediment
T	
TDB	Thermodynamic database
tetra	Tetradentate
THEREDA	Thermodynamic Reference Database, www.thereda.de
TLM	Triple layer model
TPM	Three plane model
tri	Tridentate
TRLFS	Time-resolved laser-induced fluorescence spectroscopy
TSM	Thermodynamic sorption model
U – Z	
UCODE	Universal parameter estimation code (Poeter et al., 2005)
WD	Working distance
WEIMAR	Joint research project: Weiterentwicklung des Smart-K _d -Konzepts für Langzeitsicherheitsanalysen (Further development of the smart-K _d approach for long-term safety analysis), grant numbers 02E10528, 02E11072B, funded by Federal Ministry of Economics and Energy (BMWi)
WT	UCODE statistical means to describe weighing concept for LSOF optimization
x	SEM magnification factor
XRD	X-ray Diffraction
zeta	Zeta-potential measurement

List of Symbols

A

A	$[m^2]$	Cross-section area
a_{H^+}	$[-]$	Hydrogen ion activity
\mathring{a}	$[-]$	Debye-Hückel ion-size parameter
α_i	$[-]$	Activity of solution species i
α_{EX}	$[-]$	Activity of exchange species

B, C

b	$[-]$	Debye-Hückel parameter
c	$[-]$	Index to identify conditional parameters
C	$[mol\ L^{-1}]$	Concentration
CC	$[-]$	Correlation coefficient
C_0	$[mol\ L^{-1}]$	Initial element concentration
C_1	$[F\ m^{-2}]$	Capacitance of the layer between the 0-plane and 1-plane (BSM)
C_2	$[F\ m^{-2}]$	Capacitance of the layer between the 1-plane and d-plane (TLMs, TPMs)
C_x	$[mol\ L^{-1}]$	Concentration of cation x in solution
c_{BET}	$[-]$	BET constant (Brunauer et al., 1938)
C_{Br^-}	$[mol\ L^{-1}]$	Br^- concentration
CEC	$[cmol(+) kg^{-1}]$	Cation exchange capacity
CEC_{pot}	$[cmol(+) kg^{-1}]$	Potential cation exchange capacity
CEC_{WG}	$[cmol(+) kg^{-1}]$	Cation exchange capacity of muscovite (mica WG sample) resulting from Na^+ , K^+ , Ca^{2+} , and Mg^{2+} exchange
CEV	$[unit\ of\ measure]$	Calculated error variance
C_{equil}	$[\mu g\ L^{-1}]$	Equilibrium concentration

C_{Eu}	[mol L ⁻¹]	Eu concentration, also in [mol kg solid ⁻¹]
c_f	[mg L ⁻¹]	Flux-averaged concentration
C_{H^+,OH^-}	[mol L ⁻¹]	Proton and hydroxide ion concentration in solution
CI	[unit of measure]	Confidence interval
C_{max}	[mol L ⁻¹]	Maximum element concentration, also in [mol kgs ⁻¹]
CN	[—]	Coordination number
c_r	[mol L ⁻¹]	Volume averaged or resident concentration of the liquid phase
C_{res}	[mol L ⁻¹]	Residual concentration, also in [mol kg solid ⁻¹]
C_{sol}	[μg L ⁻¹]	Element concentration in solution
C_{immo}	[μg L ⁻¹]	Sorbed/immobilized element concentration
D		
d	[mm]	Diameter
d_{50}	[μm]	Mass-median diameter of cumulative particle size distribution
d_{80}	[μm]	80% quantile of cumulative particle size distribution
D	[cm ² h ⁻¹]	Dispersion coefficient
E – J		
E_{AX}	[—]	Equivalent fraction of species A on an exchanger surface X
E_c	[mV]	Reference electrode potential
E_{obs}	[mV]	Measurement of the electrical potential
$EX_{absolute}$	[mol(+) sites kgw ⁻¹]	Absolute cation exchange site capacity
F	[C mol ⁻¹]	Faraday constant (96 485.33289 C mol ⁻¹)
f_{factor}	[—]	Charge distribution factor (Pauling's bond valence rules)
γ	[—]	Molar activity coefficient
γ_{AX}	[—]	Molar activity coefficient of exchange species A on the surface of an exchanger (X)
G_{int}^o	[J mol ⁻¹]	Chemical (intrinsic) Gibbs free-energy

G_{tot}^o	[J mol ⁻¹]	Total free Gibbs energy of sorption, $\Delta G^o = -RT \ln K$ (cf. Eq. 2.1)
H ⁺	[mol L ⁻¹]	Proton(s)
H ₃ O ⁺	[mol L ⁻¹]	Hydronium ion (aq)
H_{hyd}	[kJ mol ⁻¹]	Hydration enthalpy
ΔnH^+	[–]	Change in number of released protons
IS	[mol L ⁻¹]	Ionic strength
id	[mm]	Inner diameter
j	[–]	Indices: common ligand (OH ₂ ⁰ , OH ⁻¹ , O ⁻²)
K		
K^{app}	[unit of measure]	Apparent mass law constant
K_{a1}^{app}	[unit of measure]	Apparent deprotonation constant of Si-OH
K_{a2}^{app}	[unit of measure]	Apparent protonation constant of Si-OH
$K_{GT_c}^{B \rightarrow A}$	[unit of measure]	Conditional (<i>c</i>) cation exchange selectivity coefficient following the Gaines-Thomas (<i>GT</i>) convention, B index cation, A cation in solution
$\log K_{Al-OH}$	[unit of measure]	Intrinsic 1-pK protolysis constant, aluminol surface functional groups
K_d	[L kg ⁻¹]	Linear distribution coefficient, also in [m ³ kg ⁻¹]
$\Delta \log K_d$	[L kg ⁻¹]	Error of K_d model predictions in comparison to experimental K_d based on Davis et al. (2005)
K^{int}	[unit of measure]	Intrinsic mass law constant
K_{a1}^{int}	[unit of measure]	Intrinsic deprotonation constant of Si-OH
K_{a2}^{int}	[unit of measure]	Intrinsic protonation constant of Si-OH
K_L	[L mg ⁻¹]	Langmuir equilibrium constant
$\log K_{prot}$	[unit of measure]	General notion for protolysis reactions regardless of the electrostatic model approach
$\log K_{Si-OH}$	[unit of measure]	Intrinsic 1-pK protolysis constant, silanol surface functional groups
K_w	[unit of measure]	Dissociation constant of water at 298.15 K

$\log K$	[unit of measure]	Surface complexation constant / formation constant
$\log K_c$	[unit of measure]	Conditional selectivity coefficient
$\log K_c Na/H$	[unit of measure]	Conditional cation exchange selectivity coefficient of H^+ , index cation Na^+
$\log K_c Na/K$	[unit of measure]	Conditional cation exchange selectivity coefficient of K^+ , index cation Na^+
$\log K_c Na/Na$	[unit of measure]	Conditional cation exchange selectivity coefficient of Na^+ , index cation Na^+
$\log K_c Na/Eu$	[unit of measure]	Conditional cation exchange selectivity coefficient of Eu^{3+} , index cation Na^+
$\log K_{ClO_4^-}$	[unit of measure]	Coion association coefficient for negatively charged mineral surfaces, here: perchlorate coion
$\log K_{Eu}$		General notion for intrinsic Eu surface complexation constants without identification of specific surface complex, e.g. monodenate, bi-, tridentate, etc. – index Eu is independent of surface complex
$\log K_{Na^+}$	[unit of measure]	Counterion association coefficient for negatively charged mineral surfaces, here: sodium counterion
L		
L	[Å]	Shear plane distance
L	[m]	Length
L_{cell}	[m]	Cell length
$L_{C_{max}}$	[m]	Spatial position of the maximum Eu concentration C_{max}
λ	[–]	Surface roughness
λ	[m]	Dispersivity
LOQ	[mol L ⁻¹]	Limit of quantification
$LSOF$	[unit of measure]	Least squares objective function
M		
m	[–]	Slope
M	[g mol ⁻¹]	Molar mass

M	[g]	Solid mass
Me	[−]	Metal ion
ME	[unit of measure]	Mean error
N		
n	[−]	y-intercept
n	[−]	Number
N_A	[mol ^{−1}]	Avogadro constant (6.022140857 · 10 ²³ mol ^{−1})
N_{AX}	[−]	Molar fraction of exchange species A on the surface of an exchanger (X)
ND	[−]	Number of observations
Nf	[−]	Nernstian slope
n_j	[−]	Number of ligands j
NP	[−]	Number of estimated parameters
P		
p_0	[Pa]	Saturation vapour pressure
p	[Pa]	Partial pressure
PSD	[μm]	Particle size distribution
Pe	[−]	Péclet number
Pe_{grid}	[−]	Grid Péclet number
Δ_{pH}	[−]	Correction value of pH measurements in saline solutions (Hagemann et al., 2014)
pH_c	[−]	pH values that were corrected for electrolyte influences after Hagemann et al. (2014)
pH_{cip}	[−]	pH of common intersection point
pH_{IEP}	[−]	pH of isoelectric point
pH_{ini}	[−]	Initial pH value of a solution or suspension
pH_{max}	[−]	Maximum pH
pH_{mass}	[−]	Endpoint of mass titration experiments
pH_{min}	[−]	Minimum pH
pH_{nphe}	[−]	pH of point of zero net proton and hydroxide consumption
pH_{ppzc}	[−]	pH of pristine point of zero charge
pH_{pznpc}	[−]	pH of point of zero net proton charge

pH_{pzc}	$[-]$	pH of point of zero charge
pH_{pzse}	$[-]$	pH of point of zero salt effect
$\psi_{0,1,d}$	$[V]$	Electric surface potential of 0-plane, 1-plane, d-plane
ψ	$[V]$	Electric surface potential
psd	$[-]$	Parameter standard deviation
PSF	$[\mu\text{m}]$	Particle size fraction
PV	$[V/V_0]$	Pore volume: Amount of background electrolyte normalized to the pore space of the respective column ($PV = V/V_0$ with V $[\text{m}^3]$ volume of background electrolyte, V_0 $[\text{m}^3]$ pore space of each mineral-filled column)
$PV_{C_{max}}$	$[V/V_0]$	Peak/plateau concentration at $t = 0.5PV_{PS}$
$PV_{C_{max}}^*$	$[V/V_0]$	Pore volume of first concentration breakthrough of a Dirac function
PV_{PS}	$[V/V_0]$	Pore volume of pulse solution application
Q, R		
q	$[\text{cm h}^{-1}]$	Darcy velocity
q	$[-]$	Total relative adsorption of outer- and inner-sphere surface complexes but excluding H^+ contributions, also in $[\text{mol kg solid}^{-1}]$
q_-, q_+	$[-]$	Adsorbed anions and cations including outer- and inner-sphere surface complexes, also in $[\text{mol kg solid}^{-1}]$
Δq	$[-]$	Adsorbed ions with $\Delta q = q_+ - q_-$, also in $[\text{mol kg solid}^{-1}]$
R	$[\text{J (mol} \cdot \text{K)}^{-1}]$	Universal gas constant ($8.3144598 \text{ J (mol K)}^{-1}$)
R^2	$[-]$	Coefficient of determination
R_f	$[-]$	Retardation factor
ρ	$[\text{g cm}^{-3}]$	Specific mineral density
ρ	$[\text{Pa}]$	Vapour density at standard pressure
ρ	$[\text{bar}]$	Partial pressure at standard state
ρ_b	$[\text{g cm}^{-3}]$	Bulk density
RSD	$[\%]$	Relative standard deviation

S		
σ	$[\text{C m}^{-2}]$	Surface charge density
$\sigma_{0,1,d}$	$[\text{C m}^{-2}]$	Surface charge density at the 0-plane, 1-plane, d-plane
$\Delta\sigma$	$[\text{C m}^{-2}]$	Change of proton related relative surface charge density
σ_H	$[\text{C m}^{-2}]$	Coordinative surface charge density resulting from H^+ and OH^- adsorption
σ_{is}	$[\text{C m}^{-2}]$	Surface charge density caused by inner-sphere surface complexation processes
σ_{int}	$[\text{C m}^{-2}]$	Intrinsic surface charge density
σ_{max}	$[\text{C m}^{-2}]$	Maximum measured (relative) surface charge density
σ_{min}	$[\text{C m}^{-2}]$	Minimum measured (relative) surface charge density
σ_o	$[\text{C m}^{-2}]$	Permanent structural surface charge density
σ_{os}	$[\text{C m}^{-2}]$	Surface charge density caused by outer-sphere surface complexation processes
σ_p	$[\text{C m}^{-2}]$	Total surface charge density of a particle
σ_{sat}	$[\text{C m}^{-2}]$	Saturation surface charge density
σ_{Stern}	$[\text{C m}^{-2}]$	Stern layer surface charge density ($\sigma_{Stern} = \Delta q - \sigma_d$)
SE	[unit of measure]	Standard error
SI	$[-]$	Saturation index ($\log_{10}(IAP/\log K)$)
SLR	$[\text{g L}^{-1}]$	Solid-liquid ratio
$S - \text{OH}_2^x$	$[-]$	Protonated surface functional group, x = respective charge (x = +1 silanol sites, x = +0.5 aluminol sites)
$S - \text{OH}$	$[-]$	Neutral surface functional group
$S - \text{O}^x$	$[-]$	Deprotonated surface functional group, x = respective charge (x = -1 silanol sites, x = -0.5 aluminol sites)
sol	$[-]$	Index for species in solution
SSA	$[\text{m}^2 \text{ g}^{-1}]$	Specific surface area

SSA_{BET}	$[\text{m}^2 \text{g}^{-1}]$	Specific surface area after Brunauer et al. (1938)
SSD	$[\text{sites nm}^{-2}]$	Surface site density
T		
T	$[\text{K}]$	Absolute temperature
t	$[\text{h}]$	Time
θ	$[-]$	Fractional occupancy of surface sites
θ	$[-]$	Porosity
V		
V	$[\text{m}^3]$	Volume
v	$[\text{cm h}^{-1}]$	Pore water velocity, water flow velocity
v	$[-]$	Charge per bond (Pauling's bond valence rules)
V_0	$[\text{cm}^3]$	Total pore space of a column
Δv	$[\text{cm h}^{-1}]$	Difference between measured and fitted pore water velocity
v_m	$[\text{m}^3]$	Volume of molecules adsorbed in one mono-molecular layer
V_{tot}	$[\text{cm}^3]$	Empty column volume: 167.7 cm^3
W – Z		
ω_i	$[-]$	Weight of the i th observation
x	$[\text{m}]$	Spatial position/location
y_i	$[\text{unit of measure}]$	Observation matched by regression
y'_i	$[\text{unit of measure}]$	Simulated value of the i th observation
z	$[-]$	Charge/valence
Δz	$[-]$	Charge/valence difference
$\Delta z_{0-,1-plane}$	$[-]$	Charge distribution over the 0-plane, 1-plane (Pauling's bond valence rules)
z_{H+}	$[-]$	Charge of a proton: $z_{H+} = 1$
z_j	$[-]$	Charge of ligands ($z = 0$ for OH_2^0 , $z = -1$ for OH^{-1} , $z = -2$ for O^{-2})
z_{Me}	$[-]$	Valence of metal ion Me

Introduction

"God made the bulk; surfaces were invented by the devil"

— Wolfgang E. Pauli

1.1 Relevance of the study

In Germany, the disposal of radioactive waste in deep geological formations is currently considered to be most feasible and suitable to safely contain low (LLW) and intermediate level (ILW) radioactive waste with negligible heat generation and high level, heat-generating radioactive waste (HLW) (Bouby et al., 2010a). The Morsleben site and the Konrad mine were chosen to dispose LLW and ILW. At the moment, the waste repository Morsleben is in the licensing procedure of decommissioning (Stelljes, 2016a), Konrad finished the plan-approval procedure in 2007 and has been under reconstruction and preparation for the emplacement of LLW and ILW ever since (Stelljes, 2016b). A potential site for the disposal of HLW is still being selected according to the Site Selection Act from 2013 (Standortauswahlgesetz - StandAG (2013), revised version 2017: Act on the search for and selection of a site for a disposal facility for heat-generating radioactive waste, BMUB (2015)).

In 1974 a site selection process for LLW, ILW, and HLW had begun focusing on salt domes in the Northern Plain of Germany. Five years later the Gorleben salt dome was chosen and first explorations took place which were carried out until the year 2000 when a moratorium ended all aboveground and underground activities; then in 2012, the Gorleben exploration mine was completely closed (Fischer-Appelt et al., 2013). After the nuclear accident in Fukushima in 2011 the nuclear phase-out was accelerated in Germany planning to terminate the commercial generation of electricity from nuclear power at the latest in 2022. As a consequence, the Site Selection Act from 2013 (Standortauswahlgesetz - StandAG, revised version 2017) was passed which regulates a new site selection process for a final repository storage

for HLW in Germany where all potential sites and host rocks (crystalline rock, clay rock, rock salt) are considered anew (BMUB, 2015).

The safe containment in the so-called containment providing rock zone (CPRZ) has to be shown for the site selection process in Germany and includes, amongst others, safety analyses and a safety assessment covering a time period of 1 mio years (BMUB, 2015). An important aspect of the safety assessment and analysis is the transport of radionuclides (RNs) through the CPRZ where numerical models are used to describe flow and transport processes of relevant RNs. Sorption (adsorption, absorption, cation exchange) is a fundamental retardation process contributing to the isolation capacity of the technical (waste matrix, container), geotechnical (backfill), and geological (rock formation) barriers of a repository (Noseck et al. (2012), Bouby et al. (2010a)). Besides sorption further geochemical processes such as dissolution and precipitation reactions, hydrolysis, redox reactions, and/or e.g. colloid formation may also contribute to mobilization or immobilization of RNs. For long-term safety analyses of potential radioactive waste repositories the transport of RNs is commonly considered for the entire repository system although in Germany the safety assessment focuses on the proof of a safe containment of the waste in the CPRZ. However, mobilization scenarios of RNs and their transport through the entire repository system cannot be neglected and has to be considered. A repository system is divided in three self-contained systems: The near field including the repository and part of the host rock formation (contaminant providing rock zone); the far field which describes the geological formation and the overburden (if present), and the biosphere. Each individual system needs thorough characterization and definition to adequately simulate and assess migration and retardation processes with numerical transport models. For safety analyses, it is one aim to geochemically soundly characterize RN retardation and migration to predict different hypothetical release scenarios from repository systems as close to nature as possible and to be finally able to assess the safety of the potential repository site (Bouby et al., 2010a).

Currently, spatially and temporally constant sorption coefficients (distribution coefficients - K_d values) are used in numerical transport models to describe mobilization and immobilization of RNs in the field of long-term safety analyses. However, over the considered time period of 1 mio years it is most likely that spatially and temporally changing geochemical conditions occur which in return influence sorption and migration behaviour of RNs resulting in variable K_d values over time and space. Hence, a transient description of retardation and migration processes depending on

the geochemical surrounding seems to be favourable compared to constant descriptions. The approach of transient K_d values has been proposed and addressed in the joint research projects ESTRAL (Realistic implementation of sorption processes in transport codes for long-term safety analyses, grant numbers 02E10518, 02E11072A) funded by Federal Ministry of Economics and Energy (BMWi) and WEIMAR (Further development of the smart- K_d approach for long-term safety analyses; grant numbers 02E10528, 02E11072B, BMWi) performed by the Gesellschaft für Anlagen- und Reaktorsicherheit gGmbH and the Helmholtz-Zentrum Dresden-Rossendorf e.V. In a first step, it was the scope to develop the concept of variable K_d values, so called smart K_d values, to describe RN transport in the far field of a potential radioactive waste repository, exemplarily considering a sedimentary site in Northern Germany (Noseck et al., 2012). Since vast amounts of geophysical, hydraulic, mechanic, and mineralogical data as well as data from in-situ and laboratory experiments had been collected for the Gorleben site between 1979 - 2000 (Fischer-Appelt et al., 2013) the new approach of smart K_d values was exemplarily developed for the overburden of the Gorleben salt dome which mainly consists of tertiary and quaternary sands and minor contributions of argillaceous to silty components. Quaternary sands are mainly composed of quartz (85 wt%) and feldspars (15 wt%); whereas clay fractions, calcite, feldspar, muscovite, and accessory minerals contribute to the argillaceous to silty sediments (Klinge et al., 2002).

This thesis was part of the joint research project WEIMAR and contributed to fill the gap of knowledge regarding trivalent actinide sorption on quartz, muscovite, and orthoclase under different geochemical conditions. The trivalent lanthanide europium (Eu) is a chemical homologue for trivalent actinides such as Cm(III) and Am(III) (Geckeis et al. (2013), Lee et al. (2006)) which are produced in a nuclear reactor by neutron capture reactions and are, hence, relevant for long-term safety assessments of nuclear waste disposal sites. In this study, Eu was also used as a geochemical homologue to gather information on Eu retardation and migration under varying geochemical environments which will be used to simulate mobilization and immobilization processes of trivalent actinides with numerical transport models for long-term safety analyses. From the model perspective, there are two general approaches to describe retardation and transport processes: On the one hand, empirical models were developed which are directly based on observations and extensive measurements such as e.g. the linear K_d approach or the Langmuir sorption isotherm; on the other hand, recent, more sophisticated mechanistic model

approaches (thermodynamic sorption models) are based on profound thermodynamic system understanding including mechanistic descriptions of surface complexation but also considering cation exchange, solution speciation, and e.g. precipitation reactions (surface complexation models). With mechanistic approaches exact definitions of the solid solution interface exist which are represented with e.g. the diffuse double layer model (DDLm), the constant capacitance model (CCM), the basic Stern model (BSM), triple layer models (TLMs), or e.g. non-electrostatic models (noEDLMs). All of the latter include sorption and speciation processes with defined geochemical reactions. Whether these mechanistic models of the solid-solution interface represent realistic or even close to nature conditions is still under discussion; however, so far they display the current theory of the structure of mineral surfaces on the molecular scale.

For the application of surface complexation models (SCM) two common approaches exist to mechanistically consider sorption processes at mineral and sediment surfaces: the generalized composite (GC) and the component additivity (CA) approach (Davis et al., 2001). The GC approach describes a sediment surface without consideration of single contributions of individual mineral phases but as one assemblage. Following this approach, one generic surface site is assumed describing sorption processes on the assemblage surface. The more sophisticated CA approach on the other hand considers each mineral phase of the assemblage (e.g. sediment) individually where each surface is included with an independent, mineral-specific definition (Davis et al., 2001). For the CA approach an extensive amount of data covering solid-solution interface reactions for each mineral phase is a prerequisite. Since the availability of consistent and reliable data is often a limiting factor, the application of one or the other approach needs thorough evaluation especially considering complex natural systems. Many studies have applied the CA approach to mineral assemblages and/or natural sediments with many of them reporting good or reasonably good agreement between predicted data and measurements in the range of experimental conditions (e.g. Goldberg et al. (2007), Voegelin et al. (2001)). However, it is obvious that the predictive capability of the CA approach is limited to how well a system is defined and that the applicability of this complex approach might decrease as the complexity of the systems increase e.g. considering ternary complexes, a multitude of organic matter, colloids, and/or e.g. mutual interactions between different surfaces and phases (e.g. Alessi and Fein (2010), Bruggeman et al. (2010)).

The present study, aimed to contribute to the CA approach to mechanistically

describe Eu surface complexation, cation exchange, and precipitation reactions individually at each mineral-water interface. Therefore, surface charge models and SCMs were developed to derive surface complexation parameters (SCPs) from titration and batch experiments, respectively, for each considered mineral phase. The SCPs were then used in reactive transport models (RTMs) to predict Eu migration under different geochemical conditions. The term thermodynamic sorption model (TSM) is an umbrella term describing mechanistic surface charge models and SCMs including precipitation, cation exchange, solution speciation reactions, etc.

Although, orthoclase, muscovite, and quartz are well known minerals, to different degrees there is still a big gap of data and knowledge of solid-solution interface reactions such as surface charge development, surface complexation, and exchange reactions for these ubiquitously present minerals. Some studies dealt with the characterization of the acid-base behaviour of quartz surfaces providing sound and comprehensive measurements for the determination of the surface charge development of a silica surface. An often-applied literature data set was collected by Bolt in 1957 who used amorphous silica to describe surface protolysis reactions at different ionic strengths (ISs) covering pH values between 3 - 10. Hiemstra et al. (1989b) used this data set, for example, to introduce and parametrize their realization of the basic Stern model (BSM) with the mechanistic TSM approach called CD-MUSIC (charge distribution multi site complexation). For orthoclase and muscovite on the other hand, data is scarce and the few published measurements in literature show great scatter making comparisons or the definition of acid-base behaviour challenging for these minerals (Zorn (2000), Stillings et al. (1995), Maslova et al. (2004), Baeyens and Bradbury (1997)). Since the determination of e.g. protolysis constants depends on surface charge measurements from titration experiments it is not surprising that the few available parameter sets also differ with respect to collected data leaving no sound basis to judge which set of measurements or parameters should be preferred.

In comparison to experimental titration data, even less measurements are available of sorption processes involving Eu or chemical homologues on muscovite, orthoclase, or quartz; and also only few studies have taken the approach to determine the structure of surface complexes under varying geochemical conditions on these mineral surfaces with spectroscopic means (e.g. Stumpf et al. (2006)). Mechanistic model approaches, however, depend on the sound characterization of the surface complex structure to correctly integrate these complexes in modeling procedures. Recently, Pan et al. (2017) have published sorption (batch experiments) and spectroscopic

data of Eu on muscovite using different background electrolytes and including ligand influence. They postulated that cation exchange processes influence Eu take up at low pH values and found surface complexation reactions to occur as pH conditions rose. Bradbury et al. (2005) developed a very complex SCM using three surface complexation sites and one exchange site to describe Eu sorption on montmorillonite. For quartz, some Eu sorption data sets exist but mostly with different geochemical boundary conditions and none of the published literature provide sound SCPs to describe the uptake of Eu on quartz surfaces. For orthoclase no SCPs of Eu have been published so far and only few studies examined the structure of surface complexes of e.g. Eu or chemical homologues at the feldspar solid-solution interface (e.g. Stumpf et al. (2006)). Hence, in addition to the absence of comprehensive sorption data of trivalent actinides or lanthanides, also no clear consensus exists regarding the structure of Eu surface complexes on muscovite, orthoclase, or quartz solid-solution interfaces under varying geochemical conditions. Some spectroscopic evidence has been collected during the past decade (e.g. Stumpf et al. (2006), Stumpf et al. (2008), Pan et al. (2017)) but since surface complexation and hence the formation of surface complexes is strongly dependent on the geochemical surrounding it is obvious that not all surface reactions involving Eu or chemical homologues have been characterized or even uncovered yet.

Since sound and comprehensive data is a prerequisite to realistically assess and predict transport processes it is challenging to describe retardation and migration of trivalent lanthanides or actinides at the present state of knowledge. Consequently, only few studies have tried to mechanistically describe transport processes of Eu or chemical homologues and to the authors knowledge only one study predicted Eu transport based on batch experimental data under conditions relevant for a radioactive waste repository: Bruggeman et al. (2010) collected sorption isotherms of Eu trace concentrations under anoxic conditions in sodium hydrogen carbonate background electrolyte on illite in the presence of Boom Clay natural organic matter. They used the CA approach to describe Eu retardation and successfully predicted Eu transport with acceptable discrepancies between simulated and experimental data ($0.5 \log K_d$ units, cf. Davis et al. (2005)). So far, no studies have been published describing trivalent lanthanide or actinide transport experiments that were used to validate predictions based on mechanistic model approaches for close to nature or artificial conditions for muscovite, orthoclase, quartz, or a comparable sediment. However, speciation, sorption, and transport of other relevant actinides such as uranium(VI) have been studied in detail in the past: Kohler et al. (1996), for example, published

transport data of uranium(VI) through quartz columns under different geochemical conditions. They used RTMs based on batch experiments to, amongst others, predict uranium(VI) transport and reported satisfying simulations for most geochemical conditions. Davis et al. (2001) dedicated an entire report on uranium(VI) surface complexation on natural mineral assemblages. However, for trivalent actinides and lanthanides such publications and comprehensive work is lacking.

1.2 Objectives of the thesis

This thesis illustrates the stepwise approach to reactive transport simulations of Eu under artificial and close to nature geochemical boundary conditions: In a first step, the measurement of surface charge development and the modeling of the acid-base behaviour (mechanistic surface charge models) is addressed. The results of this preliminary step are mandatory to describe Eu surface complexation based on sorption experiments with mechanistic SCMs in a second step. The third part of this approach combines surface charge models and SCMs to develop RTMs which are used to predict Eu reactive transport processes. Each step comprised different scopes which in sum contributed to the general objectives.

The main objective of this thesis was the development of RTMs for muscovite, orthoclase, quartz, and a synthetic sediment to predict the reactive transport of the trivalent lanthanide under different geochemical conditions in order to verify or disprove the following hypotheses:

- Sorption and immobilization processes of Eu observed during batch experiments are comparable to migration and retardation processes of the trivalent lanthanide during column experiments. Hence, K_d values determined from batch experiments are comparable to K_d values obtained from column experiments under similar geochemical conditions.
- Reactive transport models (RTMs) which are based on SCMs (batch sorption data) adequately predict Eu transport through mineral filled columns under varying geochemical conditions in the range of experimental data.
- Using the CA approach it is possible to predict Eu transport through a synthetic sediment based on data from titration and batch experiments from individually contributing single mineral phases.
- Including state-of-the-art spectroscopic data from literature it is possible to identify Eu surface complexation reactions and, hence, Eu surface complexes

with SCMs that govern retardation and transport of the trivalent lanthanide under different geochemical boundary conditions.

This work contributes to fill the gap of knowledge and data of trivalent lanthanide and actinide sorption processes on ubiquitously present minerals such as muscovite, orthoclase, and quartz. The thesis provides missing SCPs for long-term safety relevant minerals, it offers valuable insight into surface charge development of these silicates, provides comprehensive transport data of Eu through mineral filled columns under saturated, steady state conditions, gives insight into the stepwise development of reactive transport models, and highlights open questions.

1.3 Outline

This thesis is structured into five sections (Sec. 1 - Sec. 5) which illustrate the stepwise approach to predict the reactive transport of Eu (Fig. 1.1). Except for the introduction (Sec. 1) and the conclusions (Sec. 5) each section is composed of an individual introductory part to the specific topic, a theoretical background section is included where necessary, materials and methods are provided in a separate section, which is followed by the results, discussion, and a summary for each section (Sec. 2 - Sec. 4).

The introduction of this thesis (Sec. 1) provides information regarding the relevance of the study, objectives, and finally the outline of the thesis.

Section 2 deals with the determination and processing of surface charge data based on titration experiments. The development of surface charge models is illustrated and the fitting procedure of SCPs with the parameter estimation code UCODE (Poeter et al., 2005) in combination with the speciation code PHREEQC (Parkhurst and Appelo, 2013) is depicted (Fig. 1.1). Different model approaches are illustrated and SCP sets presented.

In Section 3, the experimental set-up and results of batch experiments are described and the development of Eu SCMs as well as the optimization procedure of Eu surface complexation constants ($\log K_{Eu}$) is presented. As illustrated in Figure 1.1, SCMs depend on SCPs from surface charge models. Hence, Section 2 is a prerequisite for the development of mechanistic Eu SCMs.

Finally, in Section 4 transport experiments are presented and the development of RTMs is described. Reactive transport models are the synthesis of surface charge

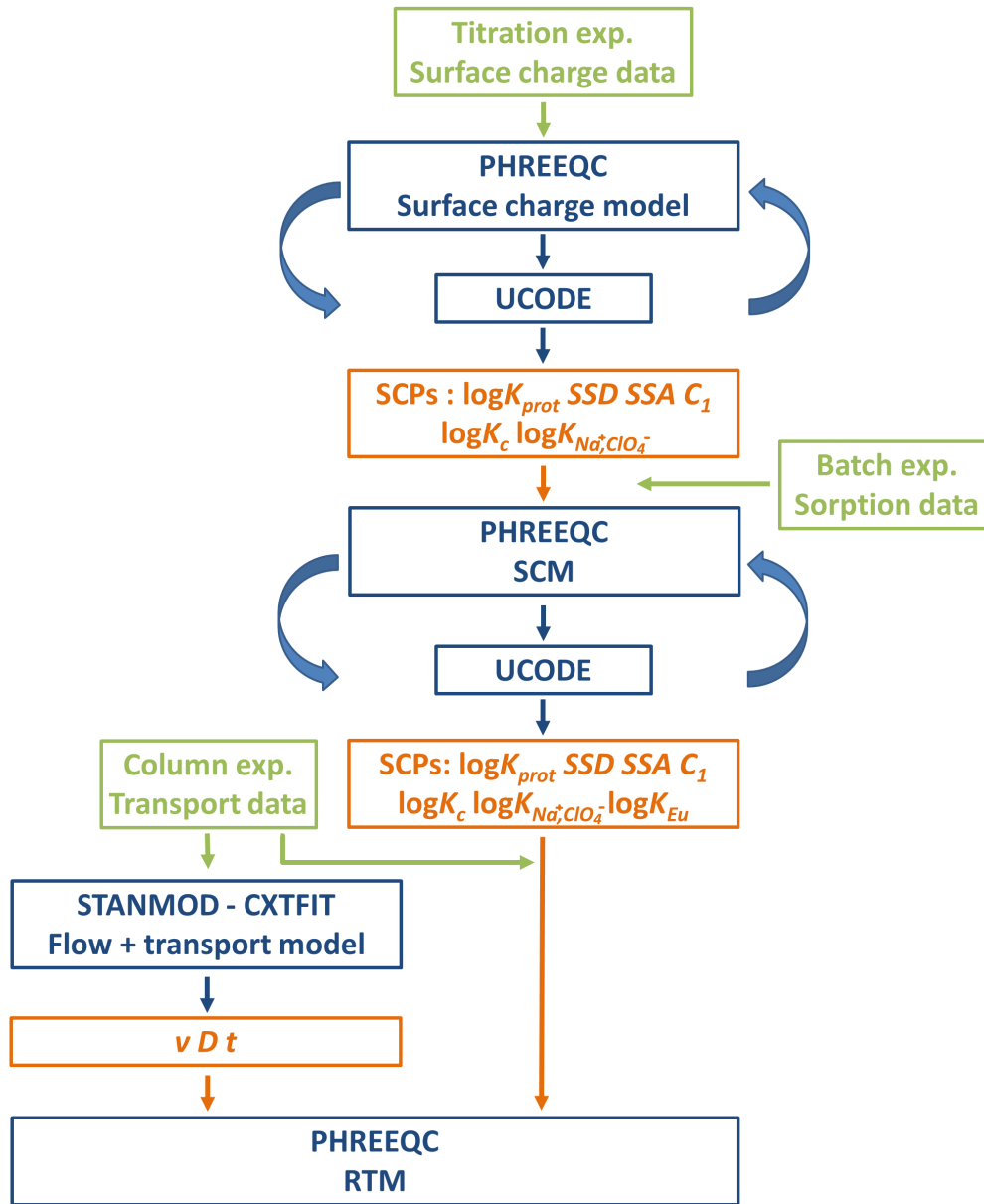
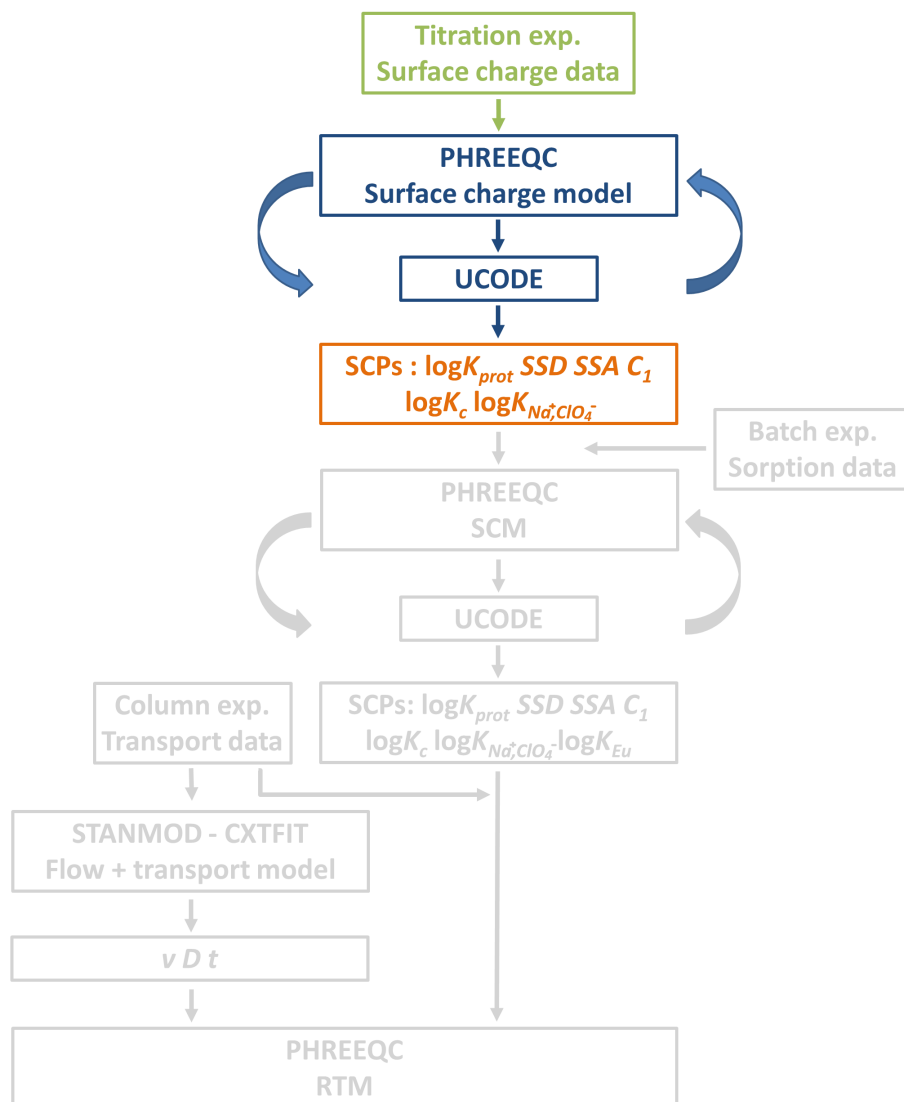


Fig. 1.1: Stepwise approach of titration, batch, and column experiments to develop RTMs for the prediction of Eu reactive transport with surface complexation parameters (SCPs) based on surface charge and sorption measurements. **Green** – experimental input data, **orange** – derived SCPs: protolysis constants ($\log K_{prot}$), surface site density (SSD), specific surface area (SSA), capacitance (C_1), conditional cation exchange coefficients ($\log K_c$), co- and counterion association coefficients ($\log K_{Na^+, ClO_4^-}$), Eu surface complexation constant ($\log K_{Eu}$), pore water velocity (v), application time (t), dispersion coefficient (D), **blue** – used codes and models, surface complexation model (SCM), reactive transport model (RTM).

models and SCMs and rely on soundly determined SCP sets from surface charge (Sec. 2) and sorption measurements (Sec. 3, Fig. 1.1). Besides RTMs, the application of the CXTFIT code (Toride et al., 1998) is illustrated in Section 4 and the determination of transport parameters is discussed. Parameters from all three model approaches (CXTFIT inherent transport model, surface charge models, SCMs) were used for reactive transport simulations of Eu where each final SCP set defined an individual RTM. Simulation results of RTMs are discussed and presented in detail.

The final conclusions presented in Section 5 offer a summarizing overview of conducted experiments, set results as well as main findings into relation to one another, and summarize final conclusions, success, and challenges of this study. Future perspectives and identified gaps of data are highlighted.

Mineral surface charge properties: Experiments and inverse modeling



2.1 Introduction

Precise knowledge of acid-base behaviour of mineral surfaces can be of great importance to realistically describe sorption processes since retardation processes (sorption, precipitation, etc.) of the majority of relevant radio nuclides (RN) are pH dependent. Potentiometric acid-base titration experiments of mineral surfaces have been widely applied (e.g. Arnold et al. (2001), Lützenkirchen et al. (2012 a), Lützenkirchen et al. (2012 b), Schwarz et al. (1983)) to characterize mineral electrostatic behaviour in terms of points of zero charge, surface charge densities, and net surface proton excess. This study combines three state-of-the-art titration techniques to characterize mineral surface charge properties.

Discontinuous electrolyte and mass titration experiments in combination with continuous potentiometric acid-base titrations were used to get insight in mineral surface protonation and deprotonation states as a function of e.g. pH, ionic strength (IS), and solid-liquid ratio (SLR). For many pure mineral oxides all three techniques result in identical pH values (pH_{ppzc}) where the surface charge density (σ [$C\ m^{-2}$]) is zero (Sec. 2.2.3). Natural or highly complex mineral surfaces do not exhibit a pH_{ppzc} due to intrinsic mineral characteristics (e.g. Lützenkirchen et al. (2012 a), Preočanin and Kallay (1998), Noh and Schwarz (1988)); hence, the definition of surface charge properties of these minerals proves to be rather challenging.

Besides gathering experimental data, their interpretation, evaluation, and simulation are key aspects of this thesis. To realistically describe complex geochemical processes in hard rock or sedimentary environments deterministic thermodynamic sorption models (TSMs) have been developed over the past approximately 50 years. Deterministic TSMs describe mineral-water interfaces during sorption processes and simulate thermodynamic processes such as protonation and deprotonation reactions (Sec. 2.4.3), surface complexation (Sec. 3, Sec. 4), cation exchange processes, surface precipitation, and dissolution processes, as well as solution speciation. The notion "deterministic" refers to models that are governed by parameters and predefined initial model boundary conditions. No randomness or stochastic correlations are included. Uncertainties are external to the deterministic model. Therefore, utilized parameter values, material properties, system boundary conditions, etc. should be well known.

Surface complexation parameters (SCPs) are utilized to describe thermodynamic processes (inverse modeling) and to physicochemically characterize system

properties with TSMs. These SCPs are determined from, e.g., titration experiments. Here, SCPs comprise protonation and deprotonation constants (pK values), conditional cation exchange equilibrium coefficients (selectivity coefficients $\log K_c$), counter- and coion associations coefficients (here for Na^+ and ClO_4^- : $\log K_{\text{Na}^+, \text{ClO}_4^-}$), the surface site densities (*SSDs*), capacitances (C_1 , C_2), and the specific surface area (*SSA*).

This section focusses on experimental details of titration experiments, the interpretation of mineral titration data via the geochemical speciation code PHREEQC (Version 3.1.2-8538, Parkhurst and Appelo (2013)), the development of deterministic surface charge models, inverse modeling approaches, and finally the determination of SCPs.

2.2 Theoretical background

The following summarizing sections intend to outline the theoretical background and provide relevant definitions. First, the utilized TSMs are briefly introduced (Sec. 2.2.1); then, the definition of protolysis constants are outlined (Sec. 2.2.2), followed by the definitions and notions of mineral surface charge properties and points of zero charge (Sec. 2.2.3). The determination of the *SSA* and *SSD* are given in Sections 2.2.4 and 2.2.5, respectively. More detailed outlining of theories and background information can be found in the mentioned literature. Additional information is summarized in the appendix (App. A.1 and App. A.2.1).

2.2.1 Electrostatic interface models: Brief overview of theory

Two types of general model approaches exist to describe sorption and desorption processes at solid-solution interfaces: a) empirical relationships such as Langmuir (1918), Freundlich (1922) and b) conceptual TSMs that describe ion-surface associations based on mechanistic approaches to characterize coordinative properties of surface complexes (e.g. diffuse double layer model, basic Stern model, etc.). Approaches from Langmuir (1918) and Freundlich (1922), as well as TSMs assume a thermodynamic equilibrium between the solid and the surrounding electrolyte. In the present study mechanistic TSMs were applied.

Different TSMs have been postulated to describe the solid-solution interface during sorption processes. In this study, TSMs that are referred to as surface charge

models focus on the determination of mineral surface charge properties (Sec. 2.2.1); TSMs that are used to calculate defined surface complexation processes of e.g. metal cations are called surface complexation models (SCMs) (Sec. 3). Each surface charge or surface complexation model is characterized by an individual set of SCPs. TSMs extend the ion-association theory of aqueous species to surface species (Davis and Kent, 1990b) through thermodynamic equilibrium reactions using measurements of *SSAs* and mostly estimated *SSDs*. Surface processes comprise protolysis reactions, surface complexation reactions, cation exchange, and anion binding (Dzombak and Morel, 1990). The present study used different TSMs: the diffuse double layer model (DDLM), a non-electrostatic model (noEDLM, EDL electric double layer), and the basic Stern model (BSM). Besides the DDLM, noEDLM, and BSM, the constant capacitance model (CCM), triple layer models (TLMs), and three plane models (TPMs) are widely used TSMs. All TSMs are based on mass law equations (Eq. 2.6 - Eq. 2.7, Sec. 2.2.2) and mole balance equations (Davis and Kent, 1990b), but involve different descriptions of the electric double layer, i.e. electrostatic interaction term (Davis and Kent (1990b), Westall and Hohl (1980)). In the noEDLM the electrostatic interaction term is not considered at all; thus, a diffuse double layer does not exist. Each TSM (except noEDLMs) considers different electrostatic planes that are prone to sorption processes.

The electrostatic (interaction) term corrects for the effect of varying surface charges and surface ionization; hence, for variations of effective mass law constants (Dzombak and Morel (1990)). It originates from the total free energy of sorption G_{tot}^o which is defined as the sum of the chemical (intrinsic) free energy G_{int}^o and the variable electrostatic term. A theoretical description of the electrostatic term is provided in Equation 2.1 (Dzombak and Morel, 1990), where F denotes the Faraday constant [C mol^{-1}], ψ the electric surface potential [V], and Δz the change of charge.

$$\Delta G_{tot}^o = \Delta G_{int}^o + \Delta z F \psi \quad (2.1)$$

Since $\Delta G^o = -RT \ln K$, where K symbolizes an equilibrium constant, T the absolute temperature [K], and R the universal gas constant [$\text{J (mol} \cdot \text{K)}^{-1}$] the following equation can be deduced from Equation 2.1 via substitution (Dzombak and Morel, 1990)

$$K^{int} = K^{app} \cdot e^{(\Delta z F \psi / RT)} \quad (2.2)$$

Here, K^{app} represents the apparent (effective/total) equilibrium constant including surface charge effects, K^{int} stands for the intrinsic equilibrium constant that does not depend on surface ionization (Dzombak and Morel, 1990).

To create a sound and consistent basis for discussions a brief theoretical overview of utilized TSMs is provided in the following.

The diffuse double layer model (DDLDM, Gouy-Chapman theory)

Surface complexation is considered as specifically sorbed, inner-sphere complexes in the DDLDM. Co- and counterions originating from e.g. solution speciation are accumulated or depleted in the so called diffuse layer (Fig. 2.1, Gouy-Chapman diffuse layer theory). The inner plane of the diffuse layer originates at the closest distance of approach of counterions (0-plane, Fig. 2.1, Davis and Kent (1990b)). The diffuse layer charge compensates the surface charge of the 0-plane. The diffuse layer potential is related to the diffuse layer charge and decreases towards the bulk of the solution (Appelo and Postma (2010), Ohshima (2006), Westall and Hohl (1980)). The thickness and the charge of the diffuse layer approximately relates to the square root of the ionic strength (IS): The higher the IS of the solution, the smaller the diffuse layer thickness (Debye-Hückel length). The zeta-potential is often considered as a good estimate of the diffuse layer potential even though it is probably more realistic that zeta-potential measurements reflect the electrical potential at a defined but unknown distance L (shear plane) within the diffuse layer (Lützenkirchen et al. (2012 b), Dzombak and Morel (1987)).

The Gouy-Chapman diffuse double layer theory considers ions as point charges, without a specific spatial volume. As a result, calculated diffuse layer potentials often exceed zeta-potential measurements (Dzombak and Morel, 1990). Figure 2.1 illustrates Gouy-Chapman relations between the surface charge and surface potential.

The basic Stern model (BSM)

The BSM used in this study follows specifications published by Stern (1924) and Hiemstra and van Riemsdijk (1996). Figure 2.1 illustrates the double layer structure of the BSM. Each plane is characterized by an electrostatic potential and electric charge. Protolysis reactions of silanol and aluminol surface functional groups are assigned to the 0-plane and contribute to the charge density σ_0 and the electrostatic potential ψ_0 (Fig. 2.1). Specific sorption of inner-sphere complexes take place in the Stern layer. Ligands of the specifically sorbed central metal ion may coordinate towards the

0-plane but also towards the bulk of the solution. Ligands of central cations that are orientated towards the bulk solution are considered to accumulate in the 1-plane. This plane holds the electrostatic potential ψ_1 and the charge density σ_1 (Fig. 2.1). The double layer in this model originates at the d-plane (Fig. 2.1). The distance between the 0-plane and d-plane is characterized by the closest approach of hydrated counter- and co-ions. In the BSM theory (Stern, 1924) the 1-plane coincides with d-plane. Counterions (cations in terms of negatively charged surfaces) may be electrostatically bound (unspecifically sorbed) as outer-sphere complexes. In the BSM, C_1 is the only model inherent capacitance for the layer between the 0- and 1-planes (Stern layer). Under consideration of charge-potential relationships of Equations 2.3 and 2.4 $C_2 \rightarrow \infty$ (Kallay et al., 2006) and the BSM is retrieved.

$$C_1 = \frac{\sigma_0}{\psi_0 - \psi_1} \quad (2.3)$$

$$C_2 = \frac{\sigma_1}{\psi_1 - \psi_d} \quad (2.4)$$

C_2 [F m^{-2}] corresponds to the capacitance of TLM and TPM, σ_0, σ_1 [C m^{-2}] to the surface charge densities of the 0-plane and 1-plane, and ψ_0, ψ_1, ψ_d [V] to the electric potentials of the respective planes.

In order to implement ligand orientation towards the 0-plane or towards the bulk solution (1-plane/d-plane) Pauling's charge distribution concept is applied in this study (cf. Sec. 2.2.2).

Non-electrostatic model (noEDLM)

The noEDLM was applied as a simple model approach to compare results of more sophisticated, complex approaches to a straightforward simple concept. The noEDLM does not involve electrostatic terms; all sorption processes result in inner-sphere (specifically sorbed) surface complexes. The surface complexation reactions correspond to thermodynamic equations used in the DDLM or BSM (Sec. 3, Input file code block 3.1).

Different noEDLM approaches exist. In this study, no protolysis reactions were considered, and all surface functional groups are conceptionally treated in the same way as solution species (Davis and Kent, 1990b). This theoretical approach is justified since for specifically sorbing cations the chemical contribution to the free

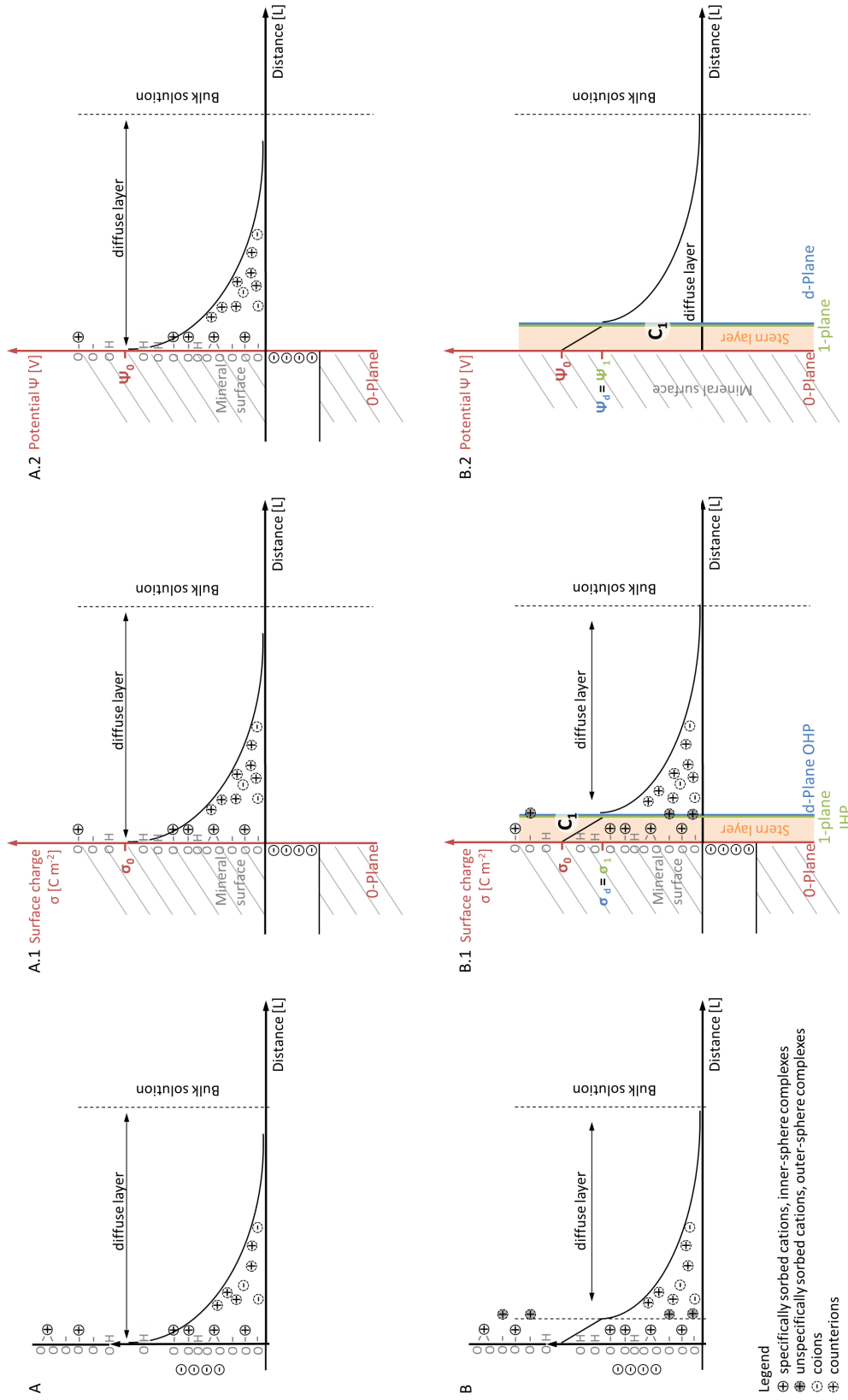


Fig. 2.1: Schematic illustration of the DDLM (A) and the BSM (B). A, B illustrate counterion distribution of the DDLM and the BSM. A.1, A.2 and B.1 and B.2 represent surface charge density σ [Cm⁻²] and surface potential ψ [V] development of the DDLM and the BSM, respectively. C_1 stands for the capacitance between the 0-plane and 1-plane, IHP for inner Helmholtz plane, OHP for outer Helmholtz plane.

energy of adsorption (Eq. 2.1) overrules the electrostatic interaction term (Davis and Kent, 1990b). Included sorption processes comprise surface complexation and cation exchange reactions.

2.2.2 1-pK vs. 2-pK approach: Surface protolysis reactions

From a historic perspective, two theoretical concepts have evolved to describe surface charge properties by means of surface acidity over the past 50 years: the classical so called 2-pK (Eq. 2.5, Eq. 2.6) and the more recent 1-pK approach (Eq. 2.23, Eq. 2.24). The pK values of these two approaches define protolysis equilibrium constants ($\text{pK} = -\log_{10}K$) of the protolysis reactions of surface functional groups differently.

According to Hiemstra (2010), the 2-pK approach was introduced in 1968 by Hingston et al. and considers protonation and deprotonation reactions of surface silanol functional groups. The 1-pK concept represents a further or alternative development where only one surface reaction is considered (Bolt and van Riemsdijk, 1979). Extensive studies have been conducted to examine the amphoteric behaviour of mineral oxides via titration experiments and subsequent model application (e.g. Lützenkirchen (1998), Kitamura et al. (1999), Wang and Anderko (2001), Bradbury and Baeyens (2009)). The term "amphoteric" describes surface functional groups that act as proton acceptors and donors (Davis and Kent, 1990b). To the author's knowledge only very few articles compare the application of both approaches to illustrate advantages and deficits of one or the other (e.g. Lützenkirchen (1998)). There seems to be no clear consensus which concept represents surface acidity as close to the molecular origin as possible. In the past, the 2-pK concept has been favoured resulting in major data collections of protonation and deprotonation constants of a vast amount of mineral surfaces (e.g. RES³T, www.hzdr.de/res3t, Brendler et al. (2003)). However, nowadays tendencies towards a preferred application of the 1-pK approach exist. The reasons will be illustrated in the following.

The 2-pK approach distinguishes between the first and second step of protonation, or, to put it in a different way: The 2-pK approach describes the deprotonation and protonation of neutral surface functional silanol groups (S-OH). Equations 2.5 and 2.6 represent surface protolysis reactions of the 2-pK approach as applied in this study. Respective intrinsic mass law equations are given in Equations 2.7 and 2.8.





Thus, from Equation 2.5 it follows

$$K_{a1}^{int} = \frac{[S - OH_2^+]}{[S - OH]\{H^+\}} \quad (2.7)$$

while Equation 2.6 yields

$$K_{a2}^{int} = \frac{[S - O^-]\{H^+\}}{[S - OH]} \quad (2.8)$$

$S-O^-$, $S-OH$, $S-OH_2^+$ represent deprotonated, neutral, and protonated silanol surface functional groups, $[]$ indicate concentrations, and $\{ \}$ activities. So far, no theoretical concept has been developed to describe the activity of surface functional groups. Therefore, the activity coefficient ($\gamma [-]$) of surface species was set unity. This approach also agrees well with γ of solids and substances in abundance where $\gamma = 1$. To account for electrostatic work in the solid-solution electrostatic interfacial gradient the variable electrostatic term $e^{-F\psi/RT}$ is included (Sec. 2.2.3). The electrostatic term converts intrinsic stability constants $K_{a1,2}^{int}$ into apparent ones $K_{a1,2}^{app}$ (Eq. 2.9, Eq. 2.10, Dzombak and Morel (1990)).

$$K_{a1}^{int} = K_{a1}^{app} \cdot e^{-F\psi/RT} \quad (2.9)$$

$$K_{a2}^{int} = K_{a2}^{app} \cdot e^{-F\psi/RT} \quad (2.10)$$

F denotes the Faraday constant [$C \text{ mol}^{-1}$], T absolute temperature [K]. ψ stands for the surface potential [V], R for the universal gas constant [$J \text{ (mol K)}^{-1}$] (Dzombak and Morel, 1990). In this study, generally, intrinsic stability constants were determined since apparent ones vary with respect to the electrostatic term due to the correlation of ψ with IS . Intrinsic stability constants are mineral-specific and in this study, they correspond to $IS = 0 \text{ mol L}^{-1}$ (Parkhurst and Appelo, 2013).

At the point of zero charge (pzc) the total particle surface charge is balanced between positive and negative surface functional groups, hence, no net surface charge

exists (Tab. 2.1, Sec. 2.2.3). Ideally (!), the assumption of zero electrostatic interaction should be valid at the pzc (Dzombak and Morel (1990), Lützenkirchen et al. (2012 a)). Assuming balanced surface charges the following applies: $[S - OH_2^+] = [S - O^-]$ (which means: $[S - OH_2^+]/[S - O^-] = 1$). Provided that the pzc is known and charge balance conditions apply Equation 2.17 can be deduced from Equations 2.7, 2.8 and Equations 2.9, 2.10 via substitution. Equation 2.17 is of particular interest for modeling studies as will be illustrated later.

Equation 2.7 yields

$$[S - OH_2^+] = K_{a1}^{int}[S - OH]\{H^+\} \quad (2.11)$$

From Equation 2.8 it follows that

$$[S - O^-] = \frac{K_{a2}^{int}[S - OH]}{\{H^+\}} \quad (2.12)$$

At balanced surface charges $S - OH_2^+ = S - O^-$ applies, yielding

$$K_{a1}^{int}[S - OH]\{H^+\} = \frac{K_{a2}^{int}[S - OH]}{\{H^+\}} \quad (2.13)$$

$$K_{a1}^{int}\{H^+\}^2 = K_{a2}^{int} \quad (2.14)$$

$$\{H^+\}^2 = \frac{K_{a2}^{int}}{K_{a1}^{int}} \quad (2.15)$$

$$2 \cdot \log_{10}\{H^+\} = \log_{10}K_{a2}^{int} - \log_{10}K_{a1}^{int} \quad (2.16)$$

Since the pH is defined as the negative decimal logarithm of the hydrogen activity $\{H^+\}$ (Eq. 2.21, Eq. 2.22) Equation 2.17 can be deduced from Equation 2.16.

$$pH_{pzc} = 0.5(\log_{10}K_{a1}^{int} - \log_{10}K_{a2}^{int}) \quad (2.17)$$

For ideal, pristine metal oxides pH_{pzc} refers to the pH of the pristine point of zero

charge (pH_{ppzc}) and is sometimes inferred from the so-called common intersection point pH_{cip} (Sec. 2.2.3). The cip can be determined via titration experiments at different ionic strengths (Sec. 2.2.3). Equation 2.17 is of particular interest since pH_{cip} is an experimental quality. Equation 2.18 makes evident that due to a symmetric distribution of protolysis constants around the pH_{cip} (Eq. 2.16), it is possible to reduce the number of adjustable parameters in geochemical optimization procedures (Eq. 2.18, Sec. 2.4.3, Lützenkirchen and Kienzler (2003)). Instead of optimizing two parameters (K_{a1}^{int} , K_{a2}^{int}) only one is required.

$$\log_{10} K_{a2}^{int} = \log_{10} K_{a1}^{int} - 2\text{pH}_{ppzc} \quad (2.18)$$

The 2-pK concept assumes three different protonation states: negatively charged (S-O^-), neutral (S-OH), and positively charged surface functional groups (S-OH_2^+). So far, no evidence has been found to support this assumption and it may even seem physically unrealistic for multidentate surface complexation reactions according to Hiemstra et al. (1989b) and Hiemstra et al. (1989a). Under the assumption that the ion-association theory of aqueous species can be extended to surface species (Davis and Kent, 1990b) and considering the dissociation reactions of water (Eq. 2.19 - Eq. 2.22) where the exclusive occurrence of OH^- (aq) and H_3O^+ (aq) is separated by 14 $\log K$ units it is proposed that stability constants of protolysis reactions of a given surface hydroxyl are also separated by similar orders of magnitude (e.g. Hiemstra et al. (1989b), Lützenkirchen and Kienzler (2003)). Consequently, for natural systems it can be assumed that only one protonation reaction takes place within naturally accessible pH conditions and the restriction to only one surface protolysis reaction appears reasonable (1-pK approach).



$$K_w = \frac{\{\text{H}_3\text{O}^+\}\{\text{OH}^-\}}{\{\text{H}_2\text{O}\}^2} = \{\text{H}_3\text{O}^+\}\{\text{OH}^-\}, \{\text{H}_2\text{O}\} = 1 \quad (2.20)$$

$$\log_{10} K_w = \log_{10}\{\text{H}_3\text{O}^+\} + \log_{10}\{\text{OH}^-\} \quad (2.21)$$

$$pK_w = pH + pOH \quad pK_w = 14 \quad \text{at} \quad 298.15 \text{ K} \quad (2.22)$$

where K_w represents the dissociation constant of water at 298.15 K. The original 1-pK approach applies the Pauling bond valence concept (Hiemstra and van Riemsdijk (1996), Hiemstra et al. (1989b)). Pauling's concept states that ions distribute their charge equally over all coordinating ligands (Hiemstra and van Riemsdijk, 1996). The charge distribution factor f_{factor} is the product of the number (n) of ligands (j) n_j and the bond valence v . The bond valence v relates to the ratio of the charge of the central metal ion z_{Me} and its coordination number CN_{Me} (Hiemstra and van Riemsdijk (1996), Hiemstra et al. (1989b)). Hence, Equation 2.23 applies for 1-pK protolysis reactions of aluminol surface functional groups. As an example: The CN_{Me} equals a +3 charge of a central Al ion ($Me = Al$) in an octahedron and results in a formal +0.5 charge that is distributed over each ligand ($Me = Al$, $CN_{Al} = 6$, $z_{Al} = 3$, $n_j = 1$, $f_{factor} = n_j \cdot z_{Al}/CN_{Al} = 0.5$). The 1-pK approach for aluminol surface functional groups therefore corresponds to (K_{Al-OH}^{int}):



Using the same calculation for a central Si^{4+} ion in tetrahedral coordination ($Me = Si$, silanol surface functional groups) the $CN_{Me} = +4$ positive charges as an aquo ion. Consequently, according to Pauling's bond charge valence concept a +1 charge is distributed over each ligand (Eq. 2.24). Hence, the application of Pauling's rules to silanol surface functional groups (Eq. 2.24) and, thus, assuming that silica surfaces act as proton donors, results in a description of a 1-pK protolysis reaction that coincides with the deprotonation reaction of the 2-pK approach (cf. Eq. 2.6 and Eq. 2.24). In this study, Equation 2.24 is attributed to the 1-pK approach, whereas the combination of Equations 2.5 and 2.6 are referred to as the 2-pK approach (amphoteric surface functional groups). The 1-pK approach for silanol surface functional groups (K_{Si-OH}^{int}) can then be written as:



Equations 2.5, 2.6, 2.18, 2.23, and 2.24 were utilized in surface charge models and SCMs.

The 1-pK as well as the 2-pK approach are thermodynamically sound

(van Riemsdijk and Hiemstra, 2006). However, considering solution speciation reactions (Eq. 2.19 - Eq. 2.22) and ligand coordinations of surface functional groups, the 1-pK concept appears more reasonable. Furthermore, the 1-pK concept is directly related to the points of zero charge (reference pH values), such as the isoelectric point (IEP, cf. Sec. 2.2.3). As a consequence, K_{Al-OH}^{int} is a measurable parameter (cf. zeta-potential measurements (Sec. 2.4) which reduces the number of fitting parameters (e.g. Lützenkirchen and Kienzler (2003), van Riemsdijk and Hiemstra (2006)). In addition, as mentioned earlier Hiemstra et al. (1989b) argue that the 2-pK concept might result in physically unrealistic coordinations of central metal ions concerning bi- or multidentate surface complexes.

2.2.3 Points of zero charge

There are various points of zero charge or reference pH values, respectively, that characterize electrostatic properties of a mineral or a solid samples. Since no standardized nomenclature has been accepted so far and to ensure consistency, definitions and notations as suggested by Sposito (1998) were used in the present study.

All points of zero charge are defined as pH values at which one of the following surface charge categories (a) - c)) equals zero at defined geochemical conditions (temperature, pressure, IS) (Sposito, 1998). In this study, the surface charge is scaled in relation to the mineral surface area and is referred to as surface charge density σ [$C\ m^{-2}$] which can be classified into three categories (Sposito (1998), Davis and Kent (1990b)):

- a) permanent structural surface charge from isomorphic substitution of e.g. Al^{3+} for Si^{4+} in the crystal lattice for, e.g. phyllosilicates, referred to as σ_o ,
- b) coordinative surface charge resulting from proton (H^+) and/or hydroxide (OH^-) adsorption, denoted σ_H , and
- c) adsorbed ions with $\Delta q = q_+ - q_-$, where q_+ , q_- represent the adsorption of cations, anions, respectively. Δq includes all adsorption processes, i.e. inner-sphere and outer-sphere surface complexation, and the diffuse layer σ_d , but excludes H^+ and OH^- contributions, $\Delta q = \sigma_{is} + \sigma_{os} + \sigma_d$ with $\sigma_{is,os}$ being the net charge of inner-sphere, outer-sphere surface complexes, respectively.

Surface charge classifications are related following Equation 2.25

$$\sigma_o + \sigma_H + \Delta q = 0 \quad (2.25)$$

which describes electroneutrality of any sample equilibrated in an aqueous background electrolyte (Sposito, 1998). The intrinsic surface charge density σ_{int} of a particle is defined as (Sposito (1998), Davis and Kent (1990b))

$$\sigma_{int} = \sigma_o + \sigma_H \quad (2.26)$$

The total particle surface charge density σ_p is defined with Equation 2.27

$$\sigma_p = \sigma_{int} + \sigma_{Stern} \quad (2.27)$$

where σ_{Stern} denotes the Stern layer surface charge density ($\sigma_{Stern} = \Delta q - \sigma_d$).

In this study, the pH was chosen to present the different points of zero charge, reference pH values, respectively (Tab. 2.1). Table 2.1 provides an overview of notions, definitions, and experimental methods of common points of zero charge.

Tab. 2.1: Definitions of reference pH values and experimental measurements (Exp. Method) used in this study. σ denotes absolute surface charge values [C m^{-2}], SLR the solid-liquid ratio, T relates to the absolute temperature [K], p [Pa] to pressure conditions, ET to electrolyte titration, MT to mass titration, IS to ionic strength, zeta to zeta-potential measurements, pot to potentiometric titrations, δ indicates a change of a variable, e.g. $\delta pH / \delta IS$ change of pH over changing IS . ^[1] utilized for natural minerals and clay minerals as an equivalent to pH_{pznpc} for pristine metal oxide surfaces.

Symbol	Name	Definition	Exp. Method
pzc	point of zero charge	$\sigma_p = 0$	ET, MT, zeta, pot
pznpc	point of zero net proton charge	$\sigma_H = 0$	pot
nphc	point of zero net proton and hydroxide consumption ^[1]	$\sigma_H = 0$	pot
IEP	isoelectric point	$\sigma_d = 0$	zeta
pzse	point of zero salt effect	$(\delta \text{pH} / \delta IS)_{T,p} = 0$	ET
cip	common intersection point	$(\delta \sigma_H / \delta IS)_{T,p} = 0$	ET, pot
mass	end point of mass titration	$(\delta \text{pH} / \delta SLR)_{T,p} = 0$	MT
ppzc	pristine point of zero charge	$\sigma_p = \sigma_H = \sigma_d = \sigma_o = 0$	ET, MT, zeta, pot

Protonation and deprotonation takes place on silanol (Si-OH) and aluminol (Al-OH) surface functional groups (Sec. 2.2.2). Assuming that the initial H^+ and/or

OH^- concentrations of the suspension and of the solid (particles) are known, that the mineral sample is free of acidic or basic impurities, that only negligible mineral dissolution processes occur, and that enough surface is provided for protonation and deprotonation reactions with respect to titrant concentration, data obtained from potentiometric acid-base titration coincides with absolute surface charges ($\text{pH}_{pznpc} = \text{pH}_{pzc} = \text{pH}_{ppzc}$). Any deviation from the pristine, ideal surfaces as described above and without the knowledge of the initial H^+ and/or OH^- concentration of the solid results in relative surface charge densities that may include biasing influences from e.g. surface impurities, mineral dissolution processes, or lattice structure. With the knowledge of the pH_{ppzc} or pH_{nphc} it is possible to transform relative surface charge data into absolute values (Lützenkirchen et al. (2012 a), Preočanin and Kallay (2006)) which is illustrated in Section 2.4.2.

The pH_{ppzc} is a material property, does not depend on the method, and can only be sufficiently determined if results of e.g. potentiometric (pH_{pznpc}), electrolyte (pH_{pzse}), and mass (pH_{mass}) titrations, as well as zeta-potential measurements (pH_{IEP}) agree (Tab. 2.1). Potentiometric titrations that are carried out at different *ISs* should exhibit a pH_{cip} for pristine metal oxide surfaces which can in return coincidence with pH_{IEP} , pH_{mass} , pH_{pzse} , and pH_{pznpc} to describe the pH_{ppzc} where $\text{pH}_{IEP} = \text{pH}_{mass} = \text{pH}_{pzse} = \text{pH}_{cip} = \text{pH}_{pznpc} = \text{pH}_{ppzc}$ is valid. For natural minerals or clays often pH_{cip} and pH_{ppzc} do not exist due to e.g. isomorphic substitutions of inter alia Si^{4+} for Al^{3+} ; hence, $\sigma_o \neq 0$ applies (e.g. Lützenkirchen et al. (2012 a)). In addition, pH_{pznpc} may change as a function of *IS*, solid-liquid ratio (*SLR*), and as a function of mineral acidic or basic impurities resulting in $\text{pH}_{pznpc} \neq \text{pH}_{ppzc} \neq \text{pH}_{pzse} \neq \text{pH}_{IEP} \neq \text{pH}_{mass}$ (e.g. non-ideal surfaces). To distinguish between pH_{pznpc} of pure metal oxide surfaces ($\text{pH}_{pznpc} = \text{pH}_{ppzc}$) and natural minerals ($\text{pH}_{pznpc} \neq \text{pH}_{ppzc}$) the term zero net proton and hydroxide consumption pH_{nphc} is used (Lützenkirchen et al., 2012 a).

The pH_{IEP} denotes the pH where the electrophoretic mobility is zero, hence, zero counterion charge occurs in the system (Davis and Kent (1990b), Lützenkirchen (2002), Sec. 2.4.1). Ideally, the particle is electrokinetically uncharged (Sposito, 1998), and $\psi = 0$ is valid for pristine metal oxides (ψ – surface potential [V]). However, pH_{IEP} can be influenced by surface impurities but also by lattice structure such as e.g. permanent negative surface charge: Phyllosilicates, for example, exhibit negative electrokinetic potentials over a wide pH rage due to isomorphic substitution which results in low pH_{IEP} (Lützenkirchen et al., 2012 a). Hence, for most natural mineral surfaces and e.g. phyllosilicates $\text{pH}_{IEP} \neq \text{pH}_{ppzc} \neq \text{pH}_{pznpc} \neq \text{pH}_{pzse} \neq \text{pH}_{mass}$ is valid.

2.2.4 Specific surface area after Brunauer, Emmett, Teller (1938)

Solids interact by means of the *SSA* with their surroundings and exert significant influence on physical and chemical conditions/environments. In this study, the *SSA* represents the reactive surface area which is assumed to be prone to adsorption of solutes [$\text{m}^2 \text{g}^{-1}$].

In TSMs the *SSA* represents a fundamental property in the description of sorption, aggregation and precipitation reactions, as well as dissolution processes, to only name a few. The *SSA* is directly correlated with the mineral's grain size, particle shape (Hodson, 2006), porosity, swelling properties, dissolution processes, coagulation, cation exchange, and soil water content (Maček et al., 2013).

Brunauer et al. (1938) generalized the sorption isotherm proposed by Langmuir (1918) and introduced simplifying assumptions extending Langmuir's monomolecular layer theory ($n = 1$, n = number of molecule layers) to more realistic multi-molecular layer ($n = \infty$) adsorption processes. Langmuir's isotherm equation of monomolecular layer adsorption follows the form

$$\theta = \frac{v}{v_m} = \frac{K_L \cdot p}{1 + K_L \cdot p} \quad (2.28)$$

where θ corresponds to the fractional occupancy of adsorption sites, v to the total volume of adsorbed gas in equilibrium with the solid, v_m to the maximum absorbed volume at monolayer coverage, K_L to the Langmuir isotherm coefficient, and p to the partial pressure of the adsorbate at adsorption-desorption equilibrium (Langmuir, 1918). On the basis of Langmuir's isotherm Brunauer et al. (1938) developed a model (Eq.2.29) to describe mono- and multimolecular layer adsorption processes (Eq. 2.29).

$$v = \frac{v_m \cdot c_{BET} \cdot p}{(p_0 - p)(1 + (c_{BET} - 1)(p/p_0))} \quad (2.29)$$

c_{BET} denotes the dimensionless BET isotherm coefficient (Brunauer et al., 1938), p_0 corresponds to the saturation pressure of the adsorbate which means the partial pressure above which no additional adsorption occurs. Equation 2.29 can be used to test and interpret experimentally collected data in its linearized form (Eq. 2.30).

$$\frac{p}{v(p_0 - p)} = \frac{1}{v_m \cdot c_{BET}} + \frac{c_{BET} - 1}{v_m \cdot c_{BET}} \cdot \frac{p}{p_0} \quad (2.30)$$

where the ordinate's intercept equals $1/(v_m \cdot c_{BET})$ and the slope corresponds to $(c_{BET} - 1)/v_m \cdot c_{BET}$. Plotting $p/(v(p_0 - p))$ against p/p_0 should give a linear function in the relative pressure range of $p/p_0 = 0.05 - 0.35$ (Brunauer et al. (1938), App. Fig. B.26). The maximum volume of adsorbed monolayer molecules v_m (Eq. 2.31), the BET coefficient c_{BET} , and the *SSA* after Brunauer et al. (1938) (SSA_{BET} [$\text{m}^2 \text{g}^{-1}$], cf. Eq. 2.32) can be determined from the slope and intercept, respectively.

$$v_m = \frac{1}{m + n} \quad (2.31)$$

m refers to the slope $(c_{BET} - 1)/(v_m \cdot c_{BET})$ and n to the intercept $1/(v_m \cdot c_{BET})$.

$$SSA_{BET} = \frac{v_m \cdot \rho \cdot N_A \cdot A}{M} \quad (2.32)$$

ρ relates to the vapour density of the adsorbate at standard pressure, N_A [mol^{-1}] to the Avogadro's constant, M [g mol^{-1}] to the molar mass of the adsorbate, and A [nm^{-2}] to the cross-section area of an adsorbate molecule (de Lange et al., 2014). The BET isotherm equation is invalid for $p/p_0 \approx p_0$ (e.g. $p/p_0 > 0.35$) since the condition of linearity is not fulfilled (sigmoidal sorption isotherm).

The isotherm was once developed to describe plain, non-porous solids (without micropores, Rouquerol et al. (2007), Brunauer et al. (1938), Davis and Kent (1990b)). Micropores (microporosity) are pores of molecular dimensions ($< 2 \text{ nm}$, Davis and Kent (1990b)). Most adsorptives tend to clump in and around micropores which violates BET model assumptions: In case of micropores the number (n) of molecular layers is limited ($n \neq \infty$) and Equation 2.29 needs adaptation as discussed in Brunauer et al. (1938) since linearity of measurements is not provided in the relative pressure range $0.05 \leq p/p_0 \leq 0.35$ (Brunauer et al. (1938), de Lange et al. (2014), Rouquerol et al. (2007)).

SSA_{BET} values of this study are provided in Section 2.3. Compared to the originally recommended relative pressure range $p/p_0 = 0.05 - 0.35$ many minerals have more restricted linear BET ranges (Davis and Kent, 1990b). In the present study, the relative partial pressure range of $p/p_0 = 0.05 - 0.2$ was used for BET isotherm regression.

BET assumptions and isotherm limitations

Equations 2.29 - 2.32 show that SSA_{BET} is highly correlated with pressure conditions and, hence, with temperature. The adsorbent surface structure and the

adsorptive physicochemical properties also play key aspects. The application of the BET isotherm is furthermore limited by the following assumptions (Brunauer et al. (1938), Rouquerol et al. (2007), de Lange et al. (2014), Davis and Kent (1990b)):

- Adsorption takes place uniformly on a plane, clear surface in the absence of micropores without clustering and without forming of clumps.
- There is no steric limitation regarding the thickness of multimolecular layers as p approaches p_0 ($n \rightarrow \infty$).
- All adsorbate molecules of a monomolecular layer cover the same area.
- The molecular cross section area can be determined from the density of the adsorptive in the liquid state.
- A hexagonal closest packing covers the entire surface of the solid.
- The heat of adsorption of the first layer is independent of the number of adsorbed molecules.
- The rate of condensation equals the rate of evaporation for the second and following layers, and the liquid state.

In addition to assumptions listed above further biasing influences comprise (Vicente et al. (1996), Mantellato et al. (2015), Macht et al. (2011), Hodson et al. (1997), de Lange et al. (2014), Naderi (2015), Davis and Kent (1990b))

- sample properties (porosity, impurities, very small surface areas),
- sample preparation (pre-conditioning procedures, water content, acid treatment, purification procedures, etc.),
- measuring conditions (adsorptive, sample size, overall sample area, outgassing conditions: pressure range, temperature, humidity),
- and device properties and measuring uncertainties – to only name a few.

It is obvious that the SSA_{BET} only represents surface areas that are accessible for the adsorptive (N_2 or Kr). Hence, information has to be supplied whether measurements exclusively reflect the external and/or internal surface area which depends on the adsorptive physicochemical properties and on the surface structure of the sample. Naderi (2015) quotes secondary literature that found SSA_{BET} to differ by factor six depending on the adsorptive N_2 or Kr for inhomogeneous or very small surfaces. Everett et al. (1974) initiated an inter laboratory comparison (15 participants) of BET measurements and came to the following conclusion: SSA_{BET} from literature should be evaluated and used with care; the largest RSD they reported equalled 7%.

Everett et al. (1974) saw the reasons for SSA_{BET} measurement discrepancies in experimental errors due to violations of experimental requirements. In Appendix B, Table B.3 offers an overview of potential error sources and error ranges reported in literature.

SSA_{BET} describes the surface of a mineral phase as a unit. Discrimination between mineral planes/faces is not possible. In the case of phyllosilicates, for example, it is assumed that in comparison to other planes only little sorption takes place at the prominent $\{001\}$ front. Surface protonation and deprotonation as well as surface complexation are supposed to mainly occur at so called edge sites. This should actually be taken into account when applying SSA_{BET} as the "reactive surface area" in geochemical speciation codes such as PHREEQC (Parkhurst and Appelo, 2013).

Measurements after Brunauer et al. (1938) are conducted under a broad range of measuring conditions and sample preparation techniques which can highly limit the basis of sound comparison and evaluation of available data. Unfortunately, in many studies only little information is provided on sample preparation, measuring conditions, data evaluation, etc. making a qualification of SSA_{BET} in terms of robustness and credibility challenging. Provided that mentioned aspects are taken into account the BET method offers a fast and reliable means to determine the SSA_{BET} of various solid surfaces. A discussion on applicability, advantages and draw backs of the BET method is given by Davis and Kent (1990b). A list of recommendations to be followed during measuring procedures is provided by the IUPAC (International Union of Pure and Applied Chemistry) in Sing et al. (1985) and by Everett et al. (1974).

2.2.5 Determination of the surface site density

The SSD [sites nm^{-2}] is a fundamental, mineral-specific property for TSMs. It describes the concentration of available or reactive sites per unit area on a mineral surface: The larger the SSA , the more sites are available for e.g. dissolution, protolysis, or surface complexation reactions for a given solid concentration. The SSD can be determined in different ways. This study used the following approaches:

- a) SSD was estimated from potentiometric titration data
- b) SSD was derived from Eu batch sorption data
- c) SSD was obtained from literature
- d) SSD was applied in optimization procedures as an adjustable parameter.

a) SSD calculated from potentiometric titration data

Ideally, mineral titration data covers different IS s, a broad pH range, exhibits a common intersection point, and, amongst others, offers information on surface charge saturation regarding protonation and deprotonation of surface functional groups. When titration reaches total deprotonation of surface functional groups (saturation) a plateau at high pH values and low surface charge densities evolves. With the Faraday constant (F [C mol⁻¹]) and Avogadro's constant (N_A [mol⁻¹]) in combination with the surface charge density where all silanol functional groups are deprotonated (σ_{sat} [C m⁻²]) a theoretical SSD [sites nm⁻²] can be derived from titration data (Eq. 2.33, cf. Fig. 2.11).

$$SSD = \frac{\sigma_{sat}}{F} \cdot \frac{N_A}{10^{18}} \quad (2.33)$$

Equation 2.33 is valid for the 2-pK approach. For the 1-pK approach the following has to be considered: The 1-pK approach only includes +0.5 charges for one site compared to full charges of the 2-pK approach; hence, the surface charge needs twice as much sites to be neutralized. Consequently, for the 1-pK approach $SSD = (\frac{\sigma_{sat}}{F} \cdot \frac{N_A}{10^{18}}) \cdot 2$ is valid.

However, saturation of surface functional groups can be IS dependent and the evolution of a plateau due to site saturation can therefore also be a function of IS (Lützenkirchen et al., 2002). In this study, only one IS was used for continuous potentiometric titration experiments (Sec. 2.4). Hence, the possible IS dependence of fully deprotonated surface functional groups could not be presented and only one SSD was derived from titration experiments with Equation 2.33.

b) SSD derived from Eu batch sorption data

Similar to potentiometric data (a) sorption data derived from e.g. batch experiments offers information to define the SSD [sites nm⁻²] (Eq. 2.34). Given that a sufficient amount of sorptive is supplied to saturate available, reactive sites and provided that geochemical conditions allow saturation of surface sites through surface complexation reactions (maximum site occupancy), a value for the SSD can be derived from batch experiments following Equation 2.34:

$$SSD = \frac{m}{(SSA \cdot M)} \cdot \frac{N_A}{10^{18}} \quad (2.34)$$

where m [mg g^{-1}] refers to the sorbed fraction of sorptive on a mineral's surface (sorbate), M to the molar mass of the sorptive [mg mol^{-1}], and SSA [$\text{m}^2 \text{g}^{-1}$] to the specific surface area. This approach is suitable to estimate $SSDs$ provided that strong surface complexes are formed that are not bulky and that do not lead to charge accumulation at the mineral's surface (Davis and Kent, 1990b). Furthermore, if mineral solubility exceeds surface complexation this approach cannot be applied either (Davis and Kent, 1990b). In this study, high mineral solubility during batch experiments (equilibration time = 24 h) can be ruled out (Sec. 3); Eu served as the sorptive (Sec. 3). The highest chosen initial Eu concentration in solution equalled $C_0 = 10^{-5} \text{ mol L}^{-1}$ (1.5 ppm). Even though 100% of C_0 were sorbed under applied geochemical conditions (Sec. 3.3) saturation of surface sites did not occur for any mineral phase (quartz, orthoclase, muscovite, cf. Sec. 2.3) since $SSD \gg C_0$. Consequently, this approach did not yield reliable values and was not pursued any further.

c) SSD obtained from literature

Only little information is available concerning muscovite and orthoclase $SSDs$. Quartz mineral surfaces, on the other hand, represent thoroughly examined interfaces. Even though it is recommended to determine SSD values individually for each sample, sometimes it is necessary to rely on trustworthy generic approaches or literature data due to lack of own experimental data. The free database RES³T (Rossendorf Expert System for Surface and Sorption Thermodynamics, www.hzdr.de/res3t, Brendler et al. (2003)) established by the Helmholtz-Zentrum Dresden Rossendorf e.V. provides an overview of mineral-specific thermodynamic sorption data – including SSD estimates.

In the present study, for quartz the SSD was obtained from Hiemstra et al. (1989a). Hiemstra et al. (1989a) presented surface complexation parameters of amorphous silica. They used two $SSDs$ to describe the charging behaviour of amorphous silica by means of the BSM. Hiemstra et al. (1989a) utilized experimental data from Bolt (1957) to develop their BSM approach. In the present study, $SSD = 4.3 \text{ sites nm}^{-2}$ was applied for modeling studies representing the best fit of Hiemstra et al. (1989a). Regarding muscovite and orthoclase, finding SSD literature values was more challenging. Arnold et al. (1999) and Zorn (2000) published $SSDs$ for albite and orthoclase. They calculated an albite $SSD = 3.1 \text{ sites nm}^{-2}$ at pH 9.5 from a back-titration experiment of the mineral (Eq. 2.33). Estimates of the SSD for muscovite were provided by Zorn (2000) and Maslova et al. (2004). Via adsorption isotherms Zorn (2000) determined $SSD = 2.61 \text{ sites nm}^{-2}$ for muscovite. Maslova

et al. (2004) derived the SSD for a muscovite mineral from titration experiments and found $SSD = 1.8 \text{ sites nm}^{-2}$ (Sec. 2.5.2). A different approach was taken by Davis and Kent (1990a) who suggested the application of a generic reference $SSD = 2.31 \text{ sites nm}^{-2}$ for any mineral. This widely utilized generic reference SSD originated from studies by Dzombak and Morel (1990) who investigated ferrihydrite with an assumed SSA of $600 \text{ m}^2 \text{ g}^{-1}$. The present study, however, did not apply the proposed reference SSD and presents specifically derived $SSDs$ for muscovite and orthoclase (Sec. 2.5).

d) SSD applied in optimization procedures as an adjustable parameter

The SSD can have major influence on model bias and parameter uncertainty, CIs, etc. of model optimizations. Since no precise SSD measurement was available for orthoclase and muscovite the SSD was subject to SCM fitting approaches provided that parameter correlations between adjustable parameters did not occur (Sec. 2.5.2). The SSD is a sensitive parameter when sorbing ions (here H^+ , OH^-) are supplied in excess and $SSD \ll C_{\text{H}^+, \text{OH}^-}$ is valid (Hayes, 1987), where $C_{\text{H}^+, \text{OH}^-}$ refers to the total or free concentration of H^+ , OH^- in the system. Optimized surface complexation constants are directly dependent on the SSD . A comparison between fitted $SSDs$ and estimated ones from the latter approaches (a) - c)) offered a means to assess SSD values (Sec. 2.5.2).

2.3 Material

All experiments in this study were conducted with identical mineral phases in order to guarantee comparability of collected results (Sec. 2, Sec. 3, Sec. 4). The following geochemical characterization of muscovite, orthoclase, and quartz were carried out

- particle size analysis via parallel beam laser diffraction
- hydrofluoric acid (HF) digestion evaluated via Inductively Coupled Plasma Mass Spectrometry (ICP MS), Optical Emission Spectrometry (ICP OES) and Atom Adsorption Spectrometry (AAS)
- determination of the SSA after Brunauer, Emmet, and Teller (SSA_{BET}) (Brunauer et al., 1938)
- Scanning Electron Microscopy (SEM) in combination with Energy Dispersive X-ray (EDX) spectroscopy
- X-ray Diffraction analysis (XRD).

A listing of tools, equipment, techniques, and institutions performing the techniques is summarized in Appendix A.2; measurements and techniques where the institution is not mentioned were performed at GRS gGmbH Braunschweig.

Unless otherwise stated mineral analyses were conducted using the untreated, pristine minerals. A detailed discussion of dissolution kinetics regarding muscovite and orthoclase is provided in Richter (2015).

2.3.1 Muscovite

The muscovite (supplier specification: mica WG) was obtained from Normag GmbH (Bad Homburg, Germany) as a fine powder. The mineral originated from China. Information regarding detailed provenience, mining, or potential preconditioning was not available. Mining conditions are covered by a trade secret. However, mineral analysis provided by Normag GmbH correspond well with HF digestion analysis of this study. Major constituents were Al_2O_3 (28.4 wt%), K_2O (9.4 wt%), Fe_2O_3 (4.9 wt%), and TiO_2 (0.65 wt%). Na_2O , CaO , and MgO were found to represent minor fractions, in sum below 3 wt%. In comparison to the ideal composition of muscovite ($\text{KAl}_3\text{Si}_3\text{O}_{10}(\text{OH})_2$) the composition of the muscovite mineral deduced from HF digestion analysis (Tab. B.2) showed reduced Al concentrations which were balanced with Fe and Mg concentrations. Deficits in K_2O were offset by Na_2O (1.0 wt%). Background concentration of Eu corresponded to 0.98 mg kg^{-1} mica mineral which refers to the Eu concentration of the pristine, untreated mineral. Eu background concentration were considered insignificant regarding artefacts in batch and column experiments. Table B.2 in the appendix presents an overview of the untreated muscovite components derived from HF digestion in comparison to the ideal structural formula and supplier data. In the following, the mineral is referred to by mica or muscovite.

Particle size fraction of the muscovite varied between $20 \text{ }\mu\text{m}$ - $400 \text{ }\mu\text{m}$. According to the cumulative distribution sum of particle sizes 50% of the sieved mineral was smaller than $153 \text{ }\mu\text{m}$ (d_{50}), 20% exceeded the mean diameter of $225 \text{ }\mu\text{m}$. Only 0.2 wt% mica grains ranged below $4.5 \text{ }\mu\text{m}$. Using separation by sedimentation (App. A.2.4) only $< 1 \text{ wt}\%$ clay fraction ($< 2 \text{ }\mu\text{m}$) in the preliminary sieved powder mica was found. In this fraction about 10 wt% montmorillonite was detected. The method of muscovite grain size separation is summarized in Appendix A.2.4.

For some experiments preconditioning of muscovite had to be performed (Sec. A.12.1) that might had altered crystal characteristics and surfaces. Alteration

affects most efficiently the clay fraction, especially, the montmorillonite portion. Therefore, the clay fraction is most suitable to detect such changes via XRD. Comparative XRD analyses were performed. In the following, "preconditioning" refers to sample preparation with $0.05 \text{ g L}^{-1} \text{ NaClO}_4$ (Sec. A.12.1), diethyleneglycol preparation denotes sample treatment for XRD analyses.

Figures 2.2 and 2.3 present XRD results of the muscovite clay fraction with and without glycol preparation in comparison to preconditioned and pristine mica samples. Generally, preconditioning did not affect mineral lattice structure. The preconditioned muscovite exhibited no higher interlayer swelling potential and no lattice structure alteration; no differences in Bragg angles were observed (Fig. 2.2, App. A.2.4). Occurrence of montmorillonite was suggested by means of a slight inconsistency at 6.2° [2Theta] as illustrated in Figure 2.3. The effect of glycolation is summarized in Appendix A.2.4.

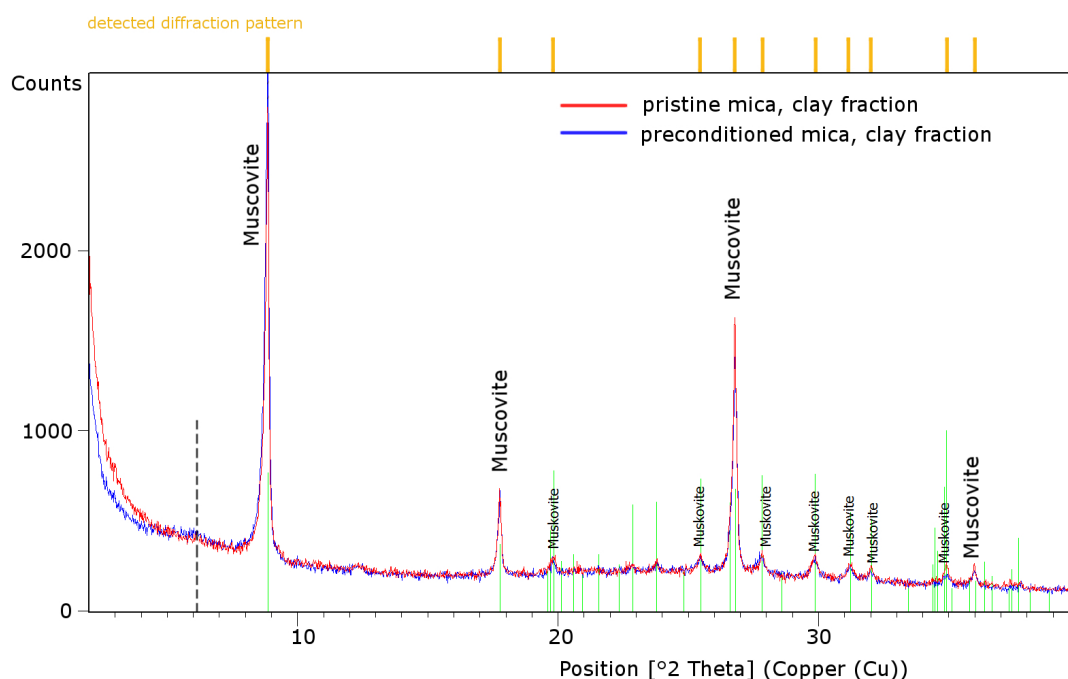


Fig. 2.2: XRD analyses of muscovite. Comparison of pristine and preconditioned mineral samples (clay fraction). Dashed line – peak position montmorillonite. Green – peak positions of ICSD (2009) database (Inorganic Crystal Structure Database), muscovite (monoclinic). Orange – XRD reflection angles.

Concluding, the preconditioned muscovite shows no interlayer swelling and no

lattice structure alteration due to preconditioning, while treatment with diethyleneglycol triggered lattice structure spreading in pristine and preconditioned samples (Fig. 2.3).

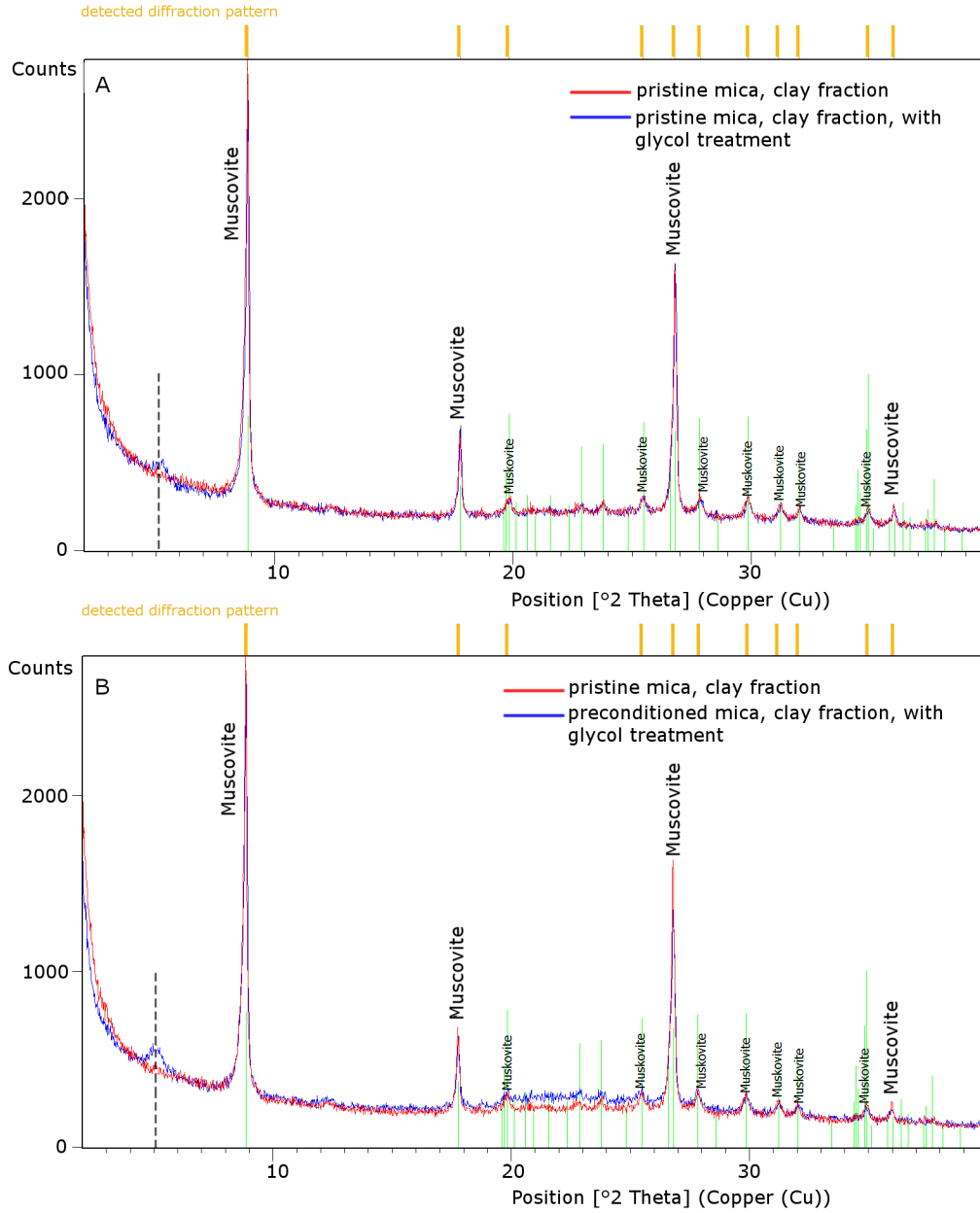


Fig. 2.3: XRD analyses of muscovite. A: Pristine sample, clay fraction compared to a pristine sample after diethyleneglycol preparation (clay fraction). B: Pristine muscovite, clay fraction compared to a preconditioned sample (NaClO_4) after diethyleneglycol preparation, clay fraction. Dashed line – peak position glycol treatment. Green – peak positions of ICDD (2005) database, muscovite (monoclinic). Orange – XRD reflection angles.

Figure 2.4 shows SEM images of preconditioned (right) and pristine (left) muscovite samples (20 μm - 400 μm). Typical muscovite characteristics such as the prominent and highly perfect {001} cleavage, the flaky, thin mineral sheets, and 60° angles are shown in both samples. No differences due to preconditioning could be detected. Both samples showed isolated Fe-oxide (FeOX) and Zr impurities. The insert of Fig. 2.4 highlights a typical FeOX impurity; the according EDX results are provided in the appendix Figure B.24. Via EDX muscovite atomic weight ratio ([At%] ratio) of K:Al:Si 1:2:3 was corroborated; some Fe and Mg impurities were identified. Results back up conclusions drawn from muscovite HF digestion and XRD analysis.

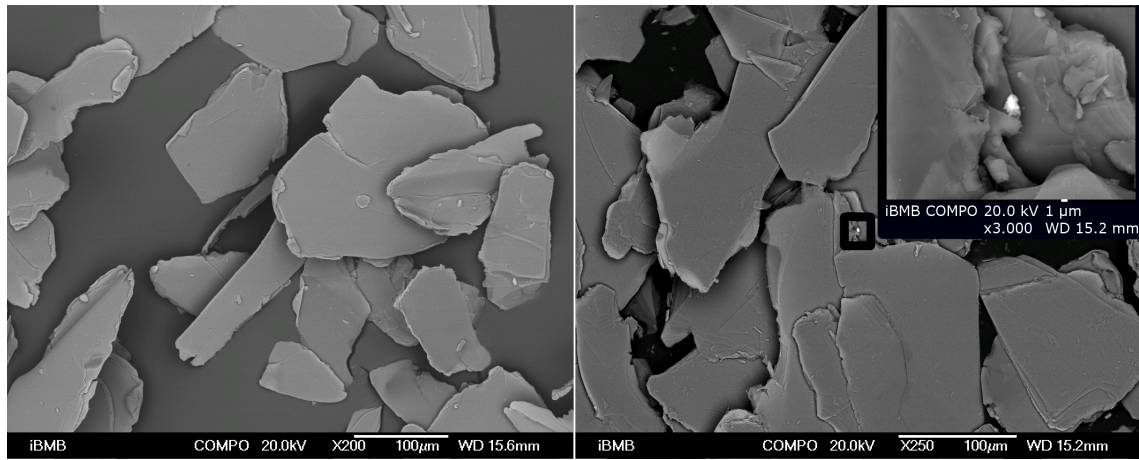


Fig. 2.4: SEM analysis of preconditioned (right) and pristine (left) muscovite, particle size fraction 20 - 400 μm . The insert illustrates FeOX of the preconditioned mica sample. FeOX and Zr impurities were occasionally found on pristine and preconditioned mica surfaces with no detectable preference of either sample. WD – working distance, x – magnification factor. COMPO – back-scattering measurement mode, sensitive to atomic number and sample density.

The SSA was determined via BET (Brunauer et al., 1938). As discussed in Section 2.2.4 correct and reliable determination of the SSA is particularly challenging. Measurements after Brunauer et al. (1938) of pristine and preconditioned samples were conducted. Table 2.2 presents an overview of BET measuring conditions and SSA_{BET} . Estimation of the SSA via the geometric SSA was not feasible due to the large range of particle size distribution and due to inhomogeneously shaped grains.

SSA_{BET} values of the muscovite samples showed the influence of particle size

and preconditioning procedures (Tab. 2.2). The SSA_{BET} decreased with increasing particle size. Preconditioning of muscovite samples for column experiments (Sec. 4) did not show significant influences on the muscovite surface (Tab. 2.2), whereas samples taken from titration experiments indicated an increase of the SSA by factor two. Since linearity of the BET isotherm had always been fulfilled in the relative pressure range of 0.05 - 0.2 p/p_0 (App. Fig. B.26) the presence of micropores could be excluded (Rouquerol et al. (2007), Sec. 2.2.4).

Table 2.2 summarizes SSA_{BET} data relevant for surface complexation and reactive transport modeling. Generally speaking, the BET method yielded reproducible results. In repetitive measurements of identical samples the relative standard deviation (RSD) ranged between 0.4% - 7.7% agreeing well with error ranges reported by Everett et al. (1974). BET analysis of different muscovite sample aliquots that experienced identical preconditioning procedures and identical measuring conditions revealed larger RSD s between 6.7% - 11%. Comparable error estimations have been reported in literature (e.g. Davis and Kent (1990b), Cases et al. (1992), Macht et al. (2011)). Since the robustness of SSA_{BET} is highly dependent on sample preparation, measurement environment, and data evaluation utilization of SSA_{BET} in TSMs must be assessed with care (Sec. 2.2.4).

Due to their structure phyllosilicates like muscovite are especially prone to exchange of interlayer cations against cations of the surrounding solution. The potential cation exchange capacity (CEC_{pot} [cmol(+) kg⁻¹]) was determined following DIN ISO 13536:1997-04 (1997) which describes the CEC_{pot} at pH 8.1 in a buffered BaCl₂-solution. However, it should be kept in mind that applying DIN ISO 13536:1997-04 (1997) to muscovite is subject to bias. The CEC determination may be blurred by excessive Ba incorporation during Ba treatment by exchange of Ba²⁺ vs. K⁺ (mineral: Öllacherite). The CEC_{pot} equalled 41.5 cmol(+) kg⁻¹ solid according to DIN ISO 13536:1997-04 (1997). This value was inconsistent with individually determined cations and, therefore, considered to be an artefact value. The cation Na⁺ contributed 0.1 cmol(+) kg⁻¹ solid, K⁺ 1.99 cmol(+) kg⁻¹, Ca²⁺ and Mg²⁺ yielded 1.82 cmol(+) kg⁻¹ and 1.37 cmol(+) kg⁻¹, respectively. In sum Na⁺, K⁺, Mg²⁺, and Ca²⁺ contributions to CEC_{pot} equalled 5.28 cmol(+) kg⁻¹ which was used as the CEC of muscovite (CEC_{WG}). As is shown in Section 3.1.2 and Table 3.1 CEC_{WG} lied well within the range of CEC values reported in literature.

Tab. 2.2: Summary of BET analyses of muscovite (mica), orthoclase (ortho), and quartz. Multipoint analysis (> 10 data points) after Brunauer et al. (1938) between $0.05 - 0.2 \, p/p_0$ (relative pressure) was evaluated. No information of vacuum conditions can be supplied. Outgassing was achieved over 100 min at 373 K. Uncertainties are indicated by *RSDs*. ^[1] adsorber gas, ^[2] correlation coefficient (CC) of BET isotherm (Brunauer et al., 1938), ^[3] measurement of identical sample, - no data available, d_{50} mass-median diameter, d_{80} 80% quantile of cumulative particle size distribution. *SSA* relates to specific surface area, SSA_{BET} to the *SSA* after Brunauer et al. (1938), *PSF* to particle size fraction. Appl. indicates preconditioning procedure and/or subsequent application to column, batch, or mineral titration experiments. Pristine indicates samples without preconditioning treatment. Preconditioning procedures are described in Appendix A.12.1. * indicates a single measurement without replicates: 5 point BET analysis, outgassing temperature 423.15 K over 2 h, $0.05 - 0.3 \, p_a/p_{a0}$ was evaluated, device: Quantachrome Autosorb Automated Gas Sorption System, Autosorb for Windows®, Version 1.19.

Sample	<i>PSF</i> [μm]	Appl.	d_{50} [μm]	d_{80} [μm]	BET measuring condition	Replicates	SSA_{BET} [m ² g ⁻¹]	Overall sample area [m ²]
mica	20 - 400	pristine	153	225	0.85 g solid $\pm < 0.01$ g, N ₂ ^[1] , CC > 0.99 ^[2]	3	0.66 ± 0.01	$0.56 \pm < 0.01$ ^[3]
	20 - 400	column	-	-	2.41 g solid ± 0.2 g, N ₂ ^[1] , CC > 0.99 ^[2]	5	0.68 ± 0.03	1.3 ± 0.1
	> 200	pristine	361	527	0.34 g solid $\pm < 0.01$ g, N ₂ ^[1] , CC > 0.99 ^[2]	3	0.46 ± 0.05	$0.16 \pm < 0.01$ ^[3]
ortho	30 - 400	pristine	171	242	3.10 g solid $\pm < 0.01$ g, Kr ^[1] , CC > 0.99 ^[2]	3	0.19 ± 0.01	$0.60 \pm < 0.01$ ^[3]
	30 - 400	column	-	-	1.84 g solid $\pm < 0.01$ g, Kr ^[1] , CC > 0.99 ^[2]	3	0.15 ± 0.01	$0.28 \pm < 0.01$ ^[3]

Continued on next page

Sample	<i>PSF</i> [μm]	Appl.	d ₅₀ [μm]	d ₈₀ [μm]	BET measuring condition	Replicates	<i>SSA_{BET}</i> [m ² g ⁻¹]	Overall sample area [m ²]
ortho	< 120	pristine	-	-	-	7	0.99 ± 0.2	-
	< 63*	titration	-	-	1.14 g solid, N ₂ ^[1] , CC > 0.99 ^[2]	-	4.3	4.9
	> 200	pristine	377	552	2.83 g solid ± < 0.01 g, Kr ^[1] , CC > 0.99 ^[2]	3	0.05 ± 0.01	0.14 ± < 0.01 ^[3]
quartz	150 - 800	pristine	349	512	4.01 g solid ± < 0.01 g, Kr ^[1] , CC > 0.99 ^[2]	4	0.06 ± 0.01	0.26 ± < 0.01 ^[3]
	150 - 800	pristine	349	512	6.27 g solid ± 1.0 g, Kr ^[1] , CC > 0.99 ^[2]	12	0.08 ± 0.01	0.47 ± 0.09

2.3.2 Orthoclase

The orthoclase (supplier specification: Kali Norflot 600) was obtained from Sibelco Deutschland GmbH, Ransbach-Baumbach, Germany. According to the supplier the orthoclase was mined in a pegmatite host rock formation, ground to a particle fraction of approximately 600 μm , and composed of 18.8 wt% Al_2O_3 , 10.5 wt% K_2O , and 3.6 wt% Na_2O . Thus, orthoclase was the predominant component of this sample (K-feldspar). The oxides Fe_2O_3 (0.1 wt%) and CaO (0.8 wt%) represent minor components (App. Tab. B.2). The composition was confirmed by HF digestion of this study (App. Tab. B.2). The Eu background concentration equalled 0.4 mg kg^{-1} solid representing insignificant potential for artefacts in the planned experiments.

Compared to the ideal structural formula of orthoclase (KAlSi_3O_8) a deficit of K_2O (4 wt%) and an excess of approximately 2 wt% SiO_2 was detected via HF analysis (App. Tab. B.2). The difference in K_2O was balanced by Na_2O (5.12 wt%) which indicates minor admixtures of albite. Albite was confirmed by EDX-analysis (Fig. 2.5) and XRD (Fig. 2.6). The excess SiO_2 was probably due to minor quartz admixtures, consistent with XRD and EDX analysis (Fig. 2.5, Fig. 2.6). The XRD measurements revealed microcline (66 wt%, semi-quantitative analysis, Rietveld method), albite (31 wt%), and quartz (3 wt%). Microcline is the low-T modification of K-feldspar and common for pegmatite occurrences. The chemical composition is identical to orthoclase, whereas the crystalline order differs (triclinic vs. monoclinic). Results of XRD and EDX analysis fully support findings of HF digestion measurements. In the following, the mineral Kali Norflot 600 is referred to as orthoclase or feldspar.

For the scheduled experiments the orthoclase sample as obtained from the supplier was milled (App. A.2.2). The sample size of 30 - 400 μm was used for titration and transport (Sec. 4) experiments (Tab. 2.2). The milled, geochemically untreated orthoclase is referred to as pristine mineral phase. Conducted SEM analyses showed typically cleaved orthoclase grains (App. Fig. B.25). The BET analysis yielded $SSA_{\text{BET}} = 0.19 \text{ m}^2 \text{ g}^{-1} \pm 3\%$ (*RSD*, Tab. 2.2) for the particle size fraction (*PSF*) 30 - 400 μm . The specific surface area after Brunauer et al. (1938) (SSA_{BET}) followed expectations: The larger the *PSF*, the smaller SSA_{BET} . Orthoclase samples from titration experiments and mineral preconditioning for column experiments (Sec. 4, App. A.12.1) exhibited minor effects on the SSA (Tab. 2.2). However, since the examined sample size for BET measurements was well below recommendations made by e.g. Macht et al. (2011) and Sing et al. (1985) ($\geq 1 \text{ m}^2$ recommended overall sample area, Tab. 2.2) influences from mineral preconditioning or experimental set-up could not explicitly be identified (Tab. 2.2). Accordingly, limitations regarding further utilization of SSA_{BET} of orthoclase have to be considered (Sec. 2.2.4).

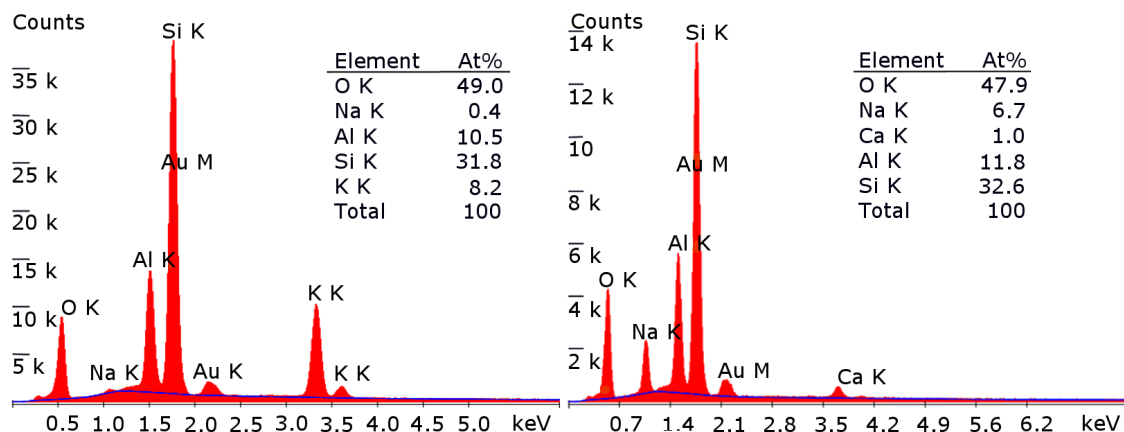


Fig. 2.5: EDX analyses (area scan) of orthoclase, *PSF* 30 μm - 400 μm . Left: Identified orthoclase particle (KAlSi_3O_8). Right: Albite grain ($\text{NaAlSi}_3\text{O}_8$). The inserts illustrate element distributions [At%] of individual mineral components. An increase in Si concentration compared to ideal microcline and albite stoichiometric formula was determined and also identified via XRD analysis, HF digestion. The Au diffraction pattern resulted from sample treatment. The blue line indicates background noise; K, L, M relate to the excitation energy of incident X-ray energy (shells of Bohr's model).

2.3.3 Quartz

Schlingmeyer Quarzsand GmbH & Co KG (Schwülper, Germany) provided the quartz sample (supplier specification: G20EAS extra). According to the supplier the quartz mineral is composed of 99.7 wt% SiO_2 which was confirmed by HF digestion analyses of this study (App. Tab. B.2). Further components relate to Al_2O_3 (0.2 wt%), K_2O (0.05 wt%), CaO (0.05 wt%), Fe_2O_3 (0.04 wt%), and TiO_2 (0.01 wt%). The Eu background concentration equalled 0.03 mg kg^{-1} solid which was deemed negligible.

The quartz sediment was deposited about 70 million years ago (Late Cretaceous fluviatile deposit), mined in the Northern Plain of Germany (Uhry, Germany) without addition of chemical agents, and was washed with local groundwater after extraction according to the supplier. Due to the non-invasive mining process the quartz sample was used without further purification or preconditioning treatment as a natural sediment. The XRD and SEM/EDX analyses (App. A.2.1) confirmed information provided by the supplier that the sample was free of humic substances and soluble salt contaminations. The quartz sediment appeared with rounded edges due to fluvial transport and without any further detectable impurities or organic

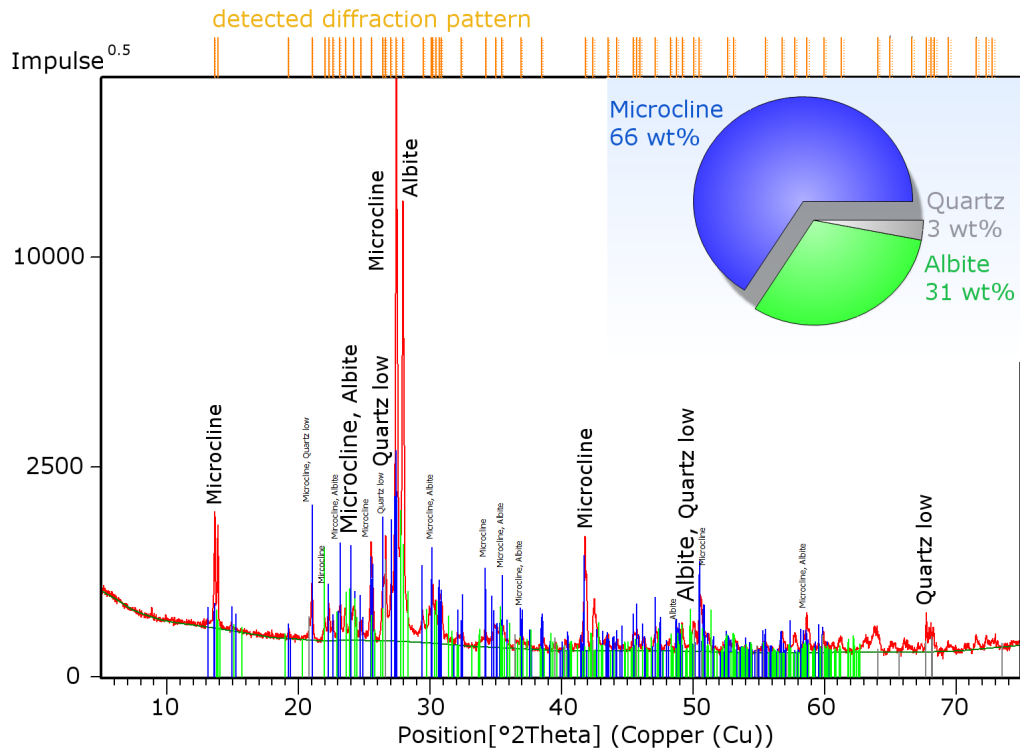


Fig. 2.6: XRD analysis of orthoclase, *PSF* 63 μm - 400 μm . Application of ICSD (2009) database. Identified mineral phases: albite (green), microcline (blue), and quartz (grey). Blue, green, grey vertical lines represent ICSD diffraction patterns, orange/red collected XRD reflection angles of orthoclase. Quartz low refers to α -quartz. The insert illustrates calculated wt% of mineral components using the Rietveld method.

components (App. Fig. B.25). The cumulative mass-median diameter was $d_{50} = 350 \mu\text{m}$ (medium sand). The *PSF* covered 150 - 800 μm and BET analysis yielded a $SSA_{BET} = 0.06 \text{ m}^2 \text{ g}^{-1} \pm 10\%$ (*RSD*, Tab. 2.2).

Table 2.2 summarizes BET measurements of pristine quartz samples. Recommended overall sample area of at least 1 m^2 (Macht et al. (2011), Sing et al. (1985)) for SSA_{BET} determinations was not met in any of the measurements (Tab. 2.2). Therefore, SSA_{BET} of the quartz mineral might have been influenced by errors $> 9.5\%$ *RSD* and should be used with care.

2.4 Methods

Section 2.4.1 offers an overview of experimental approaches of discontinuous mass, discontinuous electrolyte, and continuous potentiometric acid-base titration experiments. Data processing of relative titration data is presented in Section 2.4.2. The

application of the geochemical speciation code PHREEQC (Parkhurst and Appelo, 2013) and the universal parameter estimation code UCODE (Poeter et al., 2005) are briefly summarized in Section 2.4.3 and Appendix A.4. Finally, in Section 2.4.4, the underlying thermodynamic database is illustrated.

2.4.1 Experimental approach

Based on Noh and Schwarz (1988), Preočanin and Kallay (2006), and Lützenkirchen et al. (2012 a) a complex combination of mass and electrolyte titrations as well as potentiometric continuous acid-base titration may identify a potential pH_{nphc} as introduced in Section 2.2.3. Zeta-potential measurements can be conducted to obtain pH_{IEP} . With only one of the mentioned techniques the information in terms of pH_{nphc} or pH_{ppzc} remains incomplete while coupling all three experiments may provide information of acid-base impurities, potential dissolution processes, and charging behaviour of a given mineral.

This study applied a combination of all three titration techniques, results involve pH measurements in suspensions. Titration experiments were conducted with pristine mineral phases (Tab. 2.2). An orthoclase sample with a *PSF* 30 - 400 μm was utilized, for quartz 150 - 800 μm and for muscovite 20 - 400 μm size fractions were used, respectively (Tab. 2.2). All solutions were prepared with ultrapure water. Chemicals and tools used in experiments are summarized in Appendix A.3.

For discontinuous potentiometric mass and electrolyte titrations pH measurements were carried out with glass electrodes (App. A.3). Discontinuous means that each measurement reflects an individual sample. For each *SLR* or *IS* condition an individual sample was prepared. The experimental set-up was developed following Noh and Schwarz (1988) and Lützenkirchen et al. (2012 a). Mass and electrolyte titrations were conducted under Ar atmosphere at $295 \text{ K} \pm 2 \text{ K}$. Closed sample vials were stored under laboratory conditions at $296 \text{ K} \pm 2 \text{ K}$. Experiments were conducted in duplicate for both experimental set-ups (for more details cf. App. A.3).

Mass titration

Discontinuous mass titration experiments yielded pH_{mass} (cf. Tab. 2.1): Samples with increasing *SLRs* [g L^{-1}] in degassed $10^{-5} \text{ mol L}^{-1} \text{ NaClO}_4$ background electrolyte were prepared. Two different initial background electrolyte pH values (pH_{ini}) were chosen; $\text{pH}_{ini} = 3.0$ and $\text{pH}_{ini} = 4.5$ for quartz, for muscovite and orthoclase $\text{pH}_{ini} = 2.9$, $\text{pH}_{ini} = 4.7$. The pH_{ini} was adjusted by addition of appropriate amounts

of HNO_3 and NaOH , respectively. Samples with 5, 12.5, 50, 100, 400, 800, and 1200 g L^{-1} of each mineral were prepared and suspended in $10^{-5} \text{ mol L}^{-1}$ NaClO_4 background electrolyte (with different pH_{ini}). Suspensions were stored in 125 ml, wide-mouth Nalgene LDPE screw cap bottles. Samples were bubbled with Ar and underwent a 15 min ultrasound treatment in a water bath to accelerate equilibration (Lützenkirchen et al., 2012 a). The pH was measured after 5 h, 24 h, 2 d, and 7 d. Samples were shaken periodically. Before each pH measurement samples were stirred over approximately 1 min with a magnetic stirrer (App. A.3). During the actual pH measurements stirring was discontinued.

Electrolyte titration

Following mass titration experiments, discontinuous electrolyte titrations were performed to determine $\text{pH}_{p_{zse}}$ (cf. Tab. 2.1). Electrolyte titrations were prepared with 400 g L^{-1} solid for orthoclase and muscovite, while 1200 g L^{-1} were used for quartz. For electrolyte titrations $SLRs$ equalled ratios at which a pH_{mass} had been reached (quartz = 1200 g L^{-1} , orthoclase = 400 g L^{-1} , muscovite = 400 g L^{-1}). Increasing amounts of NaClO_4 salt were then added to the suspensions, so that salt concentrations ranged from $10^{-6} \text{ mol L}^{-1}$ to 3 mol L^{-1} . Sample equilibration and sample treatment was the same as for mass titration experiments. For high IS NaClO_4 suspensions pH measurements were corrected to exclude IS influence on the electrode's potential after Schwabe (1967) and Hagemann et al. (2014) (App. A.3.1).

Continuous potentiometric acid-base titration

Pristine minerals were used (orthoclase < 63 μm , muscovite 20 - 400 μm , quartz 150 - 800 μm). The experimental set-up was identical for all minerals. Titrations were conducted continuously, i.e. for each titration experiment one sample was prepared with a known SLR , suspension volume, and initially added volumes of acid or base; the titrant was continuously added. Suspensions were prepared with 10 mM NaClO_4 background electrolyte and equilibrated over night. For orthoclase 3.595 g were suspended in 50.5 ml background electrolyte (71.2 g L^{-1}). The SLR of the mica titration experiment equalled 190 g L^{-1} . After equilibration, defined volumes of NaOH were added to the samples to increase the pH. Titrations proceeded then from high to low pH values. Every two minutes 0.1 ml titrant (5 mM L^{-1} HClO_4) was added to the suspensions. After each titrant addition the samples were mixed with a magnetic stirrer. All chemicals were of p.a. quality. The calibration technique of the

pH meter and applied tools are summarized in Appendix A.3.

Zeta-potential measurements

The zeta-potential is the electrical potential at the shear plane (Sec. 2.2.3, Davis and Kent (1990b)) and was determined via electrophoresis measurements (for details cf. App. A.3). The pH value where the electrophoretic mobility is zero equals pH_{IEP} . Zeta potential measurements were conducted for mica and orthoclase. The particle size $< 63 \mu\text{m}$ was used for both minerals. About ten samples were prepared and the resulting suspensions (0.1 g ml^{-1} in 10 mM NaClO_4) were equilibrated until the pH values remained constant over at least 48 h. Equilibrium pH values ranged between pH 2.4 and pH 7.8. Measurements were repeated at least three times at $298.2 \text{ K} \pm 0.1 \text{ K}$.

2.4.2 Data processing of relative titration data

As illustrated in Section 2.2.3 *pristine* metal oxide surfaces can exhibit a pH_{cip} and pH_{ppzc} ; *natural* minerals on the other hand rarely have a pH_{cip} or only one specific reference pH value (e.g. pH_{nphc}). Since natural minerals were used in this study potentiometric titration data rather represented relative surface charge densities. To transform relative measurements ($\sigma [\text{C m}^{-1}]$) into absolute values, raw data (measurements) was referenced to the independently determined pH_{IEP} and/or pH_{mass} of the respective mineral (Fig. 2.11, Fig. 2.14), which unfortunately differed. Experimental surface charge was shifted such that $\sigma = 0 \text{ C m}^{-2}$ at the respective reference pH, i.e. pH_{IEP} , pH_{mass} (Sec. 2.5.2, App. A.4). The resulting charge difference is referred to as $\Delta\sigma$. The final, processed surface charge densities were treated as absolute values and used for fitting procedures with PHREEQC (surface charge models) in combination with UCODE (Sec. 2.5.2).

2.4.3 Application of PHREEQC and UCODE: Surface charge model development, parameter optimization, model limitations

Titration experiments as described in Section 2.4.1 were carried out to derive the following mineral specific SCPs: protolysis constants, *SSD*, conditional cation selectivity coefficients (Sec. 3.1.2), counterion association coefficients, and the layer capacitance. The DDLM, the BSM, and a noEDLM (Sec. 2.2.1) were applied to derive SCP sets

for muscovite, orthoclase, and quartz. The following section summarizes information of surface charge model development for SCP determination from absolute titration data (Sec. 2.4.2) but also provides general information on numerical codes relevant for the entire study.

Coupling of UCODE with PHREEQC

The determination of SCPs from absolute surface charge data (surface charge models) and batch data (surface complexation models, SCM), the development of reactive transport models (RTMs), and the application of SCPs to RTMs were major scopes of this study. Therefore, the geochemical speciation code PHREEQC (Version 3.1.2-8538, Parkhurst and Appelo (2013)) was used in combination with the universal parameter estimation code UCODE (Version 2005, Poeter et al. (2005)). Detailed information regarding the governing equations and code capabilities may be obtained from the respective manuals (Parkhurst and Appelo (2013), Poeter et al. (2005)).

Briefly, PHREEQC allows solution speciation calculations, determination of saturation indices and ion speciation and/or distributions in aqueous phases, in solid solutions, and in pure phases, as well as calculations of element distribution speciation for exchange sites and surface sites, and 1D reactive transport simulations. Equilibrium and non-equilibrium calculations are possible with PHREEQC (Parkhurst and Appelo, 2013). The Debye-Hückel and Davies expression may be used to account for electrostatic interactions of ions in dilute aqueous solutions. The Debye-Hückel and Davies approaches account for varying thermodynamic ion activities α_i and activity coefficients γ_i (index i symbolizes specific ions) both depending on ion concentrations (IS) and e.g. ion charge (z) (Parkhurst and Appelo, 2013). This study used the Davies equation to calculate γ for charged solution species. For uncharged species $\log\gamma=0.1\cdot IS$ was used (Parkhurst and Appelo, 2013). The ion exchange can be described by means of the Gaines-Thomas, the Gapon, or the Vanselow convention in PHREEQC. In this study, the activity of an exchange species α_{EX} was set to its equivalent fraction (Gaines-Thomas convention) (Parkhurst and Appelo, 2013). For surface complexation calculations PHREEQC uses the generalized two-layer model after Dzombak and Morel (1990) (DDLm) and a nonEDLM following Davis and Kent (1990a). The CD-MUSIC model option (charge distribution multi-site complexation) (e.g. Hiemstra et al. (1989b), Hiemstra et al. (1989a)) provides the implementation of more complex surface complexation models such as the BSM or TLM, and TPM (Parkhurst and Appelo, 2013).

Figure 2.7 depicts the coupling of PHREEQC with UCODE. UCODE is based on the minimization of the least squares objective function (App. A.5, App. Eq. A.48) applying a so called modified Gauss-Newton optimization (Hill, 1998), where "modified" refers to the combination of the Gauss-Newton optimization with the Levenberg-Marquardt algorithm that enables more robust fitting procedures. UCODE was applied as a shell to optimize SCPs. The parameter estimation code extracts PHREEQC results and compares extracted values with observations. If predefined UCODE conversion criteria are not met, UCODE supplies PHREEQC with new parameter values according to the modified Gauss-Newton optimization. The fitting procedure continues until user-defined UCODE convergence criteria are fulfilled.

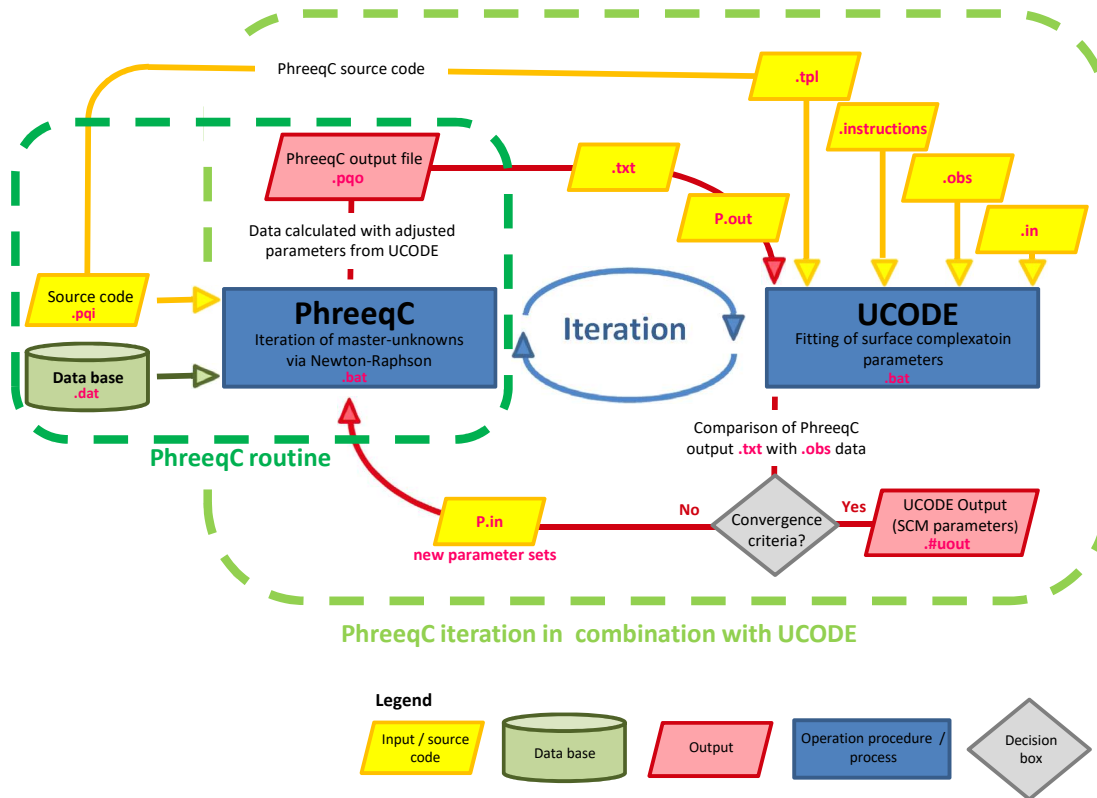


Fig. 2.7: Flowchart of PHREEQC application in combination with UCODE for parameter estimation (after Britz (2011)). Data files: .dat – database, .pqi – PHREEQC input file, .pqo – PHREEQC output file, P.out – PHREEQC output file in UCODE routine, .tpl – template file for UCODE routine, .instructions – UCODE instruction file to extract fitted data from UCODE selected output file (.txt), .obs – observations for UCODE routine, .in – definition of UCODE processes and iteration procedures, P.in – PHREEQC input file in UCODE routine, .#out – UCODE output file, .bat – PHREEQC and UCODE batch files. Files are provided in the digital appendix.

This study applied common statistical means (goodness of fit (gof)) to judge whether a fit was satisfying or whether the fitting processes had to be rerun (Hill, 1998): The 95% confidence intervals of the parameter distribution (*CI*), the least squares objective function value (*LSOF*), the mean error (*ME*), the standard errors (*SEs*), the correlation matrix for adjustable parameters, as well as the parameter standard deviation (*psd*) were taken into account (Sec. 2.5, Tab. 2.4, cf. App. A.5). No prior information was supplied for UCODE iteration procedures, no weighing of experimental data was included.

Generally, identical fit criteria were used for all fitting procedures to guarantee comparability of model output: Adjustable parameters were not constrained, parameter estimation converged as maximum fractional change of parameter values between iteration runs fell below 0.001 (Poeter et al., 2005). Parameter estimation also successfully completed if the fractional decline of the sum of squared weighted residuals was below 0.001 over three parameter estimation runs (Poeter et al., 2005). A maximum of 200 iterations was allowed before UCODE stopped without finding a (local) minimum of the least squares objective function. The maximum change of a parameter value between two iteration runs equalled $\leq 10\%$ of the initial parameter value. Gauss-Newton settings and Marquardt parameters were left at default settings (Poeter et al., 2005). A PHREEQC model run generated simulation values with respect to observations (forward) and UCODE determined the gof as well as sensitivities which were obtained by central difference perturbation. Relative perturbation amplitude equalled 1% of the final parameter value.

Whenever possible a function file was used, i.e. the calculation of adjustable parameters was linked to a second fitting parameter. This procedure was applied to reduce the number of parameters and to minimize parameter correlation problems in terms of the 2-pK approach (Sec. 2.2.2, Eq. 2.18) and concerning the estimation of symmetric counterion associations.

PHREEQC surface charge model development

In the following, the term fitting approach corresponds to the application of PHREEQC in combination with UCODE. A satisfying fitting approach yielded a calibrated surface charge model. Here calibration describes a surface charge model that yields optimized, valid, and reliable SCPs (based on gof) and that can therefore be used to simulate surface charge development where experimental data is lacking. Simulation or model run refer to a single PHREEQC calculation with SCPs from e.g.

experimental data, literature, or calibrated surface charge models; for simulations no SCP optimization is necessary. Final SCP sets represent standard conditions: $IS = 0 \text{ mol L}^{-1}$, activity coefficient of surface species = 1, while equilibrium conditions were assumed for each system.

Every surface charge model run and fitting approach involved the same database to ensure comparability (Sec. 2.4.4). The following model variants were applied to deduce SCPs from titration data (surface charge models):

- The DDLM and the BSM were used to fit absolute titration data of muscovite, quartz, and orthoclase (surface charge model).
- For quartz, the BSM utilized the SCP set from Hiemstra et al. (1989a) (1-pK approach, Sec. 2.5).
- Orthoclase and muscovite absolute surface charge values were fitted via the 1-pK and 2-pK approaches. For muscovite the 1-pK model followed recommendations made by Maslova et al. (2004).
- The reference pH values pH_{mass} and pH_{IEP} were used to define pH_{nphc} for orthoclase and muscovite titration data (Sec. 2.4.2).
- The SCPs SSD , C_1 , $\log K_{a1}^{int}$, $\log K_{a2}^{int}$, $\log K_{Al-OH}^{int}$, $\log K_{Si-OH}^{int}$ were included as estimators in surface charge models.
- The SSA_{BET} (Tab. 2.2) was utilized as a fixed parameter value.
- For muscovite, literature values were used for conditional cation exchange selectivity coefficients for Na^+ , H^+ , and K^+ (Sec. 3.1.2, App. A.6.2).
- For optimization procedures, initial values for SCPs were obtained from literature where possible, otherwise initial parameter values were manually adapted.

PHREEQC input files that were developed to simulate surface charge and surface complexation were similarly structured. In the following, the set-up of surface charge models is described. Files are provided in digital appendix. First the background solution NaClO_4 (SOLUTION 1) was defined. Then, the mineral surface (SURFACE 1) was characterized by means of the SSA_{BET} [$\text{m}^2 \text{ g}^{-1}$], SSD [sites nm^{-2}], and SLR [g L^{-1}]. In the BSM the capacitances C_1 and C_2 [F m^{-2}] had to be included with the CD-MUSIC model approach. The capacitance C_1 was an adjustable parameter. Initial guesses for C_1 did not exceed 2.1 F m^{-2} which was in accordance with recommendations made by Davis and Kent (1990a). C_2 was defined to equal 30 F m^{-2} since $C_2 \rightarrow \infty$ for the BSM by definition (Sec. 2.2.1). For each model, the

surface was pre-equilibrated with the background electrolyte following the experimental procedure. For muscovite, cation exchange processes were defined by means of EXCHANGE_MASTER_SPECIES and EXCHANGE_SPECIES. The required conditional cation exchange selectivity coefficients for Na^+ exchange ($\log K_c \text{Na}/\text{Na} = 0$), exchange of protons ($\log K_c \text{Na}/\text{H}$), and K^+ exchange ($\log K_c \text{Na}/\text{K}$) were obtained from Poinssot et al. (1999) with respect to the exchangeable cation Na^+ on the minerals surface (index cation) (Sec. 2.5.2, Tab. 2.3, App. A.6.2). Cation exchange reactions were defined via half reactions. The absolute number of available cation exchange sites [mol kgw^{-1}] was calculated from CEC_{WG} (Sec. 2.3, Sec. 3.2.2). Whether the application of literature values can be recommended is discussed in Sections 2.5, 3.1.2, and 3.3.3. Following mineral surface characterization in PHREEQC input files, surface protolysis constants were defined via SURFACE_MASTER_SPECIES and SURFACE_SPECIES. Protolysis reactions corresponded to Eq. 2.5, Eq. 2.24, and Eq. 2.23. For the BSM the -cd_music option was used to define the charge distribution. Protolysis reactions take place at the 0-plane (Sec. 2.4.3). Therefore, charge distribution describes proton accumulation or depletion at the 0-plane. Counterion and coin associations were also considered in the BSM. For NaClO_4 electrolytes counterion and coin associations relate to Na^+ and ClO_4^- . Following the definition of the respective geochemical system, batch reaction calculations were initiated for every experimental titration data point. To this end, NaClO_4 SOLUTIONs with fixed pH values, IS s, and where necessary potential cation exchange processes were defined and equilibrated with SURFACE 1. Kinetic influences were neglected in this study and instantaneous geochemical equilibrium of all investigated systems was assumed. PHREEQC and UCODE files are provided in the digital appendix.

For the definition of NaClO_4 solutions a new SOLUTION_MASTER_SPECIES Pc was defined for speciation calculations. The NaClO_4 solution served as an inert background electrolyte and dissociates into Na^+ and ClO_4^- . The following definitions were applied in PHREEQC where Pc stands for perchlorate ClO_4^- , element and species define the notation of the implemented SOLUTION_MASTER_SPECIES, alk describes the contribution of the species "Pc-" to alkalinity [eq kgw^{-1}] (positive for basic solutions, negative for acidic solutions), gfw stands for gram formula weight [g mol^{-1}], where gfw_formula represents the chemical formula of perchlorate implemented in the PHREEQC database and element_gfw represents the molar mass of ClO_4^- .

Definition perchlorate (Pc) independently from Cl-

SOLUTION_MASTER_SPECIES

#	element	species	alk	gfw_formula	element_gfw
	Pc	Pc-	0.0	Pc	99.45

SOLUTION_SPECIES

Pc- = Pc-

log_k 0.0

Input file code block 2.1: Perchlorate (ClO_4^-) definition of the NaClO_4 background electrolyte for PHREEQC calculations. Abbreviations used as priorly introduced. # indicates comments.

Surface charge model limitations

Any model approach is a simplification of observed, natural, or laboratory systems/environments. Surface charge and surface complexation models often involve assumptions concerning system properties of geochemical processes and mineral specific properties that might influence model outcome. The following simplifications and limitations were involved in mechanistic TSMs of this study (DDLm, BSM, noEDLM, 1-pK/2-pK approaches):

- For surface charge models and SCMs SSA_{BET} represents the "reactive SSA ". However, SSA_{BET} may not define the true "reactive SSA " of a mineral with respect to the SSA that actually participates in mineral surface reactions (Stillings et al., 1995). Furthermore, even though BET measurements showed variations up to 10% RSD (Sec. 2.3.1) in this study, prior information was not included in optimization procedures. Due to lack of data and better knowledge SSA_{BET} was applied as the reactive SSA in this study which is a commonly accepted strategy.
- Knowledge of $SSDs$ and site distributions is lacking, therefore different approaches exist to estimate the SSD (Sec. 2.2.5): In the present study, titration measurements, literature data, and fitting procedures were used to determine the SSD . However, different surface functional groups exist apart from singly coordinated Si-OH and Al-OH. As an example, Barrón and Torrent (1996) found evidence for doubly- and triply coordinated surface hydroxyl configurations (SHCs) on goethite and hematite surfaces. Similar SHCs might occur on orthoclase and mica surfaces which would lead to an underestimation of sites. Due to the absence of specific SSD data some studies use a generic SSD of $2.31 \text{ sites nm}^{-2}$ (Davis and Kent, 1990a) which is based on findings from Dzombak and Morel (1990). However, no consistent approach exists so far and research is still ongoing.

- The capacitance cannot be measured at mineral-water interfaces and always represents an estimated parameter, and is thus prone to errors. In the BSM C_1 is the only model inherent capacitance, $C_2 \rightarrow \infty$ (Sec. 2.2.1). The capacitance C_1 is system-dependent and precise determinations are not possible. Consequently, C_1 represents more or less best guesses. In the present study, initial parameter values for C_1 were derived from literature (Davis and Kent (1990a), Hiemstra et al. (1989a), RES³T (available at www.hzdr.de/res3t, Brendler et al. (2003)) and from experience due to prior model applications. Since C_1 influences model optimization procedures its determination is of great importance for model simulations; however, an assessment of estimated (guessed) C_1 values has been hardly possible so far.
- Due to the lack of experimental data, conditional cation exchange selectivity coefficients from literature (Sec. 3.1.2) were utilized. However, conditional cation exchange selectivity coefficients are highly dependent on the surrounding geochemical system and theoretically only apply to one geochemical *condition*: Coefficients may vary as a function of exchange sites, *IS*, cation background concentration and distribution, temperature, *SSA*, *PSF*, pH, preconditioning procedures of the mineral, and the nature of the mineral surface itself. Consequently, the selected selectivity coefficients might not represent the geochemical systems of interest even though coefficients have been thoroughly assessed.
- Zeta-potential measurements (Sec. 2.4, App. A.3) were used as an estimate of the diffuse layer potential. This is a commonly chosen approach but not necessarily correct as illustrated in Lützenkirchen et al. (2012 b).
- Since muscovite, orthoclase, and quartz used in the present study did not exhibit a pH_{ppzc} , pH_{IEP} and/or pH_{mass} had to be used to shift relative titration data with respect to a possible pH_{nphc} (Sec. 2.2.3, Sec. 2.4.2, Sec. 2.5.1). This approach was required to interpret collected data in the first place. However, whether one or the other represented the true pH_{nphc} could only be assessed by means of gof of optimization procedures (UCODE).
- Co- and counterion association affinities ($\log K_{ClO_4^-, Na^+}$) were derived from Hiemstra et al. (1989a) for quartz surface charge models. For orthoclase and muscovite $\log K_{ClO_4^-, Na^+}$ were derived from titration experiments. Since titration experiments were carried out with only one *IS*, optimized $\log K_{ClO_4^-, Na^+}$ did not represent varying activity coefficients as recommended by e.g. Hiemstra et al. (1989a). Hence, the validity of co- and counterion association coefficients was therefore limited to the specific geochemical condition of titration experiments.

2.4.4 Thermodynamic database

The database has been developed over the past eight years during joint projects of the Gesellschaft für Anlagen- und Reaktorsicherheit gGmbH, Braunschweig and the Helmholtz-Zentrum Dresden-Rossendorf e.V. The database has been under continued development ever since and the version used in this study was finalized in December 2016 and will be published summer 2018.

The database was derived from the PSI/NAGRA Thermodynamic Database (TDB) Version 12/07 (Paul Scherrer Institute (PSI)/National Cooperative for the Disposal of Radioactive Waste (NAGRA) TDB 12/07) and was formatted to fit PHREEQC applications (Thoenen et al., 2014). It comprises thermodynamic data on aqueous speciation and for solid mineral phases, and sorption parameters (Noseck et al., 2012). The database includes relevant mineral phases of the Gorleben site as well as long-term safety relevant nuclides, fission products, and matrix elements for geochemical reactions at 298 K (Noseck et al., 2012). It was extended for additional data not included in the PSI/NAGRA TDB. Regarding mineral solubility, lacking data was obtained from the NEA TDB, Vol. 13 a (Lemire et al., 2013), ANDRA Database ThermoChimie (Giffaut et al., 2014), from the Lawrence Livermore National Laboratory (LLNL) Database (based on LLNL data 0, last updated August 1986), NEA Update TDB, Vol. 5 (Giffaut et al., 2014), and THEREDA database (e.g. Voigt et al. (2007)). Aqueous speciation data was extended considering data from Lemire et al. (2013), Giffaut et al. (2014), Stefánsson and Arnórsson (2000), Richter et al. (2016), Lindsay (1980), the LLNL Database, and Guillaumont et al. (2003). Sorption parameters of multiple peer-reviewed publications were used alongside with sorption data from the RES³T database (Brendler et al., 2003). More detailed information is provided by Noseck et al. (2012).

2.5 Results and discussion

Mass, electrolyte and potentiometric titration data is presented (Sec. 2.5.1), as well as a discussion of model output and optimization procedures (Sec. 2.5.2). Tables 2.3 and 2.4 present an overview of model parametrization, optimized SCP sets, and gof of surface charge models; SCP sets comprise the SSD , C_1 , $\log K_{a1}^{int}$ and $\log K_{a2}^{int}$, $\log K_{Al-OH}^{int}$ or $\log K_{Si-OH}^{int}$, counter- and coion association affinities ($\log K_{Na+}$, $\log K_{ClO_4^-}$), as well as conditional cation exchange selectivity coefficients. Each SCP set describes an individual surface charge model and is identified via a unique ID

(identification). IDs are compiled as follows: SCP stands for surface complexation parameter, the following letter defines the respective mineral (Q – quartz, M – muscovite, FS – feldspar/orthoclase), and Roman numbers relate to the number of the SCP set, and thus, surface charge model.

Uncertainties of pH measurements from mass and electrolyte titration experiments were derived via DIN 19268 (2007) and amounted to a maximum of 0.16 pH units (cf. App. A.3.2). Determination of uncertainties of surface charge measurements (titration experiments) could not be included in this study; thus, an error estimation of titration experiments ranging between 10% - 30% was assumed following Baeyens and Bradbury (1997) (cf. App. A.3.3).

2.5.1 Experimental results

Quartz

Figure 2.8 depicts mass (A) and electrolyte (B) titration data of quartz. Titration results have to be assessed with caution since surface impurities of the natural quartz mineral potentially bias experimental raw data. Interestingly, depending on the initial pH condition (pH_{ini}), mass titration results approached two different end points (pH_{mass} , Fig. 2.8 A):

- Experiments initiated at pH_{ini} 3.0 did not show any change with increasing solid content. This implied an ideal, pristine (hydr)oxide silica surface (free of relevant basic or acidic impurities); $\text{pH}_{mass} = 2.9$ and agreed well with cited silica pH_{ppzc} (e.g. Noh and Schwarz (1988)).
- In contrast, measurements that were started at $\text{pH}_{ini} = 4.5$ converged towards $\text{pH}_{mass} = 6.5$ which contradicted the former observation.

Results supported the assumption that two "types" of silica surface functional groups might exist which behave differently depending on surrounding pH conditions. One "type" of sites behaved pH independent whereas as a second "type" of sites evolved pH depend properties. This observation could be related to findings of Lützenkirchen (1996) who observed Cd sorption processes in unexpectedly low pH ranges at silica solid-solution interfaces. Lützenkirchen (1996) had to assume that besides Si-OH groups the examined surface was partially composed of cation exchange sites due to small amounts of Na-impurities. Interestingly, similar findings were made in the present study: Quartz also showed minor surface impurities (Sec. 2.3, App. Tab. B.2) and Eu sorption processes were also observed at $\text{pH} < 4$ (Sec. 3.3). These unexpected

results highlight that assumingly well-studied surfaces like silica surfaces still bear unknowns that have yet to be uncovered.

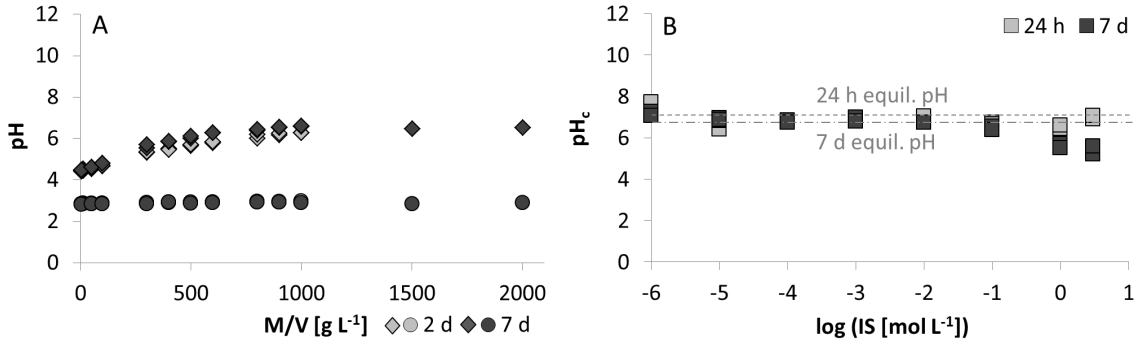


Fig. 2.8: Experimental mass (A) and electrolyte (B) titration data of quartz after 24 h, 2 d, and 7 d. Experiments were carried out in doublets. A: Discontinuous mass titration: Circles – $\text{pH}_{ini} = 3.0$, diamonds – $\text{pH}_{ini} = 4.5$. B: Discontinuous electrolyte titration: $SLR = 1200 \text{ g L}^{-1}$, dashed line illustrates reference sample (suspension without addition of NaClO_4) after 7 h, dotted-dashed line represents reference after 7 d equilibration time. pH_c stands for pH values that were corrected for electrolyte influences after Hagemann et al. (2014) (Sec. 2.4.1), IS – ionic strength [$\log(IS \text{ mol L}^{-1})$], M/V – mass volume ratio (SLR) [g L^{-1}].

Figure 2.8 B presents discontinuous electrolyte titration results using equilibration times of 24 h and 7 d ($SLR = 1200 \text{ g L}^{-1}$, increasing NaClO_4 concentrations). Horizontal lines in Figure 2.8 B depict pH measurements of reference samples after 24 h and 7 d; reference samples were suspensions with $SLR = 1200 \text{ g L}^{-1}$ in $10^{-5} \text{ mol L}^{-1}$ NaClO_4 . The pH decrease of the reference samples after 7 d (≈ 0.3 pH units) were attributed to pH-measurement uncertainties (0.16 pH units after DIN 19268 (2007), cf. App. A.3.2) and potential CO_2 influence during equilibration time. Electrolyte titration results after 7 d indicated that rising IS concentrations ($> 0.1 \text{ mol L}^{-1}$ NaClO_4) caused decreasing endpoints; hence, $\text{pH}_{mass} \neq \text{pH}_{pzse} \neq \text{pH}_{ppzc}$ could be assumed. For pristine oxide surfaces and symmetric counterion associations the pH should be independent of IS and $\text{pH}_{mass} = \text{pH}_{pzse} = \text{pH}_{ppzc}$ (e.g. Preočanin and Kallay (1998), Lützenkirchen et al. (2012 a)). To conclude, data indicated asymmetric counterion associations after 7 d that effected pH conditions at $IS > 0.1 \text{ mol L}^{-1}$. This observation might be specific for NaClO_4 and should be verified for other electrolytes.

Mass titration experiments offer a reliable means to determine a mineral's pH_{ppzc} if surface contaminations and mineral dissolution do not occur (Noh and Schwarz, 1988). If both cannot be excluded (as in the present study) Noh and Schwarz (1988) suggest that potentiometric titrations are more suitable to define a mineral's reference pH, e.g. pH_{nphc} or pH_{cip} . The pH_{nphc} for natural minerals or the pH_{pznpc} for pristine surfaces are determined via potentiometric titrations and ideally coincidence with the pH_{cip} . As potentiometric titration data was collected with only one IS ($10 \text{ mmol L}^{-1} \text{ NaClO}_4$ electrolyte concentration), a potential pH dependence of pH_{nphc} could not be verified. Due to the lack of data a literature data set had to be used: Bolt (1957) collected surface charge measurements from amorphous silica at different IS s (Fig. 2.9) and as Figure 2.9 shows, data from Bolt (1957) agreed well with titration data collected in this study. Data from Bolt (1957) exhibited a pH_{pznpc} below 4.0 (Fig. 2.9) and since both data sets agreed well Bolt's pH_{pznpc} was assumed to offer a good estimate of the quartz reference pH of this study. Whether the quartz surface of this study exhibited truly pristine mineral surface characteristics or whether the mineral surface charge development was influenced by potential impurities could not explicitly be verified.

For the subsequent surface charge modeling study data from Bolt (1957), 10 mM NaCl was used as a more comprehensive data set compared to data collected in this study (Fig. 2.9). This approach was reasonable since both potentiometric data sets at 10 mM electrolyte concentration matched well and exhibited similar reference pH values: pH_{ppzc} (Bolt, 1957), pH_{nphc} respectively (this study).

Orthoclase

Figure 2.10 depicts measurements of mass (A) and electrolyte (B) titration experiments of orthoclase. For orthoclase, mass titration experiments were carried out with two pH_{ini} values ($\text{pH}_{ini} = 2.9$ and $\text{pH}_{ini} = 4.7$) which did not converge towards the same endpoint (pH_{mass}) within 7 d (Fig. 2.10 A) as would be expected for a mineral surface with negligible impurities (e.g. Noh and Schwarz (1988)). After 7 months, pH measurements indicated an equilibrium $\text{pH} = 8.3$ (data not displayed here) that was either due to mineral dissolution, potential secondary phase precipitation, and/or governed by surface impurities. All equilibrium pH values determined either after 5 h, 7 d, or 7 months exceeded the pH_{IEP} which equalled 3.5. Hence, mass titration experiments supported the assumption of basic impurities at the orthoclase surface.

Zeta-potential measurements yielded negative electrokinetic potentials at pH

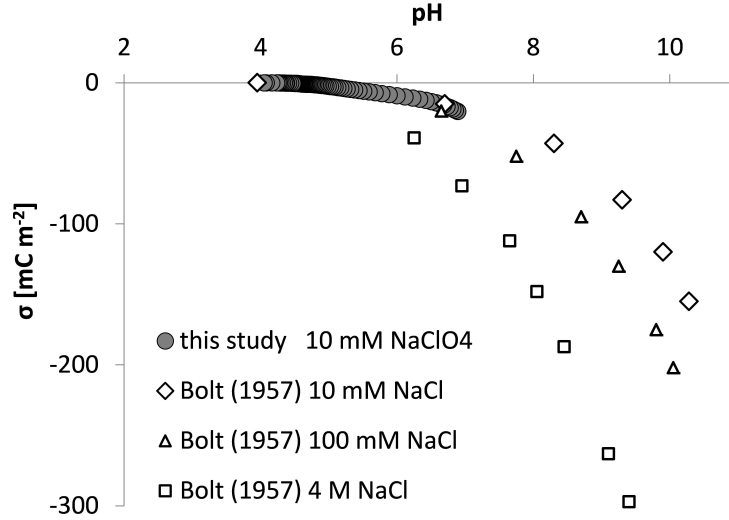


Fig. 2.9: Continuous potentiometric acid-base titration of quartz (solid symbols) in comparison to titration data of a silica sol at different electrolyte concentrations published by Bolt (1957) (open characters). Measurements of this study were determined in 10 mM NaClO_4 , Bolt (1957) used increasing concentrations of NaCl . σ corresponds to the surface charge density [mC m^{-2}].

conditions $> \text{pH}_{IEP}$ ($\text{pH}_{IEP} = 3.5$, App. Fig. B.27). The pH_{IEP} was in fair agreement with IEP values observed by Stillings et al. (1995) who report $\text{pH}_{IEP} = 1.5 - 6.1$ depending on the degree of K^+ vs. H^+ exchange on the surface. The more K^+ is exchanged for H^+ the higher pH_{IEP} . Calculated pH_{IEP} from ideally composed feldspar minerals result in a reference pH of 3.0 - 3.1 (Stillings et al., 1995). On this basis, the zeta-potentials would suggest K^+ vs. H^+ exchange at the present orthoclase surface.

Figure 2.10 B shows orthoclase electrolyte titration results. The dotted and dash-dotted horizontal lines depict the equilibrium pH of reference samples (reference suspensions: $SLR\ 400\ \text{g L}^{-1}$, $10^{-5}\ \text{mol L}^{-1}\ \text{NaClO}_4$). The pH of references changed by 0.4 pH units over the first 7 d (Fig. 2.10 B) and by 0.9 pH units over 8 months (data not displayed here). The shift in pH might be caused by Na^+ vs. H^+ exchange processes and/or be due to potential atmospheric CO_2 influence. Stillings et al. (1995) reported pH shifts of approximately 0.5 pH units after 500 d of adularia feldspar in different electrolyte solutions which they related to surface ageing processes. Considering data collected after 5 h where mineral ageing processes are not yet relevant and excluding the possibility of a CO_2 influence during 5 h equilibration

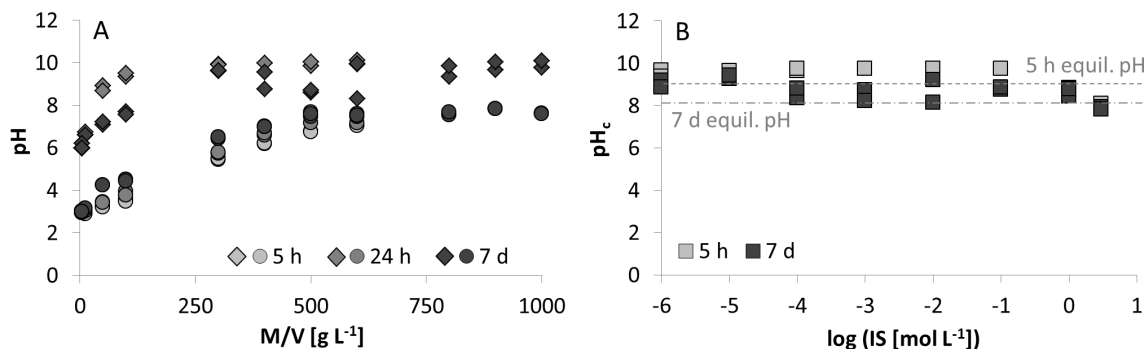


Fig. 2.10: Mass (A) and electrolyte (B) titration measurements of orthoclase after 5 h, 24 h, and 7 d. Experiments were conducted in duplicate. A: Discontinuous mass titration: Circles – $pH_{ini} = 2.9$, diamonds – $pH_{ini} = 4.7$. B: Discontinuous electrolyte titration: $SLR = 400 \text{ g L}^{-1}$, dashed line – reference sample (without addition of NaClO_4) after 24 h, dotted-dashed line – reference after 7 d equilibration time. pH_c – pH corrected for electrolyte influences after Hagemann et al. (2014) (Sec. 2.4.1). IS – ionic strength [$\log(IS \text{ mol L}^{-1})$].

time measurements indicated asymmetric counterion associations which affected pH conditions at $IS > 1 \text{ mol L}^{-1}$.

Since $pH_{mass} \neq pH_{IEP}$, a pH_{ppzc} did not exist for orthoclase. Hence, potentiometric titration measurements returned relative surface charge data that needed to be transformed into absolute values (Sec. 2.4.2). Two different approaches were followed to determine absolute surface charges from the raw data which is illustrated in Appendix A.4.1. Figure 2.11 depicts relative data in relation to the shifted processed, absolute data. Titration measurements appeared to approach a threshold at $pH > 7.6$ (Fig. 2.11). This threshold could be caused by fully deprotonated surface functional groups (Si-O^- and Al-O^-). In the absence of better information Equation 2.33 was used to obtain a rough estimate of the SSD and yielded $1.9 \text{ sites nm}^{-2}$ with $\sigma_{sat} = 0.3 \text{ C m}^{-2}$.

Figure 2.12 compares potentiometric measurements of this study with literature data: Stillings et al. (1995) used a preconditioned orthoclase from the Gotthard Massif of the Swiss Alps (adularia). Titrations were conducted at different IS s (1 - 100 mM NaCl); data collected with 1 mM NaCl electrolyte are shown. Only minor differences were observed between experiments carried out in 10 mM and 1 mM NaCl electrolyte according to Stillings et al. (1995). Zorn (2000) used a

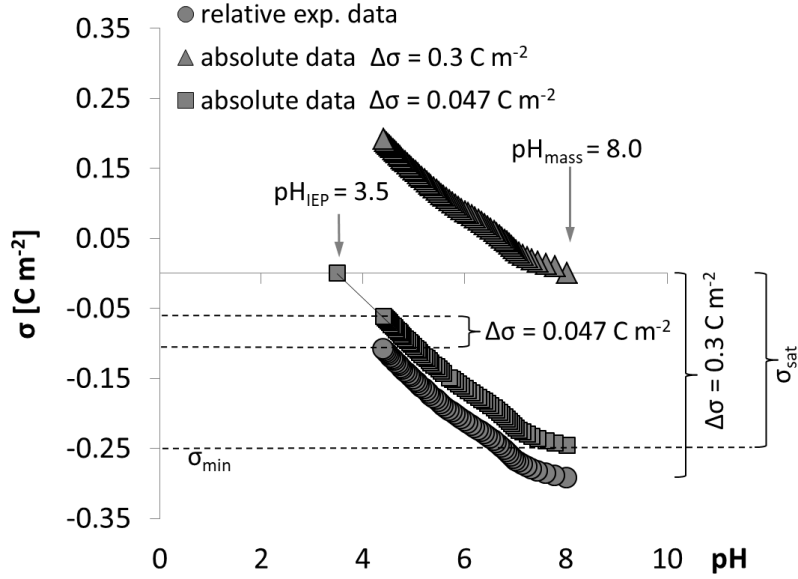


Fig. 2.11: Continuous potentiometric acid-base titration measurements of orthoclase. Circles – relative surface charge, squares – absolute data using $\Delta\sigma = 0.047 \text{ C m}^{-2}$, triangles – absolute data using $\Delta\sigma = 0.3 \text{ C m}^{-2}$. σ_{sat} – surface charge density [C m^{-2}] of fully deprotonated surfaces, σ_{min} – minimum value of absolute surface charge density.

commercial albite mineral for potentiometric measurements in 100 mM NaClO_4 . Since data is scarce albite and adularia feldspar were assumed to represent similar surfaces compared to the orthoclase of the present study (66 wt% microcline, 31 wt% albite, 3 wt% quartz, Sec. 2.3). Both literature data sets are depicted in relation to processed orthoclase titration data in 10 mM NaClO_4 with $\Delta\sigma = 0.3 \text{ C m}^{-2}$ and $\Delta\sigma = 0.047 \text{ C m}^{-2}$ (Fig. 2.12); interestingly the data sets covered a broad range of surface charge densities even though geochemical conditions and minerals were similar and supposed to be comparable. Figure 2.12 indicates $\text{pH}_{\text{pznpc}} > 7$ for the albite and adularia feldspar which would suggest $\text{pH}_{\text{mass}} \sim \text{pH}_{\text{nphc}}$ for this study. Measurements from Stillings et al. (1995) at different IS s revealed a $\text{pH}_{\text{pzse}} > 8.0$, data from Zorn (2000) exhibited $\text{pH}_{\text{pznpc}} > 7$, no information of pH_{IEP} , pH_{mass} , or pH_{pzse} is available for the albite sample. From secondary literature $\text{pH}_{\text{pzc}} = 2.0$ for albite is reported by Zorn (2000). Differences in feldspar mineral titration data and the variety of reference pH values (pH_{pzc} , pH_{pznpc} , pH_{pzse}) illustrate the complexity of mineral titration experiments and the difficulty to correctly interpret experimental data.

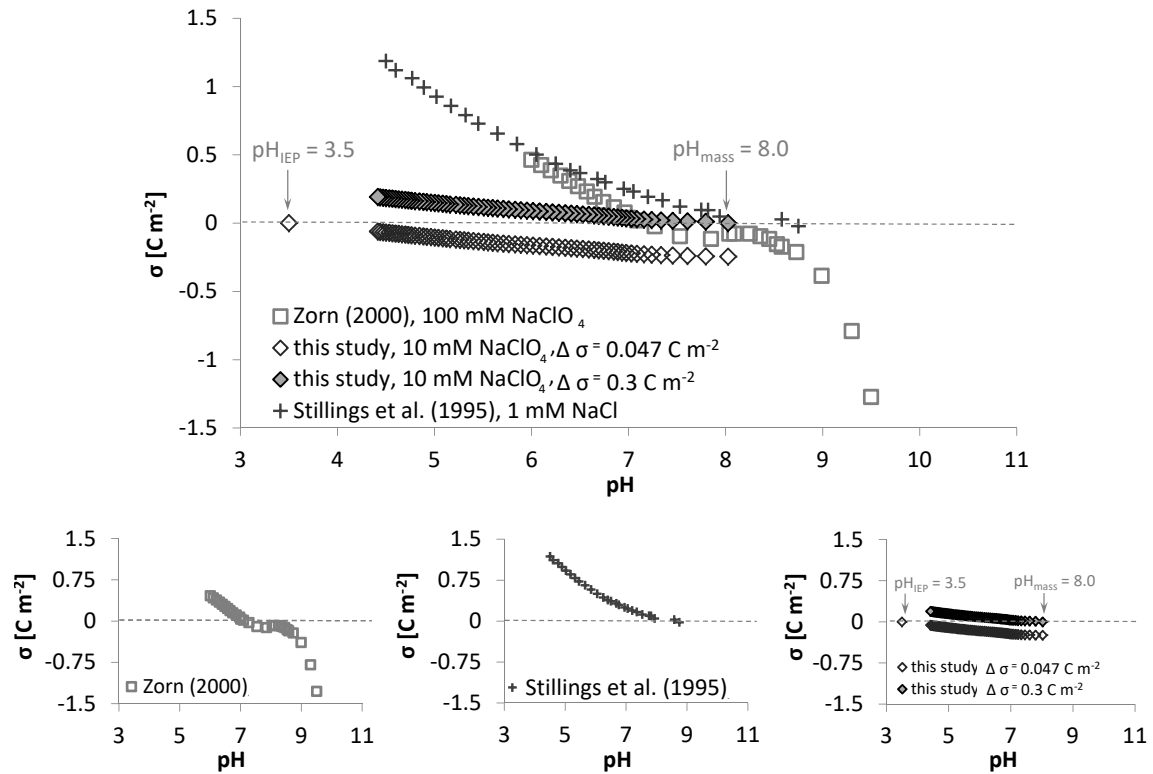


Fig. 2.12: Comparison of surface charge data from this study and literature data of feldspar minerals. Diamonds – absolute continuous potentiometric acid-base titration data of orthoclase (this study) with $\Delta\sigma = 0.3 \text{ C m}^{-2}$ (empty diamonds), with $\Delta\sigma = 0.047 \text{ C m}^{-2}$ (solid diamonds). Squares – Zorn (2000): albite in 100 mM NaClO₄. Crosses – Stillings et al. (1995): adularia feldspar in 1 mM NaCl. σ – surface charge density [C m⁻²], $\Delta\sigma$ – shift to transform relative into absolute surface charge densities (Sec. 2.4.2).

Muscovite

In Figure 2.13 results of discontinuous mass (A) and electrolyte (B) titration of muscovite are illustrated. Similar to orthoclase mass titration (Fig. 2.10) no instantaneous pH_{mass} was obtained (Fig. 2.13 A). After 7 d measurements returned $\text{pH}_{\text{mass}} \approx 7.9$ which was independent of pH_{ini} (Fig. 2.13 A). However, this pH might had been influenced by mineral dissolution or secondary phase precipitation that occurred during the equilibration time of 7 d.

As expected, zeta-potential measurements resulted in a low IEP ($\text{pH}_{\text{IEP}} = 2.4$) for the muscovite (App. B.27). An increase of pH_{mass} in relation to pH_{IEP} implied that basic impurities were situated at the muscovite surface. Zeta-potential exhibited

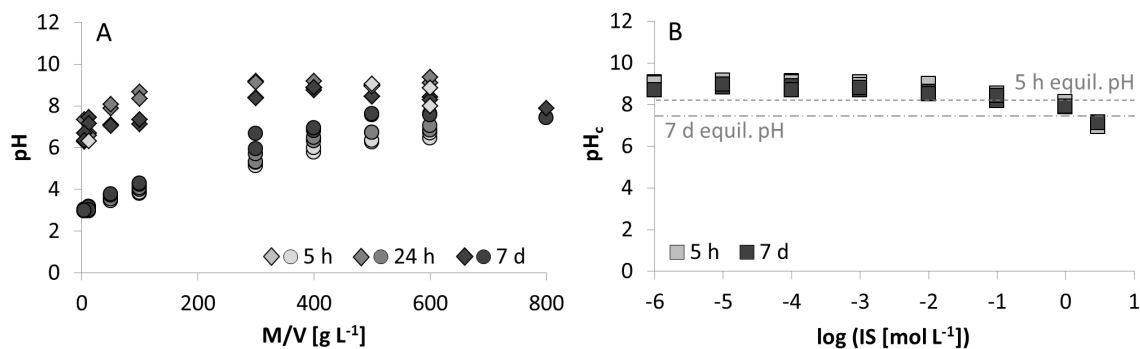


Fig. 2.13: Experimental mass (A) and electrolyte (B) titration results of muscovite after 5 h, 24 h, and 7 d. (A) Discontinuous mass titration: Circles – $\text{pH}_{ini} = 2.9$, diamonds – $\text{pH}_{ini} = 4.7$. (B) Discontinuous electrolyte titration: $SLR = 400 \text{ g L}^{-1}$, dashed line – reference after 5 h (without addition of NaClO_4), dotted-dashed line – reference after 7 d, pH_c – pH corrected for electrolyte influences after Hagemann et al. (2014) (Sec. A.3.1), IS – ionic strength [$\log(IS \text{ mol L}^{-1})$].

permanent negative surface charge above pH_{IEP} (App. B.27) which was attributed to isomorphic substitution which is typical for mica minerals. Comparing orthoclase and muscovite zeta-potential measurements showed expected results: Due to isomorphic substitution the electrokinetic potential of muscovite was smaller compared to orthoclase (App. Fig. B.27).

Figure 2.13 B depicts electrolyte titration results of muscovite. The equilibrium pH of reference samples after 5 h and 7 d are displayed. For reference samples a $SLR = 400 \text{ g L}^{-1}$, $10^{-5} \text{ mol L}^{-1} \text{ NaClO}_4$ were prepared; experimental conditions were equal to mass titration samples. The pH difference of reference samples measured after 5 h and 7 d amounts to 0.8 pH units. This pH difference might be related to cation exchange processes of the mica mineral: H^+ bound in mica mineral interlayers can exchange with K^+ or Na^+ in the suspension (Pashley, 1981). Furthermore, decreasing pH values as a function of IS were observed: At $IS > 10 \text{ mM NaClO}_4$ electrolyte concentration asymmetric counterion associations affected the pH of electrolyte titration samples; no difference between 5 h and 7 d equilibration time was observed.

As a first conclusion, muscovite mass and electrolyte titration experiments indicated basic impurities at the surface and asymmetric counterion association affinities which became relevant at $IS > 10 \text{ mM NaClO}_4$. Since $\text{pH}_{mass} \neq \text{pH}_{IEP}$ potentiometric titration yielded relative data (Fig. 2.14). As for orthoclase data

processing, mica titration measurements could be related to two different reference pH values (pH_{IEP} , pH_{mass}) to transform relative data to absolute values:

- Relative data was scaled to $\text{pH}_{IEP} = 2.4$ with $\Delta\sigma = 5 \text{ mC m}^{-2}$, and
- potentiometric titration data (raw data) was shifted to fit pH_{mass} with $\Delta\sigma = 51 \text{ mC m}^{-2}$ which would be interpreted to represent the surface charge of edge sites (Al-OH and Si-OH functional groups).

More detailed information is provided in Appendix A.4.2.

Figure 2.14 presents absolute potentiometric titration results of this study with respect to reference pH values pH_{IEP} and pH_{mass} ; a comparison with experimental data of Zorn (2000) and Baeyens and Bradbury (1997) is also shown. Zorn (2000) used a commercial muscovite and titrations were carried out in 100 mM NaClO_4 without preconditioning or purification of the mineral. Information of pH_{mass} , pH_{IEP} , or pH_{pzc} was not supplied (Zorn, 2000). Results exhibited $\text{pH}_{pznpc} \approx 5.8$. From secondary literature $\text{pH}_{pzc} = 6.6$ was reported and applied in modeling studies of Zorn (2000). Baeyens and Bradbury (1997) conducted discontinuous acid-base titration experiments of homo-ionic, purified Na-montmorillonite (SWy-1, Crook County, WY) from the Source Clay Mineral Repository (University of Missouri-Columbia). An equilibration time of 24 h was allowed previous to the titration experiments. Experiments were carried out at different IS s and equilibration times: 100 mM NaClO_4 and 500 mM NaClO_4 , 1 d - 7 d equilibration time. As expected, measurements did not intersect. Duc et al. (2005) compared montmorillonite titration data at different IS s (NaCl , NaClO_4) from Baeyens and Bradbury (1997) and Avena and De Pauli (1998) where both data sets agreed well: The studies showed that montmorillonite titration measurements did not exhibit a pH_{cip} , that surface charge data was shifted in a parallel manner with increasing IS , and that the pH_{pznpc} decreased due to increasing IS which showed that clay surfaces behave differently from pure silanol surfaces. In the absence of data, montmorillonite and muscovite titration data is compared in Figure 2.14: Despite the similar mineral structure considerable scatter of titration measurements is depicted. Especially at high and low pH values extreme surface charge density values (σ) were observed where mineral dissolution, surface precipitation, as well as cation exchange reactions interfere. Baeyens and Bradbury (1997) stated that limiting the lower end point of titration to pH 4 reduces cation exchange influences to negligible levels. In contrast, mineral dissolution reactions were determined to be still relevant also at $\text{pH} > 4.0$ (Baeyens and Bradbury, 1997). A comparison of pH_{pznpc} values in Figure 2.14 indicates that

pH_{mass} of this study would be in fairly good agreement with data provided by Baeyens and Bradbury (1997) and Avena and De Pauli (1998) (the latter data set not shown here).

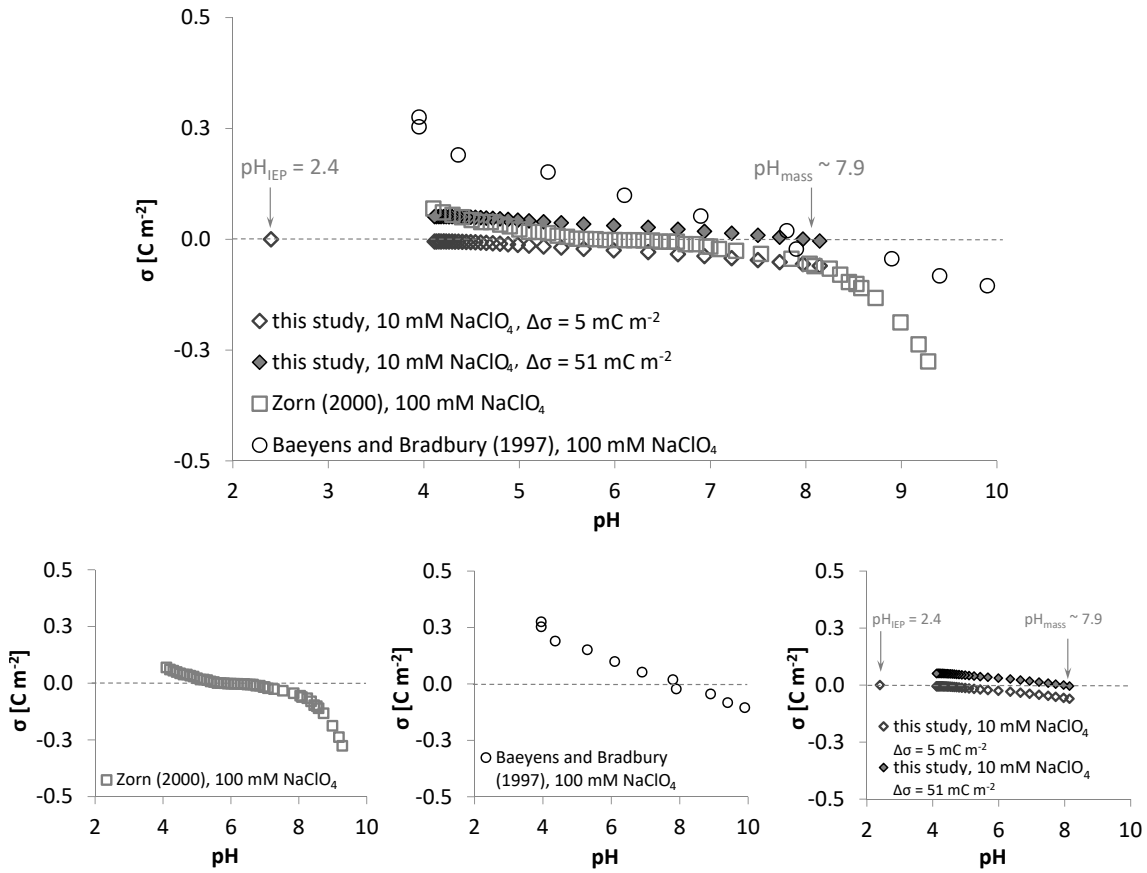


Fig. 2.14: Comparison of surface charge data from this study and literature data of clay minerals. Diamonds – absolute muscovite continuous potentiometric acid-base titration data of this study with $\Delta\sigma = 5$ mC m⁻² (open diamonds) and $\Delta\sigma = 51$ mC m⁻² (solid diamonds). Squares – titration data from Zorn (2000) (muscovite, 100 mM NaClO₄). Circles – titration data from Baeyens and Bradbury (1997) (homo-ionic, purified Na-montmorillonite, 100 mM NaClO₄), σ – surface charge density [C m⁻²], $\Delta\sigma$ shift to transform relative into absolute surface charge densities (Sec. 2.4.2).

2.5.2 Modeling results

Quartz

Figure 2.15 shows fitted and simulated results based on the Bolt (1957) data set. The DDLM approach is valid for experimental data in low IS conditions (e.g. Westall

and Hohl (1980), Appelo and Postma (2010)). Consequently, the DDLM was used to fit measurements of Bolt (1957) in 10 mM NaCl electrolyte (Sec. 2.5.1). For the DDLM the SSD was adapted from Hiemstra et al. (1989a), measured SSA_{BET} was used (Tab. 2.2), and boundary conditions involved 10 mM NaClO_4 electrolyte concentration, no atmospheric influence, $SLR = 25 \text{ g L}^{-1}$. In Figure 2.15 the red solid line illustrates the DDLM fit. Corresponding SCPs are given in Tables 2.3 and 2.4 under ID $SCP Q I$. The red dotted and red dash-dotted lines represent surface charge model simulations with SCP set $SCP Q I$ (Tab. 2.3, Tab. 2.4). As expected, the DDLM generally performed well for low IS s (Fig. 2.15) and absolute surface charge densities below -100 mC m^{-2} . However, considering IS s that exceeded 10 mM NaClO_4 (NaCl respectively) caused obvious deviations from experimental data with too low surface charge densities ($< -100 \text{ mC m}^{-2}$) at high pH values ($> \text{pH } 8$).

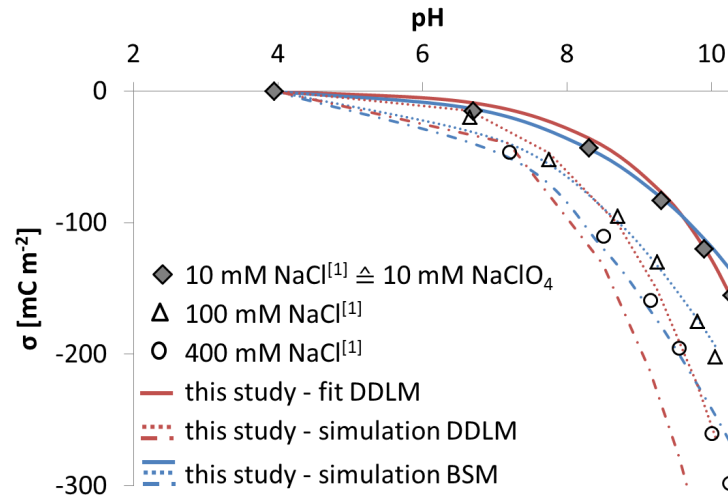


Fig. 2.15: DDLM (red) and BSM (blue) fit and simulation results of Bolt (1957)^[1] experimental titration data in the range of $IS = 10 \text{ mM}$ (diamonds) - 400 mM (circles). DDLM fit (solid red line) represents 10 mM electrolyte concentration, dotted and dash-dotted lines symbolize simulations with the DDLM $SCP Q I$. BSM refers to simulations of IS conditions of 10 mM (blue solid line), 100 mM (triangles, dotted line), and 400 mM (dash-dotted line) background electrolyte concentration with $SCP Q II$. σ represents the surface charge density $[\text{mC m}^{-2}]$.

For the BSM, SCPs from Hiemstra et al. (1989a) could be directly used ($SCP Q II$ in Tables 2.3 and 2.4, Fig. 2.15); no fitting procedure was necessary. Data from Bolt (1957) that ranged between 10 mM - 400 mM NaCl was simulated with SCPs from Hiemstra et al. (1989a) where the simulation the upper IS condition was close to the limit of applicability of the Davies theory which approximately

equals $IS = 0.5 \text{ mol L}^{-1}$ (Appelo and Postma, 2010). As illustrated in Figure 2.15 the BSM resulted in better simulations for high pH values, elevated IS , and low surface charge densities compared to the DDLM. The better performance of the BSM was model-based and due to the inclusion of counter- and coions as well as charge distribution over different electrostatic planes (0-plane, 1-plane/d-plane). However, considering conditions $IS = 10 \text{ mmol L}^{-1}$, both model approaches returned satisfying results with a narrow CI , $SE = 5 \text{ mC m}^2$, and a psd of 0.03 for the DDLM approach (Tab. 2.4). Based on the above, SCP sets $SCP Q I$, $SCP Q II$ were used in Eu SCMs as summarized in Table 2.4.

Orthoclase

Absolute surface charge densities were used to determine protolysis constants for the BSM and the DDLM (cf. Sec. 2.4.2). Detailed information on orthoclase fitting procedures is supplied in Appendix A.6.1. Tables 2.3 and 2.4 summarize approaches and SCPs ($SCP FS I - X$). Figures 2.16 and 2.17 show fitting and simulation results (DDLM, BSM) with SCPs from Table 2.4.

For $SCP FS VIII$ (2-pK BSM), C_1 , protolysis constants, counter- and coion association coefficients, as well as $\Delta\sigma$ served as fitting parameters (Tab. 2.3). The approach returned a well constrained parameter set with narrow CI s and a $ME < 4 \text{ mC m}^{-2}$ (cf. Tab. 2.4). The optimized $\Delta\sigma$ yielded 0.03 C m^{-2} (Fig. 2.17 D, D.1, cf. Tab. 2.4). Shifting raw data of titration experiments by $\Delta\sigma = 0.03 \text{ C m}^{-2}$ resulted in $\text{pH}_{nphc} = \text{pH}_{IEP}$. Unfortunately, parameter values obtained with $SCP FS VIII$ did not reflect realistic relationships which will be illustrated more closely in the following (cf. this section, pg. 107). However, due to the adequate fit (Fig. 2.17), the optimized $\Delta\sigma$ value was also used for DDLM optimizations – in addition to $\Delta\sigma = 0.047 \text{ C m}^{-2}$ and $\Delta\sigma = 0.3 \text{ C m}^{-2}$.

A comparison of DDLM fits under the assumption that $\text{pH}_{nphc} = \text{pH}_{IEP}$ ($SCP FS I, II, IV$) revealed that (cf. Fig. 2.16 and Tab. 2.4):

- a) The DDLM delivered poor fits regardless whether the 1-pK or 2-pK approach was chosen (Fig. 2.16). This was evidenced by large parameter CI s (especially for $SCP FS IV$) and by relatively high $LSOF$ values.
- b) The 1-pK approaches ($SCP FS I - II$) returned reliable, sound SCPs.
- c) The 2-pK DDLM approach ($SCP FS IV$) resulted in unrealistic SCP sets with $|\log K_{a1}^{int}| > |\log K_{a2}^{int}|$ which will be illustrated more closely in the following (cf. pg. 100).

Generally, *SCP FS I - II* and *SCP FS IV* overestimated the surface charge density at low pH values and underestimated the surface charge density for $\text{pH} \geq 8$ (Fig. 2.16 A - B, D); typical simoidal fits were obtained. The DDLM theory treats ions in the diffuse layer as point charges to neutralize the surface charge (Appelo and Postma, 2010). As a consequence, diffuse layer potentials often significantly exceed zeta-potential measurements as was also shown with surface potential simulations in this study (Fig. 2.16 A.1 - B.1, D.1). For *SCP FS I* the *SSD* was the only optimized parameter. For *SCP FS II* SCPs could be derived from measurements, no fitting was necessary. Both approaches returned relatively large *psds* and *LSOF* values (Tab. 2.4). However, *SCP FS I* and *II* still provided reasonable parameter sets compared to *SCP FS IV*.

The only DDLM 2-pK fitting procedure that did not show high parameter correlations or UCODE convergence problems was *SCP FS IV* ($\text{pH}_{nphc} = \text{pH}_{IEP}$). However, the approach *SCP FS IV* did not yield unique parameter values which was indicated by extremely large 95% *CI*s and *psds* for $\log K_{a1}^{int}$ and $\log K_{a2}^{int}$ (cf. Tab. 2.4). Optimizations of $\log K_{a1}^{int}$ and $\log K_{a2}^{int}$ showed that the *SSD* was the governing, sensitive parameter. Furthermore, for protonation and deprotonation constants that are symmetrically distributed around a reference pH (Eq. 2.16) $|\log K_{a1}^{int}| < |\log K_{a2}^{int}|$ should apply. This relationship is based on the application of the IEP as pH_{nphc} (reference pH): Silicate surfaces are negatively charged above pH_{IEP} ; hence, protonation reactions ($\log K_{a1}^{int}$) are negligible under geochemical conditions with $\text{pH} > \text{pH}_{IEP}$ and the upper boundary condition for $\log K_{a1}^{int}$ would be $|\log K_{a1}^{int}| \leq |\text{pH}_{IEP}|$. The surface charge model *SCP FS IV* violated this expectation and $\text{pH}_{IEP} = \text{pH}_{nphc}$ in the 2-pK DDLM did not yield reliable SCP sets (Tab. 2.4). The application of the 2-pK DDLM with $\text{pH}_{mass} = \text{pH}_{nphc}$ resulted in highly correlated SCPs and also large parameter uncertainties (*psd*) of $\log K_{a1}^{int}$ and $\log K_{a2}^{int}$ (data not shown here). Since the 2-pK DDLM did not return reliable SCP sets regardless of the chosen pH_{nphc} the 2-pK approach was excluded from orthoclase surface charge model approaches and, thus, also from Eu SCMs (Sec. 3).

The 1-pK DDLM simulation with $\text{pH}_{mass} = \text{pH}_{nphc}$ (*SCP FS III*, cf. Fig. 2.16) represented measurements best (cf. UCODE gof in Tab. 2.4). All SCPs could be inferred from measurements for *SCP FS III*, i.e. no fitting procedure was necessary. Since *SCP FS I - III* revealed realistic SCP sets for the DDLM all three approaches were used for Eu SCMs (Tab. 2.4).

Tab. 2.3: Summary of optimized parameters, initial parameter values, and surface reactions of surface charge models and SCP sets of muscovite (M), quartz (Q), and orthoclase (FS) for the DDLM and BSM in combination with the 1-pK and 2-pK approaches. Calib. data set – data set used for model calibration, ID – identification of fitting approach and SCP set, EM – electrostatic model, $\Delta\sigma$ – shift to transform relative (raw data) into absolute surface charge densities, SSA – specific surface area, SSD – surface site density, C_1 - capacitance of the BSM ($C_2 = 30 \text{ F m}^{-2}$), $\log K_{a1}^{int}$, $\log K_{a2}^{int}$ – protonation and deprotonation constant (2-pK approach), $\log K_{Al-OH}^{int}$, $\log K_{Si-OH}^{int}$ – protolysis constants of aluminol and silanol surface functional groups (1-pK approach), $\log K_{Na+}$, $\log K_{ClO_4^-}$ – counter- and coion association coefficients, SCP – surface complexation parameter, ζ – zeta-potential measurements. **Blue** values represent initial guesses of fitting parameters, **bold** SCP sets (IDs) symbolize SCPs that were used for Eu SCMs. [1] this study, [2] initial guess was manually adapted, [3] Hiemstra et al. (1989a), [4] calculated from titration data. For SCP M I - VIII the following conditional cation exchange selectivity coefficients were used as fix parameters: $\log K_c Na/Na = 0$, $\log K_c Na/K = -2.25$, $\log K_c Na/H = -1.75$ (Poinssot et al., 1999) (App. A.6.2, pg. 249).

Calib. data set	ID	EM	pK approach	$\Delta\sigma$ [1] [C m ⁻²]	SSA [1] [m ² g ⁻¹]	SSD [sites nm ⁻²]	C_1 [F m ⁻²]	SCPs						Surface reaction	Optimized SCP
								$\log K_{a1}^{int}$	$\log K_{a2}^{int}$	$\log K_{Al-OH}^{int}$	$\log K_{Si-OH}^{int}$	$\log K_{Na+}^{int}$	$\log K_{ClO_4^-}^{int}$		
Q [3]	SCP Q I	DDLM	1-pK	-	0.08	4.6 [3]	-	-	-	-	-7.5 [3]	-	-	S-OH = S-O- + H+	$\log K_{Si-OH}^{int}$
Q [3]	SCP Q II	BSM	1-pK	-	0.08	4.6 [3]	3.3 [3]	-	-	-	-7.5 [3]	-9.4 [3]	-9.4 [3]	S-OH = S-O- + H+ S-OH + Na+ = S-ONa + H+	-
FS [1]	SCP FS I	DDLM	1-pK	0.03	4.3	3.8 [1]	-	-	-	3.5 [1]	-	-	-	S-OH-0.5+ H+ = S-OH+0.5	SSD
	SCP FS II	DDLM	1-pK	0.047	4.3	3.8 [1]	-	-	-	3.5 [1]	-	-	-	S-OH-0.5+ H+ = S-OH+0.5 -	$\log K_{Al-OH}^{int}$ SSD
	SCP FS III	DDLM	1-pK	0.3	4.3	3.8 [1]	-	-	-	8.0 [1]	-	-	-	S-OH-0.5+ H+ = S-OH+0.5 -	$\log K_{Al-OH}^{int}$ SSD
	SCP FS IV	DDLM	2-pK	0.03	4.3	1.9 [1]	-	5.0 [2]	Eq. 2.18	-	-	-	-	S-OH = SO- + H+ S-OH + H+ = S-OH2+ -	$\log K_{a2}^{int}$ $\log K_{a1}^{int}$ SSD
	SCP FS V	BSM	1-pK	0.03	4.3 FS[1] 0.2 (ζ)	3.8 [1]	1.5 [2]	-	-	3.5 [1]	-	2.6 [2]	2.6 [2]	S-O-0.5 + Na = S_ONa+0.5 S-OH+0.5 + Pc- = S-OHPc-0.5 S-OH-0.5+ H+ = S-OH+0.5 -	$\log K_{Na+}$ $\log K_{ClO_4^-}$ - C_1 , SSD
FS + ζ [1]	SCP FS VI	BSM	1-pK	0.047	4.3 0.2 (ζ)	3.8 [1]	1.5 [1]	-	-	3.5 [1]	-	2.0 [2]	2.0 [2]	S-OH-0.5+ H+ = S-OH+0.5 S-O-0.5 + Na = S_ONa+0.5 S-OH+0.5 + Pc- = S-OHPc-0.5	- $\log K_{Na+}$ $\log K_{ClO_4^-}$
FS [1]	SCP FS VII	BSM	1-pK	0.3	4.3	3.8 [1]	1.5 [1]	-	-	8.0 [8]	-	0.5 [2]	0.5 [2]	S-OH-0.5+ H+ = S-OH+0.5 S-O-0.5 + Na = S_ONa+0.5 S-OH+0.5 + Pc- = S-OHPc-0.5	- $\log K_{Na+}$ $\log K_{ClO_4^-}$
FS + ζ [1]	SCP FS VIII	BSM	2-pK	0.03	4.3 0.2 (ζ)	1.7 [2]	1.5 [1]	6.0 [2]	Eq. 2.18	-	-	2.4 [2]	2.2 [2]	S-OH + H+ = S-OH2+ S-OH = S-O- + H+ S-O- + Na+ = S-ONa S-OH2+ + Pc- = S-OH2Pc	$\log K_{a1}^{int}$ $\log K_{a2}^{int}$ $\log K_{Na+}$ $\log K_{ClO_4^-}$

Continued on next page

Calib. data set	ID	EM	pK approach	$\Delta\sigma$ [1]	SSA [1]	SSD	C_1	SCP _s						Surface reaction	Optimized SCP
				[C m ⁻²]	[m ² g ⁻¹]	[sites nm ⁻²]	[F m ⁻²]	$\log K_{a1}^{int}$	$\log K_{a2}^{int}$	$\log K_{Al-OH}^{int}$	$\log K_{Si-OH}^{int}$	$\log K_{Na+}^{int}$	$\log K_{ClO_4}^{int}$		
FS + ζ [1]	SCP FS IX	BSM	2-pK	0.03	4.3 0.2 (ζ)	1.9 [1]	1.5 [1]	3.0 [2]	Eq. 2.18	-	-	2.5 [2]	2.5 [2]	-	$C_1, \Delta\sigma$
														S-OH + H+ = S-OH2+	$\log K_{a1}^{int}$
														S-OH = S-O- + H+	$\log K_{a2}^{int}$
														S-O- + Na+ = S-ONa	$\log K_{Na+}$
														S-OH2+ + Pc- = S-OH2Pc	$\log K_{ClO_4^-}$
	SCP FS X	BSM	2-pK	0.047	4.3 0.2 (ζ)	1.9 [1]	1.5 [2]	2.5 [2]	Eq. 2.18	-	-	2.8 [2]	2.8 [2]	-	SSD
														S-OH + H+ = S-OH2+	$\log K_{a1}^{int}$
														S-OH = S-O- + H+	$\log K_{a2}^{int}$
														S-O- + Na+ = S-ONa	$\log K_{Na+}$
														S-OH2+ + Pc- = S-OH2Pc	$\log K_{ClO_4^-}$
M [1]	SCP M I	DDL M	2-pK	0.051	0.7	0.4 [2]	-	Eq. 2.18	-8.0 [2]	-	-	-	-	S-OH + H+ = S-OH2+	$\log K_{a1}^{int}$
														S-OH = S-O- + H+	$\log K_{a2}^{int}$
	SCP M II	DDL M	1-pK	0.051	0.7	0.7 [1]	-	-	-	8.0 [1]	-	-	-	S-OH-0.5+ H+ = S-OH+0.5	SSD
														S-OH-0.5+ H+ = S-OH+0.5	$\log K_{Al-OH}^{int}$
	SCP M III	DDL M	1-pK	-0.005	0.7	3.8 [2]	-	-	-	2.4 [1]	-	-	-	-	SSD, SSA
														S-OH = S-O- + H+ -	$\log K_{Si-OH}^{int}$
	SCP M IV	DDL M	1-pK	-0.005	0.7	3.8 [2]	-	-	-	-	-6.5 [2]	-	-	-	SSD
														S-OH = S-O- + H+	$\log K_{Si-OH}^{int}$
	SCP M V	DDL M	1-pK	-0.005	0.7	1.7 [2]	-	-	-	-	-6.6 [2]	-	-	-	SSD
														S-O-0.5 + Na = S-ONa+0.5	$\log K_{Na+}$
M + ζ [1]	SCP M VI	BSM	1-pK	0.051	0.7	0.7 [1]	2.1 [2]	-	-	8.0 [1]	-	-1 [2]	-1 [2]	S-OH+0.5 + Pc- = S-OHPc-0.5	$\log K_{ClO_4^-}$
														S-OH-0.5+ H+ = S-OH+0.5	-
														-	C_1
														S-O-0.5 + Na = S-ONa+0.5	-
														S-OH+0.5 + Pc- = S-OHPc-0.5	-
	SCP M VII	BSM	1-pK	0.051	0.7	3.8 [4]	2.1 [2]	-	-	8.0 [1]	-	-0.8[2]	-0.8[2]	S-OH-0.5+ H+ = S-OH+0.5	-
														S-OH = S-O- + H+	$\log K_{Si-OH}^{int}$
														S-O- + Na+ = S-ONa	$\log K_{Na+}$
														S-OH + Pc- = S-OHPc-	$\log K_{ClO_4^-}$
														-	-
M + ζ [1]	SCP M VIII	BSM	1-pK	-0.005	0.7	1.7 [2]	0.4 [2]	-	-	-	-6.5 [2]	-4.3 [2]	-4.3 [2]	S-OH + H+ = S-OH2+	$\log K_{a1}^{int}$
														S-OH = S-O- + H+	$\log K_{a2}^{int}$
														S-O- + Na+ = S-ONa	$\log K_{Na+}$
														S-OH2+ + Pc- = S-OH2Pc	$\log K_{ClO_4^-}$
														-	SSD
	SCP M IX	BSM	2-pK	0.03	4.3 0.2 (ζ)	1.9 [1]	1.5 [1]	3.0 [2]	Eq. 2.18	-	-	2.5 [2]	2.5 [2]	S-OH + H+ = S-OH2+	$\log K_{a1}^{int}$
														S-OH = S-O- + H+	$\log K_{a2}^{int}$
														S-O- + Na+ = S-ONa	$\log K_{Na+}$
														S-OH2+ + Pc- = S-OH2Pc	$\log K_{ClO_4^-}$
														-	SSD

Tab. 2.4: Summary of final surface charge models, SCPs, and UCODE goodness of fit (gof) of muscovite (M), quartz (Q), and orthoclase (FS) DDLM and BSM approaches. Initial parameter values of optimized SCPs and surface reactions provided in Table 2.3. ID – identification of fitting approach and SCP set, EM – electrostatic model, $\Delta\sigma$ – shift to transform relative (raw data) into absolute surface charge densities, SE – standard error [unit of measure], psd – parameter standard deviation [unit of measure], $LSOF$ – least squares objective function [unit of measure], ME – mean error (in [mV] for zeta-potential fits, in $[C\ m^{-2}]$ for surface charge density), **bold SCP sets** – SCPs for Eu SCMs, **green SCP sets** – measured SCPs for Eu SCMs where no fitting procedure was necessary, results represent simulations. SCP uncertainties are indicated by means of 95% confidence intervals (CI) and $psds$ (Hill, 1998). SCPs represent unique fitting results with parameter correlation coefficients ≤ 0.85 (Poeter et al., 2005). Goodness of fit (gof: SE , psd , $LSOF$, ME) obtained from UCODE (Hill (1998), Poeter et al. (2005)), cf. Appendix A.5. For **SCP Q II** no gof (-) provided by Hiemstra et al. (1989a).

ID	EM	pK approach	$\Delta\sigma$ [1] [C m ⁻²]	SCP		CI	psd	SE	$LSOF$	ME [C m ⁻²]	ME [mV]
SCP Q I	DDLM	1-pK	-	$\log K_{Si-OH}^{int}$	-8.0	± 0.09	3.4E-02	5.2E-03	1.3E-01	-3.1E-03	-
SCP Q II	BSM	1-pK	-	$\log K_{Si-OH}^{int}$	-7.5	-	-	-	-	-	-
				$\log K_{Na+}$	-9.4	-	-	-	-	-	-
SCP FS I	DDLM	1-pK	0.03	SSD	5.9	± 2	9.7E-01	7.9E-02	0.40	-6.5E-02	-
SCP FS II	DDLM	1-pK	0.047	$\log K_{Al-OH}^{int}$	3.5	± 0.6	3.2E-01	1.1E-01	0.82	-1.1E-01	-
				SSD	3.8	± 3	1.4				
SCP FS III	DDLM	1-pK	0.3	$\log K_{Al-OH}^{int}$	8.0	± 0.2	1.3E-01	2.9E-02	5.3E-02	2.7E-02	-
				SSD	3.8	± 2	9.5E-01				
				$\log K_{a2}^{int}$	-1.6	± 100	62				
SCP FS IV	DDLM	2-pK	0.03	$\log K_{a1}^{int}$	5.4	± 100	62	7.7E-02	0.36	-6.5E-02	-
				SSD	1.9	± 0.7	0.52				
Continued on next page											

ID	EM	pK approach	$\Delta\sigma$ [1] [C m ⁻²]	SCP	CI	<i>psd</i>	<i>SE</i>	<i>LSOF</i>	<i>ME</i> [C m ⁻²]	<i>ME</i> [mV]	
SCP FS V	BSM	1-pK	0.03	logK _{Na+}	1.5	± 0.1	5.4E-02	6.3E-03	2.8E-03	-1.7E-03	-0.27
				logK _{ClO₄⁻}	1.5	± 0.2	1.1E-01				
				C ₁	2.1	± 0.1	7.2E-02				
				SSD	3.2	± 0.1	3.8E-02				
SCP FS VI	BSM	1-pK	0.047	logK _{Na+}	1.5	± 0.1	3.5E-02	6.8E-03	3.3E-03	-1.4E-03	-3.0
				logK _{ClO₄⁻}	1.5	± 0.2	1.1E-01				
SCP FS VII	BSM	1-pK	0.3	logK _{Na+}	0.7	±0.3	1.6E-1	4.4E-03	1.2E-03	-1.9E-03	-
				logK _{ClO₄⁻}	0.7	± 0.02	1.3E-02				
SCP FS VIII	BSM	2-pK	0.03	logK _{a1} ^{int}	2.6	± 0.9	4.4E-01	7.4E-03	3.8E-03	3.8E-03	-3.7
				logK _{a2} ^{int}	-4.4	± 1.2	5.8E-01				
				logK _{Na+}	2.9	± 0.4	1.9E-01				
				logK _{ClO₄⁻}	2.5	± 0.5	4.5E-01				
				C ₁	1.6	± 0.4	1.8E-01				
				Δσ	-0.03	± 0.01	5.8E-03				
SCP FS IX	BSM	2-pK	0.03	logK _{a1} ^{int}	8.5	± 16	8.1	8.1E-03	4.5E-03	-2.3E-04	0.11
				logK _{a2} ^{int}	1.5	± 16	8.1				
				logK _{Na+}	2.8	±0.3	1.6E-01				
				logK _{ClO₄⁻}	2.8	± 0.4	2.03E-01				
				SSD	1.6	± 0.05	2.4E-02				
Continued on next page											

ID	EM	pK approach	$\Delta\sigma$ [1] [C m ⁻²]	SCP	CI	<i>psd</i>	<i>SE</i>	<i>LSOF</i>	<i>ME</i> [C m ⁻²]	<i>ME</i> [mV]	
SCP FS X	BSM	2-pK	0.047	logK _{a1} ^{int}	3.1	± 8	4.5	6.1E-02	2.6E-01	6.2E-02	1.2
				logK _{a2} ^{int}	-3.9	± 7	3.5				
				logK _{Na+}	2.6	± 4	1.9				
				logK _{ClO₄⁻}	2.6	± 5	2.5				
SCP M I	DDL M	2-pK	0.051	logK _{a1} ^{int}	7.0	± 0.1	5.7E-02	4.6E-03	6.7E-04	3.8E-06	-
				logK _{a2} ^{int}	-9.0	± 1	5.4E-02				
SCP M II	DDL M	1-pK	0.051	SSD	0.6	± 0.1	4.5E-03	2.1E-03	1.5E-04	1.3E-05	-
SCP M III	DDL M	1-pK	-0.005	logK _{Al-OH} ^{int}	2.4	± 2	8.7E-01	1.3E-01	5.5E-01	2.8E-03	-
				SSD	3.8	± 2	8.9E-01				
				SSA	0.7	± 140	6.3E+01				
SCP M IV	DDL M	1-pK	-0.005	logK _{Si-OH} ^{int}	-4.9	± 0.08	3.7E-02	1.6E-03	8.1E-05	-1.8E-06	-
				SSD	0.4	± 0.2	7.6E-03				
SCP M V	DDL M	1-pK	-0.005	logK _{Si-OH} ^{int}	-6.3	± 0.1	6.6E-02	6.7E-03	1.5E-03	-1.3E-04	-
				SSD	0.6	± 0.3	1.3E-02				
SCP M VI	BSM	1-pK	0.051	logK _{Na+}	-0.2	± 0.9	2.4E-01	3.8E-03	3.4E-04	7.7E-05	-
				logK _{ClO₄⁻}	-0.2	± 0.1	3.4E-03				
SCP M VII	BSM	1-pK	0.051	C1	0.4	± 0.02	1.1E-02	4.2E-03	5.6E-04	4.2E-05	-
SCP M VIII	BSM	1-pK	-0.005	logK _{Si-OH} ^{int}	-5.5	± 0.6	2.8E-01	4.6E-03	8.8E-04	1.7E-06	-3.8E-01
				logK _{Na+}	-4.3	± 0.3	1.5E-01				
				logK _{ClO₄⁻}	-4.3	± 0.01	4.6E-03				

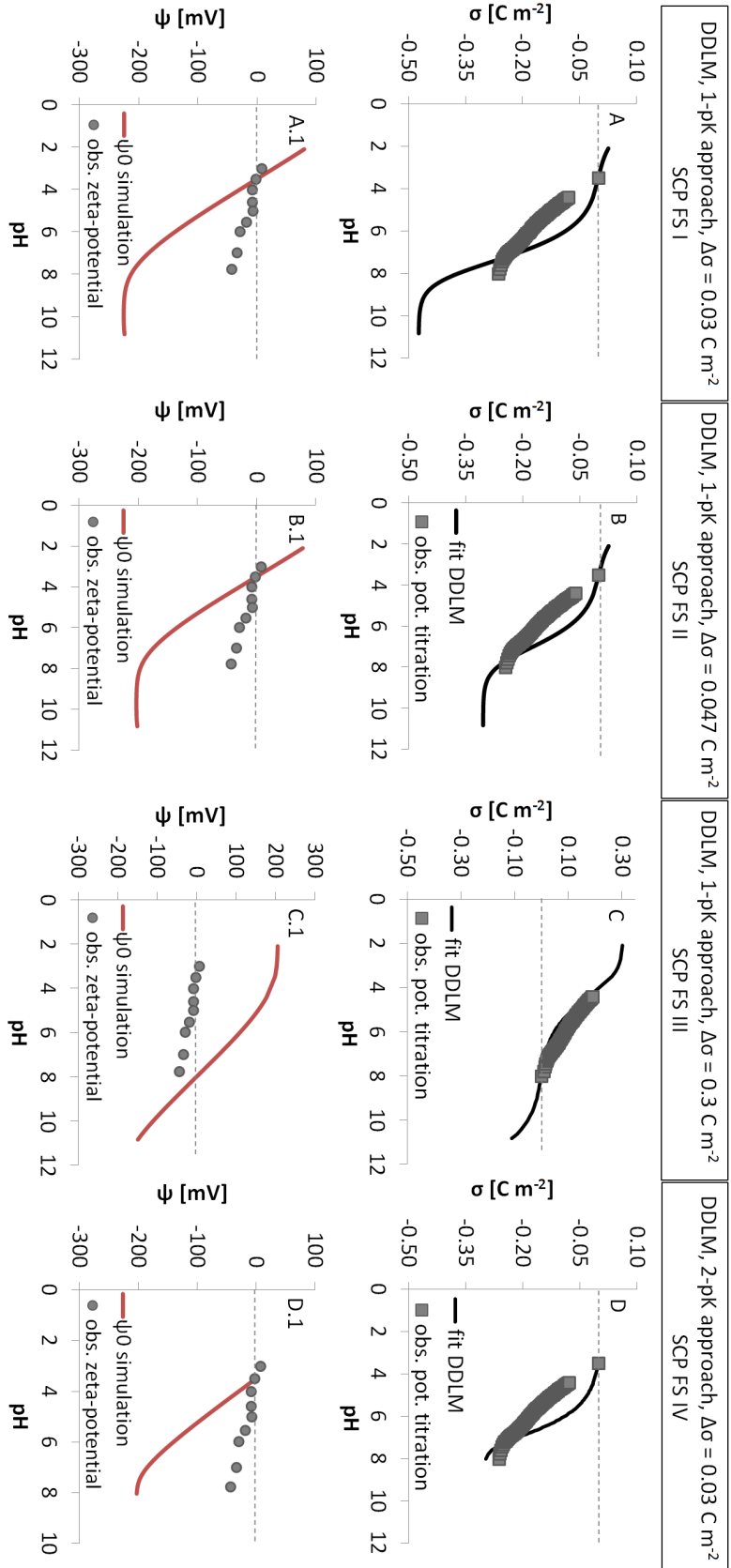


Fig. 2.16: DDLM results of absolute orthoclase acid-base titration measurements and zeta-potentials using SCPs from Table 2.4. A - D: Fitted and simulated results of absolute orthoclase acid-base titration data (obs. pot. titration) with A $\Delta\sigma = 0.03 \text{ C m}^{-2}$, 1-pK approach, B $\Delta\sigma = 0.047 \text{ C m}^{-2}$, 1-pK approach, C $\Delta\sigma = 0.3 \text{ C m}^{-2}$, 1-pK approach, D $\Delta\sigma = 0.03 \text{ C m}^{-2}$, 2-pK approach. A.1 - D.1: Simulations of surface potential at 0-plane (DDLM). Simulations correspond to respective fitting approaches. SCP FS I - IV relate to surface charge models and SCPs as given in Tables 2.3 and Tab. 2.4. σ – surface charge density [mC m^{-2}], ψ_0 – surface potential [mV] at the 0-plane (DDLM).

Figure 2.17 shows the performance of the 1-pK and 2-pK BSM (Fig. 2.17 A - C and Fig. 2.17 D - F) with SCPs from Table 2.4. In the present study, only one *IS* was available from acid-base titration experiments, so that co- and counterion association affinities should be restricted to 10 mM L⁻¹ NaClO₄ (Sec. 2.5.1). Optimizations with BSM approaches revealed $\psi_1 = \psi_d$ with $C_2 = 30 \text{ F m}^{-2}$ as depicted in Figure 2.17, where ψ_1 corresponded to fitted results and where the simulated ψ_d agreed well with ψ_1 as would be expected.

Evidently, the BSM represented measurements much better in comparison to the DDLM (cf. Fig. 2.16 and Fig. 2.17, Tab. 2.4). For *SCP FS VIII* (2-pK BSM) $\Delta\sigma$, $\log K_{a1}^{int}$ and $\log K_{a2}^{int}$, $\log K_{Na^+}$ and $\log K_{ClO_4^-}$ were optimized (Fig. 2.17 D, D.1). Derived protolysis constants fulfilled $|\log K_{a1}^{int}| < |\log K_{a2}^{int}|$; however, as symmetric co- and counter ion associations could be assumed at *IS* = 10 mM NaClO₄, $\log K_{Na^+} = \log K_{ClO_4^-}$ should apply (Sec. 2.5.1, Fig. 2.10) which was violated for *SCP FS VIII* (Tab. 2.4). Consequently, *SCP FS VIII* was excluded from further modeling studies. Nevertheless, as results represented experiments surprisingly well the fitted $\Delta\sigma$ was used for further DDLM and BSM SCM fits in addition to $\Delta\sigma = 0.047 \text{ C m}^{-2}$ and $\Delta\sigma = 0.3 \text{ C m}^{-2}$.

For BSMs that applied the 2-pK approach shifting titration data relative to pH_{mass} ($\sigma = 0.3 \text{ C m}^{-2}$) remained unsuccessful (regardless of proposed parameter combinations, results not shown here). Due to strong parameter correlations optimization of the objective function of 2-pK BSMs with $\text{pH}_{mass} = \text{pH}_{nphc}$ delivered non-unique parameters.

For 2-pK BSM approaches where $\text{pH}_{IEP} = \text{pH}_{nphc}$ was assumed ($\Delta\sigma = 0.03 \text{ C m}^{-2}$, $\Delta\sigma = 0.047 \text{ C m}^{-2}$) unique, but unrealistic SCP sets were obtained (*SCP FS VIII - X* in Tab. 2.4):

- For *SCP FS VIII* $\log K_{Na^+} > \log K_{ClO_4^-}$ was returned which did not correspond to symmetrical counterion associations as would be expected for 10 mmol L⁻¹ NaClO₄ from electrolyte titration experiments (Sec. 2.5.1); thus, SCPs were excluded from further modeling studies.
- For *SCP FS IX* $|\log K_{a1}^{int}| \leq |\text{pH}_{IEP}|$ was violated; hence, these SCPs were also excluded.
- The *SCP FS X* approach delivered realistic SCPs, but large *psds* and 95% *CI*s (Fig. 2.17 F, F.1). Thus, *SCP FS X* was also omitted for orthoclase Eu SCMs.

All 1-pK BSMs yielded acceptable fits, realistic SCP sets, adequate *psds* and *SEs* where lowest values were preferred over larger ones following suggestions made by Hill (1998) (Tab. 2.4, Fig. 2.17 A. A.1 - C, C.1). However, *SCP FS V - VII* resulted in unexpectedly

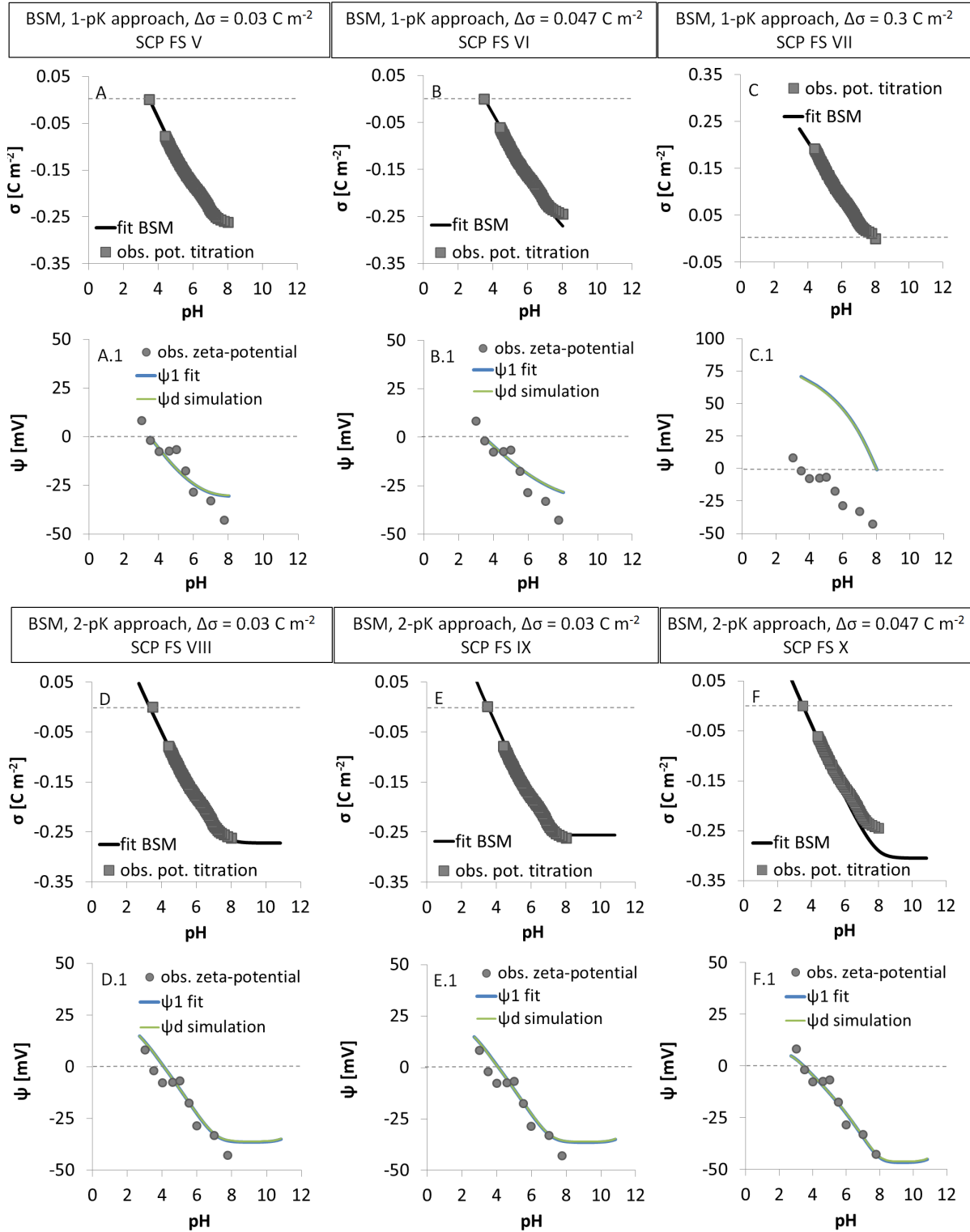


Fig. 2.17: BSM results (solid lines) of absolute orthoclase acid-base titration data (obs. pot. titration) and zeta-potentials (obs. zeta-potential) using SCPs from Table 2.4. A - F: Fitted and simulated results of absolute titration data; A.1 - F.1: Fitted and simulated zeta-potentials. σ – surface charge density [mC m^{-2}], ψ_1 , ψ_d – surface potential [mV] at the 1-plane and d-plane.

large counter-/coion association coefficients (cf. Tab. 2.4). Values of $\log K_{Na^+}$, $\log K_{ClO_4^-}$ often range below zero (e.g. Hiemstra et al. (1989a)) to contribute to charge balance but without posing competition on protolysis or potential metal ion surface complexation processes. Unfortunately, fixing $\log K_{Na^+}$ and $\log K_{ClO_4^-}$ to parameter values ranging between -1 and -0.5 resulted in large *psds* and a decline in *gof* in general (data not shown here). Despite the relatively high counter-/coion association coefficients *SCP FS V - VII* were used for Eu SCMs.

To conclude, the 2-pK approach did not yield reliable SCP sets regardless of the chosen electrostatic model (EM). The 1-pK BSMs and DDLMs returned adequate fits (Tab. 2.4, Fig. 2.16 - 2.17) and delivered realistic SCPs even though $\log K_{Na^+}$, $\log K_{ClO_4^-}$ resulted in unexpectedly high values for the BSM. Hence, *SCP FS I - III* and *SCP FS V - VII* were used for orthoclase Eu SCMs (Sec. 3).

Muscovite

Raw data of potentiometric acid-base titration measurements of muscovite were shifted to pH_{mass} and pH_{IEP} (Sec. 2.4.2, App. A.4.2); absolute data was used for surface charge model fits. Detailed information can be obtained from Appendices A.6 and A.6.2. As for quartz and orthoclase, the DDLM and BSM with the 1-pK and 2-pK approaches were used (Tab. 2.3, Tab. 2.4).

Figure 2.18 depicts DDLM fits of shifted absolute titration data and simulation results of zeta-potentials (*SCP M I - V* with SCPs from Tab. 2.4) where Figure 2.18 A and B show fits of titration data shifted relative to pH_{mass} . The constraint $pH_{mass} = pH_{nphc}$ suggested that titration measurements only reflected protolysis reactions of edge sites of the mica mineral. For $pH_{mass} = pH_{nphc}$ the 2-pK approach was required since protonation reactions accounted for positive surface charges at $pH < pH_{mass}$ (Fig. 2.18 A and A.1, *SCP M I*). Figure 2.18 A and A.1 depicts the best fit obtained with the 2-pK DDLM where $|log K_{a1}^{int}| < |pH_{mass}|$ was respected. A *SSD* of 0.4 sites nm^{-2} was determined via manual adaptation of the parameter and corresponded well with *SSDs* yielded from muscovite titration data for 2-pK model approaches where $SSD = 0.37$ sites nm^2 (Sec. 2.2.5, Sec. 2.4.2). Assuming higher, presumably more realistic *SSDs* as provided by Zorn (2000) and Maslova et al. (2004) resulted in an underestimation of surface charge at high pH and in an overestimation of surface charges at low pH, *gof* was significantly reduced (results not shown here). The 1-pK DDLM (*SCP M II*, cf. Tab. 2.4) resulted in a more adequate fit compared to *SCP M I* (2-pK DDLM): Smaller *SE* and *LSOF* values were obtained (cf. Tab. 2.4); only one fitting parameter was necessary and the optimized

$SSD = 0.6 \pm 0.1$ sites nm^2 matched estimates from titration data reasonably well where $SSD = 0.75$ sites nm^2 (for 1-pK approach). However, both DDLM pK approaches with $\text{pH}_{mass} = \text{pH}_{nphc}$ returned relatively low $SSDs$ that were possibly apparent values which corresponded well to calculations from titration measurements but were much lower than crystallographic, realistic $SSDs$ (e.g. Barrón and Torrent (1996), Maslova et al. (2004)).

From 1-pK DDLM results where $\text{pH}_{IEP} = \text{pH}_{nphc}$ was applied the following could be concluded (Fig. 2.18 C - E, Tab. 2.4):

- For *SCP M III* (1-pK DDLM) no fitting procedure was necessary, all parameters corresponded to measurements. The approach returned overestimated surface charge densities σ [C m^{-2}] between pH 4 and 8; and underestimated σ for $\text{pH} > 8$. The zeta-potential (diffuse layer potential, respectively) was overestimated for $\text{pH} < 4$ and underestimated for $\text{pH} > 5$. The gof indicted the poorest fit for *SCP M III* in comparison to alternative approaches (Tab. 2.4, Fig. 2.18 C).
- A reasonable SE and lowest values of $LSOF$ and ME were obtained for *SCP M IV* (Fig. 2.18 D, Tab. 2.4): Zeta-potentials at $\text{pH} < 4$ were fitted satisfactorily; for $\text{pH} > \text{pH}_4$ the potential was underestimated up to factor four. The optimized SSD returned 0.4 sites nm^{-2} matching the calculated SSD from titration data well. However, as discussed earlier $SSDs < 2$ sites nm^{-2} most likely underestimate realistic site densities of mica surfaces. Increasing the SSD to 1.7 sites nm^{-2} (*SCP M V*) resulted in a decrease of gof: The $LSOF$ and ME increased by two orders of magnitude (cf. Tab. 2.4).

Since no verified SSD value for phyllosilicates is known *SCP M II*, *SCP M IV*, and *SCP M V* were used for muscovite Eu DDLM SCMs: In accordance with Maslova et al. (2004) only Si-OH deprotonation reactions were taken into account (1-pK). The 2-pK DDLM indicated Si-OH protonation to contribute insignificantly to surface charge development (results not provided here).

Different BSM optimization strategies were followed; only selected results are displayed in Figure 2.19 and Tables 2.3 and 2.4. Generally speaking, BSMs fitted experimental data well (Fig. 2.19, cf. Tab. 2.4): The surface charge was well reproduced for $\text{pH}_{nphc} = \text{pH}_{IEP}$ and $\text{pH}_{nphc} = \text{pH}_{mass}$; for *SCP M VIII* ($\text{pH}_{nphc} = \text{pH}_{IEP}$) zeta-potential was also well represented. Since *SCP M VI* and *VII* accounted for protolysis reactions on edge sites ($\Delta\sigma = 0.05 \text{ C m}^{-2}$) the zeta-potential did not correspond to simulated surface potentials. Determined SCPs ranged within reasonable limits, except for *SCP M VI* where the optimized SSD fell below realistic values of approx. $SSD \geq 2$ sites nm^{-2} (e.g. Barrón

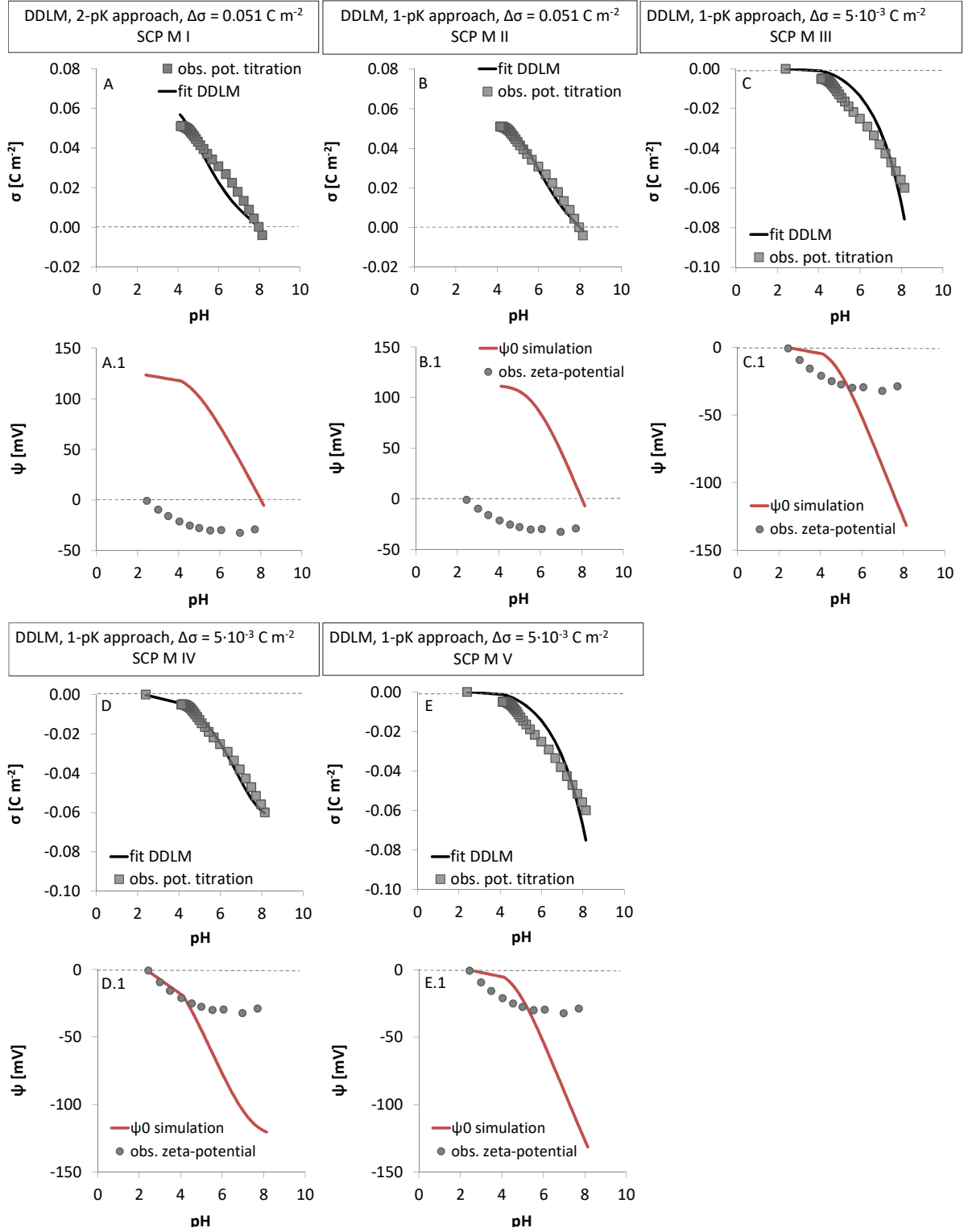


Fig. 2.18: DDLM results (solid lines) of absolute muscovite acid-base titration data (obs. pot. titration) and zeta-potentials (obs. zeta-potential) using SCPs from Table 2.4. A - F: Fitted and simulated results of absolute titration data; A.1 - F.1: Simulated zeta-potentials. σ – surface charge density [mC m^{-2}], ψ_1 , ψ_d – surface potential [mV] at the 1-plane and d-plane.

and Torrent (1996), Maslova et al. (2004), Davis and Kent (1990a)). The surface charge model approach *SCP M VIII* returned best optimization results for $\text{pH}_{nphc} = \text{pH}_{IEP}$ ($\Delta\sigma = -0.005$) even though co- and counterion association coefficients resulted in very low values indicating that electrostatic interaction of Na^+ and ClO_4^- had negligible influence.

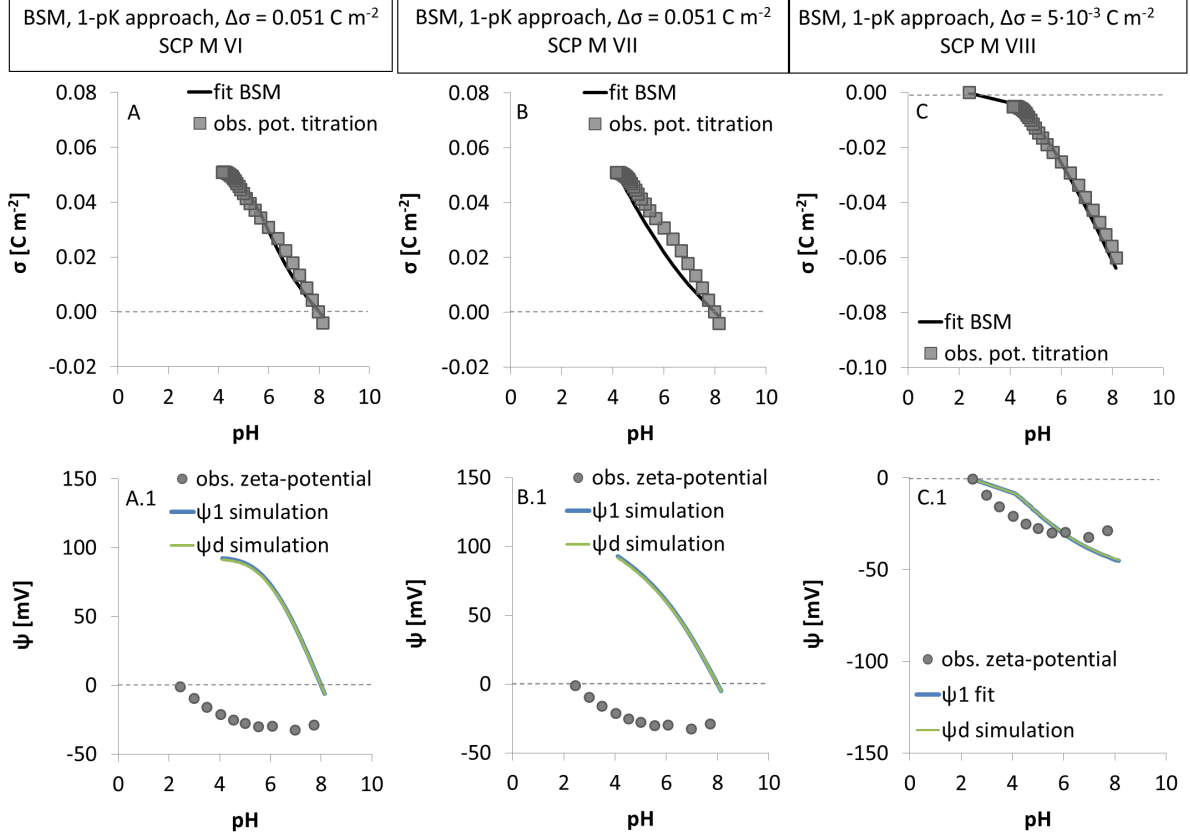


Fig. 2.19: BSM results (solid lines) of absolute muscovite acid-base titration data (obs. pot. titration) and zeta-potentials (obs. zeta-potential) using SCPs from Table 2.4. A - C: Fitted and simulated results of absolute titration data; A.1 - C.1: Fitted and simulated zeta-potentials. σ – surface charge density [mC m^{-2}], ψ_1 , ψ_d – surface potential [mV] at the 1-plane and d-plane.

To conclude, the BSM represented experimental data better than the DDLM. The *SSDs* determined with the DDLM ranged well below recommended values in literature (e.g. Maslova et al. (2004)). The BSM approaches *SCP M VII* and *VIII* returned reasonable SCPs with very low co- and counterion association coefficients; for *SCP M VI* the *SSD* corresponded well to calculated *SSD* values from measurements of the present study but probably failed to represent realistic *SSDs* of muscovite surfaces. For DDLM approaches *SCP M II*, *IV*, and *V* were used in Eu SCMs; *SCP M VI*, *VII*, and *VIII* were utilized in

Eu BSM surface complexation studies.

2.6 Summary

It was the aim to characterize surface charge properties of a muscovite, orthoclase, and quartz with titration experiments and surface charge models. Sound knowledge of acid-base properties of mineral surfaces can be of great importance to estimate sorption processes of potential pollutants as close to nature as possible at the mineral-water interfaces. Therefore, a broad experimental program was initiated: Discontinuous mass, electrolyte, and continuous potentiometric acid-base titration experiments were carried out. Extensive geochemical characterization of muscovite, orthoclase, and quartz was performed. In addition, literature data was used to verify the experimental data of this study. PHREEQC and UCODE were applied for model optimization and simulation procedures. The DDLM and the BSM were utilized to identify a surface charge model that would represent measurements best; surface charge development was modelled with the 1-pK and the 2-pK approaches.

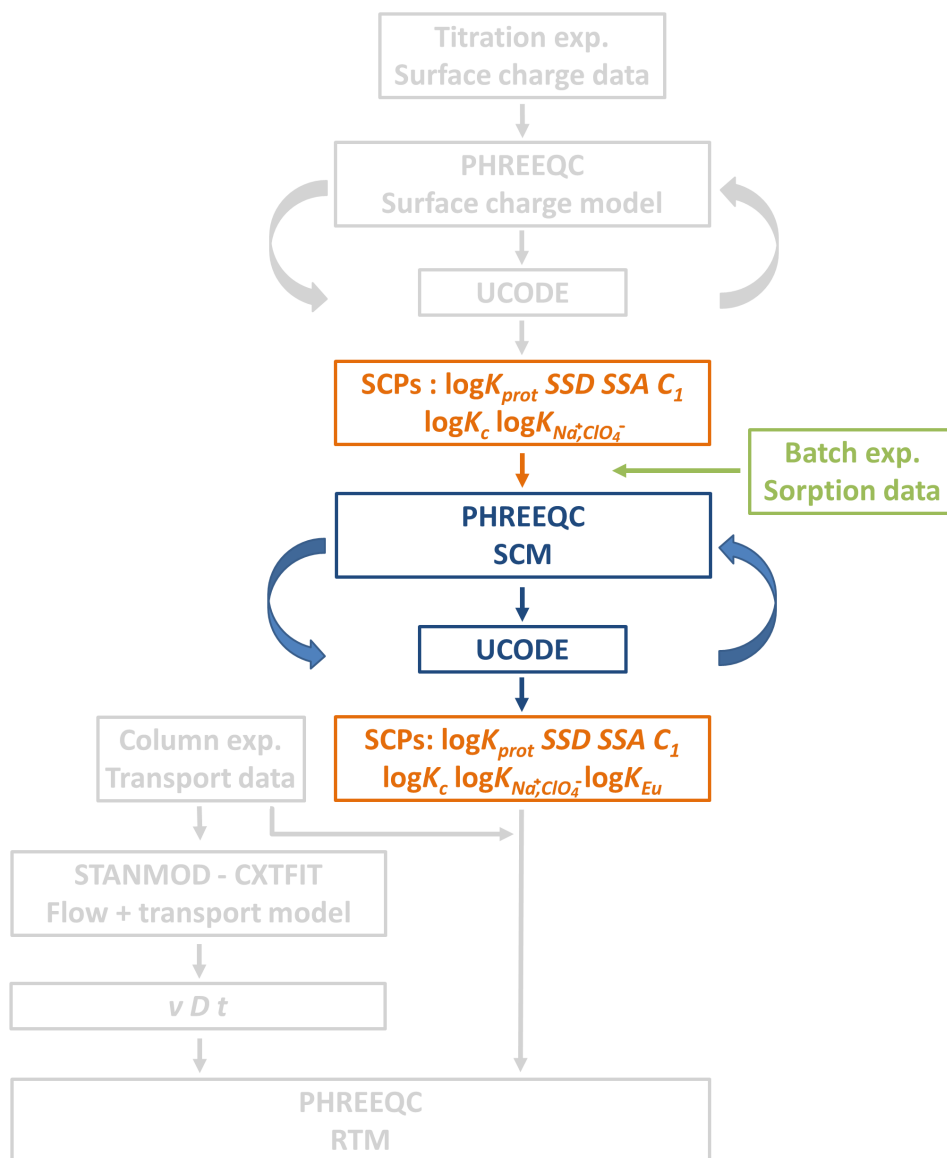
For quartz the literature data set from Bolt (1957) corresponded well with experimental data of this study. Therefore, the more comprehensive Bolt (1957)'s data was used for modeling studies (Sec. 2.5.1, Sec. 2.5.2). Hiemstra et al. (1989a) introduced a BSM for amorphous silica that described data by Bolt (1957) well. Hence, SCPs derived by Hiemstra et al. (1989a) were used in this study for quartz basic Stern surface charge models. For the DDLM, SCP sets were optimized based on data from Bolt (1957). Generally, the DDLM and the BSM represented data from Bolt (1957) well ($IS = 10 \text{ mmol L}^{-1}$ electrolyte concentration). However, for higher IS conditions and elevated pH the BSM evidently represented measurements better compared to the DDLM. Surface charge models (DDLM, BSM) and respective SCPs are provided in Tables 2.3 and 2.4.

Determination of SCPs of muscovite and orthoclase was more challenging. Zeta-potential measurements delivered IEPs. It was shown that $\text{pH}_{mass} \neq \text{pH}_{pzse}$ for both minerals which made an unambiguous referencing of the relative surface charge density from titration data impossible. Potentiometric titration data of muscovite and orthoclase were shifted relative to either pH_{mass} or pH_{IEP} under the assumption: $\text{pH}_{nphc} = \text{pH}_{mass}$ and $\text{pH}_{nphc} = \text{pH}_{IEP}$, respectively. Due to the application of pH_{mass} and pH_{IEP} , different SCP sets and surface charge models were determined (with BSM, DDLM, 1-pK and 2-pK approaches). The resulting model approaches fitted absolute experimental data with varying success which was assessed by means of *gof*. For both mineral surfaces the 1-pK

concept represented absolute titration data closest to measurements compared to the 2-pK approach; furthermore, the BSM reflected surface charge data better in comparison to DDLM results. Surface charge models and respective SCP sets are summarized in Tables 2.3 and 2.4.

Except for quartz, it was not possible to identify one precise surface charge model that represented collected titration data best even though the BSM generally revealed better fits and simulations (cf. gof Tab. 2.4) compared to the DDLM. However, considering gof (UCODE) and optimized parameter *CI*s as well as *psds* showed that only the 1-pK approach represented titration measurements adequately. This finding was in good correspondence with e.g. van Riemsdijk and Hiemstra (2006). No sound, reliable 2-pK SCP set could be derived for muscovite or orthoclase (Tab. 2.3, Tab. 2.4). In addition, considering e.g. Hiemstra et al. (1989b) and Kosmulski (2009) the 2-pK approach might be questionable for multidentate metal surface complex coordinations. Hence, only the 1-pK concept was used in Eu SCMs for muscovite, orthoclase, and quartz. The application of SCP sets in Eu SCMs (Sec. 3) and in Eu reactive transport simulations (Sec. 4) offered the opportunity to assess surface charge models and to presumingly favour one or the other model approach of the respective mineral.

Europium surface complexation: Experiments and inverse modeling



3.1 Introduction

In the past, sorption processes have often been described and assessed with constant distribution coefficients (K_d) that define a linear relationship between sorbate and equilibrium concentrations in solution (Sec. 3.2.2). The linear K_d coefficient is, however, only applicable to equilibrated systems, trace element concentrations (linear sorption processes), to reversible reactions, and does not reflect changing geochemical conditions (e.g. Geckeis et al. (2013)). In contrast to the straightforward K_d approach, the present study uses conceptual deterministic thermodynamic sorption models (TSMs) to investigate surface charge (Sec. 2) and surface complexation processes. In this study, Eu surface complexation reactions were defined based on recent literature and state-of-the-art spectroscopic data. Surface complexation models (SCMs) were developed to evaluate Eu solid-solution interface interactions based on underlying thermodynamic reactions. The notion SCM stands for mechanistic model approaches that describe surface adsorption and absorption processes but also precipitation reactions, mineral dissolution, aqueous speciation, and cation exchange processes.

Section 2 dealt with the determination of protolysis constants, the specific surface area (SSA), the surface site density (SSD), co- and counterion association coefficients ($\log K_{ClO_4^-, Na^+}$), as well as model inherent capacities (C_1) of quartz, orthoclase, and muscovite from titration measurements (surface charge models). Conditional cation exchange selectivity coefficients of Na^+ , K^+ , and H^+ for muscovite were defined ($\log K_c$). This section focuses on Eu surface complexation processes: Therefore, extensive Eu batch experiments were carried out with identical orthoclase, quartz, and muscovite samples as in Section 2. Different initial pH values (pH_{ini}), varying initial Eu concentrations (C_0), and two solid-liquid ratios ($SLRs$) were used. Experimental data was used to derive intrinsic Eu surface complexation constants ($\log K_{Eu}$) by parameter optimization via inverse modeling using the geochemical speciation code PHREEQC (Parkhurst and Appelo, 2013) in combination with the parameter estimation code UCODE (Poeter et al., 2005); the basic Stern model (BSM), the diffuse double layer model (DDLDM), and a non-electrostatic model (noELDM) were applied (Sec. 2.2). Previously estimated surface complexation parameters (SCPs) from Table 2.4 (Sec. 2) were completed with $\log K_{Eu}$ s from this section; hence, final SCP sets comprise parameters as introduced in Section 2 (Tab. 2.4) and $\log K_{Eu}$ values. The notion $\log K_{Eu}$ stands for intrinsic Eu surface complexation constant(s) in general – regardless of the considered surface complex(es).

This section focusses on (i) the experimental procedure of batch experiments

(Sec. 3.2), (ii) the development of SCMs to estimate $\log K_{EuS}$ for muscovite, orthoclase, and quartz (Sec. 3.2.2), and (iii) the evaluation of batch experimental data with SCMs (Sec. 3.3). Detailed information on parameter optimization procedures, modeling approaches, and results are provided in Sections 3.2.2 and 3.3; cation exchange processes, how they were considered, and related challenges are discussed in Sections 3.1.2 and 3.3.3.

3.1.1 Europium speciation

In this study, europium (Eu) was exclusively used in its trivalent oxidation state (Eu(III)), the term Eu^{3+} describes Eu(III) as a solvated aquo ion. Europium is a stable, trivalent lanthanide and has been widely applied as a chemical homologue for long-term safety relevant trivalent actinides such as Cm(III) and Am(III) (e.g. Tan et al. (2010), Geckeis et al. (2013)). Studying migration and retardation properties of Eu offers valuable insight into sorption processes of its long-term safety relevant chemical homologues Am(III), Cm(III), and e.g. Gd(III) (e.g. Geckeis et al. (2013), Lee et al. (2006)). Figure 3.1 A depicts Eu solution speciation under atmospheric influence in 10 mM NaClO_4 electrolyte solution ($\text{Eu } C_0 = 10^{-5} \text{ mol L}^{-1}$). Figure 3.1 B - D show Eu solution speciation under atmospheric influence, in 10 mM NaClO_4 electrolyte, and in equilibrium with the mineral phases muscovite (B), orthoclase (C), and quartz (D). Speciation calculations were simulated with PHREEQC (Version 3.1.2-8538) using the database as introduced in Sections 2.4.4 and 3.2.3. The following conclusions were drawn from Figure 3.1 A - D:

- Without mineral influence $\geq 50\%$ of Eu C_0 occurs as a trivalent cation in solution at $\text{pH} \leq 7.0$. Europium-hydroxo and Eu-carbonato species become significant at $\text{pH} \geq 7.0$. At pH 9.0, 93% of the Eu species corresponds to $\text{Eu}(\text{CO}_3)_2^-$ (Fig. 3.1 A).
- The influence of muscovite, orthoclase, and quartz on speciation calculations becomes apparent through the release of Si^{4+} ($\text{Si}(\text{OH})_4$) into the suspension due to mineral dissolution. As a result Eu speciation shifts and the $\text{EuSi}(\text{OH})_3^{2+}$ species becomes relevant. The occurrence of $\text{EuSi}(\text{OH})_3^{2+}$ is positively correlated with Si concentrations in solution resulting from mineral dissolution processes. For quartz $\text{EuSi}(\text{OH})_3^{2+}$ corresponds to 52% of the Eu species at pH 7.0; muscovite and orthoclase show smaller Si-release ratios and $\text{EuSi}(\text{OH})_3^{2+}$ contributes only 1% and 20% to Eu species distribution, respectively, at pH 7.0 (Fig. 3.1 B - D).

Simulations of the saturation indices of Eu were also performed to evaluate whether and under which conditions precipitation reactions of Eu become relevant for the studied systems (data not shown). Simulations assumed an equilibrium between the 10 mM

NaClO₄ background electrolyte, Eu $C_0 = 10^{-5}$ mol L⁻¹, and muscovite, quartz, and orthoclase, respectively. Surface complexation reactions were not taken into account. Simulation results indicated that at pH > 6.4 first Eu₂(CO₃)₃·3H₂O(s) precipitates, followed by potential precipitations of Eu(CO₃)(OH)·0.5H₂O(cr) and Eu(CO₃)(OH)(cr) (data not shown here). However, a reduction of Eu³⁺ (aq) concentrations due to e.g. surface complexation reactions (as relevant for this study) was expected to shift precipitation reactions to higher pH values. All SCM fitting procedures allowed precipitation of Eu solid phases (Sec. 3.2.3).

Since Eu(III) is a chemical homologue of Cm(III) and Am(III), studies involving Cm(III) and Am(III) were included to gather information of Eu surface complexation and speciation reactions. Unfortunately, no clear spectroscopic evidence exists on the nature of Eu surface complexes on quartz, orthoclase, or muscovite surfaces. Aquo ions of Eu³⁺ and Cm³⁺ are solvated by 8 - 9 surrounding water molecules (e.g. Stumpf et al. (2006), Stumpf et al. (2008), Kumar et al. (2012)). During inner-sphere surface complexation processes water molecules are released and Eu sorbes to the surface in a monodentate, bi- or multidentate manner (Geckeis et al., 2013). So far, the structure of Eu surface complexes has not been clearly determined but evidently strongly depends on the mineral surface structure and pH (Kumar et al., 2012), as well as IS, temperature, competing cations, complexing ligands, etc. (Geckeis et al., 2013).

Wang and Anderko (2001) published a modeling study (DDLMM) where monodentate Eu surface complexes were considered on amorphous silica surfaces. Via time-resolved laser-induced fluorescence spectroscopy (TRLFS) Stumpf et al. (2008) evaluated a siliceous bulk surface and found that Cm(III) sorbes in a bidentate, inner-sphere manner at first and is hydrolyzed in a second surface reaction. They also provided spectroscopic evidence of ternary Eu-silicic acid surface complexes at elevated Si concentrations (Si > 3.5·10⁻² mol L⁻¹). Kitamura et al. (1999) optimized monodentate log K_{Eu} with a BSM on a quartz surface and yielded adequate fitting results. Kumar et al. (2012) also postulated monodentate Eu surface complexes at pH ≤ 6 on amorphous silica surfaces. For feldspar minerals Stumpf et al. (2006) found a hydrolyzed inner-sphere Cm(III) surface complex and a surface complex that was not hydrolyzed. Both complexes were surrounded by five water molecules indicating multidentate chemical bonds to the mineral surface. Geckeis et al. (2013) published a literature review and found trivalent actinides to sorb as outer-sphere complexes to clay-type minerals at low IS and pH conditions. They also stated that on Al-bearing oxides/hydroxides and on clay-minerals three different inner-sphere complexes exist which were observed via TRLFS. Pan et al. (2017) recently

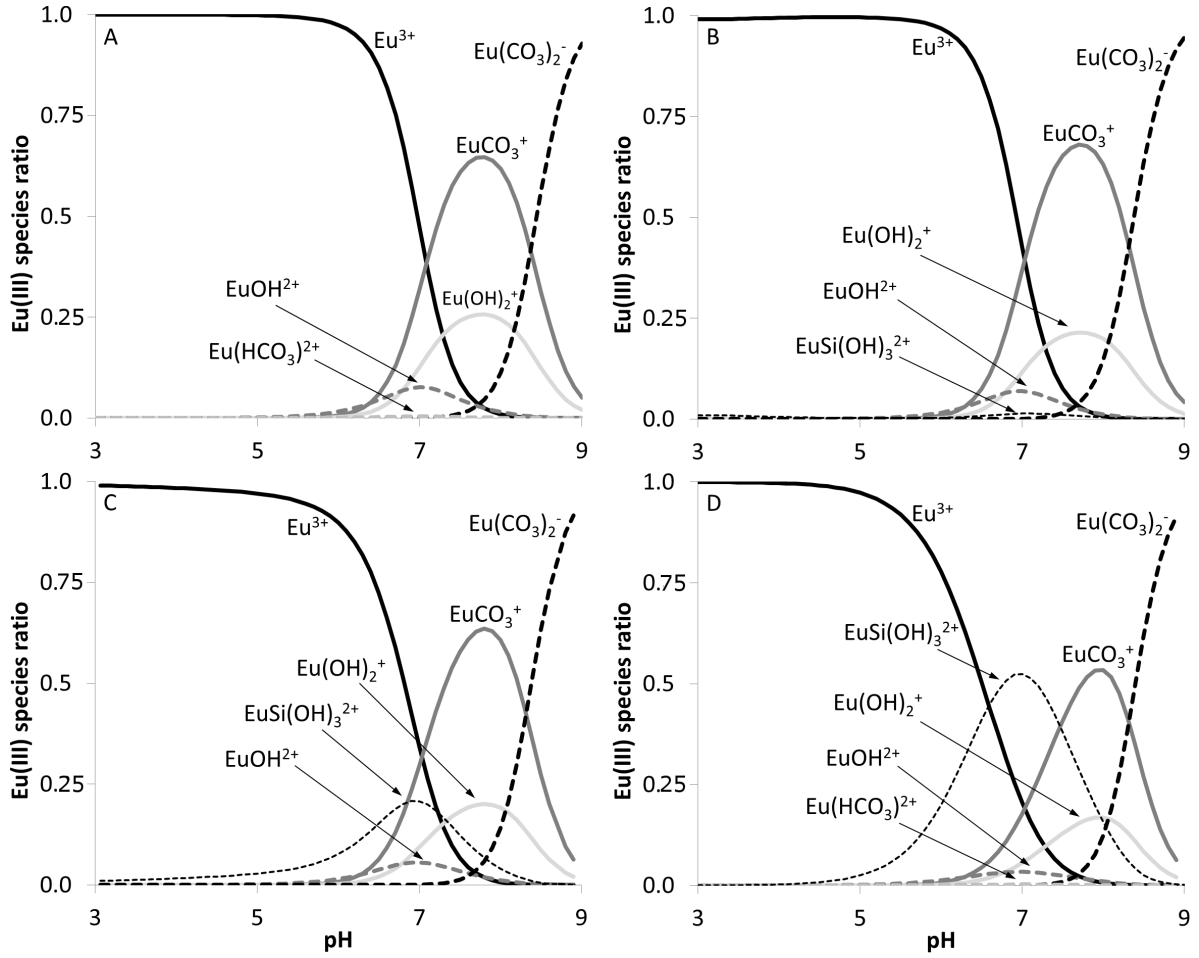


Fig. 3.1: Europium speciation under atmospheric influence without solid content (A), and Eu in equilibrium with muscovite (B), orthoclase (C), quartz (D). Eu $C_0 = 10^{-5}$ mol L $^{-1}$ in 10 mM NaClO $_4$ background electrolyte (A - D). Eu(HCO $_3$) $^{2+}$ ranged below 0.5 % in all speciation calculations.

published results on Eu surface complexation on muscovite under the influence of rising pH conditions, different ISs, and complexing ligands such as sulphate and phosphate. They concluded that at pH ≤ 5 outer-sphere complexation and cation exchange account for Eu immobilization and that at pH > 7 inner-sphere surface complexation on amphoteric sites dominate the sorption process. Pan et al. (2017) found evidence of a hydrolyzed monodentate Eu surface complex for neutral pH conditions and proposed a ternary Eu carbonato surface complex for pH conditions of ≈ 9 (fluorescence emission spectra).

As illustrated, no clear consensus of Eu surface complexes has been found yet and research is still ongoing. The structure of surface complexes depends on element-specific

sorption affinities to sorb as mono-, bi-, multidentate, or e.g. ternary surface complexes and on geochemical system properties. Additionally, the nature of surface sites has still not been fully understood either and might also have significant influence as Barrón and Torrent (1996) postulate. They consider differently coordinated surface hydroxyl coordinations (SHCs) on hematite and goethite (singly-, doubly-, triply surface hydroxyl coordinations) and suggest that these different surface sites may have influence on the nature of surface complexes and on complexation constants. Considering different SHCs would increase the number of *SSDs* which could substantiate the occurrence multidentate surface complex formations as proposed by e.g. Fernandes et al. (2016). Spectroscopic studies by Fernandes et al. (2016) and modeling studies of Polly et al. (2013) postulate bi-, tri-, and tetradentate surface complexes of trivalent lanthanides on different mineral surfaces. However, the present study aimed to develop SCMs as simple as possible while still describing experimental data as good as possible. In the absence of clear spectroscopic evidence, literature data and goodness of fit (gof) of inverse optimization procedures decided whether mono-, multidentate, or ternary surface complexes represented final $\log K_{Eu}$. However, it should already be pointed out here, that presumingly straightforward models can describe measurements well but might not reflect natural, realistic conditions.

3.1.2 Europium conditional cation exchange selectivity coefficients

The term sorption comprises adsorption processes which refers to the adherence of a chemical on a surface, absorption processes where chemicals enter the bulk of a solid, and exchange of ions which relates to the replacement of one chemical for another (Appelo and Postma, 2010). Often, it is difficult to clearly distinguish between all types of reactions.

In the present study, muscovite, orthoclase, and quartz minerals were studied. The cation exchange was only considered for muscovite. Minerals of clay and mica groups are prone to cation exchange reactions due to their crystal structure and chemical composition. The cation exchange can be described by so called conditional cation exchange selectivity constants ($\log K_{cs}$) in TSMs or more commonly by means of the cation exchange capacity (CEC). Selectivity coefficients often define the affinity of specific cations for an exchanger in a binary system. The CEC represents the quantity of cations that are available for exchange reactions at a given pH (Bergaya et al., 2006).

This study did not focus on the experimental determination of selectivity coefficients. Hence, literature values had to be used to include cation exchange processes in SCMs. In the following, the complexity and the challenges related to the application of literature parameter sets is discussed.

Table 3.1 summarizes typical CECs in centimole cations per kg solid [$\text{cmol}(+) \text{kg}^{-1}$]

for muscovite and illite. Illite is a weathering product of the mica mineral muscovite. The difference between both phyllosilicates is based on the partial exchange of lattice K^+ against hydronium ions or protons in solution at illite surfaces (Matthes, 2001). Illite typically shows larger CECs compared to muscovite which is due to higher interparticle attraction forces (higher surface charge density) (Shainberg et al., 1987). In the absence of data and since muscovite and illite have similar crystallographic properties both minerals are compared (Tab. 3.1).

Tab. 3.1: Cation exchange capacities (CECs [$\text{cmol}(+) \text{kg}^{-1}$]) of muscovite and illite.

^[1] CEC yielded from non-linear regression (detailed information provide Osman et al. (1998) and Osman et al. (1999)). CEC_{WG} denotes the CEC of muscovite (mica WG sample, this study) calculated from exchangeable cations Na^+ , K^+ , Ca^{2+} , and Mg^{2+} (cf. Sec. 2.3.1, App. A.6.2, pg. 249), phlogopite structural formula $NaMg_3Si_3AlO_{10}(OH)_2$.

Mineral	CEC [$\text{cmol}(+) \text{kg}^{-1}$]	Reference
Illite/mica	20-50	Kuntze et al. (1988)
Illite	10-40	Bergaya et al. (2006)
Illite	20-50	Appelo and Postma (2010)
Na-illite	14.6	Shainberg et al. (1987)
Na-illite	12.7	Poinssot et al. (1999)
Ca-illite	17.7	Shainberg et al. (1987)
Phlogopite (Mg-mica)	5 - 10	Cho and Korarneni (2009)
K-muscovite ^[1]	10	Osman et al. (1998)
Li-muscovite ^[1]	45	Osman et al. (1999)
Muscovite	≤ 5	Bergaya et al. (2006)
Muscovite	4.01	Pan et al. (2017)
Muscovite (CEC_{WG})	5.3	this study

As discussed in Section 2.3.1 the potential cation exchange capacity (CEC_{pot}) of muscovite was determined after DIN ISO 13536:1997-04 (1997). Due to the application of $BaCl_2$ solution it was not possible to deduce CEC_{pot} from major exchangeable cations as would be expected (DIN ISO 13536:1997-04, 1997). The cations Na^+ , K^+ , Mg^{2+} , and Ca^{2+} accounted for $5.28 \text{ cmol}(+) \text{kg}^{-1}$ (CEC_{WG}) which equalled 12.7 % of CEC_{pot} according to DIN ISO 13536:1997-04 (1997). Since CEC_{pot} was potentially biased due

to conversion of muscovite into Öllacherite (Ba-muscovite), CEC_{WG} had to be assumed to represent a realistic CEC estimation for muscovite. Table 3.1 shows that CEC_{WG} compares well to literature data.

Amongst others, Thellier and Sposito (1989) deduced selectivity coefficients for illite from experimental data. They showed that selectivity coefficients are not constant but vary even over identical geochemical boundary conditions depending on the ratio of sorbed cations over remaining cations in solution which is why they are referred to as *conditional* selectivity coefficients (e.g. Thellier and Sposito (1989), Tournassat et al. (2007), Moog (1997)). Ideal (constant) vs. naturally occurring, non-ideal (conditional) behaviour emphasizes the complexity to derive selectivity coefficients from literature. Literature coefficients must be used with care and should only be considered as a preliminary solution in the need of data. Besides highly comparable geochemical conditions (e.g. IS, pH, CEC, CEC site distribution, -density, index cation(s)) and sample properties (e.g. particle size fraction), cation ratios also need consideration. Generally, selectivity coefficients are only valid for the examined experimental system and should not easily be transferred to related systems.

A cation exchange reaction can be described according to the following equation (Tournassat et al., 2009)



where z_A and z_B refer to the charges of cation A and B , X to the exchanger surface and sol to cations in solution. The thermodynamic equilibrium constant is defined as Equation 3.36 (Tournassat et al., 2009).

$$K = \frac{(N_{AX} \cdot \gamma_{AX})^{z_B} [B_{sol}]^{z_A}}{(N_{BX} \cdot \gamma_{BX})^{z_A} [A_{sol}]^{z_B}} \quad (3.36)$$

With N_{AX} and N_{BX} corresponding to the molar fraction of the exchange species on the surface $[-]$, z to the cation's charge, γ_{AX} and γ_{BX} refer to the activity coefficient $[-]$ of exchange surface species, and $[A_{sol}]$, $[B_{sol}]$ stand for activities $[\text{mol L}^{-1}]$ of the solute species A and B , respectively. There are four main conventions to deduce selectivity coefficients from experimental cation exchange data: Gaines and Thomas (1953), Vanselow (1932), Gapon (1933), and Rothmund-Kornfeld (1918-1919). In this study, the Gaines and Thomas convention was used. The conditional (c) selectivity coefficient after Gaines

and Thomas (GT) is defined as (Tournassat et al., 2007)

$$K_{GT_c}^{B \rightarrow A} = \frac{E_{AX}^{z_B} [B_{sol}]^{z_A}}{E_{BX}^{z_A} [A_{sol}]^{z_B}} \quad (3.37)$$

E_{AX} and E_{BX} refer to equivalent fractions $[-]$ of exchange surface species AX_{z_A} and BX_{z_B} . $B \rightarrow A$ indicates that species A is exchanged against exchange species B (index cation) on the exchangers surface X . According to the Gaines and Thomas convention the activity of an exchanged species is equal to its equivalent fraction on the exchanger's surface multiplied by an activity coefficient γ_{AX} , γ_{BX} which is set unity (Tournassat et al. (2007), Bradbury et al. (2005)).

Even though muscovite and related phyllosilicates such as illite have been intensively investigated in the past there is only little information available regarding muscovite selectivity coefficients. At the current state of research only Maslova et al. (2004), Osman et al. (1998) and Osman et al. (1999) examined cation exchange reactions of preconditioned muscovite surfaces. Osman et al. (1998) and Osman et al. (1999) studied the exchange of Na^+ and H^+ of homo-ionic Li- and K-muscovite. They came to the conclusion that the exchange of hydronium ions (protons) in solution vs. Li^+ interlayer cations ($\text{Li} \rightarrow \text{H}^+$) is a very fast reaction. They further stated that the affinity of H^+ to exchange with a K-muscovite surface is comparable to that of K^+ . In PHREEQC, cation exchange processes are described in relation to the same exchangeable cation (index cation). Hence, data provided by Osman and co-workers did not provide a complete set of data to be used in this study since Li^+ and K^+ were considered as index cations. As has already been emphasized in Section 2.5.2 this study includes selectivity coefficients provided by Poinssot et al. (1999). Poinssot et al. (1999) used similar geochemical boundary conditions compared to this study (Table 3.2). They studied the exchange of K^+ and H^+ against Na^+ on homoionic Na-illite in 10 mM NaClO_4 background electrolyte. Table 3.2 provides an overview of selectivity coefficients derived from literature, respective geochemical and experimental conditions, and gives an impression of the variability of selectivity coefficients.

According to Pashley (1981) interlayer K^+ of mica minerals are almost totally replaced by H^+ at $\text{pH} \leq 6$ without showing effects of repulsive hydration/swelling forces. However, Pashley (1981) also state that the exchange of tightly bound interlayer H^+ or K^+ can occur as bulk concentrations of other cations increase even though highly hydrated cations such as Na^+ show smaller selectivity towards mica surfaces compared to cations with small hydration energies (H_{hyd}) such as e.g. H^+ , Cs^+ , and K^+ (Bergaya et al., 2006). Consequently, as Na^+ was provided in excess in the background electrolytes

Tab. 3.2: Summary of relevant cation exchange selectivity coefficients of mica minerals published in literature. [1] Tournassat et al. (2007), [2] Baeyens and Bradbury (2004), [3] Bradbury et al. (2005), [4] Bradbury and Baeyens (2005b), [5] Poinssot et al. (1999), [6] Osman et al. (1999), [7] Osman et al. (1998), [8] Maslova et al. (2004), [9] Rabung et al. (2005), CEC – cation exchange capacity, PS – planar sites (exchange sites on basal planes), typeII – type II sites, FES – frayed edge sites, one-site – type of exchange site not specified, C_x – concentration of cation 'x' in the background electrolyte (x relates to e.g. Mg^{2+} , Ca^{2+} , Cs^+ , etc.), A – cation in solution to be exchanged with the index cation (B), $\log K_c$ – conditional cation exchange selectivity coefficient, *SLR* – solid-liquid ratio, *PSF* – particle size fraction; * – homoionic, ** – no information provided of used convention, () – optimized value, does not necessarily represent realistic $\log K_c$ according to author, musc – muscovite, SWy-1 – certified montmorillonite, ref. – reference. $\log K_c Na/Ca$: $2NaX + Ca^{2+} = CaX_2 + 2Na^+$, $\log K_c Na/Mg$: $2NaX + Mg^{2+} = MgX_2 + 2Na^+$, $\log K_c Na/K$: $NaX + K^+ = KX + Na^+$, $\log K_c Ca/Eu$: $3CaX + 2Eu^{3+} = 2EuX_3 + 3Ca^{2+}$, $\log K_c Na/Eu$: $3NaX + Eu^{3+} = EuX_3 + 3Na^+$, $\log K_c K/Cs$: $KX + Cs^+ = CsX + K^+$, $\log K_c Na/Cs$: $NaX + Cs^+ = CsX + Na^+$, $\log K_c Na/H$: $NaX + H^+ = HX + Na^+$, $\log K_c Li/Na^{**}$: $LiX + Na^+ = NaX + Li^+$, $\log K_c Li/H^{**}$: $LiX + H^+ = HX + Li^+$, $\log K_c K/H^{**}$: $KX + H^+ = HX + K^+$. $\log K_{cs}$ for Na-illite from Poinssot et al. (1999) were used for SCMs.

ref.	Solid	PSF	CEC	Background electrolyte		Exchange site capacity	Exchange selectivity coefficient $\log K_c$				
		[μm]	[meq kg^{-1}]	[mmol L^{-1}]	$\log K_c \text{B/A}$		one-site	FES	typeII	PS	
[1]	Na-illite*	< 2	-	5	CaCl ₂ , MgCl ₂ , KCl	PS 88% CEC, FES 12% CEC	$\log K_c \text{Na/Ca}$		0.53		0.53
							$\log K_c \text{Na/Mg}$		0.55		0.55
							$\log K_c \text{Na/K}$		0.52		6.70
[2]	Na-illite*	< 0.5	225 ± 100	1 - 100	NaClO ₄ , C_{Ca} 10 ⁻⁴ - 10 ⁻⁸ mol L ⁻¹	PS 180 meq kg ⁻¹ typeII 45 meq kg ⁻¹	$\log K_c \text{Na/Ca}$				0.30
							$\log K_c \text{Na/Ca}$			1.90	
[3]	Ca-SWy-1*	< 2 ^[9]	760 ± 100 ^[9]	70	Ca(ClO ₄) ₂ , C_{Eu} = 9.5·10 ⁻⁹ mol L ⁻¹ , <i>SLR</i> 1 g L ⁻¹	8.7·10 ⁻¹ eq kg ⁻¹	$\log K_c \text{Ca/Eu}$	1.11			
	Na-illite*	< 0.5 ^[9]	225 ± 100	100	NaClO ₄ , C_{Eu} = 3·10 ⁻⁹ mol L ⁻¹ , <i>SLR</i> 1.8 g L ⁻¹	225 ± 100 meq kg ⁻¹	$\log K_c \text{Na/Eu}$	1.88			
[4]	Na-SWy-1*		870	100	NaClO ₄ , $C_{Eu} \leq$ 1.3·10 ⁻⁷ mol ⁻¹ , <i>SLR</i> 1.5 g L ⁻¹	8.7·10 ⁻¹ eq kg ⁻¹	$\log K_c \text{Na/Eu}$	1.48			
[5]	illite	< 63	-	-	-	0.5 meq kg ⁻¹	$\log K_c \text{Na/K}$	1.90			
	K-illite*	< 63	-	10	KCl, $C_{Cs} < 10^{-8}$ mol L ⁻¹	0.55 meq kg ⁻¹	$\log K_c \text{K/Cs}$		4.70		
						0.55 meq kg ⁻¹	$\log K_c \text{Na/Cs}$		6.95		
						0.55 meq kg ⁻¹	$\log K_c \text{Na/K}$		2.25		
						0.55 meq kg ⁻¹	$\log K_c \text{Na/H}$		1.75		
	Na-illite*	< 63	127	10	NaClO ₄ , $C_{Cs} < 10^{-8}$ mol L ⁻¹	35 meq kg ⁻¹	$\log K_c \text{Na/Cs}$				3.60
[6]	Li-musc*	-	450 ± 50	0.64	NaCl	-	$\log K_c \text{Li/Na}^{**}$	0.60			
[7]	Li-musc*	-	531	0.6	HNO ₃	-	$\log K_c \text{Li/H}^{**}$	(2.26)			
	K-musc*	-	100	0.6	HNO ₃ , 8 mM KCl	-	$\log K_c \text{K/H}^{**}$	-0.05			
[8]	Phlogopite	< 63	294	100	NaCl, <i>SLR</i> 10 g L ⁻¹	1.8 sites nm ⁻²	$\log K_c \text{K/H}$	-4.82			

in the present study (Sec. 2.4.1, Sec. 3.2, Sec. 4), cation exchange reactions of interlayer H^+ and K^+ against Na^+ were assumed which correlates well with Poinssot et al. (1999) who investigated cation exchange processes with respect to the index cation Na^+ .

Since the selectivity of cations is negatively correlated with the absolute H_{hyd} [kJ mol^{-1}] the following general order of cation selectivity is valid $\text{H}^+ > \text{Cs}^+ > \text{K}^+ > \text{Na}^+ > \text{Li}^+ > \text{Ca}^{2+}, \text{Mg}^{2+}$ (Bergaya et al. (2006), Shainberg et al. (1987), Pashley (1984)). Following e.g. Osman et al. (1999) large ions with small H_{hyd} such as Cs^+ show greater affinities towards muscovite surfaces in comparison to ions with small ionic radii and large H_{hyd} such as Li^+ . Generally, cations with high H_{hyd} are less easily incorporated as interlayer cations compared to ions with small H_{hyd} (e.g. Shainberg et al. (1987)). In the absence of data and under consideration of H_{hyd} of cations (large H_{hyd} correlated with small selectivity), cation exchange reactions of bivalent cations were neglected in this study.

There are only few studies available dealing with Eu^{3+} selectivity coefficients. Bradbury et al. (2005) conducted experimental and modeling studies on Na-illite with Eu (Tab. 3.2). In their study the cation exchange on homoionic Na-illite is described as follows $3\text{Na-clay} + \text{Eu}^{3+} \rightleftharpoons \text{Eu-clay} + 3\text{Na}^+$, where -clay symbolises the surface. The modelled conditional cation exchange selectivity coefficient $\log K_c \text{Na/Eu}$ equals 1.88 (Tab. 3.2). Overall, Bradbury et al. (2005) used three surface complexation reactions and one exchange reaction to describe Eu^{3+} uptake. Geckeis et al. (2013) published a review article on actinide mineral-water interface reactions and proposed an average value for Eu^{3+} selectivity for Na-illite of $\log K_c \text{Na/Eu} = 1.9$ which corresponds to a mean value of different literature data sets including Bradbury et al. (2005).

Since data was scarce, a combination of selectivity coefficients provided by Poinssot et al. (1999) and Bradbury et al. (2005) was used to include the selectivity of Na^+ , H^+ , K^+ , and Eu^{3+} for muscovite (Tab. 3.2). However, this approach was only chosen since selectivity coefficients for muscovite were not deduced in this study. Section 3.3.3 discusses modeling results and the applicability of conditional selectivity coefficients from literature.

3.2 Material and Methods

Batch experiments were carried out with the same pristine quartz, orthoclase, and muscovite samples as were used for titration experiments (Sec. 2.3). For batch experiments Norflot Kali MF 6.400 was used which was identical to Norflot Kali 600 but previously grinded by the supplier to a particle size $< 120 \mu\text{m}$. Hence, both orthoclase samples had identical geochemical compositions and only differed in their particle size distribution

(Tab. 2.2, Tab. B.2). A summary of tools, equipment, techniques, and involved institutions are provided in Appendix A.7.

3.2.1 Experimental set-up

Batch experiments with orthoclase and muscovite were performed previous to the present study. Detailed information of the experimental set-up provide Noseck et al. (2012) and Britz (2011). Quartz batch experiments were carried out during the course of this study (Fricke, 2014); the experimental set-up followed Noseck et al. (2012) and Britz (2011) to ensure comparability.

Pristine muscovite and orthoclase samples were sieved: 20 - 400 μm were separated for muscovite, the particle size of the orthoclase and quartz equalled ≤ 120 μm and 150 - 800 μm , respectively (Tab. 2.2). Quartz was not sieved and used as provided by the supplier. None of the solids underwent pre-conditioning procedures.

Batch experiments were prepared under laboratory conditions. Low density polypropylene (LDPE) wide mouth bottles with a volume of 125 ml were used. The *SLRs* equalled 50 g L⁻¹ and 12.5 g L⁻¹, respectively, and were prepared in 10 mM NaClO₄ background electrolyte. The NaClO₄ solution was considered an inert background electrolyte which does not interfere with Eu solution or surface complexation speciation reactions. The initial pH values (pH_{ini}) equalled 3.5 - 9 which were adjusted over several weeks via the addition of NaOH and HCl (1 - 100 mM). During NaOH and HCl addition samples were constantly stirred with a magnetic stirrer; during pH measurements stirring was discontinued. Samples were shaken head first over night. As pH_{ini} remained constant over at least 24 h, Eu was added to the suspensions. The initial Eu concentration C_0 ranged between 10⁻⁵ and 10⁻⁸ mol L⁻¹. Experiments were prepared in triplets for muscovite and orthoclase, in double for quartz. Following Bradbury and Baeyens (2005a) and Adeleye and Clay (1994) an equilibration time of 24 h was allowed. After 24 h samples were centrifuged and filtered with 0.02 μm or 0.2 μm filters. To prevent sorption processes of Eu³⁺ (aq) on container walls centrifuged and filtered samples were immediately acidified. ICP MS analyses yielded Eu concentrations of the supernatant solutions.

3.2.2 Estimation of Eu surface complexation constants with PHREEQC

This section is structured into five subsequent steps which were necessary to determine $\log K_{Eu}$ with SCMs: First the calibration data sets for muscovite, orthoclase, and quartz SCMs are discussed; then the estimation of the cation exchange site density is illustra-

ted (similar to the *SSD* of surface complexation reactions, Sec. 2.2.5). Following, the structure and development of SCMs is described: Surface complexation reactions and applied exchange reactions are specified; identification and definition of developed SCMs are presented. Then, Pauling's charge distribution factors used for charge distribution estimations over the different electrostatic planes of the BSM in PHREEQC are provided (CD-MUSIC approach, Parkhurst and Appelo (2013)). Finally the coupling of PHREEQC with UCODE is outlined; model conversion criteria as well as assessment of model results by means of *gof* are briefly illustrated.

Calibration data sets of SCMs

Batch experimental data of Eu (Sec. 3.3.1 - 3.3.3) was utilized to calibrate Eu SCMs via the estimation of $\log K_{Eu}$. Calibration refers to the calculation of data in relation to observed values via the optimization of an objective function with dependent variables, here $\log K_{Eu}$ (inverse modeling). Each data set used for SCM calibrations comprised pH_{ini} s between 3 - 9, two *SLRs*, and four initial Eu concentrations C_0 (Sec. 3.2.1). For model calibration the following data sets were considered (App. Fig. B.29):

- (i) Batch experimental raw data that was determined from the supernatant of batch samples via ICP MS [$\mu\text{g L}^{-1}$] (C_{equil}),
- (ii) relative Eu uptake [%Eu(III) immobilized] ($\%Eu(III) \text{ immobilized} = C_{equil}/C_0 \cdot 100$),
- (iii) and K_d values [L kg^{-1}] (Eq. 3.38).

From raw data (C_{equil}) it was not possible to differentiate between precipitation, adsorption and absorption, or cation exchange reactions. Therefore, the converted data set that described the relative Eu uptake was defined "%Eu(III) immobilized" rather than "%Eu(III) sorbed".

$$K_d = \frac{C_{immo}}{C_{equil}} \cdot \frac{V}{M} \quad (3.38)$$

with

$$C_{immo} = C_0 - C_{equil} \quad (3.39)$$

where C_{immo} corresponds to the sorbed/immobilized Eu concentration [$\mu\text{g L}^{-1}$], C_{equil} to the Eu equilibrium concentration in solution after 24 h [$\mu\text{g L}^{-1}$](raw data), V to the electrolyte volume [L], and M to the solid mass [kg]. Equation 3.38 describes a linear sorption isotherm (Henry isotherm) under the assumption of instantaneous equilibrium

conditions. Further information on mineral-specific data processing of calibration data sets is provided in Appendices A.9, A.10, and A.11.

For fitting procedures a uniform data distribution is recommended that evenly covers the entire range of input data to capture all system properties with optimization procedures of parameters (here SCPs). Figure 3.2 was used to identify by sight which data sets was distributed best over the entire range of measurements: For quartz (Fig. 3.2 A.1 - A.3) it was evident that data given in [%Eu(III) immobilized] showed a more uniform distribution in relation to quartz raw data C_{equil} [$\mu\text{g L}^{-1}$] or K_d values [L kg^{-1}].

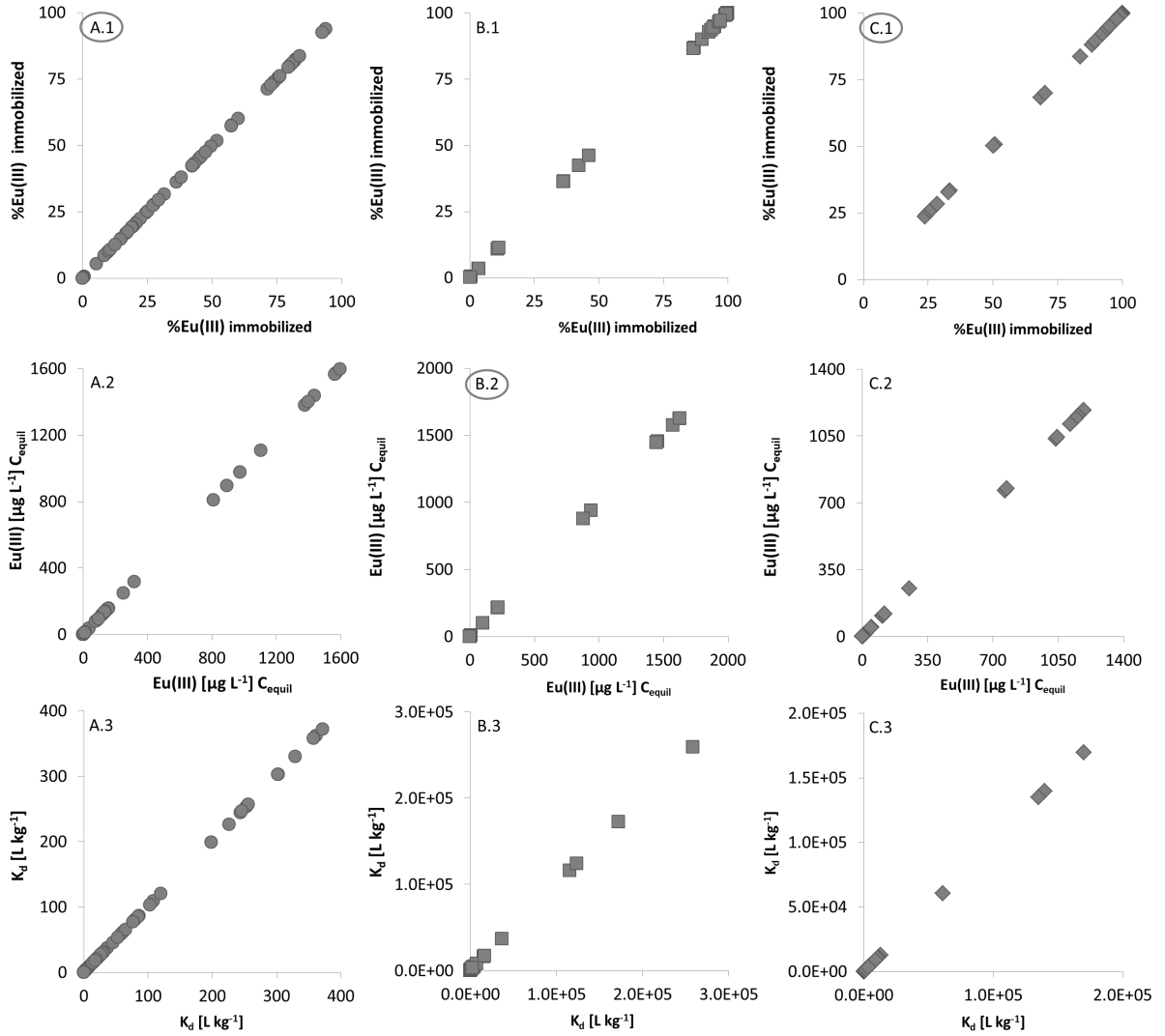


Fig. 3.2: Scatter plots of raw and processed experimental batch data of quartz (A.1 - A.3), orthoclase (B.1 - B.3), and muscovite (C.1 - C.2) plotted as a function of itself to identify data clusters. C_{equil} – Eu equilibrium concentration in solution, K_d – conventional distribution coefficient (Eq. 3.38). Circles indicate batch data used for SCM optimization procedures (data vs. pH, Fig. B.29).

For orthoclase (Fig. 3.2 B.1 - B.3) clustering of data could not be prevented; therefore, measured raw data was used for $\log K_{Eu}$ estimation. Muscovite batch measurements (Fig. 3.2 C.1 - C.3) resulted in a more evenly distributed data set as it was converted to the relative Eu uptake [%Eu(III) immobilized]. Consequently, batch data in [%Eu(III) immobilized] was used as the calibration data set for quartz (Fig. 3.2 A.1) and muscovite SCMs (Fig. 3.2 C.1); for orthoclase C_{equil} [$\mu\text{g L}^{-1}$] was used (Fig. 3.2 B.2). K_d values resulted in clustered data for all minerals, especially for orthoclase and muscovite batch experiments (Fig. 3.2, App. Fig. B.29).

Estimation of cation exchange site capacity

Similar to the *SSD* of surface complexation and protolysis reactions SCMs need sound information of the number of cation exchange sites since mechanistic TSMs discriminate between both surface processes and, hence, available sites. In this study, the Gaines-Thomas convention was used; it was therefore assumed that the activity of an exchange species α_{EX} was equivalent to its equivalent fraction (Parkhurst and Appelo, 2013). The cation exchange site capacity (absolute number of exchange sites [$\text{mol}(+)\text{sites kgw}^{-1}$]) was calculated from the cation exchange capacity of muscovite (CEC_{WG} , Sec. 3.1.2) with Equation 3.40 (simplifying assumption $L = \text{kgw}$)

$$EX_{absolute} = CEC_{WG} \cdot M/V \cdot 10^{-2} \quad (3.40)$$

where M/V corresponds to the mass-volume ratio [kg L^{-1}] and $EX_{absolute}$ to the absolute number of cation exchange sites [$\text{mol}(+) \text{sites kgw}^{-1}$].

Surface complexation model development and structure

Europium SCMs were based on surface charge models (Sec. 2.4.3); final SCP sets as given in Table 2.4 were used as fix parameter values to optimize $\log K_{Eu}$. Hence, SCMs represent a further development of surface charge models to derive $\log K_{Eu}$ via inverse modeling where all $\log K_{Eu}$ apply to zero ionic strength (IS) ($IS = 0 \text{ mol L}^{-1}$, $\gamma = 1$). All SCMs were based on the assumption that the system was in equilibrium, no kinetic processes were considered.

Each SCP set from Table 2.4 (bold IDs) described individual SCMs that were used to estimate one $\log K_{Eu}$ or a combination of Eu surface complexation constants. Hence, in this study a SCM was defined with the underlying surface charge model and proposed Eu surface complex where each surface complex or each combination made up an individual

SCM (Sec. 3.3, Tab. 3.4). Surface complexation models (SCMs) were therefore identified with IDs as introduced for surface charge models (Tab. 2.4) and an additional suffix (e.g. mono, bi, tri, etc.) which defined the kind of considered Eu surface complex(s) (Tab. 3.4). Since SCMs were based on surface charge models both TSMs were similarly structured (Sec. 2.4.3); differences are listed below:

- Pre-equilibration of the mineral with the background electrolyte during pH adjustment was allowed under atmospheric influence (ρCO_2 $10^{-3.4}$ bar).
- For muscovite, Eu^{3+} conditional cation exchange reactions and coefficients ($\log K_c\text{Na}/\text{Eu}$) were defined (Tab. 3.4) in addition to $\log \log K_c\text{Na}/\text{H}$ and $\log K_c\text{Na}/\text{K}$ with $\log K_c\text{Na}/\text{Na} = 0$.
- Surface complexation reactions (Input file code block 3.1) were included in addition to protolysis reactions (Tab. 2.3, Tab. 2.4).
- The electrolytes were equilibrated with the minerals allowing relevant solid Eu(III) phases to precipitate including carbonato species (Fig. 3.1).

Detailed, mineral-specific information on the development and set-up of SCMs for quartz and orthoclase is provided in Appendices A.9 and A.10.

PHREEQC considers cation exchange processes by half reactions with selectivity coefficients. To model the exchange composition and related processes the number of exchange sites as well as selectivity coefficients of each cation are required. The amount of exchange sites was calculated from CEC_{WG} , conditional coefficients were derived from literature (Poinssot et al. (1999), Bradbury et al. (2005), Sec. 3.1.2) and used as fix parameter values. Due to lack of data and following H_{hyd} (Sec. 3.1.2), cation exchange reactions of bivalent cations were neglected in this study. Moreover, Ca^{2+} and Mg^{2+} concentrations of muscovite ranged below 0.9 wt%; hence, significant concentrations of bivalent cations in solution originating from mineral dissolution processes could be excluded (App. Tab. B.2).

Taking current spectroscopic and modelling studies into account (Stumpf et al. (2006), Stumpf et al. (2008), Wang and Anderko (2001), Bouby et al. (2010b), etc.) mono-, bi-, and multidentate Eu surface complexes as well as combinations of surface complexation reactions were considered. Ternary Eu-hydroxo surface complexes were included, as well as hydrolyzed Eu surface species. Ternary Eu-silicic acid surface complexes were not used since experimental and simulated silicic acid in solution of this study ranged well below silicic acid concentrations applied by Stumpf et al. (2008) who postulated ternary Cm(III) silicic acid surface complexes that occurred as silicic acid concentrations reached

$3.5 \cdot 10^{-2} \text{ mol L}^{-1}$. The BSM, the DDLM, and a noEDLM were applied. As discussed in Section 2.5.2 only the 1-pK approach was used for all minerals. In the following, Eu surface complexation reactions, counter- and coion association reactions, and the charge distribution approach (-cd_music) are listed as considered in PHREEQC:

```

### Surface complexation reactions , one-pK DDLM and noEDLM
# Si-OH surface functional groups
S-OH + Eu+3 = S-OEu+2 + H+
S-OH + Eu(OH)2+ = S-OEu(OH)2 + H+
2S-OH + Eu+3 = (S-O)2Eu+1 + 2H+
3S-OH + Eu+3 = (S-O)3Eu + 3H+
# Al-OH surface functional groups
S-O-0.5 + Eu+3 = S-OEu+2.5
S-O-0.5 + Eu+3 + H2O = S-OEuOH+1.5 + H+
2S-O-0.5 + Eu+3 = (S-O)2Eu+2
3S-O-0.5 + Eu+3 = (S-O)3Eu+1.5
4S-O-0.5 + Eu+3 = (S-O)4Eu+1

### Surface complexation reactions , one-pK BSM
# Si-OH surface functional groups
S-OH + Eu+3 = S-OEu+2 + H+
-cd_music -0.625 2.625 0
S-OH + Eu+3 + H2O = S-OEuOH+ + 2H+
-cd_music -0.625 1.625 0
2S-OH + Eu+3 = (S-O)2Eu+1 + 2H+
-cd_music -1.25 2.25 0
3S-OH + Eu+3 = (S-O)3Eu + 3H+
-cd_music -1.875 1.875 0
# Al-OH surface functional groups
S-O-0.5 + Eu+3 = S-OEu+2.5
-cd_music 0.375 2.625 0
S-O-0.5 + Eu+3 + H2O = S-OEuOH+1.5 + H+
-cd_music 0.375 1.625 0
2S-O-0.5 + Eu+3 = (S-O)2Eu+2
-cd_music 0.75 2.25 0
3S-O-0.5 + Eu+3 = (S-O)3Eu+1.5
-cd_music 1.125 1.875 0
4S-O-0.5 + Eu+3 = (S-O)4Eu+1
-cd_music 1.5 1.5 0

# Counter- and coion association coefficients , one-pK, BSM
S-O- + Na+ = S-ONa

```

```
-cd_music 0 1 0
S-OH2+ + Pc- = S-OH2Pc
-cd_music 0 -1 0
```

Input file code block 3.1: Surface complexation reactions, co- and counter ion association coefficients, and charge distribution as used for electrostatic models and noEDLM approaches in PHREEQC SCMs and RTMs (Sec. 4.2.5). # indicates comments.

In the PHREEQC input file code block 3.1, S- symbolizes the surface, -cd_music denotes the charge distribution option of the CD-MUSIC model approach where the numbers represent the charge distribution ($\Delta z_{0-1-plane}$) as illustrated in Table 3.3 (Appelo and Postma (2010), Parkhurst and Appelo (2013)), Pc- relates to the perchlorate ion of the background electrolyte NaClO₄ (Input file code block 2.1, Sec. 2.4.3), and # denotes comments. The charge distribution option is described below (Tab. 3.3).

Since it was the aim to keep the number of adjustable parameters low, only one surface site was used even though literature describes different SHC (Barrón and Torrent, 1996). A clear site distribution between potentially different SHC or so-called strong, weak sites, respectively, could not be obtained from batch nor from titration experimental data. However, the advantage of more than one surface site are mostly independent surface complexation constants that do not tend to correlate strongly. Hence, optimization of more than one $\log K_{Eu}$ would seldom result in parameter correlation coefficients exceeding 0.85 (Parkhurst and Appelo (2013), Hill (1998)). Bradbury et al. (2005), for example, used three different surface sites for Eu surface complexation reactions and a cation exchange reaction to model Eu uptake on Na-illite. They estimated the *SSD* of each site and used these estimates as fix values for optimization procedures. This approach was not followed in this study.

Pauling's rules for Eu BSMs

Pauling's bond valence concept was applied for basic Stern CD-MUSIC model approaches in PHREEQC (Hiemstra et al. (1989a), Hiemstra and van Riemsdijk (1996)). Section 2.2.2 briefly describes Pauling's rules for charge distribution calculations of protolysis reactions. For Eu surface complexation reactions the same approach was followed. Table 3.3 summarizes charge distribution parameters of different Eu surface complexes as applied in the present study. The corresponding chemical equations of surface complexation reactions are described above (Input file code block 3.1).

Tab. 3.3: Pauling's bond valence parameters for Eu surface complexation reactions of mono-, bi-, and multi-dentate surface complexes for aluminol (Al-OH) and silanol (Si-OH) surface functional groups (SFG). CN – coordination number, Me – metal ion (here Eu^{3+}), z_{Me} – valence of metal cation, here Eu^{3+} , ΔnH^+ – released protons (H^+), v – charge per bond, f_{factor} – charge distribution factor over each bond, n_j – number of ligands ($n = 1$ for mono-dentate surface complexes, $n = 2$ for bi-dentate surface complexes, etc.), z_j – charge of ligands ($z = 0$ for OH_2^0 , $z = -1$ for OH^{-1} , $z = -2$ for O^{-2}), $\Delta z_{0-1-plane}$ – charge distribution over the 0- and 1-plane, Δz – difference/change of charge between 0-plane and 1-plane, mono/bi/tri/tetra – surface complex with one/two/three/four chemical bonds at the 0-plane. $z_{H^+} = 1$ (charge of a proton).

	1-pK approach, Si-OH			1-pK approach, Al-OH			
	mono	bi	tri	mono	bi	tri	tetra
CN_{Me}	8	8	8	8	8	8	8
z_{Me}	3	3	3	3	3	3	3
z_{SFG}	0	0	0	0	-0.5	-0.5	-0.5
ΔnH^+	-1	-2	-3	0	0	0	0
$v = z_{Me}/CN_{Me}$	3/8	3/8	3/8	3/8	3/8	3/8	3/8
$f_{factor} = n_j \cdot v$	3/8	3/4	1.125	3/8	3/4	1.125	1.50
n_j	1	2	3	1	2	3	4
z_j	0	0	0	0	0	0	0
$\Delta z_{0-plane}$	-0.625	-1.25	-1.875	0.375	0.750	1.125	1.50
$\Delta z_{1-plane}$	2.625	2.25	1.875	2.625	2.25	1.875	1.50
Δz	2	1	0	3	3	3	3
$\Delta z_{0-plane} = \Delta nH^+ \cdot z_{H^+} + f_{factor}$							
$\Delta z_{1-plane} = v \cdot (CN_{Me} - n_j)$							

As an example: Eu^{3+} (aq) is surrounded by 8 - 9 water molecules (e.g. Kumar et al. (2012)); therefore, the coordination number (CN) of Eu^{3+} (aq) was defined to equal 8 in this study. The charge per bond valence (v), respectively, the ratio of valences distributed over each ligand of an Eu^{3+} (aq) equals $v = z_{Me}/CN_{Me} = 3/8$ (Hiemstra et al., 1989a) with $Me = \text{Eu}^{3+}$ and $z_{Me} = 3$ for the charge of the trivalent Eu cation. The number of released ligands (n_j) multiplied with v returns in the charge distribution factor f_{factor} . In case of a tridentate Eu surface complex $f_{factor} = n_j \cdot v = 3 \cdot 3/8 = 1.125$ with $n_j = 3$ and describes the charge distribution over three surface bonds and five water molecules that are orientated towards the bulk of the solution (1-plane/d-plane).

The formation of tridentate surface complexes results in a release of three protons from a mineral Si-OH surface ($\Delta nH^+ = -3$). The charge distribution at the 0-plane for a tridentate surface complex was calculated with $\Delta z_{0-plane} = \Delta nH^+ \cdot z_{H^+} + f_{factor} = -3 \cdot 1 + 1.125 = -1.875$ with $z_{H^+} = 1$ representing the charge of a proton. Accordingly, $\Delta z_{1-plane} = v \cdot (CN_{Me} - n_j) = 3/8 \cdot (8 - 3) = 1.875$ yields the charge distribution that develops at the 1-plane. The sum of $\Delta z_{0-plane} + \Delta z_{1-plane} = -1.875 + 1.875 = 0$ and returns the charge difference between both planes Δz (Tab. 3.3). In the BSM the charge distribution over the 0-plane and 1-plane ($\Delta z_{0-plane}$, $\Delta z_{1-plane}$) were used for the PHREEQC CD-MUSIC approach (-cd_music).

For hydrolyzed monodentate Eu surface species the involved water molecule was positioned in the 1-plane. Hence, $\Delta z_{1-plane}$ was reduced by one.

Surface complexation parameter estimation of $\log K_{Eu}$

Inverse parameter optimization of $\log K_{Eu}$ was realized via coupling of PHREEQC with UCODE as illustrated in Figure 2.7 and Section 2.4.3. No weighting of experimental data was included in UCODE optimization procedures. Input files of SCMs were based on surface charge models (Sec. 2.2), and structured as illustrated above (this section, pf. 129ff). The SCP sets from Table 2.4 were used as fix parameter values for the simulation of the surface charge development; the charge distribution was applied as illustrated in the Input file code block 3.1 and Table 3.3 (CD-MUSIC approach, Parkhurst and Appelo (2013)); and $\log K_{Eu}$ s were defined with surface complexation reactions as also provided in the Input file code block 3.1. Surface complexation constants ($\log K_{Eu}$ s) served as fitting parameters without constraints.

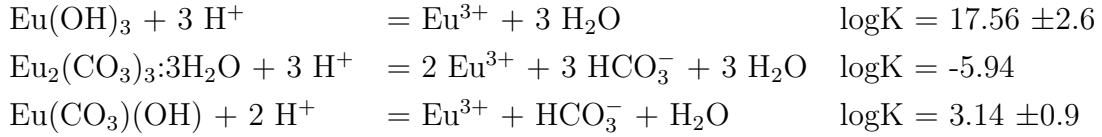
To ensure unique fitting results, gof provided by UCODE was considered (App. A.5); optimizations that yielded parameter correlation coefficients ≥ 0.85 were excluded. The standard error (SE), the parameter standard deviation (psd), the least squares objective function value ($LSOF$), and 95% parameter confidence intervals (CI) were considered for SCP assessment in the same way as for surface charge models (Sec. 2.4.3): The smaller the $LSOF$, the SE , or the psd , etc. the better the fit and, hence, parameter estimation (Hill, 1998).

Section 2.4.4 and Section 3.2.3 provide information on the database. The digital appendix supplies PHREEQC and UCODE input files.

3.2.3 Thermodynamic database

The thermodynamic database introduced in Section 2.4.4 was used. For Eu thermodynamic data the database was updated for values compiled by the SEM² research project

(Rare Earth Elements Metallurgy - Advanced methods for optimized extraction and beneficiation by ion-adsorption clays, project period June 2015 - March 2018). Furthermore, Eu solid phase solubility limits were adapted to measurements carried out with amorphous lanthanide/actinide hydroxides and -carbonates. In the absence of data, solubility measurements from amorphous Am(III), Cm(III), and Nd(III) solids were considered. Adaptations were necessary to prevent an underestimation of potential precipitation reactions: For $\text{Eu}(\text{OH})_3$ (am) and $\text{Eu}(\text{CO}_3)(\text{OH})$ (am) mean values of Eu(III), Am(III), Cm(III) solubility constants from Spahiu and Bruno (1995), NEA TDB, Vol. 13 a (Lemire et al., 2013), and Rard (1987) were included; the solubility constant of $\text{Eu}_2(\text{CO}_3)_3 \cdot 3\text{H}_2\text{O}$ (am) supplied Rard (1987). The following adaptations were used in the database (errors indicate single standard deviation of considered literature data):



3.3 Results and discussion

In the following, experimental and SCM results of Eu batch experiments with muscovite, orthoclase, and quartz are illustrated and discussed. Error bars in Figures 3.3 - 3.12 represent double standard deviations of Eu C_{equil} as described in the Appendix A.8, error bars of pH measurements depict conservative error estimations as presented in the Appendix A.3.2. Table 3.4 summarizes final SCP sets (including $\log K_{\text{Eu}}$).

3.3.1 Quartz

Figure 3.3 depicts experimental batch data of quartz. Generally, measurements followed expectations: The larger the initial Eu concentration ($\text{Eu } C_0$), the less Eu was immobilized. The uptake of Eu was also positively correlated with the pH and SLR . For 12.5 g L^{-1} maximum immobilization rates reached 82% Eu(III) immobilized, for 50 g L^{-1} a maximum of 94% Eu(III) immobilized was observed. Relatively high Eu immobilization was found at $\text{pH} < 5$ which agreed with results from Lützenkirchen (1996). A comparison of quartz batch data of this study with literature (e.g. Kitamura et al. (1999), Stumpf et al. (2008)) showed that collected data matched literature data well provided that similar geochemical boundary condition were compared (App. Fig. B.30).

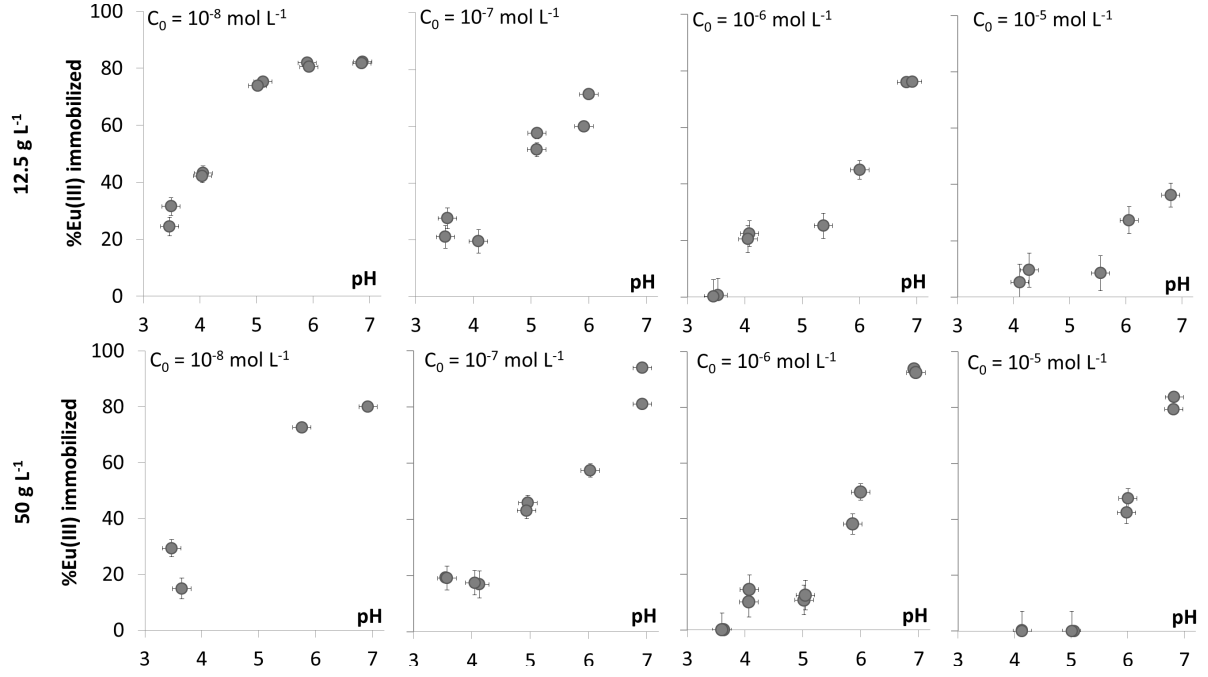


Fig. 3.3: Results of Eu batch experiments with quartz in 10 mM NaClO₄ background electrolyte, laboratory conditions ($\rho\text{CO}_2 = 10^{-3.4}$ bar, $T = 296.0 \text{ K} \pm 2 \text{ K}$). C_0 – initial Eu concentration. Top: $SLR = 12.5 \text{ g L}^{-1}$, bottom: $SLR = 50 \text{ g L}^{-1}$.

1-pK DDLM

Fitted data of a monodentate (dashed grey line), bidentate (dash-dotted grey line), a hydrolyzed monodentate (solid grey line), and a hydrolyzed bidentate (dashed black line), as well as a combination of a mono- and bidentate (solid black line) Eu surface complexes are presented in comparison to experimental data (Fig. 3.4). The latter model approach *SCP Q I mono+bi* (solid black line in Fig. 3.4) assumed a simultaneous formation of a monodentate and bidentate Eu surface complex at the mineral-water interface. Optimized SCPs mostly overestimated experimental data on average which was indicated by mainly negative *MEs* (Tab. 3.4). The *MEs* ranged between -1.3%Eu(III) immobilized for *SCP Q I bi* and +8.4%Eu(III) immobilized for *SCP Q I mono*. To the authors knowledge, no spectroscopic evidence exists for ternary Eu-hydroxo complexes on quartz surfaces; hence, *SCP Q I mono+Eu(OH)₂* was not further followed for transport simulations (Tab. 3.4). However, *SCP Q I mono+Eu(OH)₂* exemplarily showed that the consideration of Eu-hydroxo complexes did not improve model calibration (Tab. 3.4): The *ME* as well as the *LSOF* were similar compared to alternative fitting approaches (e.g. *SCP Q I bi*, *SCP Q I mono+bi*). Smallest *MEs*, *SEs*, and adequate *psds* were obtained with a bidentate Eu surface complex (*SCP Q I bi*) and a combination of bi- and monodentate

Tab. 3.4: Summary of final SCPs including $\log K_{Eu}$ of quartz (Q) and orthoclase (FS). Uncertainties of $\log K_{Eu}$ are represented as 95% confidence intervals (CI s) and parameter standard deviations ($psds$). Information on gof provided in Appendix A.5. ID – identification of SCP set/SCM, EM – electrostatic model, $\Delta\sigma$ – conversion of relative titration data into absolute values (Sec. 2.4.2), SSD – surface site density, SSA – specific surface area, $\log K_{Al-OH}$ – intrinsic protolysis constant of Al-OH (1-pK), $\log K_{Si-OH}$ – intrinsic protolysis constant of Si-OH (1-pK), $\log K_{Na^+/ClO_4^-}$ – counter-, coion association coefficients, C_1 – capacity between 0-plane and 1-plane of BSM, $\log K_{Eu}$ – Eu surface complexation constant, mono/bi/tri/tetra – identifies Eu surface stability constant for mono- and multidentate Eu surface complexes, SE – standard error in [%Eu(III) immobilized] for Q and [$\mu\text{g L}^{-1}$] for FS (cf. Sec. 3.2.2, Fig. 3.2), $LSOF$ – least squares objective function [%Eu(III) immobilized]² for Q and [$\mu\text{g L}^{-1}$]² for FS, ME – mean error [%Eu(III) immobilized] for Q and [$\mu\text{g L}^{-1}$] for FS, $\log K_{H_2O_{mono}}$ – $\log K$ of fitted hydrolyzed monodentate Eu surface complex ($\text{S-OH} + \text{Eu}+3 + \text{H}_2\text{O} = \text{S-OEuOH}+ + 2\text{H}+$), $\log K_{H_2O_{bi}}$ – $\log K$ of fitted hydrolyzed bidentate Eu surface complex ($2\text{S-OH} + \text{Eu}+3 + \text{H}_2\text{O} = (\text{S-O})_2\text{EuOH} + 3\text{H}+$), $\log K_{mono,Eu(OH)_2}$ – $\log K$ of fitted monodentate Eu surface complex in combination with a monodentate ternary Eu hydroxo complex ($\text{S-OH} + \text{Eu}+3 = \text{S-OEu}+2 + \text{H}+$, $\text{S-OH} + \text{Eu(OH)}_2+ = \text{S-OEu(OH)}_2 + \text{H}+$), EX – SCM with exchange sites, $\log K_c\text{Na/Eu}$ – conditional Eu^{3+} cation exchange selectivity coefficient with index cation Na^+ , noEDLM – non-electrostatic model, DDLM – diffuse double layer model, BSM – basic Stern model. **Bold** IDs indicate SCMs and final SCP sets that were used for Eu transport simulations (Sec. 4). For grey color see text.

ID	EM	$\Delta\sigma$	SSD [sites nm ⁻²]	$SSA_{\text{BET}}^{[6]}$ [m ² g ⁻¹]	$\log K_{\text{Si-OH}}^{[13]}$	$\log K_{\text{Al-OH}}^{[13]}$	$\text{Log} K_{\text{Na}^+/\text{ClO}_4^-}$	C_1 [F m ⁻²]	$\log K_{\text{Eu}}$	CI	psd	SE	$LSOF$	ME	
SCP Q I mono	DDLM	-	4.6 ^[1]	0.08	-8.0 ^[6]	-	-	-	$\log K_{mono}$	0.0	±0.1	6.3E-02	21	2.8E+04	8.4
SCP Q I H ₂ O _{mono}	DDLM	-	4.6 ^[1]	0.08	-8.0 ^[6]	-	-	-	$\log K_{H_2O_{mono}}$	-4.9	±0.3	1.7E-01	24	3.3E+04	-1.5
SCP Q I mono+Eu(OH) ₂	DDLM	-	4.6 ^[1]	0.08	-8.0 ^[6]	-	-	-	$\log K_{mono}$	0.7	±0.3	1.2E-01	18	1.9E+04	-1.7
									$\log K_{Eu(OH)_2}$	0.1	±0.8	3.96E-01			
SCP Q I bi	DDLM	-	4.6 ^[1]	0.08	-8.0 ^[6]	-	-	-	$\log K_{bi}$	-4.5	±0.3	1.7E-01	23	3.1E+04	-1.3
SCP Q I H ₂ O _{bi}	DDLM	-	4.6 ^[1]	0.08	-8.0 ^[6]	-	-	-	$\log K_{H_2O_{bi}}$	-11.8	±0.4	1.8E-01	27	4.4E+04	8.3
SCP Q I mono+bi	DDLM	-	4.6 ^[1]	0.08	-8.0 ^[6]	-	-	-	$\log K_{mono}$	0.8	±0.3	1.3E-01	18	1.9E+04	-1.7
									$\log K_{bi}$	-6.4	±1.5	7.5E-01			
SCP Q I mono+EX	DDLM	-	4.6 ^[1]	0.08	-8.0 ^[6]	-	-	-	$\log K_{mono}$	0.5	±0.3	1.3E-01	16	1.4E+04	-0.59
									$\log K_{c\text{Na}/\text{Eu}}$	2.6	±0.6	3.1E-01			
SCP Q I bi+EX	DDLM	-	4.6 ^[1]	0.08	-8.0 ^[6]	-	-	-	$\log K_{bi}$	-5.7	±0.4	1.7E-01	18	2.0E+04	2.8
									$\log K_{c\text{Na}/\text{Eu}}$	3.2	±0.6	3.2E-01			
SCP Q I mono+bi+EX	DDLM	-	4.6 ^[1]	0.08	-8.0 ^[6]	-	-	-	$\log K_{mono}$	0.3	±0.3	1.65E-01	15	1.4E+04	-0.40
									$\log K_{bi}$	-6.2	±1.3	3.7E-01			
									$\log K_{c\text{Na}/\text{Eu}}$	2.7	±0.6	2.98E-01			
SCP Q_{noEDLM} mono	noEDLM	-	4.6 ^[1]	0.08	-	-	-	-	$\log K_{mono}$	0.0	±0.1	6.1E-02	25	3.7E+04	-3.2
SCP Q _{noEDLM} bi	noEDLM	-	4.6 ^[1]	0.08	-	-	-	-	$\log K_{bi}$	-5.7	±1.3	1.6E-01	25	3.8E+04	6.7
SCP Q _{noEDLM} mono+bi	noEDLM	-	4.6 ^[1]	0.08	-	-	-	-	$\log K_{mono}$	0.0	±1.6	7.8E-02	26	3.8E+04	-4.3
									$\log K_{bi}$	-6.5	±2.3	1.2E+00			
SCP Q II mono	BSM	-	4.6 ^[1]	0.08	-7.5 ^[1]	-	-9.4 ^[1]	3.3 ^[1]	$\log K_{mono}$	0.6	±0.3	1.4E-01	19	2.2E+04	-1.1
SCP Q II H ₂ O _{mono}	BSM	-	4.6 ^[1]	0.08	-7.5 ^[1]	-	-9.4 ^[1]	3.3 ^[1]	$\log K_{H_2O_{mono}}$	-4.8	±0.3	1.7E-01	19	3.1E+04	-2.2
SCP Q II bi	BSM	-	4.6 ^[1]	0.08	-7.5 ^[1]	-	-9.4 ^[1]	3.3 ^[1]	$\log K_{bi}$	-4.7	±0.3	1.7E-01	22	3.0E+04	-1.0
SCP Q II mono+bi	BSM	-	4.6 ^[1]	0.08	-7.5 ^[1]	-	-9.4 ^[1]	3.3 ^[1]	$\log K_{mono}$	0.6	±0.3	1.5E-01	19	2.2E+04	-1.6
									$\log K_{bi}$	-6.1	±1.4	6.96E-01			

Continued on next page

ID	EM	$\Delta\sigma$	SSD [sites nm ⁻²]	$SSA_{\text{BET}}^{[6]}$ [m ² g ⁻¹]	$\log K_{\text{Si-OH}}^{[13]}$	$\log K_{\text{Al-OH}}^{[13]}$	$\text{Log}K_{\text{Na}^+/\text{ClO}_4^-}$	C_1 [F m ⁻²]	$\log K_{\text{Eu}}$	CI	psd	SE	$LSOF$	ME	
SCP FS I mono	DDLm	0.03	5.9 ^[13]	0.2	-	3.5	-	-	$\log K_{mono}$	0.2	±0.1	5.6E-02	64	1.4E+05	5.5
SCP FS I H ₂ O _{mono}	DDLm	0.03	5.9 ^[13]	0.2	-	3.5	-	-	$\log K_{H_2O_{mono}}$	-3.5	±0.1	5.5E-02	67	1.5E+05	4.7
SCP FS I bi	DDLm	0.03	5.9 ^[13]	0.2	-	3.5	-	-	$\log K_{bi}$	0.7	±0.1	5.6E-02	65	1.4E+05	5.3
SCP FS I tri	DDLm	0.03	5.9 ^[13]	0.2	-	3.5	-	-	$\log K_{tri}$	1.2	±0.1	5.6E-02	65	1.4E+05	5.2
SCP FS I tetra	DDLm	0.03	5.9 ^[13]	0.2	-	3.5	-	-	$\log K_{tetra}$	1.6	±0.1	5.6E-02	65	1.4E+05	5.3
SCP FS II mono	DDLm	0.047	3.8 ^[13]	0.2	-	3.5	-	-	$\log K_{mono}$	0.5	±0.1	4.02E-02	44	6.5E+04	-0.21
SCP FS II H ₂ O _{mono}	DDLm	0.047	3.8 ^[13]	0.2	-	3.5	-	-	$\log K_{H_2O_{mono}}$	-3.2	±0.1	5.5E-02	70	1.6E+05	5.1
SCP FS II bi	DDLm	0.047	3.8 ^[13]	0.2	-	3.5	-	-	$\log K_{bi}$	1.0	±0.1	4.2E-02	47	7.6E+04	-0.16
SCP FS II tri	DDLm	0.047	3.8 ^[13]	0.2	-	3.5	-	-	$\log K_{tri}$	1.4	±0.1	4.2E-02	47	7.7E+04	-0.45
SCP FS II tetra	DDLm	0.047	3.8 ^[13]	0.2	-	3.5	-	-	$\log K_{tetra}$	1.8	±0.1	3.97E-02	44	6.5E+04	-1.4
SCP FS III mono	DDLm	0.3	3.8 ^[13]	0.2	-	8.0	-	-	$\log K_{mono}$	12.7	±0.1	4.36E-02	53	9.7E+04	8.9
SCP FS III H ₂ O _{mono}	DDLm	0.3	3.8 ^[13]	0.2	-	8.0	-	-	$\log K_{H_2O_{mono}}$	5.1	±0.1	4.9E-02	62	1.3E+05	6.6
SCP FS III bi	DDLm	0.3	3.8 ^[13]	0.2	-	8.0	-	-	$\log K_{bi}$	13.6	±0.1	4.78E-02	58	1.2E+05	7.3
SCP FS III tri	DDLm	0.3	3.8 ^[13]	0.2	-	8.0	-	-	$\log K_{tri}$	14.3	±0.01	5.25E-02	63	1.3E+05	5.8
SCP FS _{noEDLM} mono	noEDLM	-	1.7 ^[9]	0.2	-	-	-	-	$\log K_{mono}$	-0.7	±0.1	2.8E-02	47	7.4E+04	-8.2
SCP FS _{noEDLM} H ₂ O _{mono}	noEDLM	-	1.7 ^[9]	0.2	-	-	-	-	$\log K_{H_2O_{mono}}$	-5.5	±0.1	4.2E-02	57	1.1E+05	7.2
SCP FS _{noEDLM} bi	noEDLM	-	1.7 ^[9]	0.2	-	-	-	-	$\log K_{bi}$	-5.1	±0.1	4.2E-02	53	9.7E+04	6.9
SCP FS _{noEDLM} tri	noEDLM	-	1.7 ^[9]	0.2	-	-	-	-	$\log K_{tri}$	-9.7	±0.1	5.5E-02	61	1.2E+05	4.0
SCP FS V mono	BSM	0.03	3.2 ^[13]	0.2	-	3.5	1.5 ^[13]	2.1 ^[13]	$\log K_{mono}$	3.2	±0.2	8.4E-02	100	3.7E+05	-34
SCP FS V H ₂ O _{mono}	BSM	0.03	3.2 ^[13]	0.2	-	3.5	1.5 ^[13]	2.1 ^[13]	$\log K_{H_2O_{mono}}$	-1.4	±0.04	1.9E-02	26	2.4E+04	-1.9
SCP FS V bi	BSM	0.03	3.2 ^[13]	0.2	-	3.5	1.5 ^[13]	2.1 ^[13]	$\log K_{bi}$	3.3	±0.1	5.5E-02	81	2.2E+05	-16
SCP FS V tri	BSM	0.03	3.2 ^[13]	0.2	-	3.5	1.5 ^[13]	2.1 ^[13]	$\log K_{tri}$	3.3	±0.1	3.9E-02	52	9.3E+04	-14
SCP FS V tetra	BSM	0.03	3.2 ^[13]	0.2	-	3.5	1.5 ^[13]	2.1 ^[13]	$\log K_{tetra}$	3.3	±0.1	3.2E-02	39	5.3E+04	-12
SCP FS VI mono	BSM	0.047	3.8 ^[13]	0.2	-	3.5	1.5 ^[13]	1.5 ^[13]	$\log K_{mono}$	3.2	±0.2	8.4E-02	110	3.9E+05	-34
SCP FS VI H ₂ O _{mono}	BSM	0.047	3.8 ^[13]	0.2	-	3.5	1.5 ^[13]	1.5 ^[13]	$\log K_{H_2O_{mono}}$	-1.4	±0.1	2.7E-02	36	4.5E+04	1.1
SCP FS VI bi	BSM	0.047	3.8 ^[13]	0.2	-	3.5	1.5 ^[13]	1.5 ^[13]	$\log K_{bi}$	3.3	±0.1	4.8E-02	68	1.6E+05	-15
SCP FS VI tri	BSM	0.047	3.8 ^[13]	0.2	-	3.5	1.5 ^[13]	1.5 ^[13]	$\log K_{tri}$	3.3	±0.1	3.4E-02	45	6.9E+04	-11
SCP FS VI tetra	BSM	0.047	3.8 ^[13]	0.2	-	3.5	1.5 ^[13]	1.5 ^[13]	$\log K_{tetra}$	3.3	±0.1	2.8E-02	36	4.3E+04	-9.5
SCP FS VII mono	BSM	0.3	3.8 ^[13]	0.2	-	8.0	0.67 ^[13]	1.5 ^[13]	$\log K_{mono}$	8.3	±0.1	5.6E-02	74	1.9E+05	-15
SCP FS VII H ₂ O _{mono}	BSM	0.3	3.8 ^[13]	0.2	-	8.0	0.67 ^[13]	1.5 ^[13]	$\log K_{H_2O_{mono}}$	2.4	±0.1	3.2E-02	41	5.7E+04	3.7
SCP FS VII bi	BSM	0.3	3.8 ^[13]	0.2	-	8.0	0.67 ^[13]	1.5 ^[13]	$\log K_{bi}$	9.6	±0.1	3.7E-02	45	6.9E+04	-9.6
SCP FS VII tri	BSM	0.3	3.8 ^[13]	0.2	-	8.0	0.67 ^[13]	1.5 ^[13]	$\log K_{tri}$	11.0	±0.1	2.93E-02	34	3.9E+04	-7.2
SCP FS VII tetra	BSM	0.3	3.8 ^[13]	0.2	-	8.0	0.67 ^[13]	1.5 ^[13]	$\log K_{tetra}$	12.4	±0.1	1.66E-02	18	1.1E+04	-1.5

complexes (*SCP Q I mono+bi*): *SCP Q I bi* returned $ME = -1.3\% \text{Eu(III)}$ immobilized and a $psd = 0.17$; *SCP Q I mono+bi* delivered $ME = -1.7\% \text{Eu(III)}$ immobilized and $psds$ ranging between 0.13 - 0.17 (Tab. 3.4). Both parameter sets were used for reactive transport simulations. For high initial Eu concentrations ($C_0 = 10^{-5} \text{ mol L}^{-1}$) fitted results show the influence of precipitating Eu-carbonates ($\text{Eu}(\text{CO}_3)(\text{OH}) \cdot 0.5\text{H}_2\text{O}(\text{cr})$, $\text{Eu}(\text{CO}_3)(\text{OH})(\text{cr})$, and $\text{Eu}_2(\text{CO}_3)_3 \cdot 3\text{H}_2\text{O}(\text{s})$) which is evident by the discontinuous progression of the fits at pH 6.6 (Fig. 3.4). Precipitation reactions resulted in an overestimation of immobilized Eu [%] for $C_0 = 10^{-5} \text{ mol L}^{-1}$, $SLR = 12.5 \text{ g L}^{-1}$. For $SLR = 50 \text{ g L}^{-1}$ precipitation reactions were necessary to increase Eu immobilization compared to approaches where precipitation was not taken into account. Excluding precipitation of Eu phases returned an underestimation of measurements of both $SLRs$ (results not shown here). Concluding, the 1-pK DDLM supports the assumption that for high Eu C_0 and elevated pH values precipitation of Eu carbonates occurred (Fig. 3.4) which was substantiated by measurements.

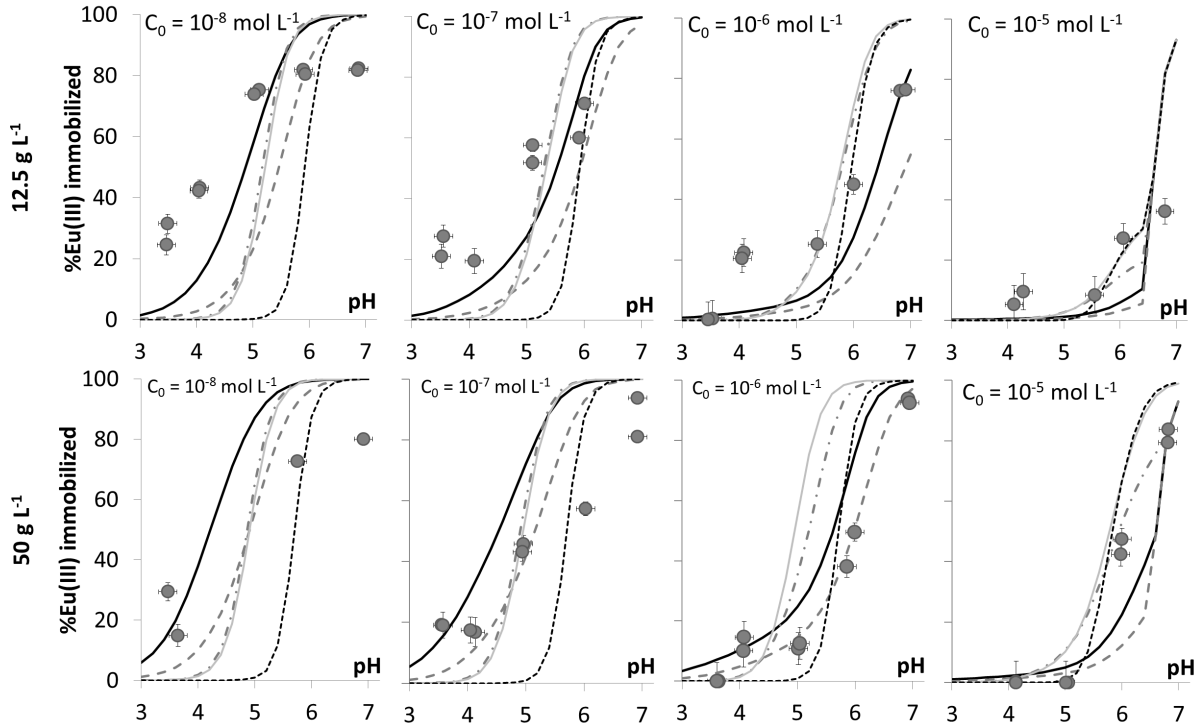


Fig. 3.4: 1-pK DDLM results: Model was calibrated with experimental quartz batch data [%Eu(III) immobilized] (10 mM NaClO_4 background electrolyte, laboratory conditions: $p\text{CO}_2$ $10^{-3.4}$ bar, $T = 296.0 \text{ K} \pm 2 \text{ K}$). C_0 – initial Eu concentration, grey solid circles – quartz batch data, monodentate Eu surface complex (dashed grey line), bidentate complex (dash-dotted grey line), hydrolyzed monodentate complex (solid grey line), hydrolyzed bidentate complex (dashed black line), combination of mono- and bidentate complexes (solid black line). See Table 3.4 for final SCPs.

Even though *MEs* indicated an overestimation of measurements on average, 1-pK DDLMs tended to underestimate Eu sorption processes for $\text{pH} < 4$ ($SLR = 12.5 \text{ g L}^{-1}$, Fig. 3.4). To consider retardation processes at low pH conditions a pH independent surface site had to be assumed. The only way to include pH independent surface reactions in PHREEQC are cation exchange processes: Therefore, 1‰ surface sites were attributed to the assumed hypothetical cation exchange (*SCP I mono+EX*, *SCP I bi+EX*, *SCP I mono+bi+EX*, Tab. 3.4, App. A.9). This approach was not considered to represent realistic mechanistic surface reactions of quartz and should only show whether Eu uptake at low pH values could be captured one way or the other. For that reason, SCPs in Tab. 3.4 are grey coloured and excluded from Eu transport simulations (Sec. 4). Model results are depicted in Figures 3.5 and 3.6.

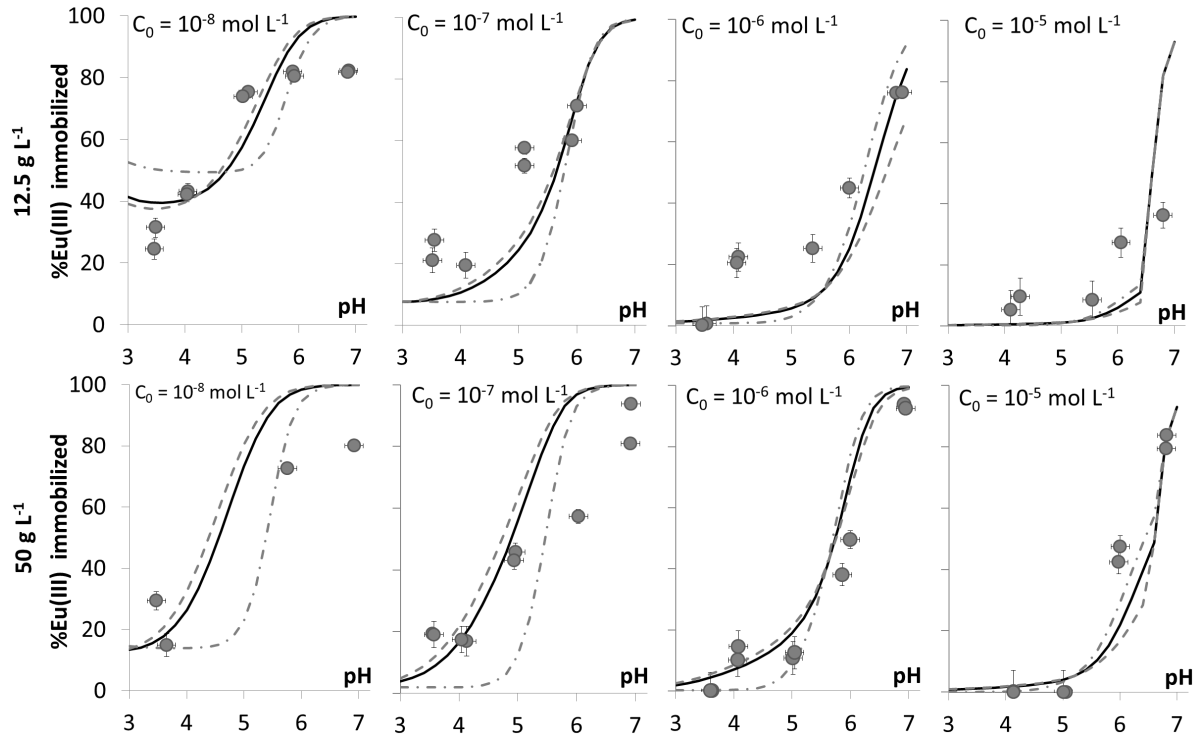


Fig. 3.5: 1-pK DDLM results including a hypothetical exchange site: Model was calibrated with quartz experimental data [%Eu(III) immobilized] and a hypothetical Na-Eu cation exchange reaction on the silica surface (10 mM NaClO_4 background electrolyte, laboratory conditions: ρCO_2 $10^{-3.4}$ bar, $T = 296.0 \text{ K} \pm 2 \text{ K}$). C_0 – initial Eu concentration, solid circles – Eu quartz batch data, monodentate Eu surface complex (dashed grey line), bidentate Eu surface complex (dash-dotted grey line), combination of mono- and bidentate Eu surface complexes (solid black line). See Table 3.4 for final SCPs.

Including cation exchange processes showed a significant improvement of gof (cf. Tab. 3.4): Mono- and bidentate surface complexes in combination with hypothetical exchange reactions (*SCP Q I mono+bi+EX*) resulted in the smallest $ME = -0.4\% \text{Eu(III)}$ immobilized, $SE = 15\% \text{Eu(III)}$ immobilized, and $LOSF = 1.4\text{E}+04\% \text{Eu(III)}$ immobilized² (Tab. 3.4). The cation exchange processes had relevant influences at low pH, as expected, and small element concentrations due to the low number of exchange sites (Fig. 3.5). Hence, for high element concentrations and large *SLRs* cation exchange became irrelevant in relation to Eu surface complexation (Fig. 3.6). Results supported Lützenkirchen (1996) who also assumed minor surface impurities on silica to act as potential cation exchangers.

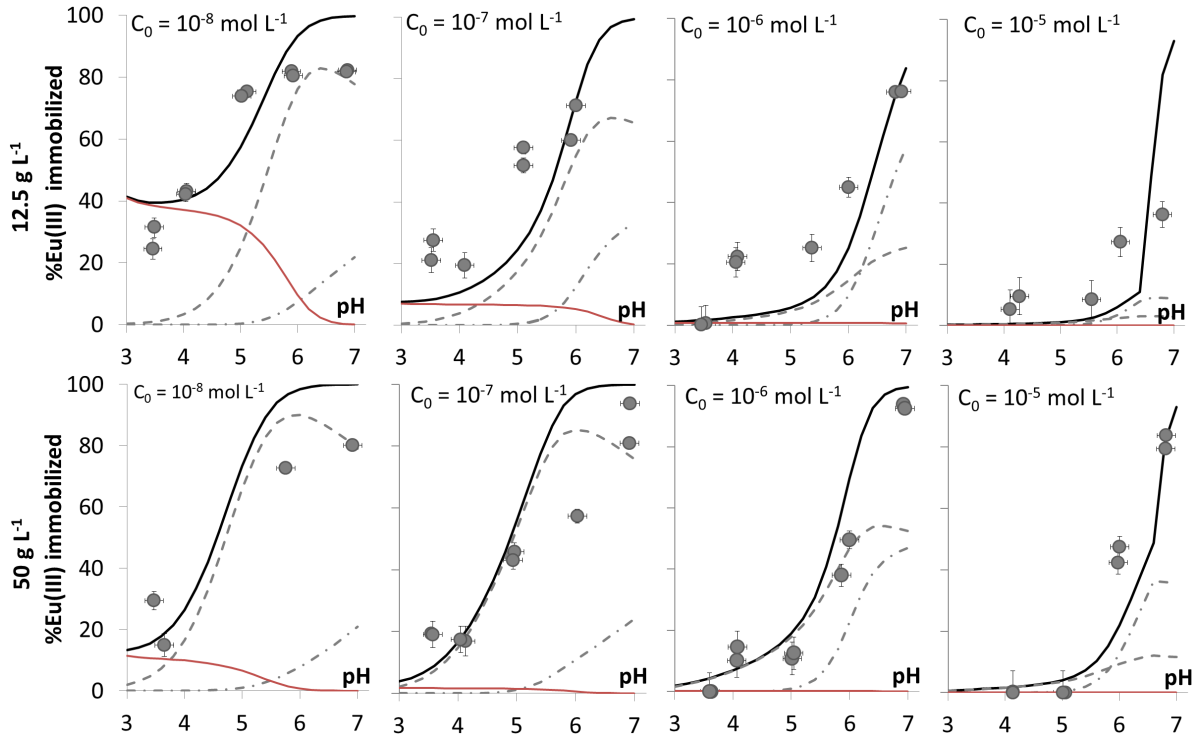


Fig. 3.6: Contributions of Eu mono- and bidentate surface complexes in combination with a hypothetical Na-Eu exchange reaction on quartz of 1-pK DDLMs: *SCP Q I mono+bi+EX* (10 mM NaClO_4 background electrolyte, laboratory conditions: $p\text{CO}_2$ $10^{-3.4}$ bar, $T = 296.0 \text{ K} \pm 2 \text{ K}$). C_0 – initial Eu concentration, solid circles – quartz Eu batch data. Contribution of monodentate Eu surface complex (dashed grey line), bidentate surface complex (dash-dotted grey line), and contribution of a hypothetical cation exchange reaction (solid red line). Overall immobilized Eu [%] of *SCP Q I mono+bi+EX* (solid black line). See Table 3.4 for final SCPs.

noEDLM

Results of noEDLM approaches (Sec. 2.2.1) are shown in Figure 3.7. A comparison between noEDLM results and EMS revealed that the noEDLMs did not reproduce experimental data equally well (cf. Tab. 3.4): For noEDLMs MEs ranged between -4.3 - +6.7%Eu(III) immobilized for $SCP Q_{noEDLM} mono+bi$ and $SCP Q_{noEDLM} bi$, respectively (Tab. 3.4). Furthermore, fitting procedures using SCP sets $SCP Q_{noEDLM} mono+bi$ and $SCP Q_{noEDLM} bi$ returned relatively large parameter CI s of $\log K_{Eu}$ s between 1.3 - 2.3 logK units (Tab. 3.4). Similar to DDLMs precipitation reactions occurred and overestimated Eu immobilization at $pH \geq 6.5$ ($SLR = 12.5 \text{ g L}^{-1}$, $Eu C_0 = 10^{-5} \text{ mol L}^{-1}$, Fig. 3.7). Due to the smaller amount of surface sites for $SLR = 12.5 \text{ g L}^{-1}$ in comparison to the larger SLR more Eu remained in solution and was therefore prone for precipitation reactions. However, before precipitation reactions abruptly increased Eu immobilization, model results levelled off at approx. 54% immobilized Eu for $SCP Q_{noEDLM} mono$ and $mono+bi$. This was due to saturation of surface sites and formation of $EuSiO(OH)_3^{2+}$ solution species (Fig. 3.7) which were not considered for surface complexation reactions in this study (Sec. 3.1).

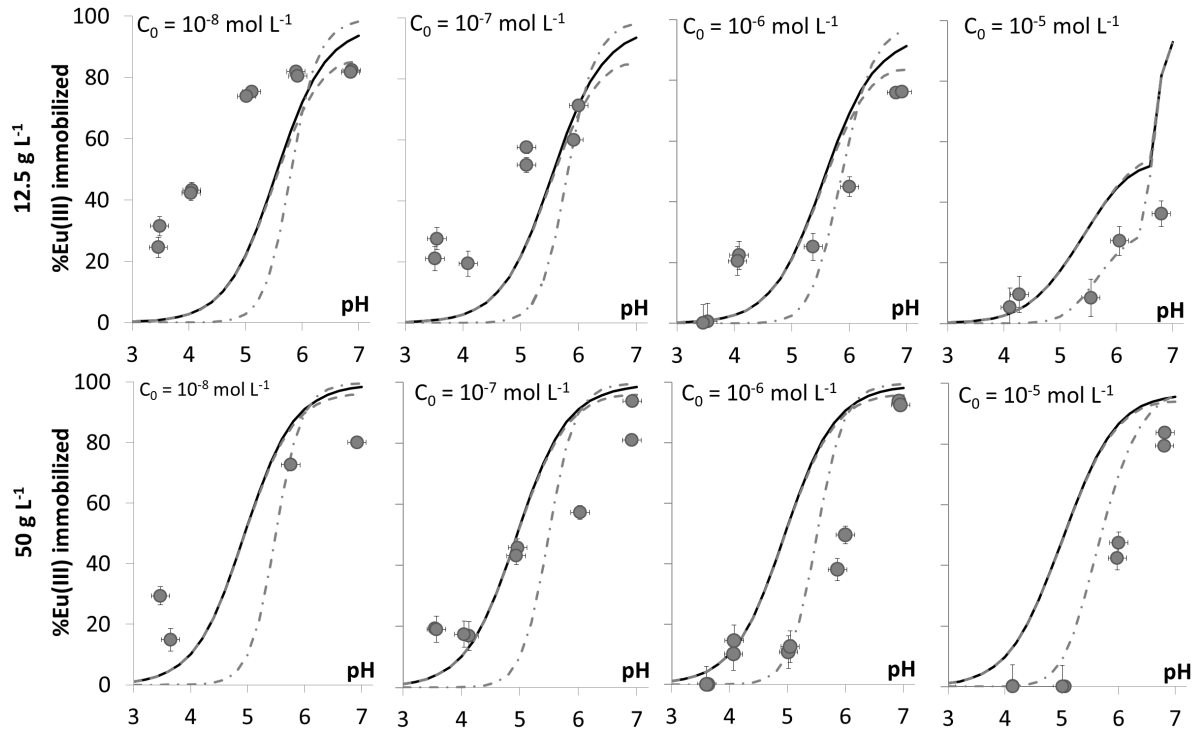


Fig. 3.7: Results of Eu batch experiments with quartz and fitted noEDLM results (10 mM $NaClO_4$ background electrolyte, laboratory conditions: pCO_2 $10^{-3.4}$ bar, $T = 296.0 \text{ K} \pm 2 \text{ K}$). Contribution of monodentate Eu surface complexes (dashed grey line), bidentate complex (dash-dotted grey line), mono- + bidentate surface complex (solid black line). See Table 3.4 for final SCPs.

Comparing fitted results of *SCP Q_{noEDLM mono}* and *SCP Q_{noEDLM mono+bi}* revealed similar findings (Tab. 3.4) since $\log K_{bi}$ turned out to be negligible for optimization procedures (Fig. 3.7). Consequently, a combination of mono- and bidentate surface complexes and hence increasing the number of adjustable parameters was not justified considering gof (Tab. 3.4) where similar *SEs* and *LSOF* values were returned for *SCP FS noEDLM mono* and *mono+bi*. Thus, *SCP Q_{noEDLM mono+bi}* was excluded from Eu reactive transport simulations (Sec. 4).

To conclude, considering gof of *SCP Q_{noEDLM mono}* revealed that a monodentate Eu surface complex reproduced Eu surface complexation on silica surfaces adequately which was in accordance with Wang and Anderko (2001) and Kitamura et al. (1999). Since *SCP Q_{noEDLM bi}* and *Q_{noEDLM mono+bi}* resulted in large parameter *CI*s, *LSOF* values, and *ME*s compared to *SCP Q_{noEDLM mono}*, only *SCP Q_{noEDLM mono}* was used for noEDLM reactive transport models.

1-pK BSM

For 1-pK BSMs monodentate, bidentate, a combination of mono- and bidentate surface complexes, as well as a hydrolyzed Eu surface species were used (Fig. 3.8). The *ME*s ranged between -2.2%Eu(III) immobilized and -1.0%Eu(III) immobilized, for *SCP Q II bi* and *SCP Q II H₂O_{mono}*, respectively. Precipitation of Eu carbonates became evident for $\text{pH} \geq 6.5$ for $\text{Eu } C_0 = 10^{-5} \text{ mol L}^{-1}$ as it had already been observed for DDLMs and noEDLMs. The BSM returned better fitting results compared to noEDLMs and partially also compared to DDLMs (cf. Tab. 3.4) which was indicated by smaller *SE*s, *ME*s, and *LSOF*s as well as smaller parameter *CI*s and *psds* (cf. Tab. 3.4). However, all optimized BSM $\log K_{Eu}$ s overestimated experimental data on average (negative *ME*s). Considering gof, it was not possible to clearly identify a BSM approach that fitted measurements best since only small differences in gof could be observed. For example: *SCP Q II bi* yielded *ME* = -1.0%Eu(III) immobilized which equalled the optimum of *ME* = 0 best; however, considering the *psd*, *SE*, and the *LSOF SPC Q II mono* resulted in slightly smaller values. Since two fitting parameters did not result in a significantly better fitting result of experimental data an increase of adjustable parameters was not justified compared to *SCP Q II mono* and *SCP Q II bi*. Furthermore, *SCP Q II mono+bi* resulted in a relatively large parameter *CI* of $\log K_{bi}$ in comparison to *SCP Q II mono* and *SCP Q II bi* (cf. Tab. 3.4). Therefore, only *SPC Q II mono* and *SPC Q II bi* were used for Eu transport models.

Not many SCMs of Eu on quartz or amorphous silica have been reported in literature

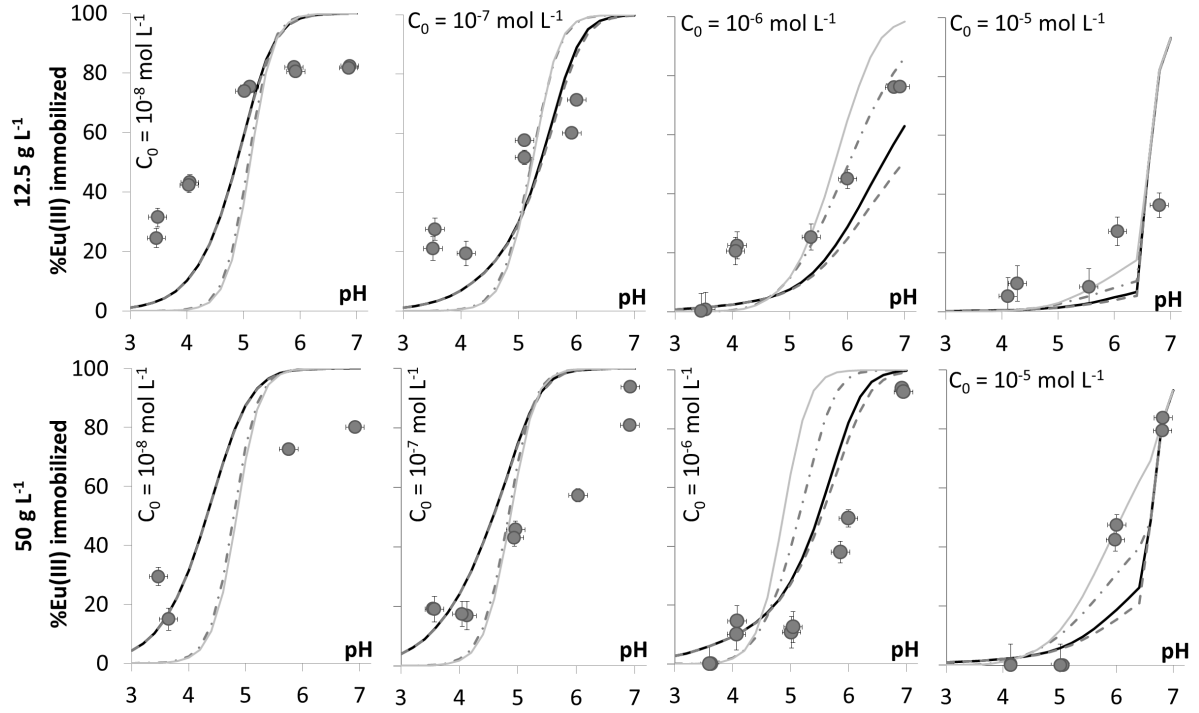


Fig. 3.8: Batch data of quartz with Eu and 1-pK BSM results using mono-, bi-, and mono- combined with bidentate surface complexes (10 mM NaClO₄ background electrolyte, laboratory conditions: ρCO_2 10^{-3.4} bar, T = 296.0 K \pm 2 K). C_0 – initial Eu concentration, solid circles – quartz Eu batch data. Contribution of monodentate Eu surface complex (dashed grey line), bidentate Eu surface complex (dash-dotted grey – line), mono- + bidentate surface complex (solid black line), hydrolyzed monodentate surface complex – solid grey line. See Table 3.4 for final SCPs.

that used similar model approaches and geochemical boundary conditions. Table 3.5 compares published data and final SCPs of the present study. Cited literature exclusively comprises studies that used monodentate Eu(III) and Am(III) surface species and excluded the influence of organic matter, ligands, or ternary surface complexes. For the DDLM $\log K_{Eu}$ agree well, for noEDLM approaches no comparable study was available. However, for the BSM a comparison of results was rather challenging since the BSM of Kitamura et al. (1999) used a substantially different capacity C_1 resulting in major differences of $\log K_{Eu}^{int}$ and $\log K_{Na+,ClO_4}^{int}$. Rearranging Equation 2.3 to Equation 3.41 illustrates the influence of C_1 :

$$\psi_0 - \psi_1 = \frac{\sigma_0}{C_1} \quad (3.41)$$

With Equation 3.41 it becomes obvious that a small C_1 results in large electrostatic potential differences ($\psi_0 - \psi_1$) between the 0-plane and the 1-plane. On the other hand, as the electrostatic potential difference increases at constant C_1 , σ_0 increases. Surface complexation reactions, protolysis reactions, and co-, counterions compensate for σ_0 . Hence, the smaller C_1 the larger $\psi_0 - \psi_1$, and the stronger surface complexation constants are necessary to achieve charge balance with respect to the bulk solution. This is evident by SCPs of Kosmulski (2009) in comparison to final SCPs of this study (Tab. 3.5).

Tab. 3.5: Comparison of quartz Eu SCPs from literature and final SCPs of this study. Ref. – literature reference, EM – electrostatic model, M^{3+} – trivalent metal cation, C_1 – capacitance of the layer between 0-plane and 1-plane, int – intrinsic constants, BSM – basic Stern model, noEDLM – non-electrostatic model, DDLM – diffuse double layer model, mono – monodentate surface complex, SSA – specific surface area, $\log K_{Na+}^{int}$ – counterion association coefficient, $\log K_{Eu}^{int}$ – Eu(III), Am(III) surface complexation constant, $\log K_{Si-OH}^{int}$ – surface protolysis constant.

ref.	EM	M^{3+}	denate	C_1 [F m ⁻²]	$\log K_{Si-OH}^{int}$ [4]	$\log K_{Na+}^{int}$	$\log K_{Eu}^{int}$
[1]		Eu		$5.3 \cdot 10^{-7}$	-6.57	1.84 ± 0.3 [5]	4.55 ± 0.08
[3]	BSM	Eu	mono	3.3	-7.5	-9.4 [6]	0.6 ± 0.3
[3]	noEDLM	Eu		-	-	-	0.0 ± 0.12
[2]		Am		-	-7.2	-	-0.23 ± 0.05
[3]	DDLM	Eu	mono	-	-8.0	-	0.0 ± 0.1

[1] Kitamura et al. (1999), Ar-atmosphere, 100 mM and 10 mM NaClO₄ background electrolyte, sorbent: quartz mineral, $2.6 \cdot 10^{-6}$ mol L⁻¹ and $2 \cdot 10^{-10}$ mol L⁻¹ Eu, pH 2.5 - 4, SSD 100 g L⁻¹, SSA 0.51 m² g⁻¹, SSD 5 sites nm⁻².

[2] Wang and Anderko (2001), ρCO_2 $10^{-3.4}$ bar, background electrolyte 0.005 M artificial groundwater, $2.1 \cdot 10^{-9}$ mol L⁻¹ Am(III), SLR 15.2 g L⁻¹, SSA 2.8 m² g⁻¹, SSD 2.31 sites nm⁻².

[3] this study, ρCO_2 $10^{-3.4}$ bar, 10 mM NaClO₄ background electrolyte, sorbent: quartz (G20 EAS extra), 10^{-5} - 10^{-8} mol L⁻¹ Eu, pH 3.5 -7, $SLRs$: 12.5 g L⁻¹, 50 g L⁻¹, SSA 0.08 m² g⁻¹, SSD 4.6 sites nm⁻².

[4] $S-OH = S-O^- + H^+$

[5] $S-O^- + Na^+ = S-ONa$

[6] $S-OH + Na^+ = S-ONa + H^+$

3.3.2 Orthoclase

Fitting results and batch measurements are illustrated as [%Eu(III) immobilized] for reasons of comparability to quartz and muscovite model results even though orthoclase $\log K_{Eu}$ optimization and model calibration used the Eu raw data set [$\mu\text{g L}^{-1}$] (cf. Sec. 3.2.2).

Measurements of orthoclase batch experiments are shown in Figure 3.9. Generally, results followed expectations: Immobilization of Eu [%] was positively correlated with

increasing pH and SLR . Smaller initial Eu concentrations (C_0) returned larger relative Eu uptake in comparison to high C_0 (e.g. Fig. 3.10, App. Fig. B.31). Unfortunately, during experimental set-up sorption affinities/immobilization rates of Eu were underestimated for the considered geochemical systems. Hence, much data described almost 100% Eu immobilization, only high Eu C_0 delivered a sorption edge as intended (App. Fig. B.31). In future, for this system smaller $SLRs$ should be used to receive a more comprehensive picture of sorption affinities of the trivalent lanthanide.

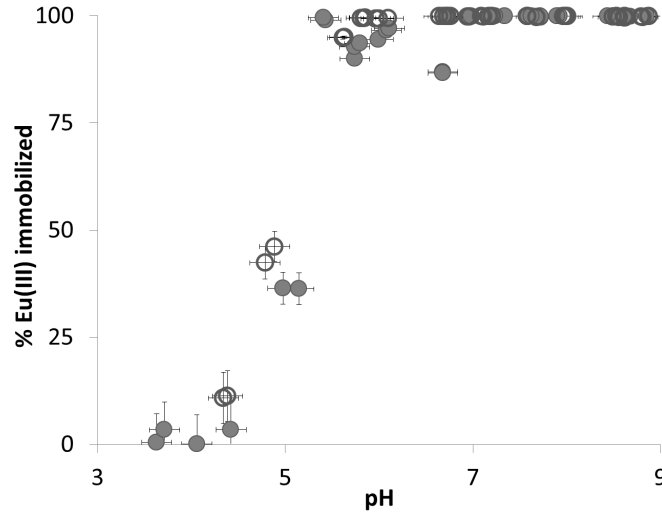


Fig. 3.9: Results of Eu batch experiments with orthoclase (10 mM NaClO_4 background electrolyte, laboratory conditions: $p\text{CO}_2$ $10^{-3.4}$ bar, $T = 296.0 \text{ K} \pm 2 \text{ K}$). Data comprise two $SLRs$ (12.5 g L^{-1} (solid circles)) and 50 g L^{-1} (open circles)), four Eu C_0 with $10^{-5} - 10^{-8} \text{ mol L}^{-1}$ as a function of pH (cf. also App. Fig. B.31).

1-pK DDLM, noEDLM

Figure 3.10 shows noEDLM results (black) and DDLM results with $\Delta\sigma = 0.03 \text{ C m}^{-2}$ ($SCP \text{ FS I}$), $\Delta\sigma = 0.047 \text{ C m}^{-2}$ ($SCP \text{ FS II}$), and $\Delta\sigma = 0.3 \text{ C m}^{-2}$ ($SCP \text{ FS III}$) (cf. Sec. 2.4.2). Both inverse mechanistic modelling approaches (DDLM, noEDLM) generally described measurements adequately with similar gof (cf. Tab. 3.4): Parameter CI s and $psds$ indicated accurately fitted $SCPs$; SE s ranged between $44 - 70 \mu\text{g L}^{-1}$ and ME s were closely distributed around the optimum value of $ME = 0 \mu\text{g L}^{-1}$ for all DDLMs and nonEDLMs (ME s = $-8.2 - 8.9 \mu\text{g L}^{-1}$, cf. Tab. 3.4). Since only few data points described Eu sorption edges most fits returned similar results (overlapping model results in Fig. 3.10) with the exception of $SCP \text{ FS}_{noEDLMmono}$. The model approach $SCP \text{ FS}_{noEDLM mono}$ underestimated relative Eu uptake [%] (Fig. 3.10) which was due to Eu solution speciation reactions: At $\text{pH} \geq 7.0$ only 34% Eu^{3+} aquo ions existed, the

remaining Eu formed EuCO_3^+ (30%), $\text{EuSiO}(\text{OH})_3^{2+}$ (21%), $\text{Eu}(\text{OH})_2^+$ (9%), and EuOH^{+2} (5%) solution complexes (Fig. 3.1 C). Since no spectroscopic evidence exists of ternary carbonato- or hydroxo-complexes on feldspar surfaces only Eu^{3+} was considered for surface complexation reactions. Hence, relative Eu uptake decreased at $\text{pH} \geq 7.0$ and precipitation occurred. At $\text{pH} \geq 7.5$ and $SLR = 12.5 \text{ g L}^{-1}$ Eu precipitation reactions became evident and instantly immobilized increasing amounts of aqueous Eu-carbonate and Eu-hydroxo complexes (Fig. 3.10). Considering the $SLR = 50 \text{ g L}^{-1}$ this effect was less pronounced since more Eu^{3+} was sorbed by surface complexation, hence, less Eu^{3+} remained in solution to undergo solution speciation reactions. Figures B.33 and B.32 in the appendix show fits of the DDLM and noEDLM individually.

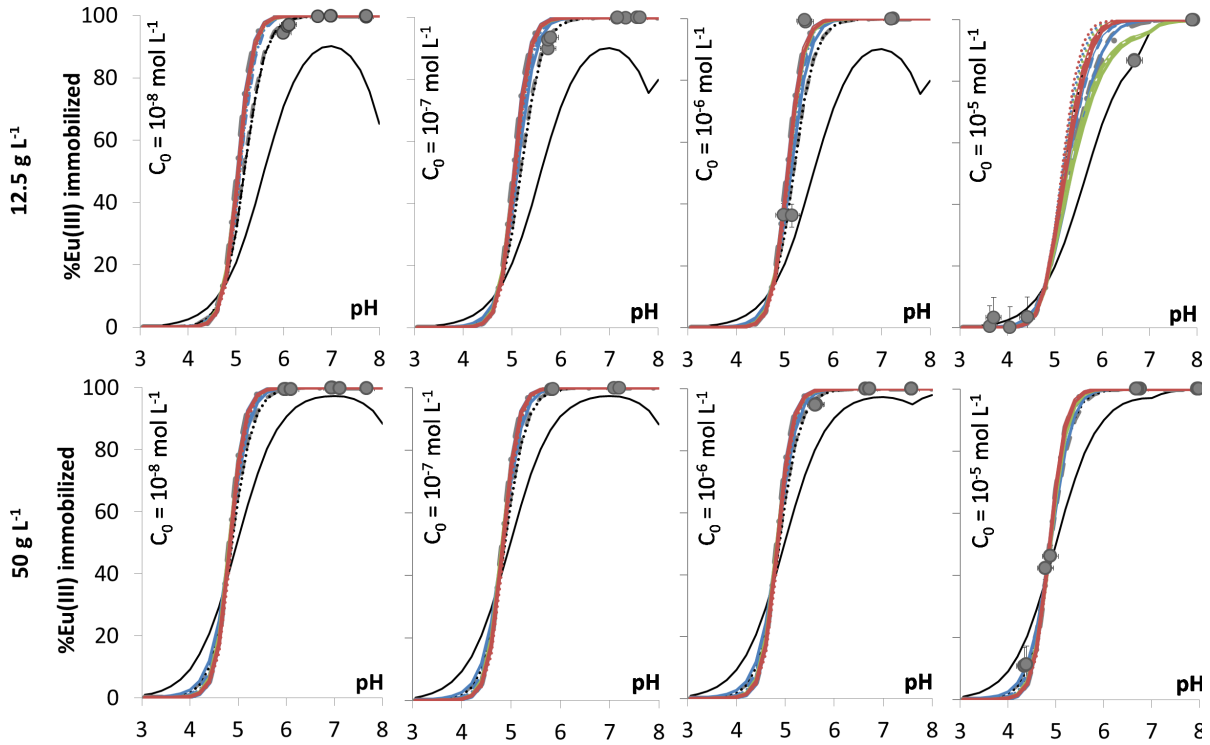


Fig. 3.10: DDLM and noEDLM results of orthoclase Eu batch data. Red – $\Delta\sigma = 0.03 \text{ C m}^{-2}$ (DDLM, *SCP FS I*), green – $\Delta\sigma = 0.047 \text{ C m}^{-2}$ (DDLM, *SCP FS II*), blue – $\Delta\sigma = 0.3 \text{ C m}^{-2}$ (DDLM, *SCP FS III*), black – noEDLM, solid line – monodentate Eu surface complex, dashed line – bidentate, dash-dotted line – tridentate surface complex, double solid line – tetradentate, dotted line – hydrolyzed monodentate surface complex, C_0 – initial Eu concentration. Model results partially coincide, hence, lines overlap. For final SCP sets cf. Table 3.4.

To conclude, experimental data was adequately represented by DDLM and noEDLM SCP sets which was indicated by gof of fitting approaches (Tab. 3.4). No explicit pre-

ference between Eu surface complexation reactions or even EM or noEDLM could be identified with gof; however, it was evident that *SCP FS_{noEDLM} mono* overestimated Eu batch raw data [$\mu\text{g L}^{-1}$] in comparison to all remaining model approaches that underestimated batch data [$\mu\text{g L}^{-1}$] (cf. Tab. 2.4). Nevertheless, gof and *psds* ranged within the same order of magnitudes for the noEDLMs compared to DDLMs and BSMs. Hence, all final DDLM and noEDLM SCP sets were used for Eu transport simulations (Sec. 4) to specify a SCM that represented transport data and therefore batch data best.

1-pK BSM

Results of fitting approaches using the BSM are illustrated in Figure 3.11 where major differences could be observed. Results reflected the influence of strong co- and counterion association coefficients $\log K_{\text{Na}^+/\text{ClO}_4^-}$ (*SCP FS V*, *SCP FS VI*, *SCP FS VII*): SCMs *SCP FS V mono - tetra* and *SCP FS VI mono - tetra* (Tab. 3.4) used $\log K_{\text{Na}^+/\text{ClO}_4^-} = 1.5$ determined from surface charge models (Tab. 2.4). Due to the high $\log K_{\text{Na}^+}$ Na^+ posed competition on Eu surface complexation reactions (Sec. 2.5.2) which resulted in less Eu^{3+} that sorbed to the orthoclase surface. Consequently, at elevated pH, remaining Eu^{3+} aquo ions formed Eu-carbonato and -hydroxo solution species (Fig. 3.1). As for the DDLM and noEDLM, no ternary surface complexes were considered, and precipitation reactions of Eu-carbonato and -hydroxo phases occurred ($\text{pH} \geq 7.0$). This effect was again more pronounced for smaller *SLRs* [g L^{-1}]. For *SCP FS VII mono - tetra* (Tab. 3.4) $\log K_{\text{Na}^+/\text{ClO}_4^-} = 0.67$ which resulted in less pronounced competition between Eu^{3+} and Na^+ for sorption sites. This was evidenced by larger relative Eu uptake with increasing pH.

Overall, BSM results supported the assumption that multidentate surface complexes or hydrolyzed Eu species accounted for Eu surface complexation which agrees with modeling studies of e.g. Fernandes et al. (2016), Polly et al. (2013), and Stumpf et al. (2006). Based on this finding tri-, tetradenate, and the hydrolyzed monodentate surface species were considered in Eu transport studies.

Comparison of 1-pK BSM, DDLM, noEDLM

So far, no clear preference could be identified considering $\Delta\sigma$ values: Data was fitted equally well with both electrostatic models (EMs) and results did not allow to prefer one $\Delta\sigma$ over another or even to exclude potentially unrealistic $\Delta\sigma$ values.

Comparing EMs with noEDLMs showed that the exclusion of surface protolysis reactions had only minor effects on model outcome. This finding supports the assumption that even though more sophisticated SCMs that consider the electrostatic influence might

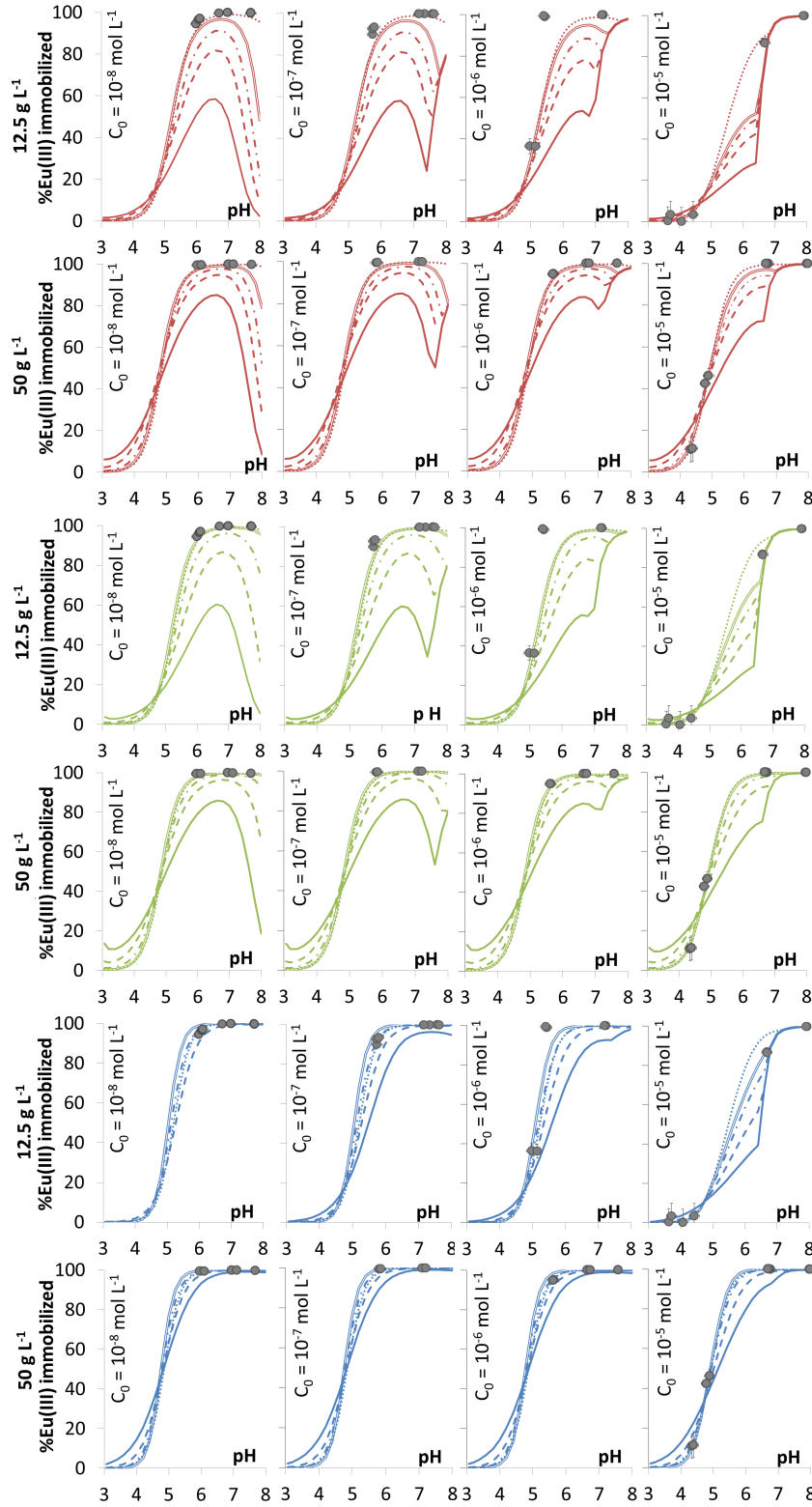


Fig. 3.11: BSM results of orthoclase Eu batch experiments: $\Delta\sigma = 0.03 \text{ C m}^{-2}$ (*SCP FS V*), $\Delta\sigma = 0.047 \text{ C m}^{-2}$ (*SCP FS VI*), $\Delta\sigma = 0.3 \text{ C m}^{-2}$ (*SCP FS VII*), solid line – monodentate, dashed line – bidentate, dash-dotted line – tridentate, double solid line – tetradentate, dotted line – hydrolyzed monodentate Eu surface complex, C_0 – initial Eu concentration. Model results partially coincide, hence, lines overlap. For final SCPs cf. Table 3.4.

represent solid-solution interfaces more realistically; simple, straight forward noEDLMs also reproduce experimental data of complex systems sufficiently. However, the development of process understanding can only be gained by state-of-the-art mechanistic SCMs that describe surface reactions according to the present scientific understanding.

Even though a vast amount of batch experimental data had been collected, only few data points described the sorption edge of Eu on orthoclase leaving no clear indication from SCMs for a favourable Eu surface complex: Considering gof of DDLM and noEDLM no preference of a surface complex or SCM could be identified (Tab. 3.4); BSM fits indicated better agreement with experimental data when hydrolyzed or multidentate surface species were considered providing a first hint of potentially realistic surface complexation reactions.

The application of SCPs to predict a similar geochemical problem is a means to verify estimated SCP sets. Therefore, final orthoclase DDLM SCPs from surface charge models were used in a master thesis (Steinbrecher, 2017) to predict surface protolysis reactions and to estimate Cs^+ surface complexation constants for orthoclase. Respective batch experiments comprised three *SLRs*, four initial Cs^+ concentrations ($C_0 = 10^{-8} - 10^{-5} \text{ mol L}^{-1}$), and five pH_{ini} . The experimental set-up equalled batch experiments of the present study. Sorption experiments were evaluated with the DDLM (PHREEQC, UCODE) where surface charge was described with *SCP FS I - III* from the present study; SCMs used monodentate Cs^+ surface complexes. Inverse modeling results suggested that *SCP FS II* represented Cs^+ surface complexation processes adequately; fitting results using *SCP FS I* and *SCP FS III* did not represent Cs^+ batch data as close to measurements as *SCP FS II* according to Steinbrecher (2017). Such a clear conclusion could not be drawn from inverse modeling of surface charge or Eu batch experimental data and offered first indications for a preferred final SCP set to describe orthoclase surface charge development (*SCP FS II*, Tab. 2.4). In the next step, Eu reactive transport models were used to provide further information whether findings of Steinbrecher (2017) could be substantiated (Sec. 4.4.2). To the authors best knowledge, no literature is available dealing with the determination of $\log K_{Eu}$ or chemical homologues on orthoclase or similar mineral surfaces making further verifications of final SCPs challenging.

3.3.3 Exclusion of muscovite from further modeling studies

Figure 3.12 shows muscovite batch data in comparison to quartz and orthoclase measurements. Muscovite batch experiments were performed under identical conditions as for quartz and orthoclase. Due to the high adsorption capacity of muscovite only the experiments with the low *SLR* and high Eu concentrations yielded sorption edges. The

higher SLR and low Eu concentrations resulted in 100% Eu immobilization. Sorption edges were substantiated for:

- $SLR = 12.5 \text{ g L}^{-1}$, $C_0 = 10^{-6} \text{ mol L}^{-1}$
- $SLR = 12.5 \text{ g L}^{-1}$, $C_0 = 10^{-5} \text{ mol L}^{-1}$
- $SLR = 50 \text{ g L}^{-1}$, $C_0 = 10^{-5} \text{ mol L}^{-1}$

These experimental results are shown in Fig. 3.12 and evidently corroborate the findings of quartz and orthoclase experiments: Quartz returned lowest, and muscovite yielded highest relative Eu immobilization rates (Fig. 3.12). As expected, Eu immobilization [%] was positively correlated with rising pH and $SLRs$. Lowest Eu uptake equalled 24%Eu(III) immobilized at pH 3.2 for muscovite; smaller values were not collected. That the lowest measured Eu uptake equalled approx. one forth of C_0 even at low pH was attributed to cation exchange processes which agreed well with findings from Pan et al. (2017). However, for future experiments smaller $SLRs$ and/or smaller Eu C_0 are recommended to collect more data in the range of the sorption edge; geochemical boundary conditions should consider different sorption capacities of quartz, muscovite, and orthoclase.

For muscovite a noEDLM, the BSM, and the DDLM were used for $\log K_{Eu}$ estimations. In SCMs, SCPs from surface charge models (*SCP M II, IV, V and VI - VIII*, Tab. 2.4) were utilized as fix parameter values as for orthoclase and quartz SCMs. The 1-pK as well as the 2-pK approach were used. Exchange processes of Na^+ , K^+ , H^+ , and Eu were considered by means of half reactions; conditional cation exchange selectivity coefficients of Poinssot et al. (1999) and Bradbury et al. (2005) were used (Sec. 2.5.2). Following literature studies (Tertre et al. (2006), Lee et al. (2013), Kumar et al. (2013), Fernandes et al. (2016)), different Eu surface complexes were included:

- monodentate,
- bidentate,
- tridentate,
- tetradentate,
- hydrolyzed mono-,
- hydrolyzed bidentate,
- combination of monodentate and hydrolyzed monodentate surface complexes.

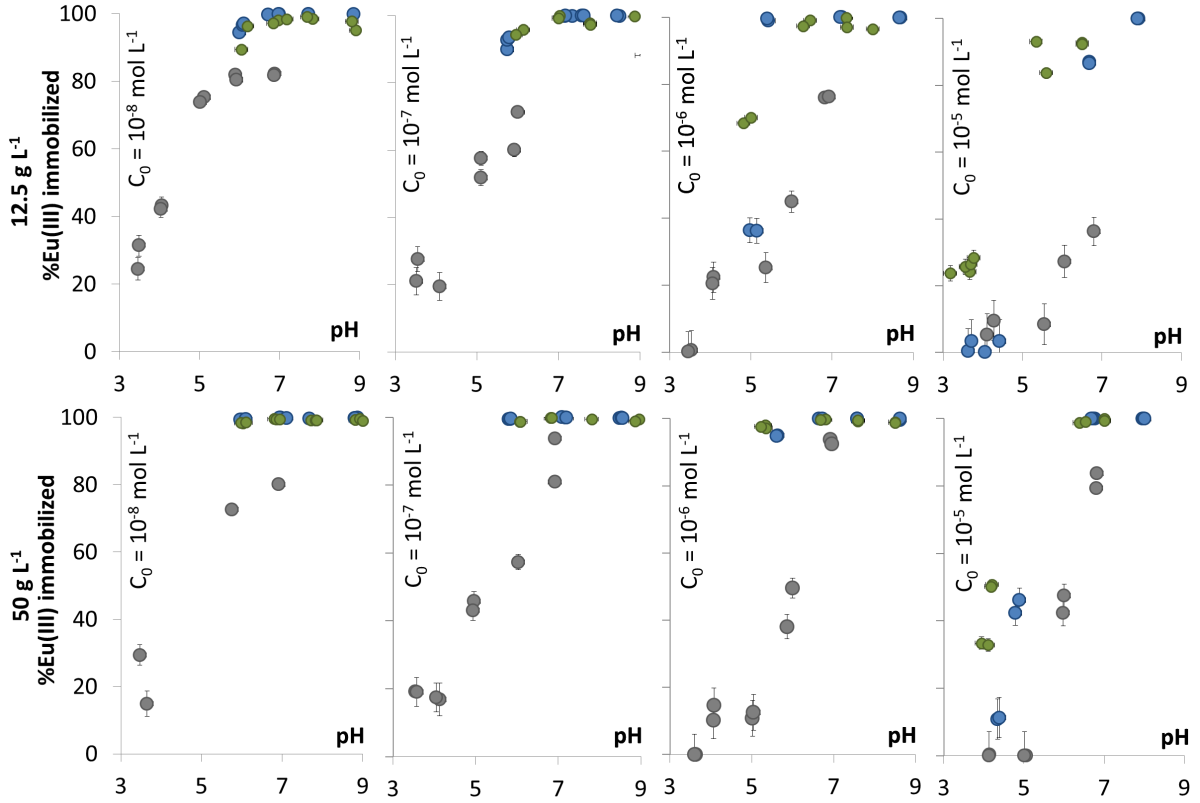


Fig. 3.12: Results of Eu batch experiments with orthoclase (blue), quartz (grey), and muscovite (green) (10 mM NaClO₄ background electrolyte, laboratory conditions: ρCO_2 $10^{-3.4}$ bar, $T = 296.0 \text{ K} \pm 2 \text{ K}$). C_0 – initial Eu concentration.

However, none of the EMs or nonEDLMs yielded valid model results: All optimizations resulted in convergence problems of PHREEQC. No $\log K_{Eu}$ could be determined for the muscovite surface. Non-convergence was based on the application of $\log K_c\text{Na}/\text{H}$, $\log K_c\text{Na}/\text{K}$ from Poinssot et al. (1999) and $\log K_c\text{Na}/\text{Eu}$ from Bradbury et al. (2005) (with $\log K_c\text{Na}/\text{Na} = 0$) which caused mass law equations to not converge during optimization procedures. Hence, mass balances of all relevant elements failed. This finding showed that $\log K_c$ s did not represent the considered geochemical system correctly since $\log K_c$ s are highly system-dependent and cannot be easily transferred from literature. The selectivity of cations towards mineral surfaces is apart from lattice characteristics and geochemical surrounding also dependent on H_{hyd} of the index and exchanging cations (Sec. 3.1.2). Generally speaking, $\log K_c\text{Na}/\text{Eu}$ seemed to be too large by orders of magnitudes to be adequate for muscovite Eu SCMs. Furthermore, the exchange site capacity was determined using CEC_{WG} (Eq. 3.40). As discussed in Section 2.3.1 CEC_{WG} was an approximation and might also be afflicted with errors.

To identify whether non-convergence was truly based on erroneous $\log K_c$ s, cation exchange reactions were excluded from EM and noEDLMs for testing purposes: As a result all SCMs without exchange processes converged for all postulated Eu surface complexation reactions. However, as expected optimized $\log K_{Eu}$ highly underestimated Eu uptake [%Eu(III) immobilized] at low pH (data not shown here). Under the aspect that muscovite is a typical cation exchanger SCMs without cation exchange were not further considered even though models converged. In future, $\log K_c$ s for muscovite have to be determined to correctly evaluate batch data. This finding supports the following statement (Parkhurst and Appelo, 1999): "...ion-exchange modeling requires data on material from the study site for appropriate model application." which also agrees well with findings from Voegelin et al. (2000) who postulated that the reliable definition of the CEC at relevant geochemical conditions is a "... key prerequisite for accurate transport modeling."

In the absence of $\log K_{Eu}$ and adequate $\log K_c$ s for muscovite, reactive transport models could not be developed based on the present study and simulation of Eu transport in muscovite environments must be postponed to future research projects.

3.4 Summary

Sorption of Eu on muscovite, orthoclase, and quartz was investigated with batch experiments. Experimental data was evaluated via mechanistic SCMs. The scope was to define $\log K_{Eu}$ and to identify preferential SCPs from surface charge models (Sec. 2, Tab. 2.4).

Batch experiments comprised two *SLRs*, four initial Eu concentrations C_0 , and four pH_{ini} . Experiments were carried out in doublet (quartz) and triplet (muscovite, orthoclase). Element analysis of Eu was achieved via ICP MS measurements; data was used for SCM calibration to retrieve $\log K_{Eu}$ via inverse modeling. Therefore, PHREEQC SCMs (noEDLM, BSM, DDLM) were developed and UCODE was applied as an universal parameter estimation code. Final SCPs are summarized in Table 3.4.

Quartz batch data covered pH 3 - 7; Eu sorption edges were adequately represented. The application of a bidentate (*SCP Q I bi*) and a combination of a mono- and bidentate surface complex (*SCP Q I mono+bi*) for SCM calibration represented experimental data satisfactorily for the DDLM which was evidenced by gof of model approaches (Tab. 3.4); for the noEDLM a monodentate Eu surface complex (*SCP Q_{noEDLM} mono*) yielded adequate fitting results (cf. gof in Tab. 3.4). The model approaches *SCP Q II mono* and *bi* returned fits as close to measurements as possible for the BSM (cf. gof in Tab. 3.4). A

comparison of gof between EMs and noEDLMs revealed that EMs fitted experimental data more realistic whereas the optimized $\log K_{mono}$ of *SCP Q I* could be substantiated with literature data. Unfortunately, for the noEDLM no comparable models have been published so far; similar to the BSM approach where $\log K_{Eu}$ of BSMs were available but a comparison was rather challenging due to highly different values of C_1 (Sec. 3.3.1, Tab. 3.5). However, mono- as well as bidentate surface complexes have been evidenced via TRLFS measurements or modeling studies for Eu or chemical homologues on silica surfaces which substantiates the chosen model approaches of the present work at the current state of knowledge (e.g. Stumpf et al. (2008), Kumar et al. (2012)).

Interestingly, experimental batch data of quartz were best reproduced considering a theoretical exchange site at the silica surface. This approach suspected minor surface impurities to act as potential cation exchangers as had already been assumed by Lützenkirchen (1996). These unexpected results highlight the need for more research to uncover the last unknowns of even presumingly well studied mineral-water interfaces.

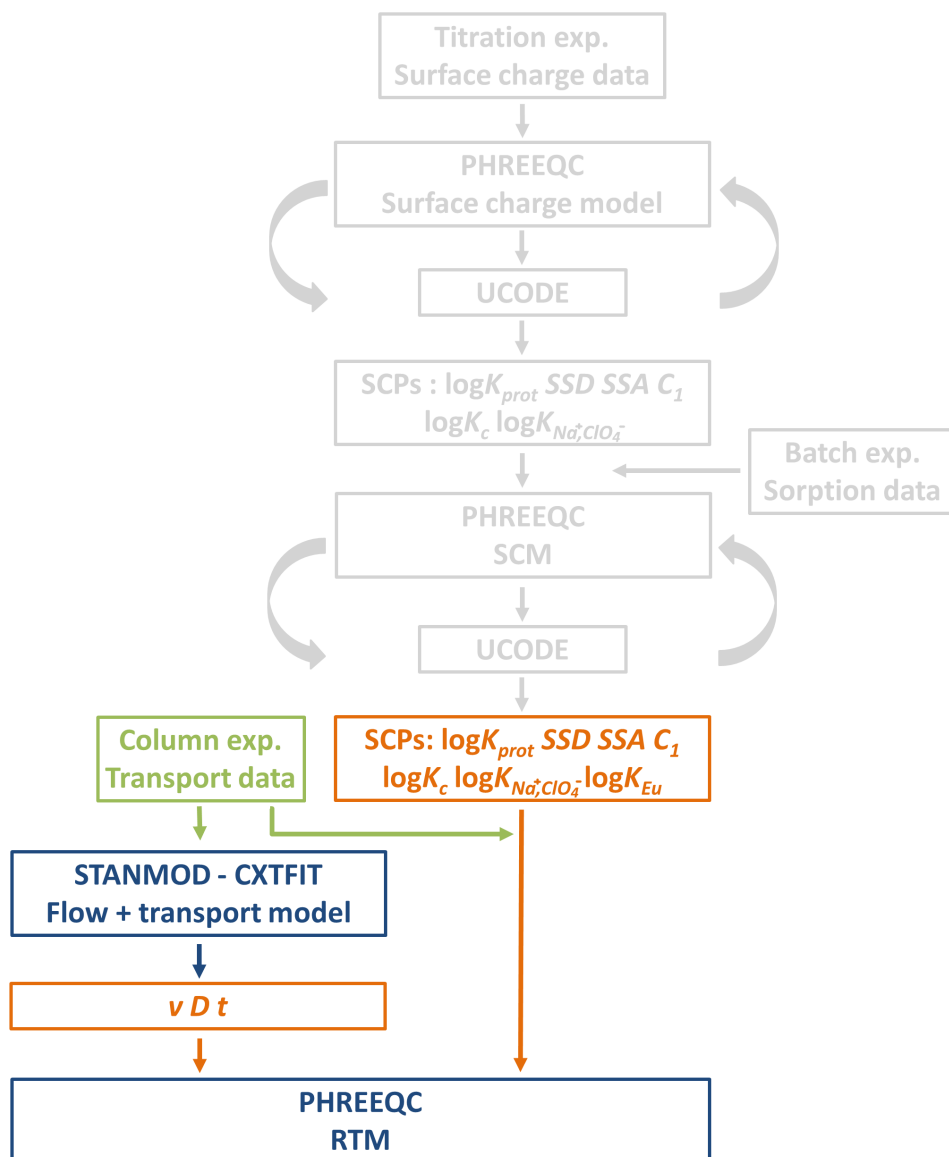
Orthoclase batch experiments were performed analogue to quartz and covered pH 3 - 9; however, due to much data that described 100% Eu immobilization sorption edges were more indeterminate than for quartz and could be only be substantiated for low *SLRs* and high Eu C_0 , respectively. The DDLM, BSM, and noEDLM were used to optimize orthoclase $\log K_{Eu}$. All SCMs fitted experimental data equally well (Tab. 3.4); hence, no preference of a certain EM, a $\log K_{Eu}$, or $\Delta\sigma$ value could be identified.

Muscovite batch experiments also covered pH 3 - 9 and followed a similar experimental set-up compared to orthoclase and quartz. Analogue to orthoclase, most batch data described 100%Eu(III) immobilized and only high Eu C_0 returned sorption edges which were were situated between pH 3.5 - 7. Smallest Eu uptake equalled 24%Eu(III) immobilized at pH 3.2 which was attributed to cation exchange processes. Neither the application of the DDLM, nor the BSM, or noEDLM converged since mass balances of all relevant elements failed. All SCMs showed major convergence problems of PHREEQC due to the implementation of cation exchange processes. Cation exchange processes could not be described realistically with $\log K_c$ s from literature. As a consequence, $\log K_{Eu}$ could not be derived for the muscovite mineral. Future research studies have to predominantly focus on the assessment and determination of muscovite $\log K_c$ for the considered system to be able to realistically include cation exchange processes in mechanistic SCMs.

Generally, it should be pointed out that to reach the full potential of mechanistic SCMs sound data and solid supplementary information is necessary: For example, only few published data of Eu surface speciation on quartz, orthoclase, and muscovite was

available (Sec. 3.1); hence, suggested surface complexation reactions and SCPs of this study were derived via optimization procedures and no assessment other than the chemical plausibility and gof was possible. The determination of SCPs from batch experiments is commonly accepted and their assessment with gof is a straight forward means to evaluate sorption data (e.g. Kitamura et al. (1999), Bouby et al. (2010b), Bradbury and Baeyens (2005b)). However, ideally, spectroscopic measurements should accompany surface complexation studies (e.g. Pan et al. (2017), Kar et al. (2011), Tertre et al. (2006), Rabung et al. (2005)).

Europium transport: Experiments and simulation



4.1 Introduction

So far, the present study focused on the determination of Eu surface complexation parameters (SCPs) with surface charge models (Sec. 2) and surface complexation models (SCMs) (Sec. 3) that were calibrated with experimental titration and batch data, respectively. The SCPs determined in the previous sections (Tab. 3.4) are prerequisites for reactive transport models (RTMs) which are the main focus of this section. In the present study, RTMs simulate Eu transport processes based on mechanistic surface charge models and SCMs under consideration of inner and outer sphere surface complexation as well as aqueous speciation calculations (PHREEQC, Version 3.1.2-8538). Hence, each SCM that yielded reasonable fitting results of batch experiments (Sec. 3.3) formed the basis for respective RTMs. Therefore, SCPs from Table 3.4 were used to predict the reactive transport of Eu through porous, homogeneous orthoclase and quartz columns. Since it was not possible to adequately describe the cation exchange for muscovite under the given geochemical conditions (Sec. 3.3.3), RTMs could only be developed for mineral systems without the influence of cation exchange processes. The simulation and assessment of Eu migration through muscovite columns has to be subject to upcoming research projects.

The generalized composite (GC) and the component additivity (CA) approach are the two common approaches to predict sorption processes of metal cations with mechanistic models. For the CA approach, surface complexation constants may be derived from batch or column experiments, and/or e.g. spectroscopic measurements for all individual mineral phases. In this study, Eu surface complexation constants ($\log K_{EuS}$) were derived from batch experiments and subsequently used to predict Eu transport through mineral-filled columns. Numerous studies have dealt with the estimation of SCPs from e.g. batch experiments (cf. RES³T, www.hzdr.de/res3t, Brendler et al. (2003)) of which some included the examination of the surface charge development of quartz, orthoclase, or muscovite surfaces in detail (e.g. Hiemstra et al. (1989a), Arnold et al. (1999), Maslova et al. (2004), cf. Sec. 2); however, only few focussed on surface complexation of trivalent lanthanides or actinides on these surfaces (e.g. Wang and Anderko (2001), Stumpf et al. (2006), Pan et al. (2017), cf. Sec. 3); and even less studies have drawn conclusions between SCPs derived from titration as well as Eu batch experiments and the performance of RTMs. Regardless whether mechanistic (surface charge model, SCM, RTM) or empirical approaches (linear distribution coefficient K_d , retardation factor R_f) are considered SCPs or K_d values derived from titration and/or batch experiments sometimes do not represent retardation during transport processes adequately. Discrepancies between

surface complexation constants and K_d values of batch and column experiments have been tried to be explained with the following arguments (Hanna et al. (2014), Hanna et al. (2010), Curtis et al. (2001), Porro et al. (2000), Maraqa et al. (1998))

- Desorbed antecedent species might be transported out of a column system during transport experiments while in batch experiments these species remain in solution and continue to compete for sorption sites affecting exchange and sorption equilibria in the systems.
- Substantially different solid-liquid ratios (*SLRs*) may cause differences in batch and column experiment K_d values which is referred to as the "solids effect" in literature.
- It is also discussed that batch experiments reflect true equilibrium conditions while column experiments might not be in local equilibrium but influenced by kinetics of sorption or desorption processes during transport processes.
- The loss of particles, variations in flow rates, and the presence of immobile water during column experiments are also assumed to influence sorption coefficients and surface complexation constants determined with transport experiments.
- Mixing differences and differences in solid-particle spacing have also been reported to explain the discrepancy in sorption coefficients between both methods.
- The organic content of a sample has likewise been discussed to influence local equilibrium conditions: With increasing organic matter an increase of sorption nonequilibrium during transport experiments has been observed.

However, the true reason or the actual mechanism causing the differences have not yet been resolved (e.g. Porro et al. (2000)). To further complicate matters, K_d values do not reflect a uniform sorption tendency with respect to the experimental set-up, meaning that sorption coefficients have been reported to be stronger, weaker, and sometimes equal between batch and column experiments (e.g. Hanna et al. (2014)).

To illustrate the ongoing discussion dealing with the difference between K_d values and surface complexation constants from batch and transport experiments a brief overview of some relevant literature is provided in the following: Curtis et al. (2001) and Kohler et al. (1996) studied U(VI) transport through porous, homogeneous quartz columns under variable geochemical conditions and evaluated the applicability of SCMs calibrated with experimental batch data to predict column experiments. Non-electrostatic models (noEDLMs) were developed from batch experimental data; RTMs were derived to predict U(VI) transport. They used different surface complexes to describe U(VI) surface complexation under the given geochemical conditions and came to the conclusion

that RTMs with SCPs from batch experiments predicted transport data reasonably well. Observed differences were attributed to the fact that column experiments were conducted with pH conditions at the lower pH range of batch experiments. Rusch et al. (2010) investigated retardation processes of salicylate on quartz and goethite surfaces and also reported good agreement between reactive transport simulations and measurements applying surface complexation constants determined with SCMs from batch experimental data. Similar, Hanna et al. (2009) concluded that SCMs can be useful to predict heavy metal leaching from roadside soil.

In contrast, Hanna et al. (2010) found that the transport of gentisic acid through hematite-coated sand could not be predicted under dynamic conditions with parameters obtained from batch experiments considering mechanistic as well as empirical approaches. Hanna et al. (2014) studied the sorption of phthalic acid on goethite surfaces with flow-through experiments; a mechanistic approach (three plane model) was used to first derive surface complexation constants from batch experiments which were then applied to predict transport processes of phthalic acid. Results showed that the breakthrough curve at pH 6 could not be reproduced in detail with the RTM (breakthrough at pH 3 could be adequately simulated). Porro et al. (2000) (i) and Maraqa et al. (1998) (ii) chose empirical approaches to

- (i) determine Sr^{2+} K_d values from batch and column experiments with crushed basalt and
- (ii) to investigate retardation coefficients of benzene and dimethylphthalate in different soils (Oakville sand and Pipestone sand) with batch and column experiments.

Both studies proposed different K_d values for each experimental set-up.

To the authors knowledge, only very few studies (e.g. Bruggeman et al. (2010)) have fitted Eu SCPs from batch experiments to subsequently use these parameters in RTMs describing Eu retention on natural minerals or sediments under close to nature conditions. No study has yet tried to use one set of SCPs from batch experiments to simulate reactive transport under varying geochemical conditions. The advantage of one SCP set for a range of geochemical conditions in contrast to a set for each environment is the reduction of the amount of SCP sets necessary to predict transport processes of relevant radionuclides such as Am or Cm but also other potentially hazardous pollutants under varying geochemical conditions.

The considered mineral phases orthoclase, quartz, and muscovite of the present study (Sec. 2.3) are ubiquitously present in the Northern Plain of Germany and have

therefore been of great interest for long-term safety analysis of potential radioactive waste repositories ever since. Since 1979 the Gorleben site in Northern Germany was considered a potential final waste disposal site; hence, extensive geological, geochemical, hydrogeological, hydrological, and geotechnical studies and explorations had been conducted compiling vast amounts of data (e.g. Klinge et al. (2002), Fischer-Appelt et al. (2013)). For this study hydrogeological, geological, and geochemical information of the Gorleben site were used to design boundary conditions of column experiments in order to investigate Eu transport under close to nature conditions. Therefore, column experiments were carried out under steady-state and saturated flow conditions with natural, pure mineral phases (Sec. 2.3) and a synthetic sediment with a simplified mineral distribution as found at the Gorleben site (80 wt% quartz, 10 wt% muscovite, 10 wt% orthoclase; Klinge et al. (2002) and Noseck et al. (2012)).

The objectives of this section are (1) to conduct column experiments and to collect Eu transport data under varying artificial and close to nature geochemical conditions for saturated flow conditions, (2) to develop RTMs based on surface charge models and Eu SCMs (Sec. 2, Sec. 3), (4) to predict Eu transport under varying geochemical conditions with one set of SCPs, (5) and to verify the applicability of SCPs determined from batch and titration experiments (Tab. 3.4) to Eu RTMs.

4.2 Material and methods

Column experiments were carried out with pure muscovite, orthoclase, and quartz mineral phases as introduced in Section 2.3. Additionally a synthetic sediment composed of 10 wt% muscovite, 10 wt% orthoclase, 80 wt% quartz was used. The mineral distribution of the synthetic sediment was based on Noseck et al. (2012) and represented a simplified composition of the sediment found at the Gorleben site in Northern Germany. Grain sizes and SSA_{BET} of mineral samples are reported in Table 2.2.4. In the following section, the experimental set-up of column experiments and reactive transport models are described in detail. Appendices A.12 and B.4 supply further information on equipment, techniques, chemicals, and supplementary data, respectively; Appendix A.12.1 provides information on preconditioning of mineral samples for column experiments.

4.2.1 Experimental set-up of column experiments

A total amount of 26 column experiments were conducted during this study (Tab. 4.1), hence, easy handling of columns and experimental set-up was of decisive interest. A new column design was developed (Fig. 4.1, cf. App. Fig. B.35) where all components could

be easily screwed together. Great attention was paid to recovery rates: Columns, column tubing, and tube connectors were composed of perfluoroalkoxy alkane polymers (PFA); pump tubing was composed of Fluran[®]; frits were made of sintered polytetrafluoroethylene (PTFE) with a mean pore diameter of 10 μm . Sealing rings framed each frit and were also composed of PTFE (Fig. 4.1, App. Fig. B.35). The materials PFA and PTFE are highly resistant to almost all chemicals with only some exceptions (Sächting, 1995) and were therefore used to prevent potential Eu sorption on containing walls.

Columns were homogeneously dry-packed with preconditioned muscovite or orthoclase (Sec. A.12.1), or quartz samples. Homogeneity was reached with a stepwise packing procedure: Within five steps equal amounts of solid were tightly compacted in each column (122.5 mm in length, 41 mm in diameter) to ensure uniform bulk densities and homogeneous hydrodynamic properties. After packing, columns were filled with degassed background electrolyte under vacuum conditions. Vacuum conditions reduced the possibility of air intrusions in the columns during flooding and prevented the formation of preferential flow paths.

Geochemical equilibrium with background electrolytes (NaClO_4 , Na_2SO_4 , and/or an artificial groundwater; Tab. 4.1, cf. App. Tab. A.1) was achieved during the first days to weeks of the column experiment before the pulse solution was added. An equilibrated column system was characterized by $\text{pH}_{\text{equil}} \approx \text{pH}_{\text{ini}}$ (effluent pH = influent pH) and by a steady effluent composition (ICP MS, ICP OES analyses). The term background electrolyte (BE) describes the influent; pH adjustment of the influent took place via addition of appropriate amounts of 65% HNO_3 and/or 1 mol L^{-1} NaOH ; no buffer was used. Background electrolytes were kept in lightproof containers and were renewed approximately every two to four days to prevent major algae growth. After equilibrium was reached in the columns a pulse input of Eu and NaBr took place (pulse/peak solution). The NaBr served as an ideal, conservative tracer to characterize hydraulic transport parameters of each experiment (Tab. 4.2). For each experiment ≈ 1.5 pore volumes (PVs [V/V_0]) of pulse solution (PS) were injected into the columns; the pulse concentration contained 10^{-5} mol L^{-1} Eu and 10^{-5} mol L^{-1} NaBr in the respective BE for each transport experiment.

A constant flow rate of $\approx 0.3 \text{ cm}^3 \text{ min}^{-1}$ (steady state flow conditions) was ensured during the experiments via a peristaltic pump from the bottom of each column through the system (Fig. 4.1). The initial pH (pH_{ini}) of background electrolytes was also kept constant at pH_{ini} 3.5 and 5.5. The flow rates were gravimetrically verified and the pH was measured periodically. The flow rate was slow enough to reach equilibrium between the electrolyte and the mineral surface (Sec. 4.3.1, Sec. 4.4.1) and resulted in feasible

experimental time frames ranging between 11 and 37 d (Tab. 4.1). The effluent was sampled every 13 minutes and used for pH measurements as well as ICP MS analysis for Eu and Br. Experimental set-up was realized under ambient conditions (Fig. 4.1).

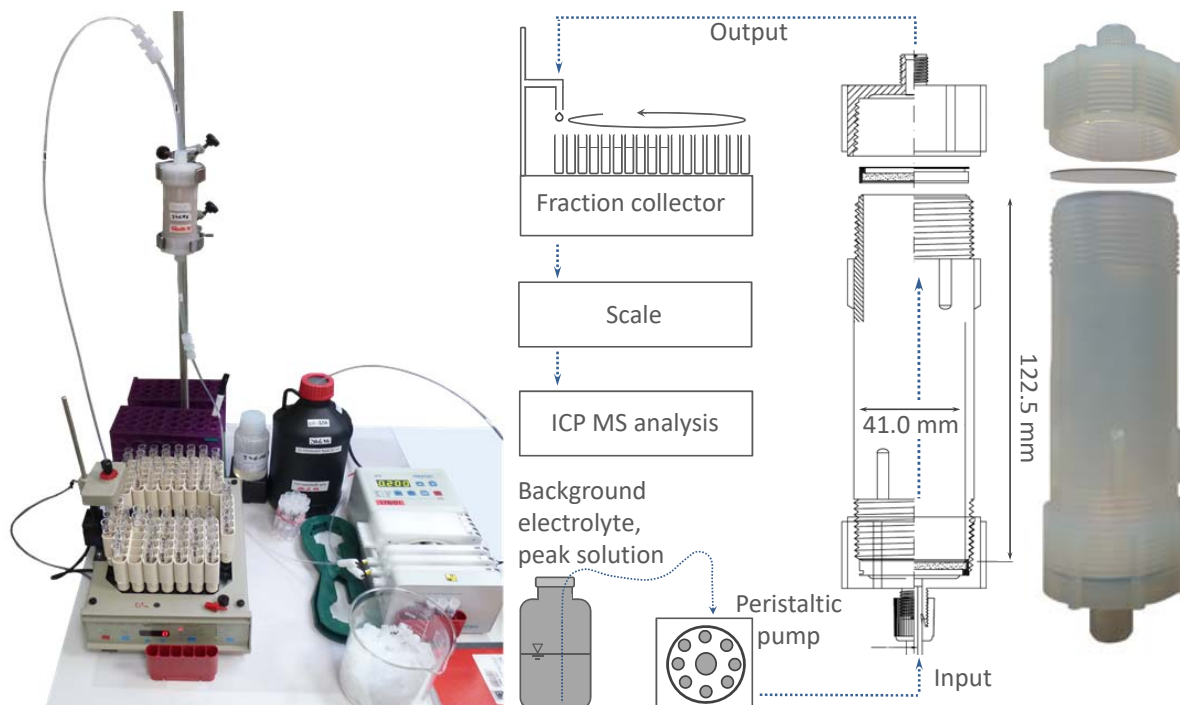


Fig. 4.1: Experimental set-up of column experiments. Background electrolyte stored in lightproof containers, column, tubing, tube connectors made out of PFA, frits and sealing rings composed of PTFE. Frits and sealing rings were situated at both ends of the column.

Column experiments returned Eu spatial distributions (SDs) and/or Eu, Br breakthrough curves (BTCs). The BTCs were collected in the effluent of each column with a time increment of 13 minutes (fraction collector). For Eu SDs the body of each column was separated into 24 equally spaced samples. Mineral samples were dried at 378 K overnight and were subsequently suspended in 5% HNO_3 to remobilize sorbed Eu from the mineral surfaces. Suspensions were filtered with 0.2 μm syringe filters and analysed via ICP MS for Eu.

After each experiment the empty column system (columns, frits, tubing) was leached with 5% HNO_3 in order to remobilize potentially sorbed Eu from containing walls. Samples were analysed via ICP MS for residual Eu. Recovery rates were calculated for each column experiment and represented the sum of Eu from BTCs and/or SDs and

leached column systems (Tab. 4.2). Eu background concentrations of the minerals was negligible (Sec. 2.3) and not included in recovery rate calculations.

Table 4.1 shows the experimental matrix of column experiments with boundary conditions. Varying geochemical conditions were used to characterize Eu transport:

- The NaClO_4 solution was applied as an inert background electrolyte to show sorption behaviour of Eu without the influence of the background electrolyte.
- Sulphate (SO_4^{2-}) is a constituent of the natural groundwater at the Gorleben study site (Noseck et al. (2012), Klinge et al. (2002)); hence, the Na_2SO_4 background electrolyte represented the influence of sulphate ligands on Eu solution speciation and surface complexation.
- The artificial groundwater was used as a background electrolyte to simulate geochemical conditions as close to nature as possible and showed the influence of SO_4^{2-} as well as competing cations on surface complexation and solution speciation. A detailed composition of the artificial groundwater is provided in Appendix A.12.2 (App. Tab. A.1).

Typical pH values of the Gorleben groundwater range between pH 6 - 8 (Klinge et al., 2002). Considering batch results (Sec. 3.3) Eu had been completely immobilized at $\text{pH} \geq 7$ regarding all systems (Fig. 3.12). Hence, to design a feasible experimental set-up for transport experiments with manageable experimental time frames pH_{ini} had to be reduced compared to natural pH conditions. Therefore, taking batch results into account $\text{pH}_{ini} = 3.5$ and $\text{pH}_{ini} = 5.5$ were used for column experiments.

Tab. 4.1: Summary of quartz (Q), orthoclase (FS), muscovite (mica), and synthetic sediment (SynSed) column experiments including geochemical conditions. Flow rates equalled 0.3 ml min^{-1} , except for ^[1] where flow rates were reduced to $\approx 0.1 \text{ ml min}^{-1}$. All experiments were carried out in double, except for ^[2] which represent single experiments, 1.5 PVs of the peak solution were used for the pulse input of Eu, $\text{Br} = 10^{-5} \text{ mol L}^{-1}$. Table A.1 in the appendix provides the composition of the artificial groundwater. The initial pH of the influent (background electrolyte) is symbolized by pH_{ini} , ID stands for the identification/name of the column experiment.

Solid	ID	pH_{ini}	Exp. time frame	Background electrolyte
		[d]		
Quartz	Q-i	3.5	12 ^[2]	10 mmol L^{-1} NaClO_4
	Q-ii	5.6	11	10 mmol L^{-1} NaClO_4
	Q-iii	5.6	12	5 mmol L^{-1} Na_2SO_4

Continued on next page

Solid	ID	pH _{ini} [d]	Exp. time frame	Background electrolyte
Quartz	Q-iv	5.5	12	50 mmol L ⁻¹ Na ₂ SO ₄
	Q-v	5.5	12	artificial groundwater
	Q-vi	5.5	37 ^[1]	5 mmol L ⁻¹ Na ₂ SO ₄
Orthoclase	FS-i	3.6	18	10 mmol L ⁻¹ NaClO ₄
	FS-ii	3.5	8	50 mmol L ⁻¹ Na ₂ SO ₄
	FS-iii	5.5	10	50 mmol L ⁻¹ Na ₂ SO ₄
Muscovite	mica-i	3.6	14 ^[2]	10 mmol L ⁻¹ NaClO ₄
	mica-ii	3.6	22	5 mmol L ⁻¹ Na ₂ SO ₄
	mica-iii	5.5	23 ^[2]	50 mmol L ⁻¹ Na ₂ SO ₄
	mica-iv	5.5	23 ^[2]	artificial groundwater
Synthetic sediment	SynSed-i	3.5	18	10 mmol L ⁻¹ NaClO ₄
	SynSed-ii	5.5	35	artificial groundwater

4.2.2 Data processing of breakthrough curves

Breakthrough curves of Br and Eu were corrected for the volume of the tubing and frits which is referred to as dead volume. This volume is crucial to determine the correct temporal position as well as PVs of BTCs and was determined gravimetrically in this study.

The volume of the tubing and tube connections was measured for each column experiment individually; the dead volume of the frits which comprised the pore volume of the frits *and* the space in front of the frits in the caps for both ends of the column was measured for selected columns. Since all column systems were identical the dead volume of the frits was assumed to be similar for all transport experiments.

4.2.3 Determination of retardation factors

The retardation factor R_f [–] as well as the linear distribution coefficient K_d assume linear sorption isotherms (Henry isotherm) that do not consider kinetic effects, diffusion and dispersion processes, local nonequilibrium conditions, or e.g. interrelations of geochemical processes and changing geochemical conditions that may occur during transport experiments and under natural conditions. Exclusively linear sorption processes would result in symmetrical SDs and BTCs that can be evaluated and assessed with the R_f and the linear K_d approaches. Under the assumption of a linear sorption isotherm

(K_d approach, Henry isotherm) and hence, an instantaneously equilibrated system the R_f [–] is related to the linear K_d [$\text{cm}^3 \text{g}^{-1}$] (Eq. 3.38) as follows (Eq. 4.42)

$$R_f = 1 + \frac{\rho_b K_d}{\theta} \quad (4.42)$$

where ρ_b relates to the bulk density [g cm^3] (Eq. A.58 in App. A.12.3) and θ to the water content which was assumed to be equal to the porosity [–] of the column. The R_f describes the position of a BTC or a SD of a potential pollutant in relation to the BTC of an ideal tracer (e.g. Br^-). In this study, R_f values were calculated from experimental data and reactive transport simulations (no fitting); K_d values were calculated from experiments and simulations considering Equation 4.42.

Even though R_f as well as the K_d approaches are only applicable to linear sorption processes without biasing influences (kinetics, high dispersion, diffusion, etc.), in this study R_f and K_d values were used as a measure to compare simulated with experimental results of *all* column experiments. Hence, for asymmetrical BTCs and/or SDs the R_f and K_d describe the first Eu peak concentration; hence, calculated K_d and R_f values should only be considered rough estimates keeping in mind that Eu transport processes did not follow linear properties for most experiments (Sec. 4.4.2).

4.2.4 Transport parameter determination with CXTFIT

The CXTFIT code (Toride et al., 1998) is part of the free software package STANMOD (STudio of ANalytical MODels, Version 2.0, Simunek et al. (1999)) and comprises three different transport models: the conventional, deterministic, 1D equilibrium **advection-dispersion** equation (**ADE**, Eq. 4.43), a chemical and physical nonequilibrium transport model, and a stochastic stream tube model. The former was used in this study to optimize solute transport parameters (conventional 1D **ADE**) which were fitted using a nonlinear least squares objective function method (Simunek et al., 1999).

Under the assumption of homogeneous media, steady flow, equilibrium conditions, and linear sorption properties Equation 4.43 was used to simulate 1D transport problems of Br breakthrough in this study (Toride et al., 1998)

$$R_f \frac{\partial C_r}{\partial t} = -v \frac{\partial C_r}{\partial x} + D \frac{\partial^2 C_r}{\partial x^2} \quad (4.43)$$

considering Equation 4.44 for BTCs

$$C_f = C_r - \frac{1}{Pe} \frac{\partial C_r}{\partial x} \quad (4.44)$$

where R_f [–] corresponds to the retardation factor (Eq. 4.42), C_r refers to the volume averaged or resident concentration of the liquid phase [mol L^{−1}], C_f to the flux-averaged concentration [mg L^{−1}], D is the dispersion coefficient [cm² h^{−1}], v [cm h^{−1}] relates to the pore water velocity (also water flow velocity), and Pe to the Péclet number (App. Eq. A.55). In Equation 4.43 t relates to the time [h], x to the location [cm], and C to the concentration [mg L^{−1}]. Detailed information provides Toride et al. (1998).

Breakthrough curves of the ideal NaBr tracer that were corrected for the dead volume of the tubing and frits (Sec. 4.2.2) were used as calibration data sets to determine solute transport parameters with CXTFIT for each column experiment. For transport parameter optimization procedures Br concentrations were used as a function of time [h] as flux-averaged concentration [mg L^{−1}], fitted transport parameters were not constrained, and the total Br mass was included whereas the solute mass was known and kept constant throughout the fitting procedures. The ideal Br tracer was injected as a pulse input over ≈ 1.5 PVs (boundary value problem: pulse input, solute mass is known and kept constant). No initial concentration was allowed in the system (initial value problem: zero initial concentration $C_r(t = 0) = 0$).

The D [m² h^{−1}] served as an adjustable parameter. Where necessary, the application time t [h] was also optimized (cf. Sec. 4.3); v [cm h^{−1}] was used as a control since it was a measured parameter (Tab. 4.2). Fitted dispersion coefficients D were converted to dispersivities (dispersion length) λ [m] ($\lambda = D/v$) for each experiment and used in PHREEQC transport simulations as a fixed solute transport parameter.

4.2.5 PHREEQC 1D reactive transport

PHREEQC combines 1D flow and transport processes with geochemical speciation calculations and offers four different transport models, whereas the 1D **advection-dispersion-reaction** equation (ADRE, Eq. 4.45) was used in this study. Under the assumption that v and D are equal for all solute species, Equation 4.45 was used for transport simulations of Eu (Parkhurst and Appelo, 1999).

$$\frac{\partial C_{sol}}{\partial t} = -v \frac{\partial C_{sol}}{\partial x} + D \frac{\partial^2 C_{sol}}{\partial x^2} - \frac{\partial C_{immo}}{\partial t} \quad (4.45)$$

C_{sol} [mol L⁻¹] is the total element concentration in solution, $\frac{\partial C_{immo}}{\partial t}$ [mol L⁻¹ s⁻¹] is the change of the immobilized concentration over time [s] where C_{immo} stands for the immobilized concentration [mol L⁻¹], x is the location [m] (Parkhurst and Appelo, 1999). Transport simulations with PHREEQC were based on explicit finite differences that were calculated forward in time. Each column was discretised into 180 cells with a length of 0.07 cm ($Pe_{grid} < 2$ with Pe_{grid} representing the grid Péclet number to prevent numerical dispersion). Dispersion was simulated central in space (mean velocities in the middle of each spacial decrement), whereas advection was calculated upwind (upstream velocities). All columns were defined with two flux boundary conditions (Cauchy boundary condition) at each end (Eq. 4.46) (Parkhurst and Appelo, 2013):

$$C_{sol}(x_{end}, t) = C_0 + \frac{D}{v} \cdot \frac{\partial C_{sol}(x_{end}, t)}{\partial x} \quad (4.46)$$

where t is the time [s], x_{end} [m] the last cell of the column; x stands for the location [m], C_0 relates to the initial Eu concentration [mol L⁻¹] of the pulse solution (with the simplifying assumption 1 kgw = 1 L).

PHREEQC simulated the reactive transport of Eu for homogeneous porous columns using equilibrium-controlled surface and solution speciation reactions for each time-step, transport parameter λ was derived from CXTFIT optimizations of the dispersion coefficient D (App. Eq. A.57). RTMs were based on surface charge (Sec. 2) and SCMs (Sec. 3); hence, limitations and challenges as discussed in Sections 2.4.3 and 3.4 also applied for Eu RTMs. The summarized final SCP sets in Table 3.4 were used as fixed parameter values for transport simulations; no fitting or optimization of parameters was performed. Surface complexation and co- and counterion association coefficient reactions as introduced in Section 3.2.2 (Input file code block 3.1) were used. Due to lack of data, counterion association coefficients determined via titration experiments in NaClO₄ background electrolyte were used as rough estimates for column experiments carried out with Na₂SO₄ solution. For DDLM reactive transport simulations that considered the artificial groundwater (Sec. 4.2.1, Tab. 4.1) a competitive surface complexation reaction for Al³⁺ was included (Kuan et al. (2004), Input file code block 4.2). The constant was derived for quartz surfaces and applies for the DDLM (Kuan et al., 2004). Again, in the absence of more detailed data, the surface complexation constant of Kuan et al. (2004) was also used to describe Al³⁺ surface complexation reactions in orthoclase DDLMs as a rough estimate. However, as no parameter value was available for the BSM or the noEDLM competition for surface sites had to be neglected for the latter two model approaches.

```

# Quartz Al inner sphere surface complex – DDLM
# Al competing cation reaction
# Constant obtained from RES3T, KIW04 DDL, no parameter available for
  noEDLM or BSM
# RES3T: http://www.hzdr.de/res3t
  S-OH + Al+3 = S-OAl+2 + H+
  log_k 0.5

```

Input file code block 4.2: Competing surface complexation reaction for Al^{3+} on quartz (DDL) (Kuan et al., 2004) as used in PHREEQC SCMs. S- refers to a mineral surface. # indicates comments.

Advection was considered to be the main transport process for solutes due to high pore water velocity $v \approx 3.2 \pm 0.7 \text{ cm h}^{-1}$ (mean value over all transport experiments \pm standard deviation, cf. Tab. 4.2), dispersivities on the mm scale (small dispersion influence), and large Péclet numbers (Tab. 4.2); diffusion was expected to be negligible (estimated diffusion coefficient = $10^{-10} \text{ m}^2 \text{ s}^{-1}$). Transport processes were only considered in the mobile, liquid phase - no colloidal transport was taken into account. The digital appendix provides PHREEQC RTMs.

The reactive transport was simulated in two steps: First, the transport of the pulse solution was simulated as it was shifted through the column; the second step initiated the transport of the background electrolyte pushing the Eu and Br peak injection further down the column. To avoid numerical dispersion effects the grid Péclet (Pe_{grid}) number was defined with Equation A.56 in Appendix A (Leonard (1979), Parkhurst and Appelo (2013)). All columns were equally discretized in 180 cells to guarantee comparability. Since $\text{pH}_{ini} \approx 3.5$ and ≈ 5.5 no precipitation reactions were considered since first Eu precipitates occur at $\text{pH} \geq 6.4$ (Sec. 3.1.1); the influence of CO_2 was also excluded due to low pH_{ini} and to reduce simulation times.

Davis et al. (2005) offered the basis to judge whether a reactive transport simulation was satisfying or not: They stated that an error of model predictions in comparison to experimental data ranging between 0.5 - 1 $\log K_d$ units ($|\Delta \log K_d|$) evidenced system understanding. Davis et al. (2005) found that in most cases sorption trends and the magnitude of experimental data was satisfactorily represented over a range of experimental conditions if discrepancies between simulations and experiments stayed within the given K_d error range. To compare experimental transport data with PHREEQC simulations the K_d and R_f were calculated from measurements and predictions (cf. Sec. 4.2.3). For RTM evaluation smallest $|\Delta \log K_d|$ values were preferred over larger ones in this study.

4.2.6 Thermodynamic database

The thermodynamic database as introduced in Section 2.4.4 and Section 3.2.3 was used. The database has been under constants improvement ever since; the release from December 2016 was used in this study and will be published in summer 2018.

4.3 Results and discussion of Br and Eu transport experiments

This section summarizes experimental results of Eu transport experiments through homogeneous porous media. Appendix B.4, Figures B.36 - B.42 present supplementary information and data; Table 4.1 offers an overview of the experimental matrix of column experiments; Table 4.2 summarizes recovery rates, transport parameters, R_f (Eq. 4.42) and K_d values from measurements and predictions (cf. Sec. 4.2.3).

Column experiments yielded Br BTCs and Eu SDs or Eu BTCs depending on the geochemical conditions. Since all ideal tracer BTCs followed expectations without exception, Br BTCs of quartz column experiments are exemplarily depicted (Sec. 4.3.1) whereas tracer BTCs of orthoclase, muscovite, and the synthetic sediment can be found in the appendix (App. B.4, Fig. B.39 - B.42).

4.3.1 Quartz

Figure 4.2 compares Eu SDs, Br BTCs, and the pH development of transport experiments Q-i and Q-ii (10 mmol L⁻¹ NaClO₄ inert background electrolyte, pH_{ini} = 5.6 (black) and pH_{ini} = 3.5 (blue), cf. Tab. 4.1). Column experiment Q-ii was performed in duplicate (open, solid symbols). All geochemical boundary conditions except the pH were identical for both experimental set-ups. Figure 4.2 A depicts the SD of Eu in the quartz columns and the pH influence on Eu transport processes: The higher the pH, the more retarded the Eu peak in the column which agrees well with findings from batch experiments (Fig. 3.3). The R_f between both pH conditions differed by factor 2.4 with the larger R_f representing the higher pH_{ini} (Tab. 4.2). The Br tracer behaved as an ideal tracer which was illustrated by a steep front and back of the BTCs (Fig. 4.2 B.1 - B.2). In addition, $C_{Br-} = 0.5 \cdot C_0$ was fulfilled as approximately 1 PV had passed the column which was also substantiated by a large grid Péclet number $Pe_{grid} = 190$ (cf. Tab. 4.2, C_{Br-} – effluent Br concentration (aq), C_0 – initial Br pulse solution concentration (aq), cf.

Sec. 4.2.3, App. Fig. B.43). The slight spreading of the BTCs were caused by dispersion processes (Sec. 4.4.1, App. Fig. B.43). Even though pH_{ini} was kept constant, Figure 4.2 C.1 depicts differences between pH_{ini} (influent) and the effluent pH of the column for column experiments Q-ii (pH_{ini} 5.6). The variation in pH was attributed to sorption processes of Eu on the quartz surface: As Eu surface complexes were formed, H^+ were released from the surface by this decreasing the electrolyte pH; as the pH decreased Eu sorption affinities reduced (cf. Fig. 3.3) and the lanthanide migrated through the column. The correlation between the formation of surface complexes and the reduction of the effluent pH was observed for most column experiments where the influent H^+ concentration was comparable to the pulse concentration of Eu. Hence, experiments with $\text{pH}_{ini} \approx 5.5$ mostly showed variable pH conditions; in contrast to $\text{pH}_{ini} \approx 3.5$ where the pH was not affected from surface complexation reactions due to a two orders of magnitudes higher H^+ concentration of the background electrolyte.

The findings of the present study agreed well with studies from Kohler et al. (1996), Curtis et al. (2001), and Hanna et al. (2014): Kohler et al. (1996) and Curtis et al. (2001) studied U(VI) transport through quartz under variable geochemical conditions and found a strong dependence of U(VI) retardation with pH. In an unbuffered column system they measured temporal pH variations in the effluent of the columns which they also related to U(VI) surface complexation reactions. Hanna et al. (2014) studied the transport of phthalic acid through goethite-packed columns and made similar observations.

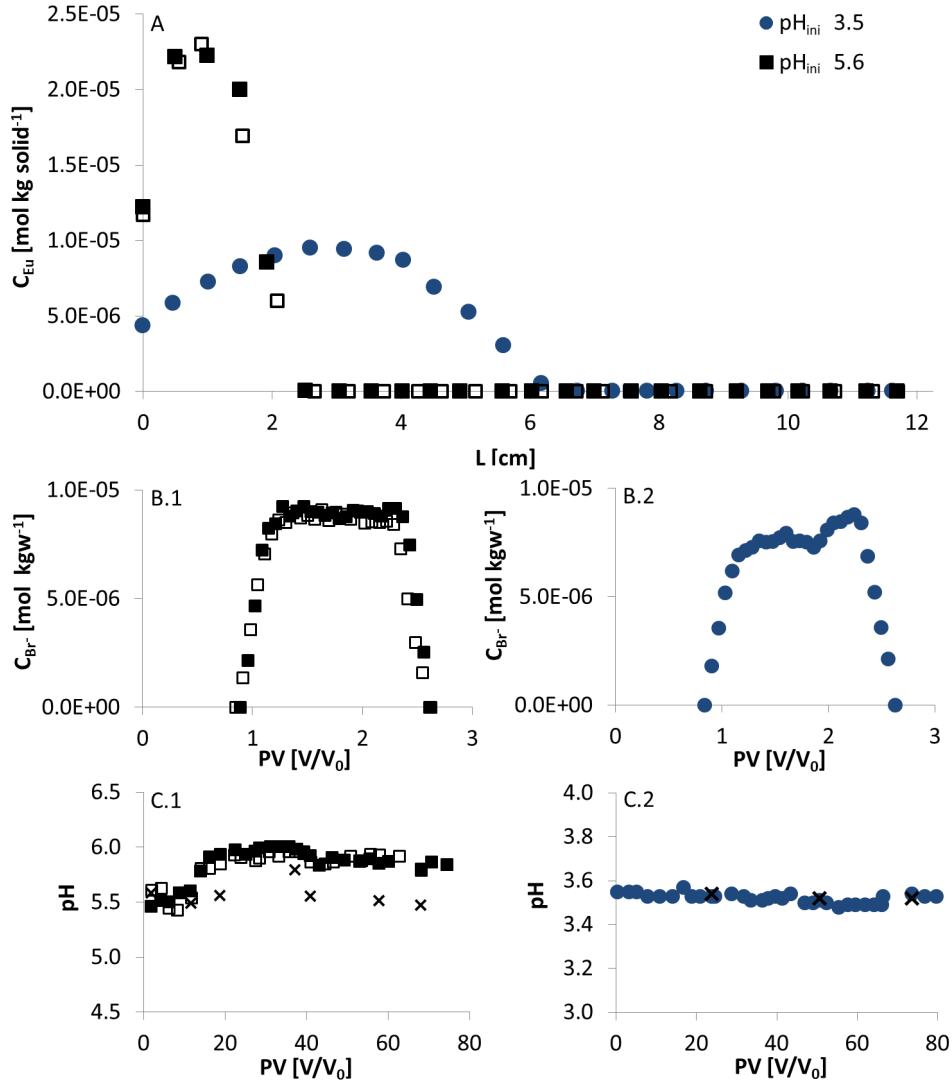


Fig. 4.2: Results of quartz column experiments Q-i and Q-ii. A: 10 mmol L⁻¹ NaClO₄ at $pH_{ini} = 3.5$ (blue, Q-i, $t = 81$ PV, $R_f = 380$) and $pH_{ini} = 5.6$ (black, Q-ii, $t = 75$ PV, $R_f = 920$). Q-i single experiment (solid symbols), Q-ii performed in duplicate (open, solid symbols). B.1 - B.2: Br BTCs, C.1 - C.2: Effluent pH development. For experimental details cf. Tables 4.1 and 4.2. Bottom of the column $L = 0$ cm, column top $L = 12.25$ cm, x - pH_{ini} , C_{Eu} , C_{Br^-} - Eu and Br concentrations (aq), PV - pore volume, L [cm] - column length.

A comparison of calculated K_d values from column and batch experiments in inert NaClO₄ solution revealed that batch experiments underestimated sorption processes of Eu on quartz surfaces at low pH values (Fig. 4.11 A). Batch experiments returned a mean $K_d = 11$ L kg⁻¹ at $pH \approx 3.5$ and a mean $K_d = 64$ L kg⁻¹ for pH conditions ranging between 5 and 6 (cf. Fig. 4.11 A); calculated K_d values from column experiments

on the other hand equalled $K_d = 88 \text{ L kg}^{-1}$ for Q-i ($\text{pH}_{ini} = 3.5$) and $K_d = 210 \text{ L kg}^{-1}$ for Q-ii ($\text{pH}_{ini} = 5.6$, Tab. 4.2). However, as e.g. Maraqa et al. (1998) and Porro et al. (2000) state the true mechanism explaining the differences between retardation processes measured with batch and column experiments has not yet been resolved (Sec. 4.1) and studies have reported greater adsorption for column and flow through experiments on the one hand, but also larger distribution coefficients for batch experiments in relation to comparable transport experiments on the other hand (Hanna et al., 2010).

Experiments displayed in Figures 4.3 - 4.5 were carried out in duplicate (open, solid symbols) and show the influence of sulphate (SO_4^{2-}) on Eu solution speciation and, hence, transport processes: As $\text{Eu}(\text{SO}_4)^+$ and $\text{Eu}(\text{SO}_4)_2^-$ solution complexes were formed, the concentration of free Eu^{3+} ions (aq) decreased resulting in decreasing Eu sorption rates and increased mobility (according to solution speciation calculations, App. Fig. B.36). Figure 4.3 shows results of column experiments Q-iii and Q-iv ($\text{pH}_{ini} \approx 5.5$, 5 and $50 \text{ mmol L}^{-1} \text{ Na}_2\text{SO}_4$): The smaller ligand concentration yielded an Eu SD (Q-iii, Fig. 4.3 A), the larger one resulted in a BTC where Eu travelled almost as fast as the ideal tracer with $R_f = 1.8$ (Q-iv, Tab. 4.2, cf. App. Fig. B.38) due to negatively charged Eu solution complexes with the ligand under the chosen geochemical conditions (App. Fig. B.36).

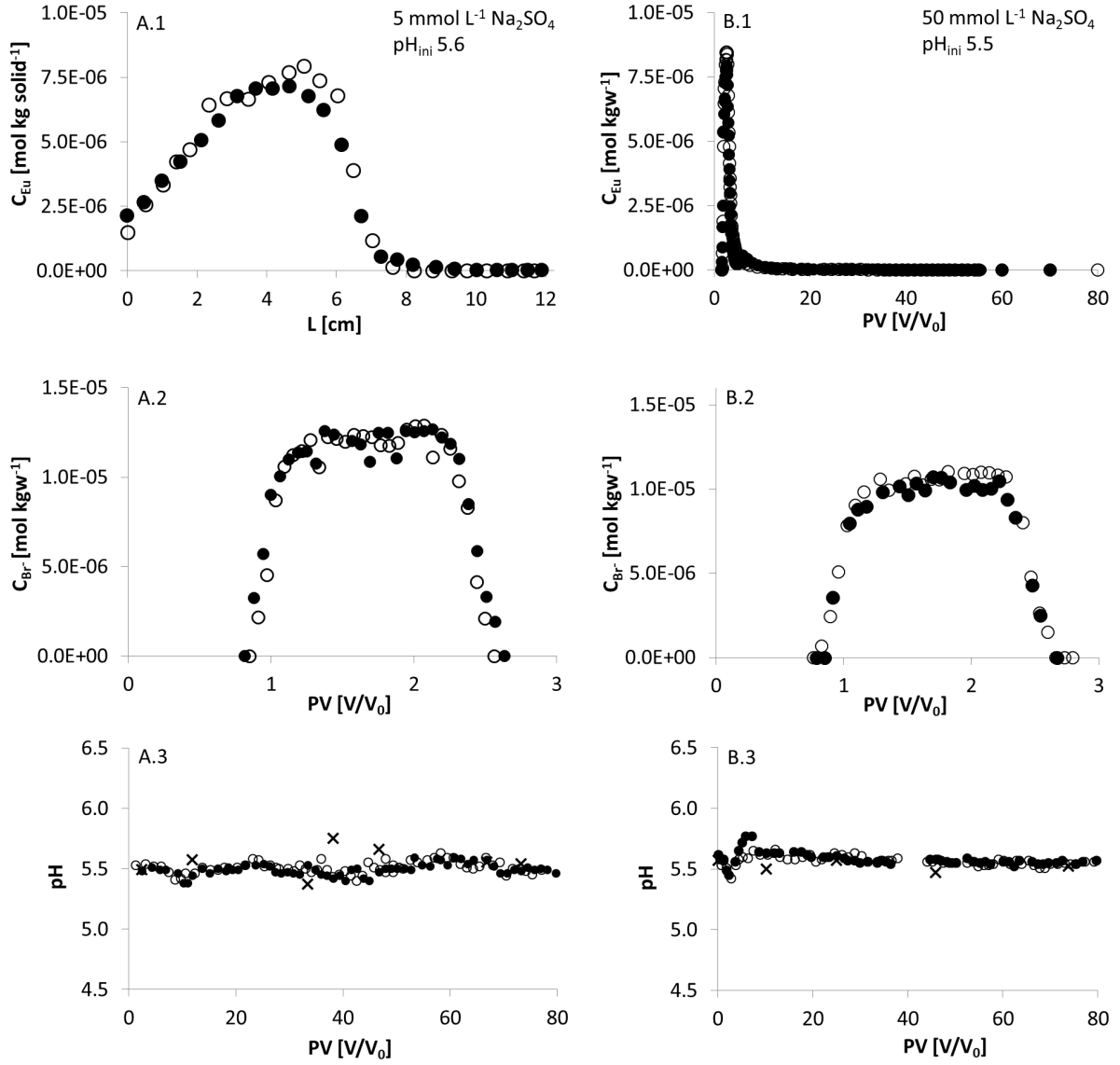


Fig. 4.3: Quartz column experiment Q-iii (A, 5 mmol L⁻¹ Na₂SO₄) and Q-iv (B, 50 mmol L⁻¹ Na₂SO₄) at pH_{ini} = 5.6, and pH_{ini} = 5.5, respectively. Experiments were carried out in duplicate (open, solid symbols). A.1 - B.1: Eu SDs (Q-iii, $t = 80$ PV, $R_f = 190$) and BTCs (Q-iv, $R_f = 1.8$), respectively, A.2 - B.2: Br BTCs, A.3 - B.3: Effluent pH development. For experimental details cf. Tables 4.1 and 4.2. Bottom of the column $L = 0$ cm, column top $L = 12.25$ cm, x - pH_{ini}, C_{Eu} , C_{Br-} - Eu and Br concentrations (aq), PV - pore volume, L [cm] - column length.

Figure 4.4 presents a close-up of Figure 4.3 B.1 and B.3 (Q-iv). Since experiments were carried out in doublet two data sets were derived for one geochemical boundary

condition (Fig. 4.4 A, B). Interestingly, both data sets showed differences in the pH development and Eu BTCs even though column experiments were run identically (identical background electrolytes and pulse solutions). Nevertheless, both measurements provided a consistent picture of Eu migration through the columns where each Eu peak development was mirrored by the pH (Fig. 4.4): Eu surface complexation resulted in a H^+ release into the solution and consequently the pH dropped which could be observed for both experiments. Under the depleted pH conditions Eu sorption decreased (cf. Fig. 3.3) and the lanthanide migrated through the column resulting in a high (first) Eu peak. Since most of the Eu had already left the column after the injection of 1.5 PVs of pulse solution was finished, the pH rose due to protonation of $Si-O^-$ which was also observed for both experiments. However, as the pH rose and exceeded pH_{ini} for the first data set (Fig. 4.4 A) the residual Eu was stronger retarded in the column and a second peak was formed. In comparison, the second data set (Fig. 4.4 B) described only one Eu peak, without a small second peak at the end and without an increase of the effluent pH in relation to pH_{ini} .

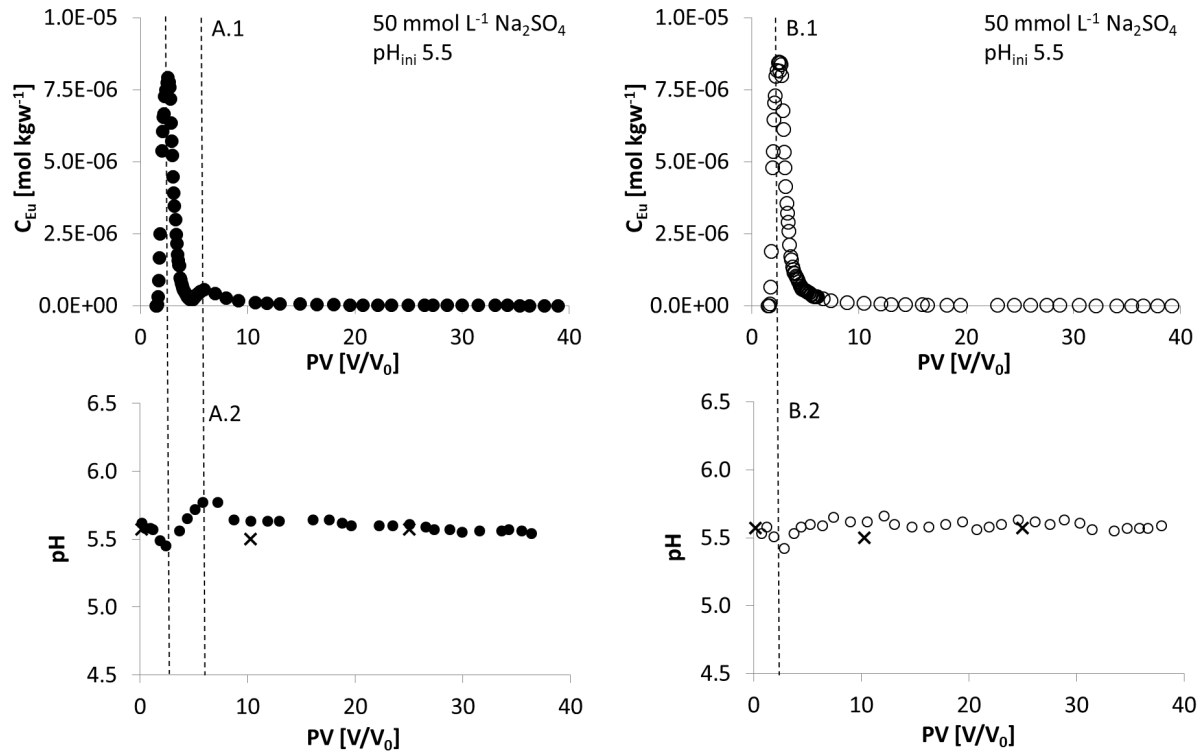


Fig. 4.4: Eu retardation (A.1 - B.1) and pH development (A.2 - B.2) of quartz column Q-iv: 50 mmol L⁻¹ Na₂SO₄, $pH_{ini} = 5.5$. Labelling corresponds to Figure 4.3.

The comparison of Eu transport processes under inert NaClO_4 electrolyte conditions (Q-ii) and under the presence of SO_4^{2-} (Q-iii) in solution yielded expected results (Fig. 4.5): At pH 5.5 89% of the initial Eu concentration (C_0) occurred as $\text{Eu}(\text{SO}_4)_4^+$ and $\text{Eu}(\text{SO}_4)_2^-$ in the Na_2SO_4 system (App. Fig. B.36); since the monovalent cation and anion show reduced sorption affinities in relation to the trivalent Eu^{3+} cation, the Eu sulphate species migrated faster through the column. This was also mirrored by smaller R_f values for the sulphate-influenced system (Tab. 4.2).

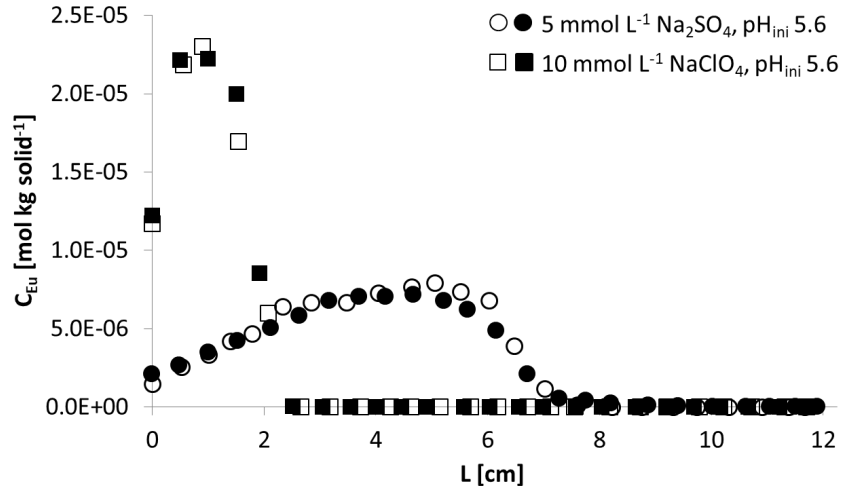


Fig. 4.5: Sulphate (SO_4^{2-}) ligand influence on Eu transport processes in quartz columns. Comparison of an inert background electrolyte (Q-ii: NaClO_4 , squares, $t = 75$ PV, $R_f = 920$) with a SO_4^{2-} ligand background electrolyte (Q-iii, circles, $t = 80$ PV, $R_f = 190$) at $\text{pH}_{\text{ini}} = 5.6$. Experiments were carried out in doublets (solid, empty characters). For experimental details cf. Tables 4.1 and 4.2. Bottom of the column $L = 0$ cm, column top $L = 12.25$ cm, L [cm] – column length, C_{Eu} – Eu concentration [mol kg s^{-1}].

The asymmetrical shape of Q-iii (Na_2SO_4 system) with the relatively steep front and slight tailing (Fig. 4.5) lead to the assumption that the system could had been influenced by

- kinetics (sorption/desorption-related nonequilibrium),
- diffusion from immobile regions,
- or concentration-dependent sorption processes.

To verify or to disprove these assumptions and to substantiate the assumption of equilibrated geochemical conditions during column experiments a second set of transport experiments was initiated: Figure 4.6 illustrates Eu transport under identical geochemical boundary conditions as Q-iii but with different water flow velocities ($v = 83 \text{ cm d}^{-1}$,

Q-iii (black circles) and $v = 31 \text{ cm d}^{-1}$, Q-vi (blue squares), Tab. 4.2, Fig. 4.6). If a local nonequilibrium of Eu surface reactions caused the asymmetrical shape of the SDs then the front would be expected to travel further down the column for the faster flow rate: The residence time was prolonged by factor 2.7 for the slower flow rate and hence more time was available for surface complexation and Eu retardation. However, since both velocities resulted in similar Eu SDs the assumption of geochemical equilibrium during column experiments was substantiated. Kinetic effects of Eu sorption and/or desorption processes could also be ruled out due to similar shapes of the SDs. Furthermore, it could be shown that R_f and K_d calculations returned comparable values for Q-iii ($K_d = 45 \text{ L kg}^{-1}$) and Q-vi ($K_d = 50 \text{ L kg}^{-1}$) which indicated that sorption processes were independent of the flow rate (Tab. 4.2). Based on these findings it was expected that neither dispersion nor stagnant/immobile zones had major influence on Eu transport which is further addressed and substantiated in Section 4.4.1 using the CXTFIT code (Simunek et al., 1999). Since batch experiments showed concentration dependent Eu immobilization (Sec. 3.3) results obtained from column experiment Q-iii and Q-vi suggested that the asymmetric SDs could be due to high relative retardation of low Eu concentrations and less relative immobilization of high Eu concentrations under the given geochemical conditions.

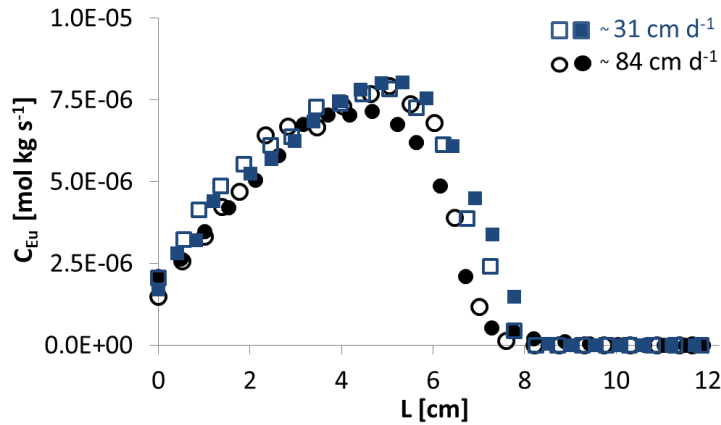


Fig. 4.6: Influence of different pore water velocities ($v = 83 \text{ cm d}^{-1}$ (Q-iii, black, $t = 80 \text{ PV}$), $v = 31 \text{ cm d}^{-1}$ (Q-vi, blue, $t = 94 \text{ PV}$)) on Eu transport through quartz columns with $5 \text{ mmol L}^{-1} \text{ Na}_2\text{SO}_4$ background electrolyte at $\text{pH}_{ini} \approx 5.5$. Experiments were carried out in doublets (solid, empty characters). For experimental details cf. Tables 4.1 and 4.2. Bottom of the column $L = 0 \text{ cm}$, column top $L = 12.25 \text{ cm}$, $L [\text{cm}]$ – column length, C_{Eu} – Eu concentration $[\text{mol kg s}^{-1}]$.

Figure 4.7 presents a comparison of Eu transport through quartz columns with $50 \text{ mmol L}^{-1} \text{ Na}_2\text{SO}_4$ ($\text{pH}_{ini} = 5.5$, Q-iv) and artificial groundwater ($\text{pH}_{ini} = 5.5$, Q-v)

(cf. App. Tab. A.1). Both experimental set-ups resulted in Eu BTCs whereas the Eu sorption in artificial groundwater (Fig. 4.7 A.1 and A.2, blue) was stronger retarded compared to Eu sorption in the Na_2SO_4 system (Fig. 4.7 A.1, black). The breakthrough of Eu occurred due to solution speciation reactions of the trivalent lanthanide where the free Eu^{3+} cation was complexed to monovalent anions ($\text{Eu}(\text{SO}_4)_2^-$) and monovalent cation species ($\text{Eu}(\text{SO}_4)^+$, $\text{Eu}(\text{CO}_3)^+$) with highly reduced sorption affinities compared to the trivalent Eu^{3+} cation (cf. App. Fig. B.36 - B.37). Speciation calculations with PHREEQC showed that at $\text{pH}_{ini} = 5.5$ only 5.4% Eu^{3+} exists in 50 mmol L^{-1} Na_2SO_4 solution compared to 60.5% in the artificial groundwater (App. Fig. B.37 B); hence, due to the greater abundance of the trivalent cation, Eu was stronger retarded in the artificial groundwater system. The pH development in the effluent of the artificial groundwater experiment exhibited noteworthy trends (Fig. 4.7 C): First the pH rose 0.2 pH units to subsequently decrease as would be expected due to surface complexation reactions. At this point, the initial rise of the pH could not be explained by Eu surface or solution complexation processes and is further discussed in Section 4.4.2.

Quartz column experiments in 5 mmol L^{-1} Na_2SO_4 , $\text{pH}_{ini} = 5.6$ (Q-iii, Fig. 4.5) yielded $R_f = 190$ compared to the transport experiments with artificial groundwater, $\text{pH}_{ini} = 5.5$ (Q-v, Fig. 4.7) where $R_f = 16$. At first glance this is somehow contradictory since solution speciation calculations (App. Fig. B.36 - B.37) revealed that only 11% Eu^{3+} are present at pH 5.5 in 5 mmol L^{-1} Na_2SO_4 compared to 60.5% Eu^{3+} in the artificial groundwater at the same pH. The fact that Eu travelled faster under the influence of artificial groundwater with a more than five times higher abundance of Eu lead to the assumption that cations in the artificial groundwater posed competition on Eu surface complexation resulting in enhanced transport of the lanthanide. This assumption was verified with reactive transport simulations and is further discussed in Section 4.4.2.

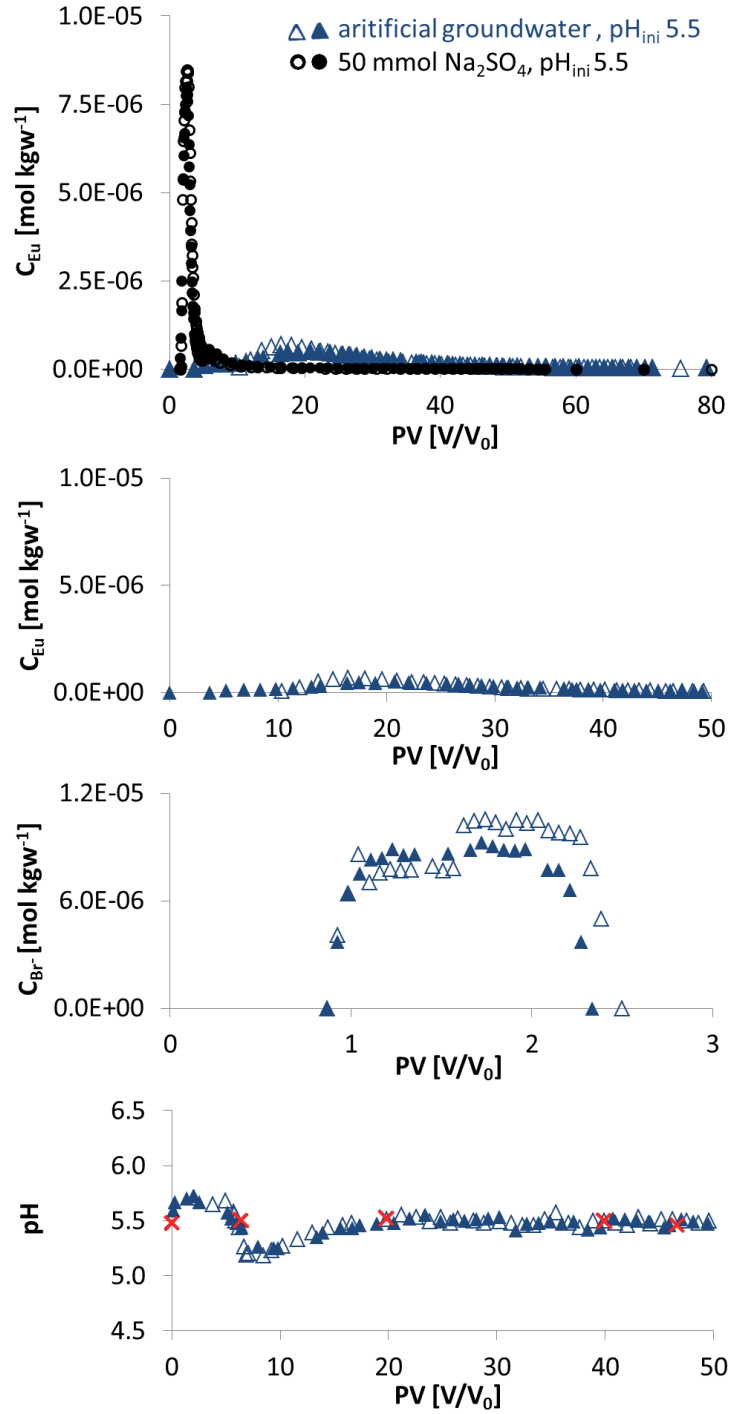


Fig. 4.7: Comparison of Eu transport through quartz columns using an artificial groundwater (blue triangles, Q-v) and 50 mmol L⁻¹ Na₂SO₄ background electrolyte (black circles, Q-iv), pH_{ini} = 5.5 (A.1, A.2). B: Br BTCs, C: Effluent pH development. Experiments were carried out in doublets (open, solid symbols). For experimental details cf. Table 4.1 and Table 4.2. x – pH_{ini}, C_{Eu} , C_{Br^-} – Eu and Br concentrations (aq), PV – pore volume.

4.3.2 Orthoclase

Figure 4.8 shows Eu retardation in quartz (Q-i) and orthoclase (FS-i) columns using $10 \text{ mmol L}^{-1} \text{ NaClO}_4$ background electrolyte at $\text{pH}_{\text{ini}} \approx 3.5$. As expected from batch experiments (Fig. 3.12) Eu showed stronger sorption affinities towards the orthoclase surface which was reflected by R_f values that differed by factor 4.5 between both minerals (Tab. 4.2). A difference between pH_{ini} and the effluent pH of FS-i occurred over the entire experimental time frame and equalled $\approx 0.2 \text{ pH}$ units (Fig. 4.8 B).

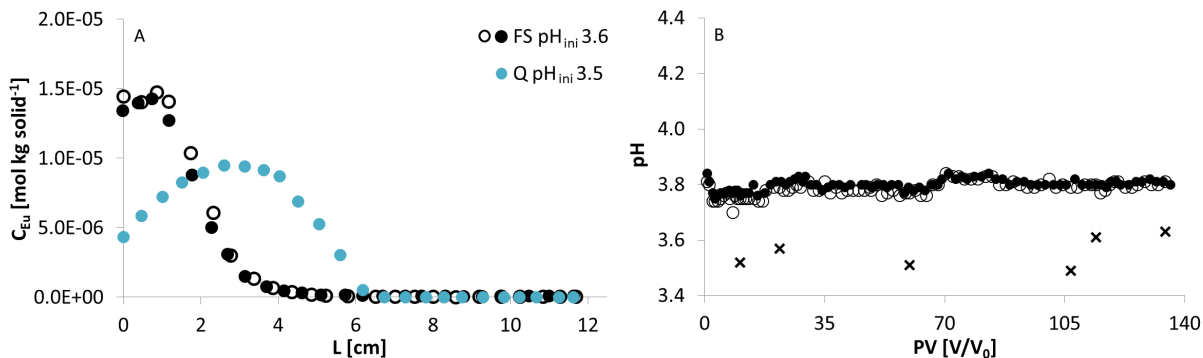


Fig. 4.8: Eu transport through quartz (Q-i, blue, $t = 81 \text{ PV}$, $R_f = 380$) and orthoclase (FS-i, black, $t = 136 \text{ PV}$, $R_f = 1700$) columns using $10 \text{ mmol L}^{-1} \text{ NaClO}_4$ background electrolyte, $\text{pH}_{\text{ini}} \approx 3.5$. Orthoclase experiments carried out in doublets (solid and empty characters). For experimental details cf. Tables 4.1 and 4.2. A: Eu SDs of quartz (blue) and orthoclase (black), B: pH development of orthoclase column experiment FS-i. Bottom of the column $L = 0 \text{ cm}$, column top $L = 12.25 \text{ cm}$, x - pH_{ini} , C_{Eu} - Eu concentration (aq), PV - pore volume, $L [\text{cm}]$ - column length.

The SO_4^{2-} ligand showed comparable effects on orthoclase transport experiments as observed for quartz columns: The high ligand concentration resulted in a faster Eu breakthrough (comparison Fig. 4.8 and Fig. 4.9). Furthermore, the higher the pH the more Eu surface complexation occurred which agreed well with orthoclase batch experiments where small pH values resulted in low relative Eu immobilization compared to high pH conditions (comparison Fig. 4.9 and Fig. 3.12). The latter observations were confirmed by experimental R_f and K_d values (Tab. 4.2). The pH development during orthoclase transport experiments also agreed with prior observations: No influence of Eu surface complexation could be observed at $\text{pH}_{\text{ini}} \approx 3.5$, whereas at $\text{pH}_{\text{ini}} \approx 5.5$ a clear pH response to Eu surface complexation was measured (Fig. 4.9 B, C).

Orthoclase Eu BTCs at $\text{pH}_{\text{ini}} 3.5$ in Figure 4.9 (FS-ii, $50 \text{ mmol L}^{-1} \text{ Na}_2\text{SO}_4$

background electrolyte) describe a fast Eu breakthrough with a steep rise and fall of measured Eu concentrations in the column effluent: The peak concentration was reached between 3 - 4 PVs, only a small tailing was observed, and after 20 PVs had passed the columns the Eu concentration (C_{Eu}) dropped below the limit of quantification ($LOQ = 4 \cdot 10^{-11} \text{ mol L}^{-1}$). In contrast, Eu transport at $pH_{ini} 5.5$ (FS-iii, Fig. 4.9, $50 \text{ mmol L}^{-1} \text{ Na}_2\text{SO}_4$) resulted in a much longer tailing where the Eu breakthrough occurred between 4 - 6 PVs and the LOQ was not reached after 74 PVs had passed the columns. This finding could imply that desorption processes or diffusion processes from e.g. immobile water/stagnant zones decelerated Eu breakthrough or that concentration-dependent sorption processes took place under the chosen geochemical conditions. Section 4.4.1 discusses whether the first or the latter assumption was more likely to affect Eu BTCs.

The comparison between K_d values of batch and column experiments revealed similar results as had already been observed for quartz: Orthoclase batch experiments returned smaller K_d values compared to K_d values calculated from transport experiment simulations where $K_d = 390 \text{ L kg}^{-1}$ was found for FS-i ($10 \text{ mmol L}^{-1} \text{ NaClO}_4$, $pH_{ini} = 3.6$, Tab. 4.2). The K_d values of batch experiments covered more than three orders of magnitude between pH 3.7 - 5.8 (cf. Fig. 4.11 B): At pH 3.7 batch experiments returned a mean $K_d = 1.6 \text{ L kg}^{-1}$, pH 5.0 corresponded to $K_d \approx 31 \text{ L kg}^{-1}$, pH 5.8 returned a mean $K_d = 2000 \text{ L kg}^{-1}$ (Fig. 4.11 B).

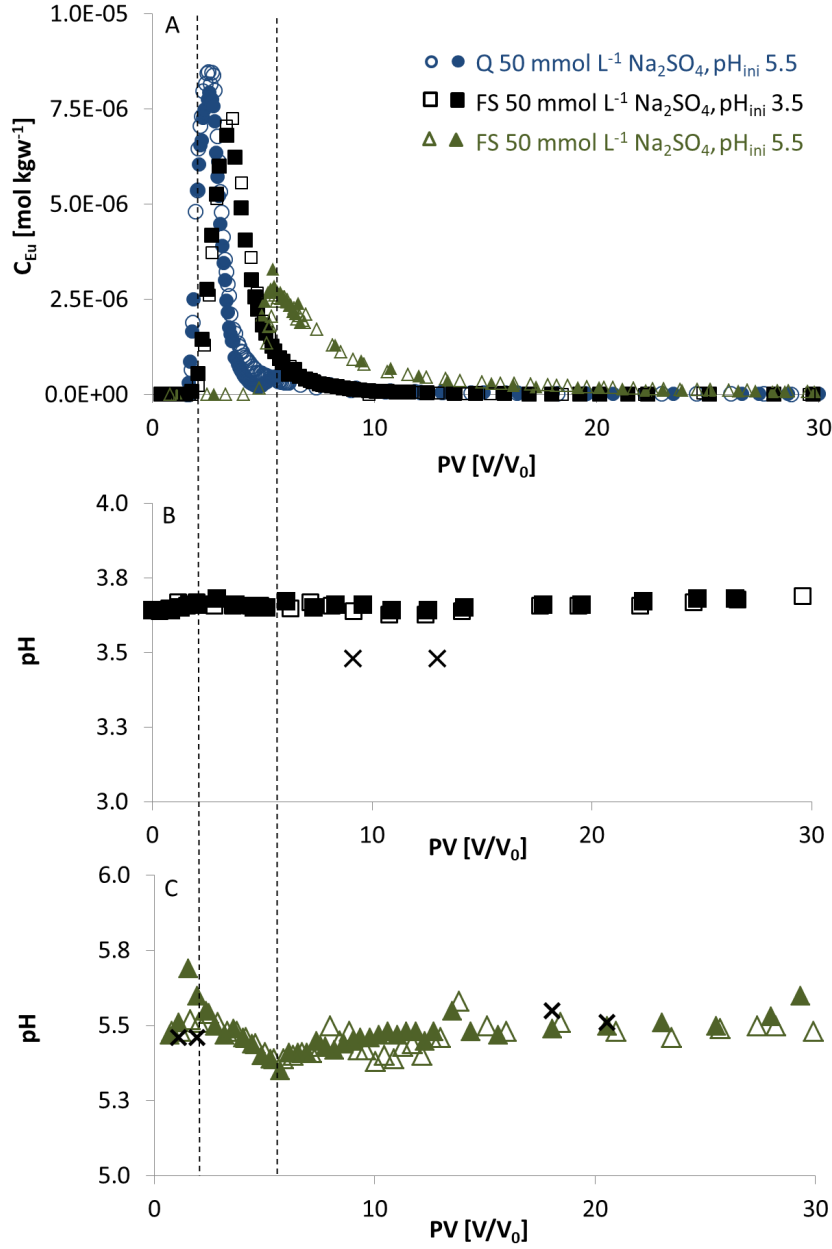


Fig. 4.9: Eu transport through quartz (Q-iv, blue) and orthoclase (FS-ii (black), FS-iii (green)) columns using 50 mmol L⁻¹ Na₂SO₄ background electrolyte, pH_{ini} = 3.5 and 5.5. A: Eu BTCs, B: pH development of FS-ii, C: pH development of FS-iii. Experiments carried out in doublets (solid, empty characters). For experimental details cf. Tables 4.1 and 4.2. Bottom of the column $L = 0$ cm, column top $L = 12.25$ cm, x – pH_{ini}, C_{Eu} – Eu concentration (aq), PV – pore volume, L [cm] – column length.

4.3.3 Muscovite

The comparison of quartz, orthoclase, and mica column experiments yielded a consistent and comprehensive picture of Eu transport: Eu showed highest retardation in muscovite columns (mica-i $R_f = 2600$) followed by orthoclase (FS-i $R_f = 1700$) and quartz (Q-i $R_f = 380$) systems under identical geochemical conditions (10 mmol L⁻¹ NaClO₄ background electrolyte, pH_{ini} \approx 3.5, Fig. 4.10) which agreed well with immobilization tendencies from batch experiments (cf. Fig. 3.12). Figure 4.10 illustrates very strong Eu retention at pH_{ini} 3.6 under inert background electrolyte conditions for the muscovite column which was attributed to cation exchange processes (Eu³⁺ vs. e.g. K⁺, Na⁺, Ca²⁺, Mg²⁺) and which was also in good agreement with conclusions drawn from batch experiments (Sec. 3.3.3). Furthermore, results were corroborated by findings from Pan et al. (2017) who postulated outer-sphere surface complexation (cation exchange processes) to be relevant at pH < 5 for muscovite surfaces. Initial background electrolyte pH values (pH_{ini}) and the effluent pH differed up to \approx 0.3 pH units throughout column experiment mica-i (Fig. 4.10); correlations between surface complexation and pH could not clearly be identified from experimental data.

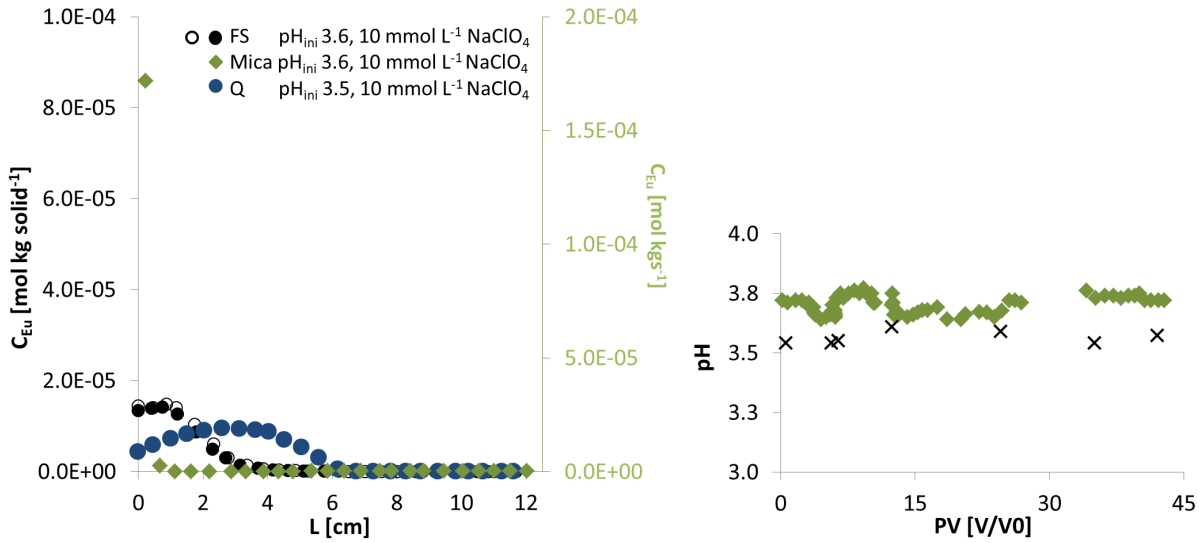


Fig. 4.10: Eu transport through quartz (Q-i), orthoclase (FS-i, black), and muscovite (mica-i) columns using 10 mmol L⁻¹ NaClO₄ background electrolyte, pH_{ini} \approx 3.5. A: Eu SDs of Q-i ($t = 81$ PV, $R_f = 380$), FS-i ($t = 136$ PV, $R_f = 1700$), and mica-i ($t = 42$ PV, $R_f = 2600$), respectively, B: pH development of column experiment mica-i. Experiment carried out in doublets (solid and empty characters). For experimental details cf. Tables 4.1 and 4.2. Bottom of the column $L = 0$ cm, column top $L = 12.25$ cm, x – pH_{ini}, C_{Eu} – Eu concentration (aq), PV – pore volume, L [cm] – column length.

As had already been observed for orthoclase and quartz, muscovite column experiments resulted in larger K_d values compared to batch experiments (Fig. 4.11 C). Under inert background electrolyte conditions, $\text{pH}_{\text{ini}} = 3.6$ transport experiments mica-i returned $K_d = 1400 \text{ L kg}^{-1}$ (Sec. 4.2.3) in relation to batch experiments with a mean $K_d = 21 \text{ L kg}^{-1}$ at $\text{pH} \approx 3.5$ (Fig. 4.11 C, Tab. 4.2). The K_d values of muscovite batch experiments ranged over more than one order of magnitude between pH 3.5 - 5.4: At $\text{pH} \approx 5.4$ the mean $K_d \approx 780 \text{ L kg}^{-1}$; and at $\text{pH} \approx 6.3$ the mean $K_d \approx 2000 \text{ L kg}^{-1}$. Different theories exist trying to resolve the reason for the observed discrepancies (Sec. 4.1); however, the underlying processes and mechanisms have yet to be uncovered.

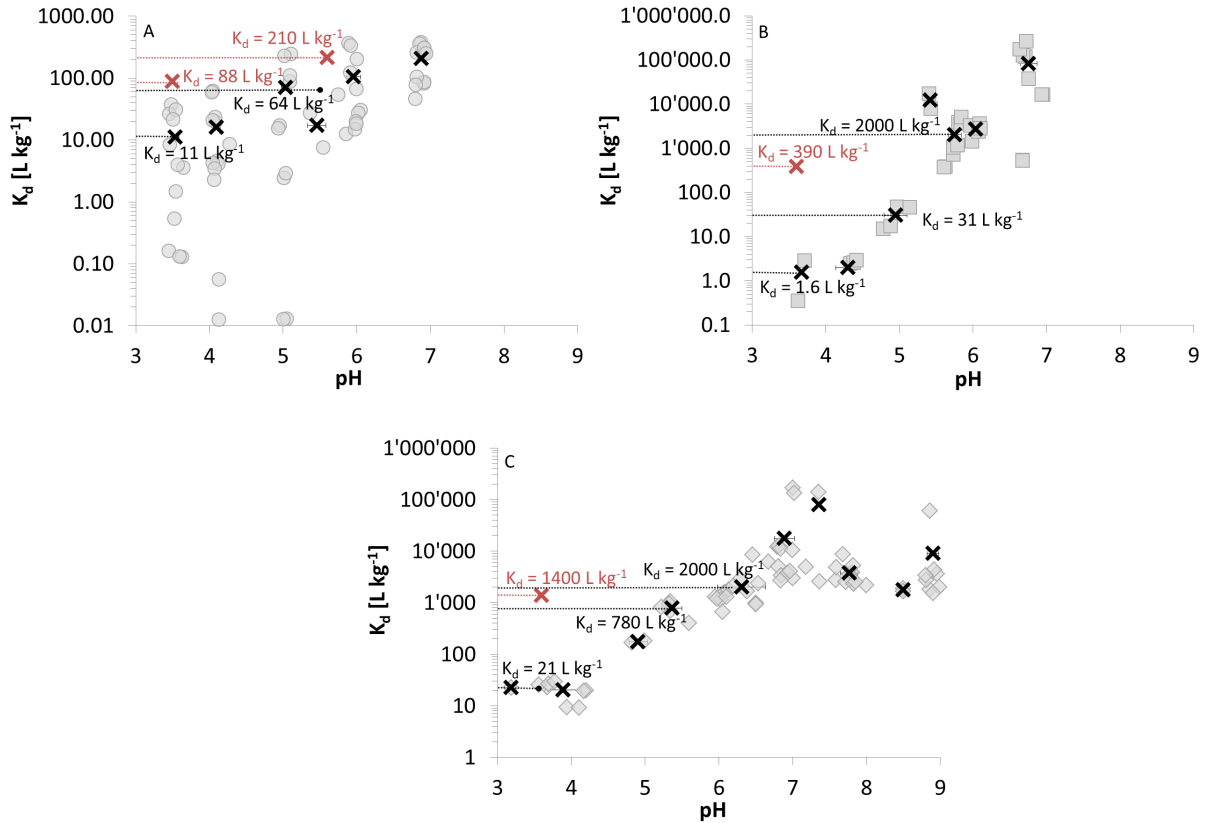


Fig. 4.11: Eu immobilization on quartz, orthoclase, and mica surfaces: Comparison of mean batch (black) and column K_d values (red). Solid grey symbols represent batch results of quartz (A), orthoclase (B), muscovite (C). Black crosses: Mean K_d of batch experiments for the respective pH. Red crosses: Calculated K_d of column experiments (10 mmol L⁻¹ NaClO₄ background electrolyte, Eu $C_0 = 10^{-5} \text{ mol L}^{-1}$), $\text{pH}_{\text{ini}} = 3.5$ available for quartz, orthoclase, muscovite column experiments, $\text{pH}_{\text{ini}} = 5.5$ only available for quartz columns under inert background electrolyte conditions (10 mmol L⁻¹ NaClO₄). Error bars indicate the standard deviation of pH values considered for batch mean K_d values. Ideally K_d values of column and batch experiments overlap.

Figure 4.12 compares the influence of pH and different background electrolytes on Eu migration through muscovite columns: Under inert NaClO_4 conditions at $\text{pH}_{\text{ini}} = 3.6$ (mica-i) Eu was retarded in the first centimetre of the column (Fig. 4.12 A, green, $R_f = 2600$); due to solution speciation with ligand Eu migration was enhanced in the Na_2SO_4 background electrolyte (mica-ii) and in the artificial groundwater (mica-iv) (App. Fig. B.36 - B.37). As had already been observed for quartz column experiments, Eu migrated fastest under the influence of the artificial groundwater at $\text{pH}_{\text{ini}} = 5.5$ (mica-iv, black, $R_f = 400$) in comparison to $5 \text{ mmol L}^{-1} \text{Na}_2\text{SO}_4$ background electrolyte (mica-ii, red, $R_f = 1200$, $\text{pH}_{\text{ini}} 3.6$, cf. Tab. 4.2). This was attributed to an increased competition for sorption and exchange sites between cations in solution (cf. App. Tab. A.1) and Eu (surface complexation), and Na^+ , K^+ , Ca^{2+} , Mg^{2+} , and Eu^{3+} (cation exchange), respectively, resulting in less uptake of Eu in columns equilibrated with the artificial groundwater.

The strong asymmetrical shape for mica-iv ($\text{pH}_{\text{ini}} = 5.5$, artificial groundwater, Fig. 4.12 A) lead to the assumption of potential non linear and/or concentration-dependent sorption processes, kinetic influences, and/or local nonequilibrium conditions in the column. However, as for orthoclase and quartz columns this assumption was further verified with transport simulations (Sec. 4.4.1 and 4.4.2).

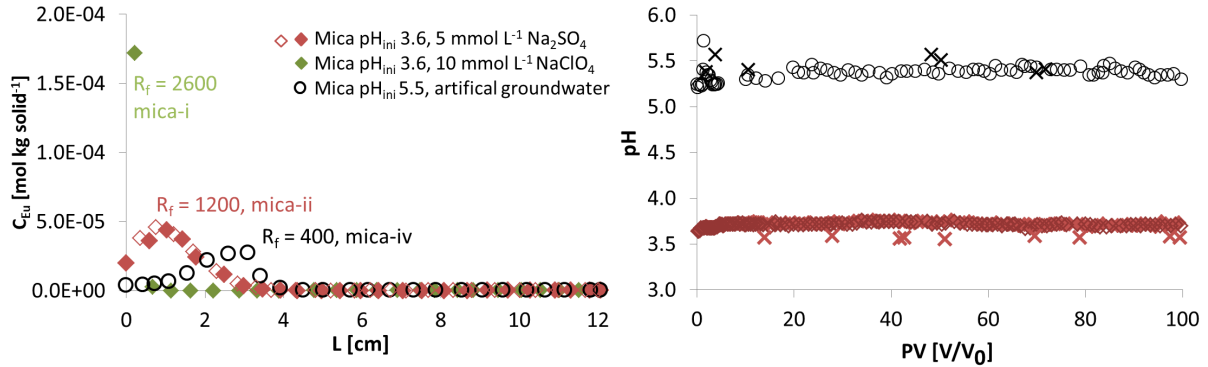


Fig. 4.12: Eu transport through muscovite (mica) columns (mica-i, ii, iv) using $10 \text{ mmol L}^{-1} \text{NaClO}_4$, $5 \text{ mmol L}^{-1} \text{Na}_2\text{SO}_4$, and an artificial groundwater as background electrolytes, $\text{pH}_{\text{ini}} = 3.6$ (red, green) and 5.5 (black). A: SDs of muscovite column experiments: $t = 42 \text{ PV}$ for mica-i, $t = 100 \text{ PV}$ for mica-ii, $t = 123 \text{ PV}$ for mica-iv. Mica-ii carried out in doublets (solid and empty characters). B: pH development of column experiments mica-ii (red) and mica-iv (black), pH development of mica-i cf. Fig. 4.10 B. For experimental details cf. Tables 4.1 and 4.2. Bottom of the column $L = 0 \text{ cm}$, column top $L = 12.25 \text{ cm}$, x – pH_{ini} , C_{Eu} – Eu concentration (aq), PV – pore volume, L [cm] – column length.

Figure 4.13 (A) shows expected Eu retardation trends under identical geochemical boundary conditions for quartz (Q-iv), orthoclase (FS-iii), and muscovite (mica-iii) (50 mmol L⁻¹ Na₂SO₄, pH_{ini} = 5.5): All experiments yielded BTCs due to solution speciation reactions of Eu with the SO₄²⁻ ligand (App. Fig. B.36); furthermore, Q-iv ($R_f = 1.8$) showed the smallest Eu retardation in relation to FS-iii ($R_f = 4.8$) and mica-iii ($R_f = 52$, (Fig. 4.13). No explicit correlation between Eu surface complexation and pH development in the effluent of mica-iii could be observed (Fig. 4.13 B) which might indicate that exchange reactions accounted for Eu retardation in addition to surface complexation on amphoteric surface sites: Inner-sphere surface complexation of Eu ions releases H^+ into the solution which can decrease the effluent pH; cation exchange processes on the other hand, release interlayer cations such as e.g. Na⁺, K⁺ (besides H^+) into the solution which in sum might have only minor influence on the pH since less H^+ is released.

The comparison of mica-ii (5 mmol L⁻¹ Na₂SO₄, Fig. 4.12) and mica-iii (50 mmol L⁻¹ Na₂SO₄, Fig. 4.13) revealed that increasing sulphate concentrations resulted in enhanced Eu transport which was also observed for quartz column experiments in this study (Fig. 4.5 and Fig. 4.7). The correlation between increasing ligand concentration and faster Eu transport was attributed to rising Eu(SO₄)₂⁻ and decreasing Eu³⁺, Eu(SO₄)⁺ concentrations (Fig. B.36) which highly reduce sorption affinities of Eu. Similar observations were reported by Pan et al. (2017) who investigated Eu surface complexation on muscovite inter alia under sulphate influence with batch experiments. Furthermore, mica-ii showed that rising ligand concentrations overruled the effect of increasing pH conditions (Fig. 4.12 and 4.13). Comparable results were observed by Kohler et al. (1996) who amongst others investigated the effect of fluoride complexation on U(VI) transport through quartz columns at different pH values. They found enhanced U(VI) migration with increasing fluoride concentrations that also overruled the effect of rising pH conditions.

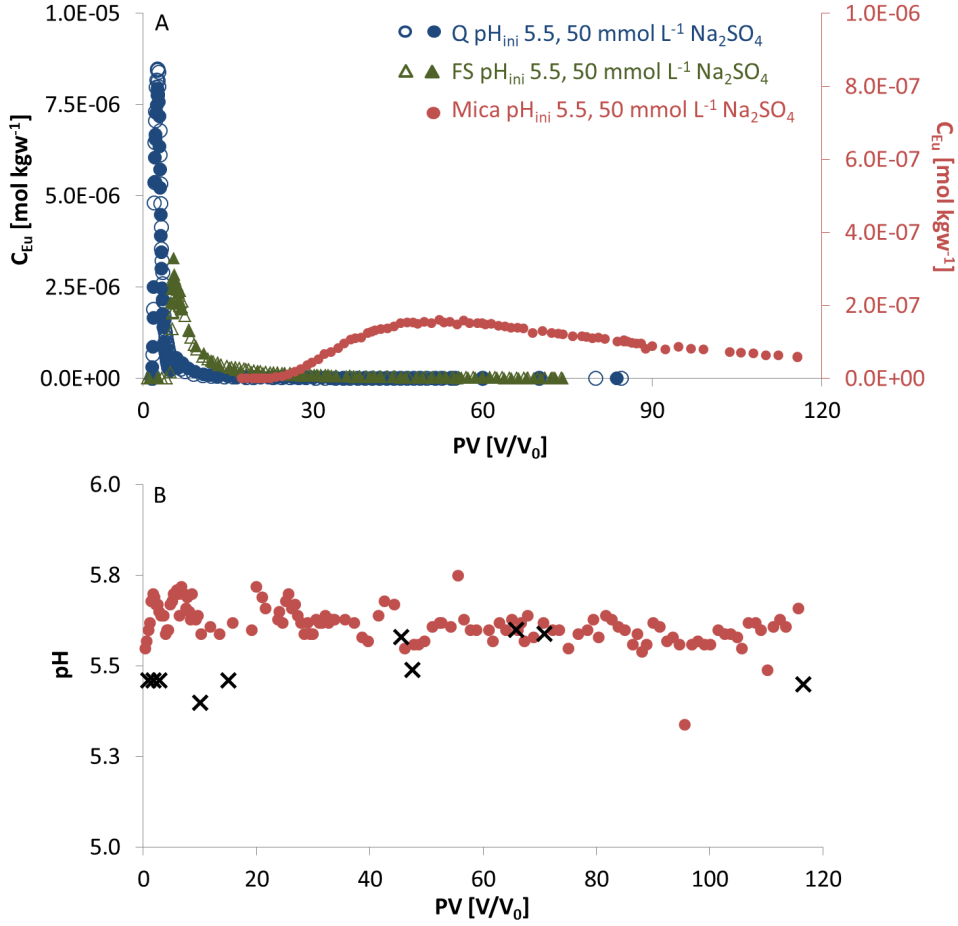


Fig. 4.13: Eu transport through quartz (Q-iv, blue), orthoclase (FS-iii, green), and muscovite (mica-iii, red) columns with 50 mmol L⁻¹ Na₂SO₄ background electrolyte, $pH_{ini} = 5.5$. Only FS-iii and Q-iv carried out in doublets (solid and empty characters). A: Eu BTCs of Q-iv, FS-iii, and mica-iii, respectively. B: pH development of mica-iii. For experimental details cf. Tables 4.1 and 4.2. x denotes pH_{ini} , C_{Eu} – Eu concentration (aq), PV – pore volume.

4.3.4 Synthetic sediment

A comparison of column experiments with muscovite, orthoclase, quartz, and the synthetic sediment (SynSed) revealed a sound picture of Eu retardation processes (Fig. 4.14, App. Fig. B.41): For column experiment SynSed-i (Tab. 4.1) $R_f = 1800$ which was 4.7 times larger compared to Q-i ($R_f = 380$), similar to the retardation in orthoclase (FS-i $R_f = 1700$), but smaller than Eu retardation in muscovite columns (mica-i $R_f = 2600$) under identical geochemical conditions (10 mmol L⁻¹ NaClO₄, $pH_{ini} = 3.5$). This implied that transport was governed by surface reactions on muscovite and/or orthoclase surfaces

even though both minerals contributed only 10 wt% each. Muscovite batch experiments revealed that at pH 3.5 approximately 20% Eu was immobilized due to cation exchange processes (Sec. 3.3.3), whereas orthoclase batch experiments showed Eu immobilization below 3.5% at comparable geochemical conditions (Fig. 3.12). Quartz batch experiments also returned high relative Eu uptake at low pH values but only for small initial Eu concentrations (C_0) (Fig. 3.12, Sec. 3.3.1); for Eu $C_0 = 10^{-5}$ mol L⁻¹ retardation decreased to below 5% at pH ≤ 4 (Sec. 3.3.1, Fig. 3.12). Hence, Eu retardation in synthetic sediment column experiments at pH_{ini} \approx 3.5 were mainly attributed to cation exchange processes at the muscovite surface, retardation on quartz and orthoclase probably contributed minor. No pH variation of the effluent was observed (App. Fig. B.41) which was due to the high H^+ concentration of the background electrolyte (pH_{ini} \approx 3.5).

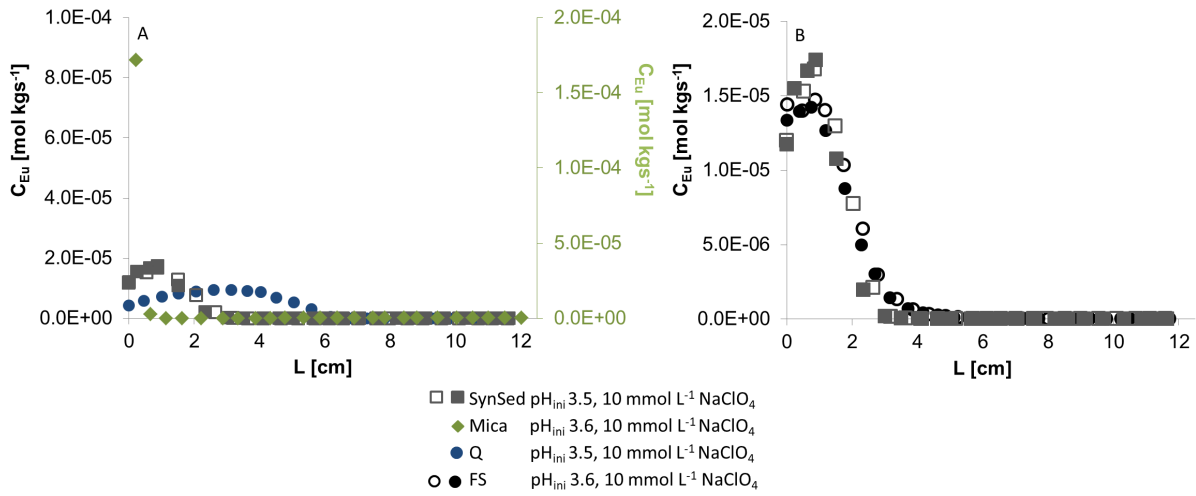


Fig. 4.14: Eu transport through A: quartz (Q-i, blue, $t = 81$ PV, $R_f = 380$), muscovite (mica-i, green, $t = 42$ PV, $R_f = 2600$), and synthetic sediment (SynSed-i, grey, $t = 122$ PV, $R_f = 1800$) columns using 10 mmol L⁻¹ NaClO₄ background electrolyte, pH_{ini} \approx 3.5; and B: comparison of FS-i (black) and SynSed-i (10 mmol L⁻¹ NaClO₄, pH_{ini} \approx 3.5). Experiments carried out in doublets (solid and empty characters). For experimental details cf. Tables 4.1 and 4.2. Bottom of the column L = 0 cm, column top L = 12.25 cm, x - pH_{ini}, C_{Eu} - Eu concentration (aq), PV - pore volume, L [cm] - column length.

In column experiment SynSed-ii (close to nature geochemical boundary conditions: pH_{ini} = 5.5, artificial groundwater) Eu was stronger retarded ($R_f = 120$) compared to Q-v ($R_f = 16$) but less retarded in relation to Eu transport through pure muscovite columns (mica-iv $R_f = 390$) under identical conditions (Fig. 4.15 A, B). These findings agreed well with batch and previous column experiments (Fig. 3.12, Sec. 4.3.1 - 4.3.3). Variations

of the pH in the effluent of SynSed-ii showed a similar pH development compared to orthoclase and quartz columns: The pH decreased gradually and reached lowest values as the Eu peak occurred; as the bulk Eu concentration left the column pH values in the effluent increased and returned to pH_{ini} (Fig. 4.15 C, cf. Fig. 4.9 and Fig. 4.4).

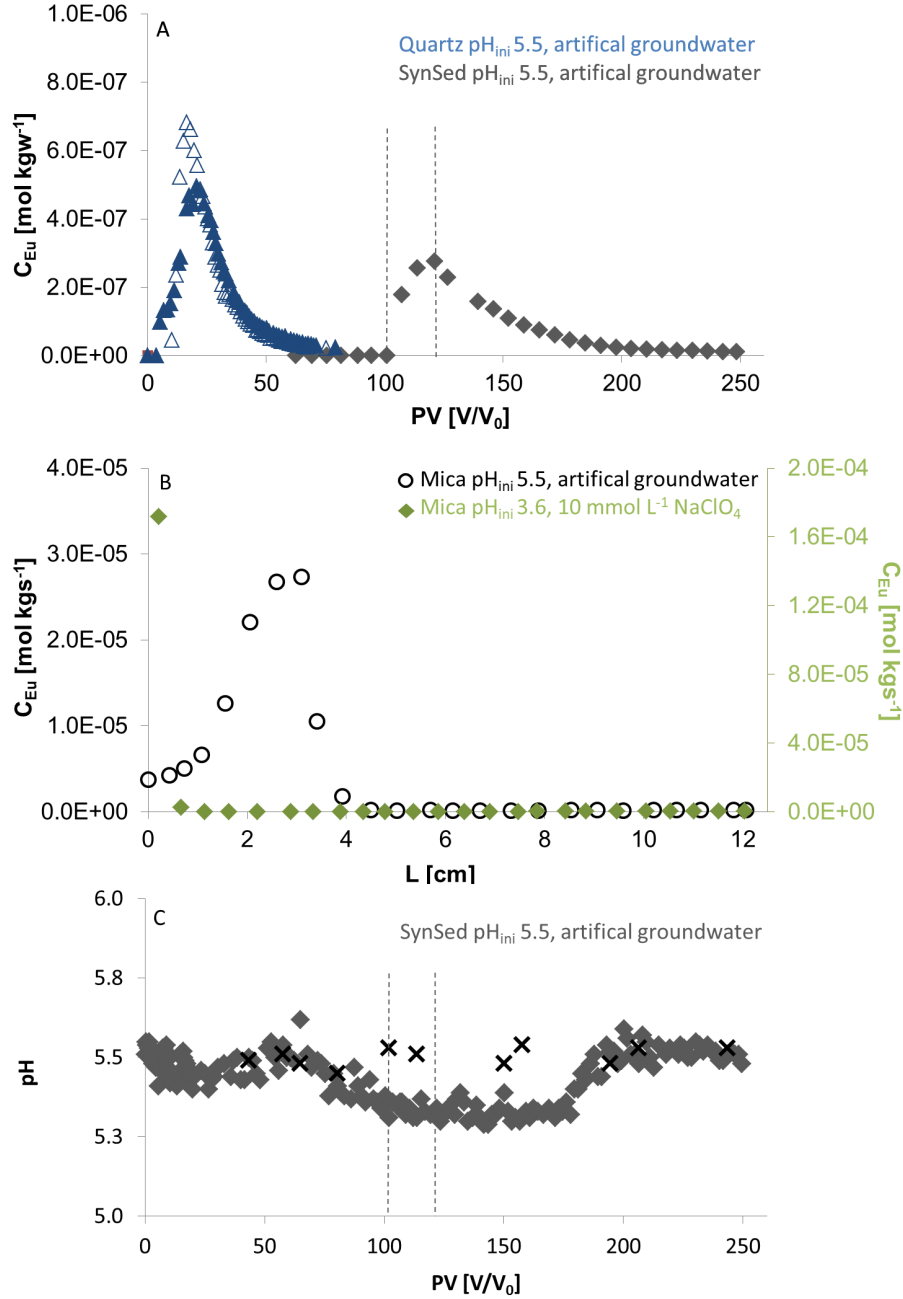


Fig. 4.15: A: Eu BTC of Q-v (quartz) and SynSed-ii (synthetic sediment). B: Eu SD of mica-iv (mica, black open circles, $t = 123$ PV, $R_f = 390$) and mica-i ($t = 42$ PV, $R_f = 2600$). C: pH development of SynSed-ii. Q-v carried out in doublets (solid and empty characters). For experimental details cf. Tables 4.1 and 4.2. Bottom of the column $L = 0$ cm, column top $L = 12.25$ cm, x - pH_{ini} , C_{Eu} - Eu concentration (aq), PV - pore volume, L [cm] - column length.

Transport experiments with the synthetic sediment and artificial groundwater at $\text{pH}_{ini} = 5.5$ (SynSed-ii) implied that Eu was transported approximately 2.6 m a^{-1} under close to nature experimental conditions ($v = 3.58 \text{ cm h}^{-1}$, $R_f = 120$, cf. Tab. 4.2). However, this approximation should not be taken as an indication for lanthanide or actinide migration velocity in natural groundwater systems for the following reasons:

- To ensure feasible experimental time frames the pH of transport experiments was reduced by approximately 2 pH units compared to natural conditions proposed by Klinge et al. (2002) (pH 6 - 8). Hence, Eu transport under natural conditions would be expected to result in significantly higher retardation and smaller transport velocities due to enhanced surface complexation under increased pH conditions.
- Furthermore, the synthetic sediment was free of humic substances and did not include clay fractions which could additionally contribute to immobilization but also mobilization processes of the trivalent lanthanide in natural groundwater systems.
- In addition to sulphate phosphate is another ubiquitously present ligand in natural systems and tends to form solution complexes with Eu (Pan et al., 2017). In contrast to sulphate, Eu phosphate complexes in solution enhance sorption affinities and ternary Eu phosphate surface complexes could form on mica surfaces (Pan et al., 2017). This process also contributes to Eu retardation and was not considered in the present study.

However, results of these transport experiments are relevant for first verifications of predictive transport simulations using optimized SCPs from SCMs and provide information to verify the CA approach which should be subject to future research projects. These results must not be taken to draw final conclusions for transport processes of trivalent actinides and lanthanides in natural groundwater systems of potential radioactive waste repository sites since experiments were conducted only as a first approach by using close to nature geochemical boundary conditions; they do not reflect natural systems in detail.

4.4 Results and discussion of 1D reactive transport simulations

In the following, transport parameter optimizations with CXTFIT (Sec. 4.4.1) and Eu reactive transport simulations with PHREEQC through homogeneous porous quartz and orthoclase columns are presented, compared, and discussed. As it was not possible to correctly describe the cation exchange for muscovite under the given geochemical

conditions (Sec. 3.3.3) RTMs could only be developed for the pure quartz and orthoclase systems; experiments with muscovite and the synthetic sediment (80 wt% quartz, 10 wt% muscovite and orthoclase) had to be excluded from transport studies and should be subject for future research projects. As a consequence, it was not possible either to apply or verify the CA approach in this study and the simulation of Eu reactive transport processes based on the CA approach through the synthetic sediment had to also be postponed.

Tables 4.2, 4.3, and 4.4 summarize major findings of transport simulations: Table 4.2 compares transport parameters from measurements with fitted ones (CXTFIT model); Tables 4.3 and 4.4 compare K_d values from simulated Eu transport with K_d values from experimental data (cf. Sec. 4.2.3). Additional information supply Appendix A.12.3 and Figures B.43 - B.48 in Appendix B.

4.4.1 Transport parameter determination from Br breakthrough curves

Parameter optimizations with CXTFIT transport models yielded adequately fitted transport parameters for all column experiments which was characterized by mean squared errors (*MSEs*) on the ppm (parts per million) scale (cf. Tab. 4.2). Therefore, fitting results of two Br BTCs (Q-iii, Q-vi: 5 mmol L⁻¹ Na₂SO₄, pH_{ini} ≈ 5.5) are exemplarily illustrated and discussed in the following section. A summary of all fitted transport parameters including goodness of fit (gof) provides Table 4.2; CXTFIT models and fitting results of remaining column experiments may be obtained from the digital appendix.

Transport parameter optimization of column experiment Q-iii with CXTFIT returned a very small dispersion coefficient ($D = 0.23 \text{ cm}^2 \text{ h}^{-1}$) and hence a small dispersivity $\lambda = 0.06 \text{ cm}$ (App. Eq. A.57) which ranged on the mm scale indicating that the column was homogeneously packed without preferential pathways (App. Fig. 4.16, Tab. 4.2). Potential influences of dead end pores or dispersion processes (including diffusion) played therefore also only minor roles during transport experiments. The large Péclet number of ≈ 250 (Tab. 4.2, App. Eq. A.55) indicated that transport processes in the column were strongly dominated by advection.

For Q-iii fitting procedures, the dispersion coefficient D , the pore water velocity v [cm h⁻¹] and the application time of the pulse solution t [h] served as adjustable parameters. Optimizations returned a time difference of 0.3 h between the fitted application time $t = 5.3 \text{ h}$ and the experimental application time $t = 5.0 \text{ h}$ (initial value) which was attributed to an erroneously determined dead volume (Sec. 4.2.2); the fitted v returned

$3.68 \pm 0.08 \text{ cm h}^{-1}$ which agreed well with measurements where $v = 3.61 \pm 0.11 \text{ cm h}^{-1}$. Since the flow rate was precisely measured the pore water velocity v was assumed to be accurate which was substantiated with the CXTFIT optimization procedure. The time difference between measured and fitted application time of the pulse solution t was attributed to the stepwise packing procedure (Sec. 4.2.1): It was assumed that due to the compaction of the mineral in the columns the space in front of the frits was individually reduced for each experiment. Hence, the application of an identical dead volume of the frits for each column experiment (Sec. 4.2.2) turned out to be unfavourable and resulted in biased corrections of BTCs. For future column experiments the dead volume of the frits should be individually determined for each experiment to exclude this potential error source.

Using D and v (without t) as adjustable parameters for fitting approaches of erroneously corrected Br BTCs resulted in substantial discrepancies between measured and fitted water flow velocities (Δv) which can be explained with the following example: The smaller the pore volume of a column V_0 (e.g. underestimation of the dead volume), the faster the water flow velocity is required to transport the same volume/amount of e.g. pulse solution through the column in an identical application time t . Hence, differences in optimized and experimental v indicate dead pore space, air intrusions in the column, or incorrectly determined dead volume (Sec. 4.2.2). As each column was saturated under vacuum conditions (Sec. 4.2.1) the columns were fully saturated and it could be assumed that e.g. air intrusions did not occur. Furthermore, Br BTCs did not show pronounced tailings which was substantiated with small dispersivities λ and indicated an erroneously defined dead volume. Hence, the application time t [h] was included in optimization procedures which resulted in differences between optimized and measured application times t for columns with erroneous dead volume (up to 0.3 h). Using three fitting parameters (D, v, t) was only applied for quartz column experiments and revealed a consistent picture of Br BTCs where Δv equalled only 2% on average. However, as v was calculated from the measured flow rate, for orthoclase and muscovite only D and if necessary t were used as fitting parameters (cf. 4.2). Since the discrepancies between fitted and measured application time t could be comprehensively explained the approach to include t as an adjustable parameter was justified for this study.

Since the shape of tracer BTCs and the dispersivity λ should be independent of the pore water velocity v for ideal tracers and homogeneous columns, column experiment Q-iii was repeated with the identical geochemical boundary conditions but with v reduced by factor 2.7 (Q-vi). It was also the aim to verify whether the shape of the SD of column

Tab. 4.2: Summary of transport parameters of quartz (Q-i – Q-vi), orthoclase (O-i – O-iii), muscovite (mica-i – mica-iv), and synthetic sediment (SynSed-i, SynSed-ii) column experiments. Errors of the measured pore water velocity v given as the single standard deviation $[\text{cm h}^{-1}]$. R_f , K_d calculated from measurements. Parameter uncertainties of CXTFIT optimizations represent 95% confidence intervals. Appendix A.12.3 provides additional information for [1] – [7]. Dispersivity was used in PHREEQC simulations as a fixed transport parameter and was calculated with D from CXTFIT fits following Eq. A.57 ([6]) in Appendix A.12.3. For PHREEQC $Pe_{grid} < 2$ to prevent numerical dispersion. - indicates that the parameter was not used for CXTFIT optimization. PV – pore volume, art. GW – artificial groundwater, $C_{Eu,Br}$ – Eu, Br concentration (aq), PS – pulse solution, BE+PS – background electrolyte + pulse solution in PV $[V/V_0]$, Δv – difference between fitted (CXTFIT) and measured v .

			Quartz						Orthoclase			Muscovite				SynSed	
			Q-i	Q-ii	Q-iii	Q-iv	Q-v	Q-vi	FS-i	FS-ii	FS-iii	mica-i	mica-ii	mica-iii	mica-iv	SynSed-i	SynSed-ii
Measurements																	
Background electrolyte		$[\text{mmol L}^{-1}]$	NaClO ₄	NaClO ₄	Na ₂ SO ₄	Na ₂ SO ₄	art. GW	Na ₂ SO ₄	NaClO ₄	Na ₂ SO ₄	Na ₂ SO ₄	NaClO ₄	Na ₂ SO ₄	Na ₂ SO ₄	art. GW	NaClO ₄	art. GW
			10	10	5	50	App. Tab. A.1	5	10	50	50	10	5	50	App. Tab. A.1	10	App. Tab. A.1
Pulse solution	C_{Eu}	$[\text{mol L}^{-1}]$	1.1·10 ⁻⁵	1.1·10 ⁻⁵	1.0·10 ⁻⁵	9.5·10 ⁻⁶	9.2·10 ⁻⁶	1.0·10 ⁻⁵	1.0·10 ⁻⁵	1.0·10 ⁻⁵	1.1·10 ⁻⁵	1.0·10 ⁻⁵	9.9·10 ⁻⁶	9.6·10 ⁻⁶	9.8·10 ⁻⁶	1.0·10 ⁻⁵	9.9·10 ⁻⁶
	C_{Br-}	$[\text{mol L}^{-1}]$	7.5·10 ⁻⁶	9.0·10 ⁻⁶	1.2·10 ⁻⁵	1.0·10 ⁻⁵	8.8·10 ⁻⁶	1.0·10 ⁻⁵	9.1·10 ⁻⁶	1.1·10 ⁻⁵	9.8·10 ⁻⁶	1.0·10 ⁻⁵	1.0·10 ⁻⁵	8.5·10 ⁻⁶	7.5·10 ⁻⁶	8.7·10 ⁻⁶	1.0·10 ⁻⁵
pH _{ini}		$[-]$	3.5	5.6	5.6	5.5	5.5	5.5	3.6	3.5	5.5	3.6	3.6	5.5	5.5	3.5	5.5
BE+PS	PV	$[V/V_0]$	81	75	80	85	80	94	136	60	75	42	100	116	123	122	250
Application time PS	t	$[h]$	5.2	5.0	5.3	5.0	5.3	15	4.7	4.6	4.7	8.3	7.8	7.2	7.2	4.6	5.1
Pore water velocity ^[3]	v	$[\text{cm h}^{-1}]$	3.61	3.63	3.47	3.64	3.42	1.309	3.59	3.94	3.92	1.53	2.34	2.600	2.55	3.43	3.58
			±0.11	±0.11	± 0.04	±0.101	±0.05	±0.04	±0.07	±0.05	±0.08	±0.07	±0.04	±0.03	±0.13	±0.06	±0.06
Darcy velocity ^[2]	q	$[\text{cm h}^{-1}]$	1.38	1.39	1.32	1.39	1.31	0.499	1.33	1.36	1.35	0.924	1.35	1.49	1.47	1.31	1.37
Bulk density ^[7]	ρ_b	$[\text{g cm}^{-3}]$	1.64	1.64	1.64	1.64	1.64	1.64	1.63	1.64	1.64	1.13	1.19	1.19	1.19	1.64	1.64
Total pore space ^[1]	V_0	$[\text{cm}^{-3}]$	61.7	61.7	61.7	61.7	61.7	61.7	55.97	55.9	55.7	96.2	92.9	92.9	92.9	61.8	61.9
Total porosity	θ	$[\text{cm}^3/\text{cm}^{-3}]$	0.382	0.382	0.382	0.382	0.382	0.381	0.371	0.346	0.345	0.604	0.574	0.575	0.575	0.381	0.382
Recovery rate Eu		$[\%]$	97	96	90	100	105	100	95	95	103	101	101	67	96	94	105
Recovery rate Br-			102	98	100	95	94	96	102	102	100	98	101	98	97	98	100
Retardation factor	R_f	$[-]$	380	920	190	1.8	16	210	1700	2.6	4.8	2600	1200	52	390	1800	120
Distribution coefficient	K_d	$[\text{m}^3 \text{ kg}^{-1}]$	8.8E-02	2.1E-01	4.5E-02	1.8E-04	3.4E-03	5.0E-02	3.9E-01	3.4E-04	7.9E-04	1.39	5.7E-01	2.4E-02	1.9E-01	4.1E-01	2.8E+01
		$[\text{L kg}^{-1}]$	88	210	45	0.18	3.4	49.7	390	0.34	0.79	1400	570	24	190	410	410
CXTFIT																	
Dispersion coefficient	D	$[\text{cm}^2 \text{ h}^{-1}]$	0.23	0.13	0.17	0.28	0.095	0.06	0.502	0.296	0.297	0.054	0.201	0.28	0.1602	0.35	0.11
			±0.097	±0.05	±0.08	±0.19	±0.09	-	± 0.29	±0.3	±0.17	±0.03	±0.06	±0.09	±0.05	±0.13	±0.04
Péclet number ^[4]	Pe	$[-]$	190	346	249	162	440	267	88	163	162	350	143	116	195	120	409
Pore water velocity	v	$[\text{cm h}^{-1}]$	3.68	3.60	3.50	3.83	3.59	1.35	-	-	-	-	-	-	-	-	3.50
			±0.08	±0.03	±0.07	±0.11	±0.106	±0.03	-	-	-	-	-	-	-	-	±0.04
	Δv	$[\text{cm h}^{-1}]$	0.067	-0.0304	0.032	0.18	0.17	0.039	-	-	-	-	-	-	-	-	-0.084
Application time PS	t	$[h]$	5.1	-	5.0	-	4.7	14.9	4.5	4.9	4.8	8.0	-	-	-	-	-
			±0.095	-	±0.098	-	±0.14	±0.29	±0.13	±0.17	±0.09	±0.14	-	-	-	-	-
Coefficient of determination	R^2	$[-]$	0.991	0.993	0.991	0.978	0.972	0.988	0.984	0.964	0.991	0.985	0.994	0.993	0.994	0.994	0.996
Mean square error	MSE	$[\text{mg L}^{-1}]$	3.7E-04	3.6E-04	1.1E-03	1.7E-03	1.6E-03	8.7E-04	1.3E-03	4.6E-03	1.0E-03	1.5E-03	6.1E-04	5.5E-04	3.4E-04	4.7E-04	5.2E-04
Optimized parameters			v, D, t	v, D	v, D, t	v, D	v, D, t	v, t	D, t	D, t	D, t	D, t	D	D	D	D	v, D
PHREEQC																	
Dispersivity ^[6]	λ	$[\text{cm}]$	0.06	0.04	0.05	0.07	0.03	-	0.14	0.08	0.08	-	-	-	-	-	-
Grid Péclet number ^[5]	Pe_{grid}	$[-]$	1.1	1.9	1.4	0.9	2.6	-	0.5	0.9	0.9	-	-	-	-	-	-

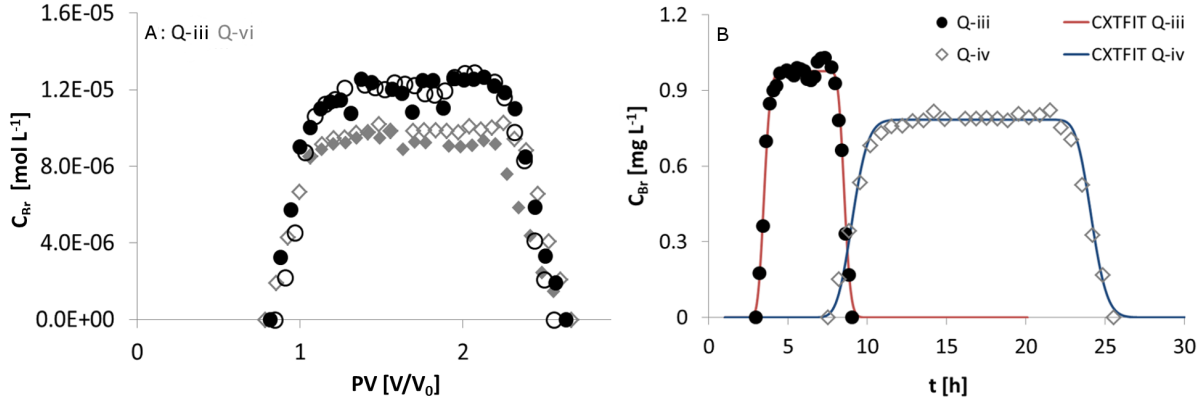


Fig. 4.16: A: Experimental Br BTCs (black, grey symbols) of Q-iii and Q-vi. B: Experimental and fitted BTCs of Q-iii (red line = fit with $q = 84 \text{ cm d}^{-1}$) and Q-vi (blue line = fit with $q = 32 \text{ cm d}^{-1}$) (Tab. 4.1). Reduced Br C_0 of Q-vi due to new pulse solution preparation. The time lag of both BTCs resulted from reduced pore water velocities by factor 2.7 for Q-vi. Table 4.2 provides further information including optimized transport parameters. t [h] - considered experimental time frame.

experiment Q-iii (Fig. 4.5) was caused by dispersion and/or diffusion influences or rather by concentration dependent surface complexation (cf. Sec. 4.3.1, pg. 4.3.1 - 4.3.1). As illustrated in Figure 4.16 A the shape of the Br BTCs did not change with reduced v and CXTFIT results of Q-vi indicated that λ did not differ with decreasing v either (Fig. 4.16 B). Using D as a fix parameter that was reduced by factor 2.7 ($D = 0.06 \text{ cm}^2 \text{ h}^{-1}$) in relation to the optimized D of column Q-iii ($D = 0.17 \text{ cm}^2 \text{ h}^{-1}$) resulted in an acceptable fit (Tab. 4.2, Fig. 4.16 B) and substantiated the assumption that the dispersivity λ was independent from the pore water velocity.

All Eu transport experiments resulted in similar ideal Br tracer BTCs (App. Fig. B.39 - B.42, Sec. 4.3.1); hence, the following conclusions drawn from column Q-iii and Q-vi were assumed to be applicable to all column experiments:

- The columns were homogeneously packed, advective transport dominated the system.
- The occurrence of stagnant zones, dead end pores, or preferential path ways could be excluded due to dispersivities λ on the mm scale.
- The dead volume carried incalculable errors for many column experiments which resulted in application time differences between fitted and measured values.
- The dispersivity was independent of v substantiating the fact that columns were homogeneously packed without preferential path ways and negligible diffusion and/or dispersion processes.

To conclude, based on Br tracer BTCs the asymmetrical shapes of Eu BTCs or SDs (Fig. 4.5, 4.9, 4.12) as well as differences in K_d values between batch and column experiments could not be attributed to high dispersivities or diffusion from stagnant zones, inhomogeneously packed columns, or local nonequilibrium. Hence, concentration-dependent surface complexation and/or interrelation between surface complexation reactions and solution composition (e.g. interaction of pH and surface complexation) presumingly governed Eu migration under the given geochemical conditions. Both of the latter effects had already been observed during batch (Fig. 3.12: concentration dependence) and column experiments (Fig. 4.4: interrelation between Eu transport and pH).

4.4.2 1D reactive Eu transport simulations

Experimental results from batch and column experiments revealed large differences in calculated K_d values (Sec. 4.2.3) which covered over three orders of magnitude for orthoclase and up to two orders of magnitude for quartz and muscovite (cf. Fig. 4.11). Hence, it was refrained from using batch experiments to predict Eu transport with an empirical approach such as the linear K_d due to the large discrepancies that occurred between batch and column experiments. Furthermore, it could be assumed that transport experiments which revealed spatial and temporal pH variations due to Eu surface complexation could not be represented by the empirical K_d approach neither since geochemical interactions and hence, potentially variable sorption affinities over the experimental time frame of the column experiments cannot be represented with the linear (constant) K_d approach. Consequently, this study focused on mechanistic reactive transport model simulations of Eu using SCPs sets from batch experiments.

Transport simulations of quartz column experiments pH_{ini} 3.5 (Q-i)

Reactive transport simulations of Q-i resulted in BTCs regardless of the SCM and SCP set (App. Fig. B.44, Tab. 3.4) whereas measurements returned a SD for Eu retardation (quartz, 10 mmol L⁻¹ NaClO₄, pH_{ini} 3.5, Fig. 4.2). The mean calculated R_f value over all simulation approaches equalled 2 ± 1 (standard deviation, App. Fig. B.44) showing that predicted Eu migration was retarded only by factor two on average in comparison to the ideal Br tracer (R_f from column experiment Q-i = 380, cf. Tab. 4.2). Differences between predictions and experimental data expressed in $|\Delta \log K_d|$ (Sec. 4.2.5) exceeded at least 2 for all simulations (Tab. 4.3) representing unsatisfying predictions (Davis et al. (2005), cf. Sec. 4.2.5). The following reasons were identified for insufficient RTM

performance: All SCMs underestimated Eu immobilization during batch experiments at low pH values (Sec. 3.3.1) which consequently resulted in an underestimation of predicted Eu transport through quartz columns at low pH. Furthermore, pH_{ini} 3.5 of column experiments represented the lower pH range covered by batch experiments where only very few data was available for SCM calibrations. Hence, extrapolation of SCPs to geochemical conditions that were not profoundly substantiated by batch data failed.

Transport simulations of quartz column experiments $\text{pH}_{\text{ini}} \approx 5.5$ (Q-ii - Q-v)

Table 4.3 compares K_d values from measurements and reactive transport simulations of quartz column experiments Q-i – Q-v (cf. Tab. 4.1); green values represent an acceptable discrepancy ($|\Delta \log K_d|$) between experiments and predictions below $0.5 \log K_d$, orange values ranged within $0.5 - 1.0 \log K_d$, and red values exceed $1.0 \log K_d$ (Davis et al., 2005). According to Davis et al. (2005) predictions where $0.5 \leq |\Delta \log K_d| \leq 1$ between measurements and simulations applies demonstrate profound system understanding. Discrepancies that exceed $1 \log K_d$ unit represent insufficient predictions of measurements. In Table 4.3, negative $\Delta \log K_d$ s indicate stronger retention of simulated Eu transport in comparison to K_d values from measurements, positive values represent less retardation with respect to experimental data (Sec. 4.2.3).

Tab. 4.3: Summary of K_d values calculated from experimental data and reactive transport simulations of quartz column experiments (Q-i - Q-v). Differences between K_d values from measurements and predictions are provided as $\Delta \log K_d$. A transport simulation proves system understanding if $0.5 \leq |\Delta \log K_d| \leq 1$ (Davis et al., 2005): $|\Delta \log K_d| \geq 1$, $0.5 \leq |\Delta \log K_d| \leq 1$, $|\Delta \log K_d| < 0.5$. For details on SCMs cf. Section 3 and Table 3.4. * PHREEQC converge problems after 50 PVs. K_d [L kg⁻¹] – calculated distribution coefficient (cf. Sec. 4.2.3).

	Q-i		Q-ii		Q-iii		Q-iv		Q-v	
	K_d	$\Delta \log K_d$	K_d	$\Delta \log K_d$	K_d	$\Delta \log K_d$	K_d	$\Delta \log K_d$	K_d	$\Delta \log K_d$
Experimental K_d	88		214		45		0.18		4.4	
SCP Q I bi	0.041	3.3	200	0.028	18	0.39	7.7	-1.6	34	-0.89
SCP Q I mono+bi	0.17	2.7	58	0.57	5.6	0.902	2.8	-1.2	8.2	-0.27
SCP Q noEDLM mono	0.76	2.1	188	0.06	9.7	0.66	1.9	-1.01	55	-1.09
SCP Q II mono	0.14	2.8	48	0.65	7.04	0.802	2.9*	-1.2*	21	-0.67
SCP Q II bi	0.047	3.3	119	0.25	20.1	0.35	3.09	-1.2	43	-0.99

Column experiment Q-ii (10 mmol L⁻¹ NaClO₄, pH 5.6) was satisfactorily predicted with all SCP sets (Tab. 4.3, Fig. 4.17); best results were obtained with *SCP Q I bi* for Q-ii (DDLm, bidentate surface complex). The shape of the SD, the maximum peak concentration (C_{max}), as well as the pH development were accurately predicted with

SCP Q I bi (Fig. 4.17 Q-ii); all RTMs described the initial drop in pH due to surface complexation which returned to pH_{ini} during the course of the simulations. The noEDLM also yielded a satisfying simulation; however, the prediction did not reflect the shape of the SD nor C_{max} adequately (Fig. 4.17 Q-ii).

Transport experiment Q-iii (5 mmol L⁻¹ Na₂SO₄, pH 5.6) was also adequately simulated with all SCMs; here, best results with the smallest $|\Delta \log K_d|$ values yielded *SCP Q I bi* (DDLm, bidentate surface complex) and *SCP II bi* (BSM, bidentate surface complex). Only RTMs using bidentate surface complexes yielded SDs where the position of the maximum Eu concentration ($L_{C_{max}}$) was predicted in the column, all other approaches resulted in BTCs within the experimental time frame of 80 PVs (App. Fig. B.45 A). For *SCP II bi* the maximum Eu concentrations C_{max} [mol kgs⁻¹] as well as the shape of the SD were adequately predicted (steeper front compared to a more shallow back of the SDs); however, the spatial position $L_{C_{max}}$ was accelerated in comparison to measurements. Hence, RTMs underestimated Eu immobilization which was the case for all simulation approaches (Fig. 4.17 Q-iii, App. Fig. B.45). Each RTM predicted an initial pH decrease for Q-iii that could not be substantiated with pH measurements (Fig. 4.17 Q-iii). However, the discrepancy faded after 5 PVs and the simulations returned to $\text{pH}_{ini} = 5.6$ (Fig. 4.17 Q-iii). In the following (> 20 PVs), peaks of predicted pH developments of *SCP Q I mono+bi*, *SCP Q noEDLM mono*, and *SCP Q II mono* as well as *SCP Q I bi* coincided with simulated BTCs (App. Fig. B.45 B) as had already been observed from experiments (cf. Fig. 4.4).

Quartz transport experiments carried out with 50 mmol L⁻¹ Na₂SO₄, $\text{pH}_{ini} = 5.5$ (Q-iv) could not be satisfyingly predicted with RTMs; neither the shape, nor C_{max} [mol L⁻¹] were adequately predicted which was evidenced by $\Delta \log K_d > 1$ (Tab. 4.3, Fig. 4.17 Q-iv). Furthermore, the RTM that was based on *SCP Q II bi* revealed convergence problems after ≈ 50 PVs had passed the column and returned major surface charge imbalances as well as non converging mass balances for Na⁺, sulphate, and the ionic strength (IS) which implied that the RTM was ill-defined. Whether the non-convergence was exclusively caused by the surface charge model and e.g. lacking co- and counterion association coefficients (value for $\log K_{Na+}$ used from titration experiments, cf. Sec. 4.2.5) could not be profoundly reasoned based on the current state of data and knowledge. However, as a complete breakthrough of Eu was predicted within 50 PVs results are nevertheless displayed in Figure 4.17 Q-iv. Interestingly, the pH developments of Q-iv predicted with different RTMs partly followed observations: An initial decrease caused by surface complexation reactions was followed by an increase of pH that exceeded pH_{ini} (Fig. 4.17 Q-iv).

However, the increase of predicted pH conditions beyond pH_{ini} was delayed in comparison to measured values for all model approaches.

A comparison of predicted immobilization tendencies of Eu under sulphate influence (Q-iii: 0.005 mmol Na_2SO_4 and Q-iv: 0.05 mmol Na_2SO_4) showed that for Q-iii transport processes were overestimated and hence, retardation was underestimated. For predictions of Q-iv on the other hand, migration of Eu was underestimated and therefore immobilization of the trivalent actinide was overestimated. Even though both systems experienced Eu-sulphate speciation in solution, sorption tendencies that were predicted with the same RTMs showed contradictory developments in relation to measurements for Q-iii and Q-iv. This once more indicates that RTMs were ill-defined and that Eu transport under sulphate influence has not yet been understood. Experimental batch data of Eu with a sulphate background electrolyte is necessary to compare immobilization processes of Eu during batch and column experiments offering a first means to assess RTMs and helping to better define surface reactions with sulphate electrolytes.

For reactive transport simulations of column experiment Q-v (artificial groundwater, pH_{ini} 5.5) all but the nonEDLM predicted Eu transport under the influence of the artificial groundwater reasonably well with $|\Delta\log K_d|$ ranging between 0.27 and 0.99 for the electrostatic models (EMs) (cf. Tab. 4.3, Fig. 4.17 Q-v). Generally, Eu transport was underestimated (negative $\Delta\log K_d$ values) which mostly resulted in SDs within the experimental frame of 80 PVs (App. Fig. B.46) instead of BTCs as had been observed during transport experiments. Only *SCP Q I mono+bi* (DDLm, combination of mono- and bidentate surface complex) yielded a BTC but still overestimated Eu retardation indicated by a shifted occurrence in PV $[\text{V}/\text{V}_0]$ of the Eu peak concentration (C_{max} $[\text{mol L}^{-1}]$); however, the shape of the BTC which was characterized by a steep front and long tailing was adequately simulated. Competing cations (Ca^{2+} , Al^{3+} , Mg^{2+} , Na^{+}) that were contained in the artificial groundwater posed competition for sorption sites on Eu surface complexation which decreased Eu retardation and accelerated Eu migration. To consider the competition of all competing cations on Eu sorption processes more data would be necessary for the different mechanistic model approaches. At this time, only an Al^{3+} competing surface complexation reaction for DDLms (Kuan et al., 2004) was available which did not fully compensate the influence of all competing cations but improved simulation results significantly (cf. App. Fig. B.47). From RTM simulations it could be concluded that Al^{3+} might account for some competition posed on Eu sorption and that the remaining cations should also be considered in RTMs to more realistically predict Eu transport under the influence of artificial groundwater. However, so far no

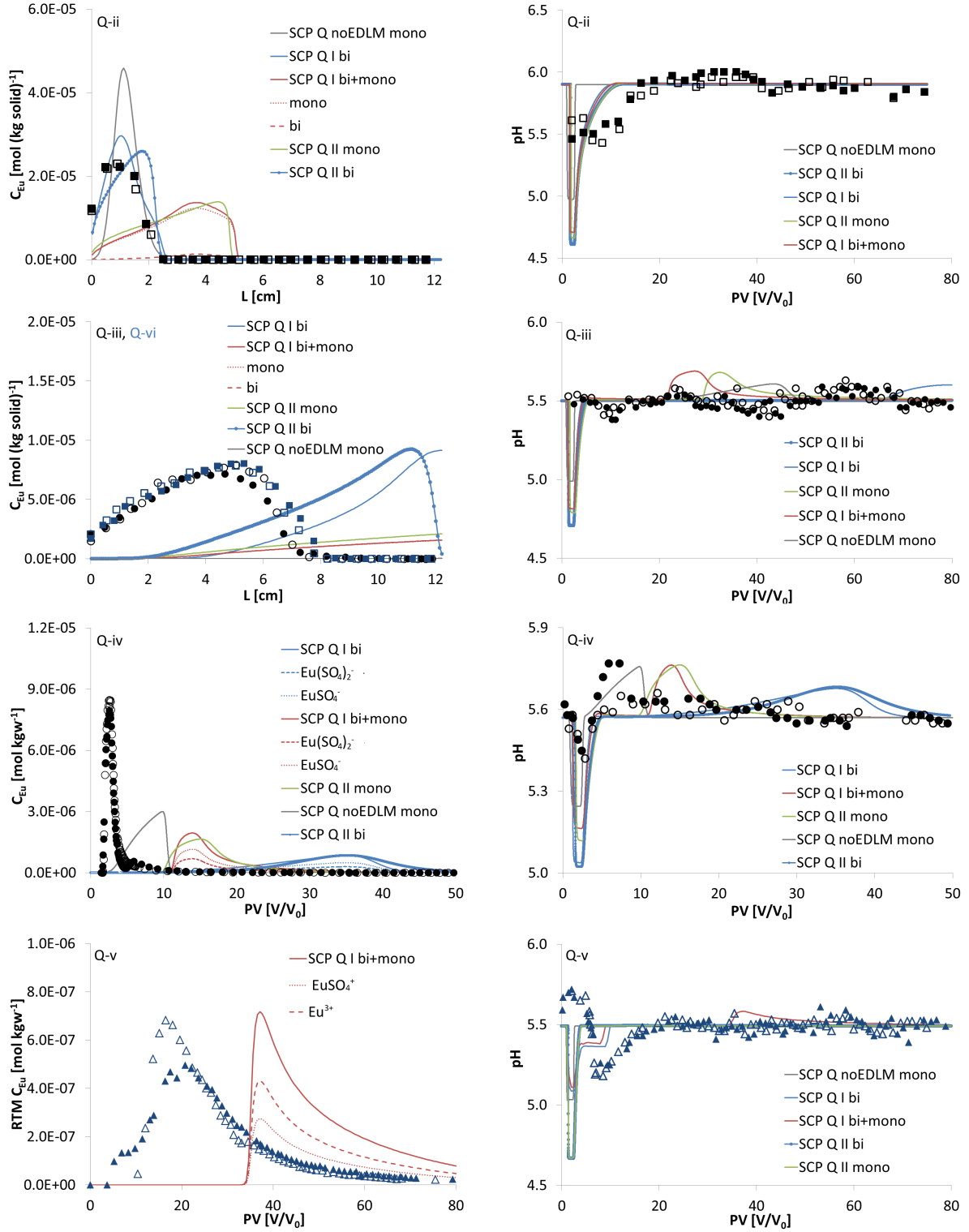


Fig. 4.17: Reactive transport simulations of Eu through quartz columns, $pH_{ini} \approx 5.5$ (Q-ii - Q-v). Simulated SDs relate to the following PV (cf. Tab. 4.2): Q-ii $t = 75$ PV, Q-iii $t = 80$ PV. Reactive transport models (RTMs) - coloured solid lines. Labelling of plots identical to Figures 4.2 - 4.7. For details cf. Tables 3.4 and 4.2.

such data has been available for remaining cations leading to simplified models that do not take individual competing cations into account as had been done for this study. The predicted pH development of Q-v (Fig. 4.17 Q-v) did not follow experimental data: The initial pH increase that had been observed during column experiments (Sec. 4.3.1) could not be verified or described with RTM simulations. To fully explain the reproducible experimental pH development further research is necessary. The complexity of the influence of the artificial groundwater on Eu migration has not yet been fully uncovered and hence, RTMs could only reflect the system based on the current state of knowledge.

Considering the performance of RTMs for Q-i - Q-v it was not possible to explicitly identify a Eu surface complex or EM that described Eu transport processes through homogeneous quartz columns adequately for all geochemical conditions (Fig. 4.17). However, considering that smaller $|\Delta\log K_d|$ are preferred over larger ones, from Table 4.3 it was concluded that the DDLM and the BSM predicted Eu transport equally well; the noEDLM simulated Q-ii and Q-iii adequately but showed discrepancies for Q-v compared to the EMs. Based on these results it was not unambiguously possible to prefer EMs over the noEDLM. Since the combination of a monodentate and bidentate surface complex (*SCP Q I mono+bi*) did not yield more precise results for the DDLM and keeping in mind that it was the scope to develop as simple as possible RTMs the application of a bidentate Eu surface complex was preferred over a combination of surface complexes (Tab. 4.3). At this state of knowledge and in the absence of spectroscopic data as well as batch experiments under sulphate influence or artificial groundwater, a bidentate Eu surface complex seemed to describe Eu transport processes over the different geochemical conditions best for EM approaches (Tab. 4.3). To substantiate the assumption of a bidentate Eu surface complex spectroscopic data and additional batch experiments are needed for identical geochemical conditions. So far, results are only substantiated by TRLFS studies carried out by Stumpf et al. (2008) who found evidence of a tridentate Cm complex on a quartz surface.

To conclude, SCPs derived from batch experiments resulted in sufficient Eu transport simulations ($|\Delta\log K_d| \leq 1$) for all column systems except for pH_{ini} 3.5 and high ligand concentrations using EMs (DDLM, BSM). To address the influence of sulphate, competing cations, and low pH conditions on Eu surface complexation in detail further research is necessary to better assess and describe Eu surface complexation during transport experiments. A better definition of the system would result in a more realistic formulation of RTMs that then return more reliable predictions and increased system understanding.

Transport simulations of orthoclase column experiments $\text{pH}_{\text{ini}} \approx 3.5$ (FS-i – FS-ii)

As for quartz column experiments, it was not possible either to sufficiently predict Eu transport through orthoclase columns at $\text{pH}_{\text{ini}} \approx 3.5$ ($|\Delta \log K_d| > 1$) regardless of the background electrolyte and simulation approach (Tab. 4.4). Predictions of Eu transport under inert background electrolyte conditions (FS-i) resulted in tracer-like BTCs for all model approaches where C_{max} [mol L⁻¹] passed the column within 1.0 – 2.5 PVs (App. Fig. B.48); the mean calculated R_f over all predictions equalled 1.2 ± 0.2 (standard deviation). Transport of Eu in 50 mmol L⁻¹ Na₂SO₄, pH_{ini} 3.5 (FS-ii) also showed no retardation (mean $R_f = 1.1$, Fig. 4.18) which was due to solution speciation reactions with the ligand and the low pH_{ini} (App. Fig. B.36). Figure B.48 in Appendix B and Figure 4.18 in this section exemplarily illustrate simulation results of FS-i and FS-ii; the remaining predicted BTCs are provided in the digital appendix.

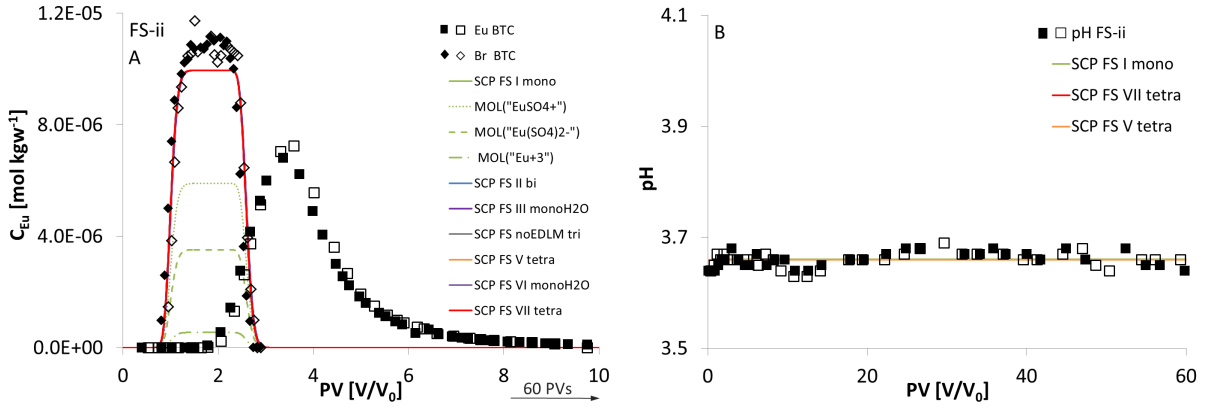


Fig. 4.18: Reactive transport simulations of Eu through orthoclase columns (FS-ii). A: Comparison between experimental Eu transport data (black solid and empty squares) and Br BTCs (black solid and empty diamonds) with Eu transport predictions (colored lines). B: Predicted (solid lines) and measured pH development (squares). FS-ii was conducted in duplicate (solid, empty symbols). Simulation results of RTMs overlap. Labelling corresponds to Figure 4.9. For details cf. Tables 3.4 and 4.2.

The insufficient performances of RTMs ($|\Delta \log K_d| > 1$) for FS-i and FS-ii were attributed to the following reasons:

- As shown in Section 3.3.2 only few data was available from orthoclase batch experiments below pH 5.4 (sorption edge) and only two data points described

Eu surface complexation at pH 3.7 (Fig. 3.12). Hence, it was assumed that the extrapolation of $\log K_{EuS}$ to low pH values failed due to lack of data.

- Eu retardation of FS-i yielded an experimental K_d that was ≈ 240 times larger compared to K_d values obtained from batch experiments at similar pH values (Fig. 4.11). Consequently, SCPs derived from batch experiments highly underestimated Eu surface complexation during column experiments.
- Since DDLMs resulted in 0%Eu(III) immobilized at pH 3.5 for batch experiments Eu transport at pH_{ini} 3.5 was simulated to travel as fast as an ideal tracer.
- In RTMs Eu surface complexation was counterbalanced by Eu solution speciation with the sulphate ligand (App. Fig. B.36). Hence, due to negligible surface complexation reactions Eu migration was simulated to travel as fast as the ideal Br tracer for FS-ii transport experiments.

As it had already been discussed earlier (e.g. Sec. 4.1) the underlying reasons and mechanisms causing the discrepancies between batch and column experiments have not yet been resolved. However, SCPs derived from batch experiments and predicted Eu BTCs show a consistent picture: The generally small Eu immobilization during batch experiments resulted (necessarily) in an underestimation of Eu retardation in orthoclase columns. To be able to describe sorption and transport processes closer to experimental data with RTMs more system understanding is required under the given geochemical conditions. As for quartz, more experimental data (batch and spectroscopic data) would increase the ability to better define a system with RTMs and therefore predict transport processes closer to measurements and eventually more realistically.

Tab. 4.4: Comparison of K_d values calculated from experiments and simulations of orthoclase transport experiments (FS-i – FS-iii). Differences between K_d values from measurements and predictions are provided as $\Delta \log K_d$. A simulation proves system understanding if $0.5 \leq |\Delta \log K_d| \leq 1$ (Davis et al., 2005): $|\Delta \log K_d| \geq 1$, $0.5 \leq |\Delta \log K_d| \leq 1$, $|\Delta \log K_d| < 0.5$. Column experiment FS-ii returned identical BTCs for all model approaches (Fig. 4.18) with a mean $K_d = 0.03 \text{ L kg}^{-1}$ and $|\Delta \log K_d| > 1$. For details on SCMs see Section 3 and Table 3.4. * RTM predictions returned identical results, $K_d [\text{L kg}^{-1}]$ – distribution coefficient \pm standard deviation.

	FS-i		FS-iii	
	K_d	$\Delta \log K_d$	K_d	$\Delta \log K_d$
Experimental K_d	390		0.79	
SCP FS I mono			0.72	0.038
SCP FS I H₂O_{mono}	0.025		0.83	-0.019
SCP FS I bi	$\pm 1.04\text{E-}3$	> 4	0.74	3.04E-2
SCP FS I tri			0.93	-0.072
SCP FS I tetra			1.07	-0.13

Continued on next page

	FS-i		FS-iii	
	K_d	$\Delta \log K_d$	K_d	$\Delta \log K_d$
SCP FS II mono			0.48	0.214
SCP FS II H ₂ O _{mono}	0.027		0.65	0.083
SCP FS II bi	$\pm 2.5\text{E-}3$	> 4	0.52	0.18
SCP FS II tri			0.57	0.14
SCP FS II tetra			0.68	0.064
SCP FS III mono			0.72	0.039
SCP FS III H ₂ O _{mono}	0.042		0.82	-0.018
SCP FS III bi	± 0.021	> 3	0.74	0.031
SCP FS III tri			0.93	-0.071
SCP FS noEDLM mono				
SCP FS noEDLM H ₂ O _{mono}	0.014		0.019*	> 1
SCP FS noEDLM bi	$\pm 3.2\text{E-}4$	> 4		
SCP FS noEDLM tri				
SCP FS V H ₂ O _{mono}	0.109		0.038	
SCP FS V tri	± 0.027	> 3	± 0.016	> 1
SCP FS V tetra				
SCP FS VI H ₂ O _{mono}	0.12		0.033	
SCP FS VI tri	± 0.039	> 3	$\pm 2.4\text{E-}3$	> 1
SCP FS VI tetra				
SCP FS VII H ₂ O _{mono}	0.083		0.33	0.38
SCP FS VII tri	± 0.022	> 3	0.46	0.24
SCP FS VII tetra			0.84	-0.025

Transport simulations of orthoclase column experiments pH_{ini} 5.5 (FS-iii)

For FS-iii DDLMs yielded adequate predictions of Eu transport under sulphate influence with $|\Delta \log K_d| < 0.5$ (Tab. 4.4, Fig. 4.19). This is interesting since for quartz column experiments under 50 mmol L⁻¹ Na₂SO₄ influence (Q-iv) Eu transport simulations did not represent measurements accurately ($|\Delta \log K_d| > 1$, cf. Tab. 4.3). At this point and based on collected data of this study, it was not possible to elucidate or clarify why Eu transport predictions through quartz and orthoclase columns under identical geochemical conditions yielded different performances of RTMs. Again, this highlights the need for more research to better understand Eu surface complexation and retardation processes. Batch data of Eu including the sulphate speciation reactions would help to set up and verify RTMs and would offer a means to compare batch and column experiments and to distinguish whether similar sorption tendencies under ligand influence can be observed; spectroscopic data would improve the definition of Eu surface complexation reactions in RTMs and would reveal whether e.g. ternary complexes might influence Eu retardation.

Simulation approaches with the BSM (*SCP FS V*, *SCP FS VI*, cf. Fig. 4.20 A) and with the noEDLM (*SCP noEDLM*, cf. Fig. 4.21) yielded tracer-like Eu BTCs. From RTM predictions that were based on basic Stern SCMs an average $R_f = 1.2 \pm 0.05$ (standard deviation) for *SCP FS V* and *SCP FS VI* was calculated; noEDLMs resulted in a mean $R_f = 1.1$, respectively. The tracer-like Eu breakthrough of *SCP FS V* and *SCP FS VI*

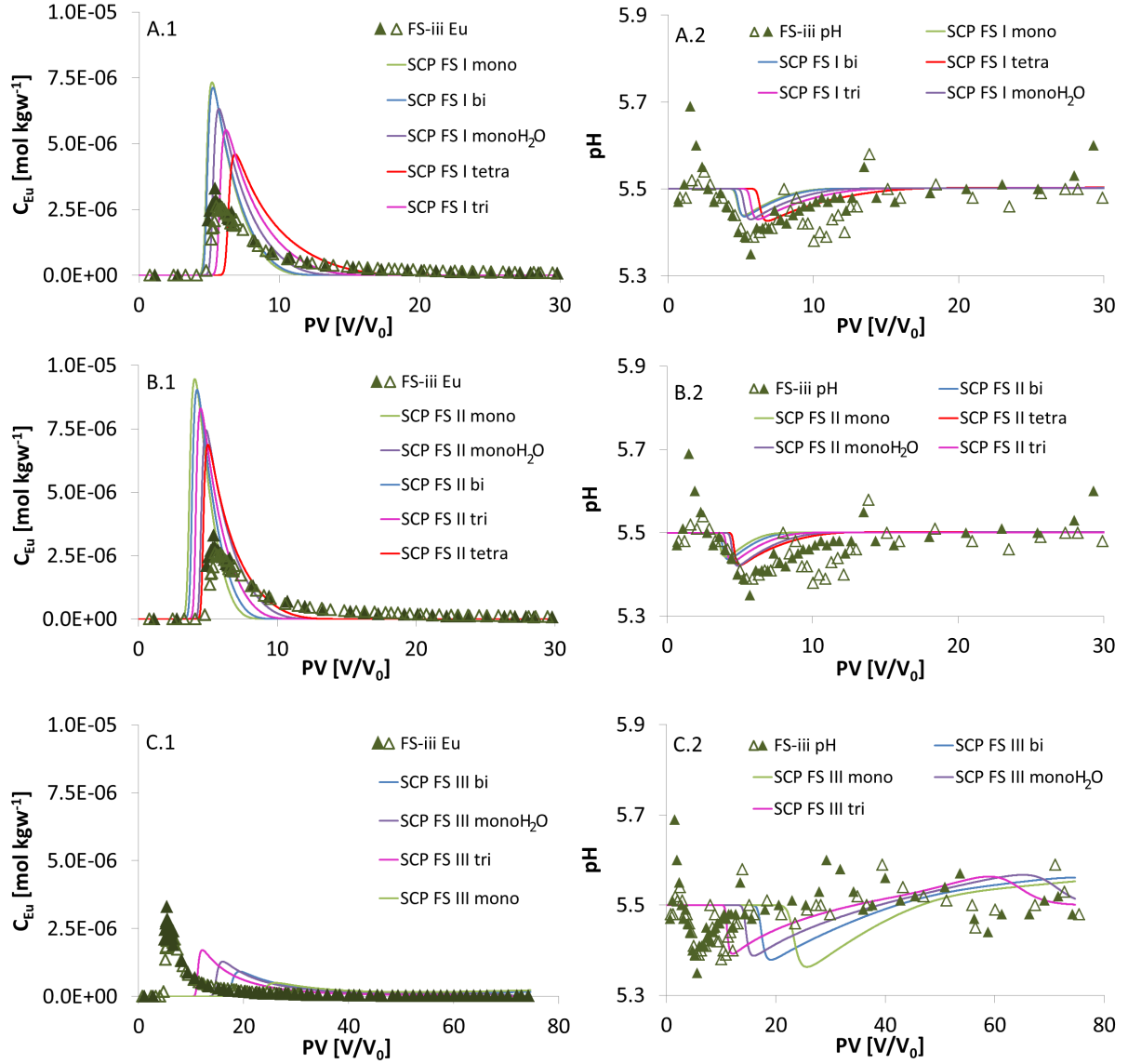


Fig. 4.19: Eu DDLM transport simulations of column experiment FS-iii. Comparison between experimental (open, solid symbols) and predicted (solid, dashed lines) Eu BTCs (A.1 - C.1) and pH development (A.2 - C.2). A: Predictions of *SCP FS I mono* - *SCP FS I tetra*, B: Predictions of *SCP FS II mono* - *SCP FS II tetra*, C: Predictions of *SCP FS III mono* - *SCP FS III tetra*. Labelling corresponds to Figure 4.9. For details cf. Tables 3.4 and 4.2.

occurred due to the high counterion association coefficient ($\log K_{Na+}$); consequently, smaller $\log K_{Na+}$ values allowed more Eu to sorb to the orthoclase surface resulting in higher retardation during transport simulations as it was observed for *SCP FS VII* (Fig. 4.20 B, cf. Tab. 2.4). Thus, counterions posed competition on Eu surface complexation which reduced the immobilization of Eu (Sec. 3.3.2) and which therefore enhanced Eu transport. Overall, BSM approaches for FS-iii were ill-defined due to lack of specific co- and counterion coefficients for Na_2SO_4 : The simplified model approach to use $\log K_{Na+}$ from titration experiments as rough estimates for the Na_2SO_4 background electrolyte was chosen due to lack of data and did not return satisfying predictions of Eu migration under high sulphate influence (mostly $|\Delta \log K_d| > 1$).

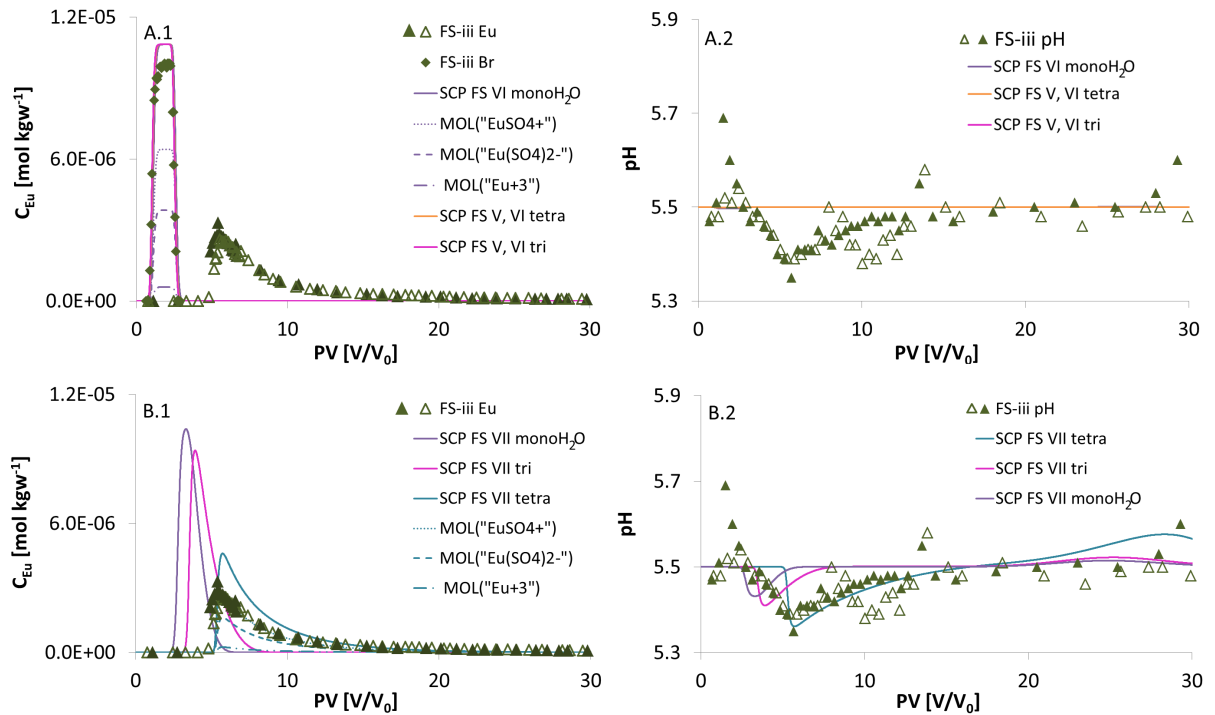


Fig. 4.20: Eu BSM transport simulations of column experiment FS-iii. Comparison between experimental (open, solid symbols) and predicted (solid, dashed lines) Eu BTCs and pH development. A.1: Predictions of *SCP FS V H₂O_{mono} - tetra* and *SCP FS VI H₂O_{mono} - tetra*, B.1: Predictions of *SCP FS VII H₂O_{mono} - tetra*, A.2/B.2: Predicted and measured pH development. Labelling corresponds to Figure 4.9. For details cf. Tables 3.4 and 4.2.

To conclude, a preferable RTM and hence a SCP set from batch experiments could not be identified that predicted Eu transport through orthoclase columns best. Therefore,

it also was not possible either to confirm or refute results proposed by Steinbrecher (2017) as it was initially intended (Sec. 3.3.2). Furthermore, influences of different surface charge models on RTM simulations could not be clearly observed either. However, a comparison of transport simulations using EMs and noEDLMs showed that all noEDLMs resulted in inadequate predictions with $|\Delta \log K_d| > 1$. Consequently, the consideration of the surface charge development of orthoclase seemed to enhance RTM performance even though one specific preferable surface charge model could not be presented. Once again, more research is needed to undoubtedly describe the surface charge development of mineral and sediment surfaces under different geochemical influences (especially sulphate) and to uncover the reasons for large discrepancies between batch and column experiments.

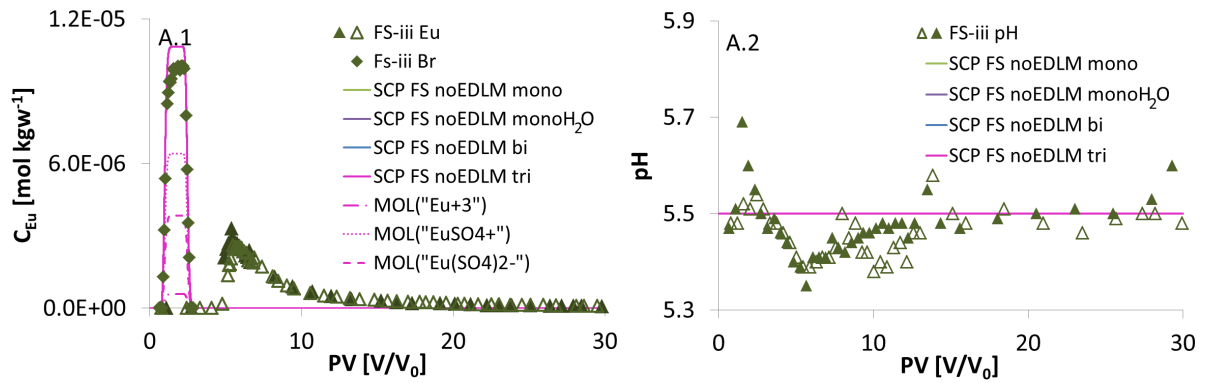


Fig. 4.21: Eu noEDLM transport simulations of column experiment FS-iii. Comparison between experimental (open, solid symbols) and predicted (solid, dashed lines) Eu BTCs and pH development. A.1: Predictions of *SCP FS noEDLM mono* - *SCP FS noEDLM tri*, A.2: Predicted and measured pH development. Labelling corresponds to Figure 4.9. For details cf. Tables 3.4 and 4.2.

4.5 Summary and first conclusions

Column experiments were carried out with orthoclase, quartz, muscovite, and a synthetic sediment under varying geochemical conditions to study Eu transport through homogeneously packed columns. Three different kinds of background electrolytes were used (NaClO_4 , Na_2SO_4 , artificial groundwater) with two different initial pH values (pH_{ini} 3.5 and 5.5). All columns were equilibrated before a pulse injection of the ideal NaBr tracer and Eu was initiated. Most transport experiments were conducted in duplicate to demonstrate reproducibility of results. From Br BTCs transport parameters were

determined with the code CXTFIT. Measurements of Eu transport was used to verify reactive transport model simulations with PHREEQC RTMs which were based on surface charge models and SCMs from Sections 2 and 3, respectively. In the absence of reliable cation exchange selectivity coefficients ($\log K_c$) Eu retardation in muscovite and the synthetic sediment columns could not be simulated.

Experimental results revealed a consistent and sound picture of Eu migration which matched sorption tendencies observed with batch experiments well: For quartz Eu showed lowest retardation compared to orthoclase and muscovite; the retention in the synthetic sediment column was mainly governed by the mica mineral. Interrelations between Eu surface complexation and the pH could be observed; sulphate solution complexation reactions with Eu resulted in expected enhanced migration of the trivalent lanthanide; and cations in the artificial groundwater (e.g. Ca^{2+} , Mg^{2+} , Al^{3+} , etc.) posed competition on Eu surface complexation which also limited Eu retardation and triggered faster transport processes.

In this study, Eu surface complexation constants ($\log K_{EuS}$) were derived from batch experiments and used in RTMs (DDLm, BSM, noEDLM). Generally, RTMs and the simulation of Eu transport under different geochemical conditions was a synthesis of surface charge and surface complexation models and it was assumed that surface complexation constants from batch experiments were transferable to column experiments. It was the scope to develop straightforward models with the smallest amount of parameters possible that still accurately described the reactive transport and retardation of Eu over a range of experimental conditions ($|\Delta \log K_d| < 1$, Davis et al. (2005)). Thus, it was not the aim to predict Eu migration in detail but to capture main features and tendencies with SCPs from batch experiments. However, to predict Eu transport and retardation processes as close to measurements as possible Eu sorption during batch experiments should yield similar K_d values in relation to column experiments under comparable geochemical conditions. In this study batch experiments revealed up to three orders of magnitude lower distribution coefficients which resulted in evident differences between experimental Eu transport data and predictions.

From reactive transport simulations of quartz column experiments the following conclusions were drawn:

- Eu transport at $\text{pH}_{ini} \approx 3.5$ could not be accurately represented with any RTM.
- At $\text{pH}_{ini} \approx 5.5$ (10 mmol L⁻¹ NaClO₄ and 5 mmol⁻¹ Na₂SO₄ background electrolyte) most RTMs resulted in adequate predictions ($|\Delta \log K_d| < 1$).
- Eu migration under the influence of 50 mmol L⁻¹ Na₂SO₄ could not be sufficiently described ($|\Delta \log K_d| > 1$).

- The implementation of a competing surface complexation reaction of Al^{3+} resulted in reasonably well representations of Eu transport processes in artificial groundwater for most model approaches.
- Bidentate surface complexes seemed to describe Eu transport best for the DDLMs and BSMS regarding the different geochemical conditions.
- Spectroscopic evidence under similar geochemical conditions would be needed to further substantiate the latter finding.
- Batch experiments that include the complexing affect of a sulphate ligand would offer valuable information of Eu surface complexation and would offer a good means to more realistically set-up RTMs which has to be considered for future research projects.

Orthoclase RTM predictions revealed the following:

- Transport experiments at $\text{pH}_{ini} \approx 3.5$ could not be accurately predicted with any RTM, regardless of the background electrolyte ($|\Delta \log K_d| > 1$).
- Reactive transport simulations based on the DDLM *SCP FS VII* yielded adequate predictions for column experiments with pH_{ini} 5.5 and 50 mmol L^{-1} Na_2SO_4 background electrolyte ($|\Delta \log K_d| < 1$).
- The RTMs that were based on basic Stern SCM *SCP FS V* and *VI* resulted in less adequate simulations compared to DDLM approaches which was probably mainly attributed to the lack of co- and counterion association coefficients for Na_2SO_4 .
- Predictions with noEDLM approaches were not able to satisfyingly simulate any column experiment ($|\Delta \log K_d| > 1$).
- No preferable orthoclase SCP set or RTM could be identified that predicted migration processes of the trivalent lanthanide best.
- Whether Eu retardation in orthoclase columns would be adequately simulated under inert background electrolyte conditions or low ligand concentrations at $\text{pH}_{ini} = 5.5$ as it was the case for quartz, should be verified in future research projects with new sets of transport experiments.

The reasons for the insufficient simulations of pH_{ini} 3.5 for orthoclase and quartz transport experiments could be found in the absence of sufficient data since experimental conditions of column experiments exceeded experimental conditions of batch experiments at the lower pH range. Furthermore, transport results revealed that even though retardation tendencies during Eu column experiments agreed well with observations from batch experiments, K_d values differed by orders of magnitude between both experimental

set-ups considering comparable geochemical conditions. The goodness of fit (gof) of SCMs also had influence on RTM simulations: Quartz and orthoclase batch experiments were underestimated with SCMs at low pH values; thus, RTM predictions at low pH conditions also underestimated Eu retardation resulting in a faster predicted migration of Eu in comparison to measurements. It should also be mentioned that RTMs combine all simplifications, limitations, as well as parameter uncertainties of surface charge and SCMs; thus, even though the transferability of $\log K_{Eu}$ from batch to column experiments was challenging for some geochemical conditions in this study results did not necessarily indicate that the approach is generally not applicable. Transport simulations of this study rather highlighted that the acid-base behavior of ubiquitously present minerals is still not yet fully understood, that surface complexation constants for competing surface complexation reactions of the different EMs are lacking, that no data for the exact definition of Na_2SO_4 co- and counterion association coefficients on the examined mineral phases is available, that no adequate spectroscopic evidence could be found in literature to more precisely back up proposed surface complexes, and that fundamental batch experimental data describing Eu immobilization under the influence of sulphate is also not available and lacking. All of the latter result in simplified RTMs that can only offer first impressions of Eu transport under the chosen geochemical conditions. Findings call for a more sophisticated and accurate experimental determination as well as definition of surface complexation constants and emphasize the need for more research to

- clearly identify lanthanide surface complexes for relevant geochemical conditions and mineral phases,
- improve the understanding of the solid-solution interface,
- further support the development of thermodynamic databases,
- and finally to improve the performance of RTMs.

From this study it was concluded that parametrization of SCMs should be performed with measurements that cover a broad range of experimental conditions relevant for transport processes. However, to assess the applicability of surface complexation constants from batch to transport processes, for selected geochemical conditions batch experiments should be accompanied by column experiments whenever possible.

Main conclusions and future perspectives

"Thus, all the models may be viewed as being of the correct mathematical forms to represent the data but are not necessarily an accurate physical description at the interface. In other words, all models can be used to describe experimental data...the "intelligence" of the data, on the other hand, is not sufficient to gain insight into the physical nature of the interface."

— Sposito (1998)

The correct or at least an adequate description of the mineral-water interface is a prerequisite for a successful simulation of e.g. radionuclide transport processes with mechanistic thermodynamic sorption models (TSMs) regardless whether ions, compounds, ligands, or e.g. colloids are considered. The more complex a systems gets, the more data is necessary to accurately characterize it and the more challenging it becomes to correctly represent this system with sophisticated mechanistic model approaches. Since sound and trustworthy data is often the limiting factor empirical approaches have been used many times to describe natural or complex environments with more straightforward approaches such as the linear distribution coefficient (constant K_d). Eventually, only small differences between the more sophisticated and the simpler models might be observed. However, profound system and process understanding may only be obtained with mechanistic approaches that intend to describe the mineral-water interface as close to nature as possible always trying to consider the present scientific state-of-the-art. Nevertheless, one should be aware that the "state-of-the-art" not necessarily describes the solid-solution interface correctly and that any new advancement in science might change the current state of knowledge drastically.

This study focussed on the characterization of Eu transport and retardation processes via the determination of Eu surface complexation parameters (SCPs) of muscovite, orthoclase, and quartz to subsequently simulate the reactive transport of the trivalent

lanthanide under varying geochemical conditions with mechanistic reactive transport models (RTMs). Therefore a vast amount of experiments were carried out: Discontinuous mass and electrolyte, as well as continuous potentiometric acid-base titration experiments were performed for each mineral which described the surface charge development of the solids; batch experiments under varying geochemical conditions were conducted to collect Eu sorption data for all three considered solid phases; and transport experiments with Eu were completed covering artificial laboratory environments but also complex, close to nature conditions using orthoclase, muscovite, quartz, and a synthetic sediment (10 wt% orthoclase, 10 wt% muscovite, 80 wt% quartz).

To finally simulate Eu reactive transport, surface charge and surface complexation models (SCMs) were developed using the geochemical speciation code PHREEQC (Parkhurst and Appelo, 2013). In combination with the parameter estimation code UCODE (Poeter et al., 2005) SCPs were optimized using titration and batch measurements. The diffuse double layer model (DDLm), the basic Stern model (BSM), as well as a non-electrostatic model were applied. Fitted final SCP sets were then used as fixed parameter values in RTMs to predict Eu migration under varying conditions.

It was proposed that SCPs derived from surface charge models and SCMs could be applied as fixed parameters in RTMs to predict Eu transport processes in different geochemical surroundings. It was the scope to determine mineral-specific SCP sets that were capable to reproduce major retardation tendencies of Eu under varying geochemical conditions. The goal was to develop TSMs with the least amount of necessary parameters to still represent major Eu retardation and transport trends. Thus, it was not the aim to precisely capture every detail for one geochemical condition but rather to be able to reproduce general sorption and immobilization tendencies for a range of geochemical environments. Since SCPs were fitted with SCMs that were based on titration and batch experimental data it was assumed that sorption and immobilization processes during static batch experiments and steady state transport experiments were comparable; thus, determined parameters and K_d values were thought to be transferable from batch to column experiments. Furthermore, a comparison between the component additivity (CA) and the generalized composite approach (GC) was intended.

Titration experiments of quartz revealed that the mineral showed similar surface charge characteristics compared to a more comprehensive literature data set of Bolt (1957) that was collected using an amorphous silica phase. Thus, to cover a broader range of geochemical conditions quartz surface charge models of this study used the more extensive

literature data set from Bolt (1957). The 1-pK approach was applied to optimize DDLM SCPs (protolysis constant); with the BSM the surface charge was simulated also using the 1-pK approach but utilizing SCPs (protolysis constant, C_1 , $\log K_{Na^+, ClO_4^-}$, surface charge density) provided by Hiemstra et al. (1989b). Hiemstra et al. (1989b) derived the SCP set via parameter optimization with the BSM based on data from Bolt (1957). Both approaches (DDLM, BSM) reflected experimental data adequately.

For orthoclase and muscovite mass and electrolyte titration experiments revealed two different potential reference pH values (pH_{mass} , pH_{IEP}) in comparison to quartz where only one pH_{pznpz} was observed (Bolt, 1957). Due to the different reference pH values different surface charge models were developed for orthoclase and muscovite whereas plausibility of fitted parameters as well as goodness of fit (gof) were used to identify reasonable surface charge models and hence SCPs. Fitting procedures revealed that neither muscovite, nor orthoclase surface charge development was adequately represented with the 2-pK approach. Hence, only the 1-pK approach was applied to characterize surface charge properties of orthoclase, muscovite, and quartz. Consequently, only the 1-pK approach was used for subsequent Eu SCM approaches and RTMs.

Batch experiments revealed expected results: Quartz showed lowest Eu immobilization tendencies compared to orthoclase and muscovite. Interestingly quartz showed relatively high Eu immobilization at low pH values which matched observations made by Lützenkirchen (1996). For muscovite approximately 24% Eu uptake was observed at pH 3.2 which was attributed to cation exchange processes. It was shown that Eu immobilization was positively correlated with increasing pH values, solid-liquid-ratio, and initial Eu concentration for all minerals. Unfortunately, for muscovite and orthoclase only few data could be collected in the range of the sorption edge.

Batch data was used to estimate Eu surface complexation constants ($\log K_{Eu}$ s) based on surface charge models and respective SCPs. For quartz, gof showed that electrostatic models (DDLM, BSM) fitted batch experimental data better compared to noEDLMs. The comparison of gof for the quartz DDLMs revealed that a bidentate surface complex as well as a combination of a mono- and bidentate surface complexes yielded best fitting results. For the BSMs the application of a monodentate and bidentate surface complex resulted in adequate fits of quartz batch data. For orthoclase $\log K_{Eu}$ optimization with SCMs (DDLM, noEDLM, BSM) returned similar results for all approaches which was attributed to the indeterminate sorption edges (few data). Since no preferential sorption model (regardless of the used reference pH value) could be identified, all developed SCMs were used for Eu reactive transport simulations through orthoclase columns. Hence, at

this point, no explicit preference of an orthoclase surface charge model and SCM could be determined. For muscovite parameter optimization of $\log K_{Eu}$, PHREEQC revealed major convergence problems which was due to inadequate conditional cation exchange coefficients derived from literature. Thus, no Eu SCM for muscovite could be developed and consequently the reactive transport of Eu through systems involving muscovite had to also be postponed to future research projects. It has to be pointed out that no spectroscopic measurements were carried out in this research; hence, proposed Eu surface complexes from this study were exclusively based on chemical plausibility, literature, and gof of SCMs. To fully reach the potential of mechanistic TSMs spectroscopic evidence of Eu surface complexes has to be collected for the considered systems to truly reflect realistic conditions in SCMs with the current state of knowledge.

Column experiments were carried out with different initial pH values (pH_{ini}) and background electrolyte solutions (NaClO_4 , Na_2SO_4 , artificial groundwater) for muscovite, orthoclase, quartz, and a synthetic sediment. Sorption tendencies that had already been observed from batch experiments were substantiated: Quartz column experiments showed lowest Eu retardation compared to orthoclase, muscovite, and the synthetic sediment. Muscovite column experiments revealed highest retardation of Eu even at low pH values. Comparing batch and column experiments, it became evident that Eu immobilization during batch experiments returned orders of magnitude lower K_d values compared to column experiments conducted under similar geochemical boundary conditions for all three considered minerals. Especially at low pH values major differences between batch and column experiments occurred. Hence, since RTMs used SCPs derived from surface charge models and SCMs, transport of Eu at pH_{ini} 3.5 could not be adequately simulated for any mineral or background electrolyte. Calculated K_d values from measurements and predictions of column experiments differed by more than 1 log unit ($\Delta \log K_d$) which was considered as inadequate predictions following suggestions made by Davis et al. (2005).

Quartz transport experiments carried out with $10 \text{ mmol L}^{-1} \text{ NaClO}_4$, $5 \text{ mmol L}^{-1} \text{ Na}_2\text{SO}_4$, and the artificial groundwater at pH_{ini} 5.5 were adequately predicted with the DDLM and BSM using a bidentate Eu surface complex ($|\Delta \log K_d| < 1$). The noEDLM returned satisfying results for the inert NaClO_4 background electrolyte and the Na_2SO_4 system considering a monodentate surface complex; the column experiment carried out with the artificial groundwater at pH_{ini} was not adequately predicted. Hence, from electrostatic RTMs (DDLM, BSM) it was proposed that a bidentate Eu surface complex adequately predicts Eu transport over varying geochemical conditions. Reactive transport simulation of quartz column experiments with $50 \text{ mmol L}^{-1} \text{ Na}_2\text{SO}_4$, pH_{ini} 5.5, on the

other hand, did not yield satisfying results with any SCM and, thus, SCP set from batch experiments ($|\Delta \log K_d| > 1$). The insufficient prediction was attributed to an ill-defined system due to lacking precise data: Under the influence of high ligand concentrations ternary surface complexes as well as co- and counterion associations might cause relevant influence on Eu retardation processes; however, as no spectroscopic, thermodynamic, batch, and/or according surface charge data of the quartz surface or ternary Eu-sulphate surface complexes was available no such reactions could be considered in RTMs.

The simulation of Eu transport through orthoclase columns revealed larger challenges compared to quartz: As mentioned above no adequate prediction was obtained for column experiments with pH_{ini} 3.5 – regardless of the background electrolyte. Only simulations of column experiments carried out with 50 mmol L⁻¹ Na₂SO₄, pH_{ini} 5.5 predicted measurements adequately ($|\Delta \log K_d| < 1$). Again, no preferential SCP set and hence, SCM or Eu surface complex could be identified that simulated measurements best. Additional batch experiments and/or spectroscopic data (especially under sulphate-ligand influence) is needed to define a preferred Eu surface complex and surface charge model that describe Eu migration under the different geochemical conditions accurately ($|\Delta \log K_d| < 1$). Additional transport experiments would verify whether Eu migration processes through orthoclase columns could be adequately represented with SCPs from batch experiments for pH_{ini} 5.5 with 10 mmol NaClO₄, 5 mmol Na₂SO₄, or the artificial groundwater as it was the case for quartz.

Since no converging SCM could be developed for muscovite, $\log K_{Eu}$ s could not be derived for the phyllosilicate and the simulation of the reactive transport of Eu through muscovite columns has to be subject to future research projects. As a consequence, predictions of the migration of the trivalent lanthanide through the synthetic sediment could also not be presented. Therefore, it was also not possible either to validate or even compare the GC approach with the more sophisticated CA approach. Future studies should focus on the determination of sound muscovite SCPs especially cation exchange selectivity coefficients to offer the basis for trustworthy reactive transport simulations using the CA or GC approach.

Generally, it was shown that the simulation of Eu migration through quartz environments resulted in adequate predictions for most geochemical conditions using SCPs from titration and batch experiments and that sophisticated electrostatic models yielded better predictions compared to the more straightforward noEDLM approaches. However, even for the presumingly well known quartz surface there is still a lack of knowledge regarding low pH values. For orthoclase, reactive transport simulations with

SCPs from titration and batch experiments also yielded adequate predictions but did not allow detailed insight into Eu surface complexation or surface charge development. As for quartz, Eu transport at low pH could not be satisfyingly simulated either. Thus, even though a vast amount of information has been collected throughout the past decades there is still a big need for data especially aimed to uncover surface charge behaviour and lanthanide surface complexation over a range of geochemical conditions for ubiquitously present minerals such as muscovite, orthoclase, and also in part of quartz surfaces to substantially contribute to the understanding of solid-solution interface reactions. In this study it could only be shown but not dealt with in detail that co- and counterion association coefficients as well as conditional cation exchange coefficients need sound and thorough definitions since they exhibit great influence on surface complexation and hence reactive transport models. It was pointed out that to the authors knowledge so far the majority of SCMs and RTMs presented in literature do not differentiate between reactive specific surface area and total specific surface area which has influence on the sorption and retardation capacity of a mineral or sediment in general via the availability of reactive sites on a minerals surface. Furthermore, the definition of surface sites that may actually participate in solid-solution interface reactions has yet not been fully uncovered either. Also, this study may only propose potential surface complexes that may contribute to lanthanide retardation in the considered systems. However, whether these surface complexes accounted for Eu uptake or rather a combination of different mono- and/or multivalent surface complexes can only be substantiated with spectroscopic measurements.

Hence, whether it is feasible to trustworthy predict the transport behaviour of e.g. metal cations with SCPs from titration and batch experiments could not be answered in all detail for the considered minerals due to lack of data. Since at the present time this approach is widespread also for long-term safety relevant analyses (e.g. Noseck et al. (2012), Bradbury and Baeyens (2009), Bradbury and Baeyens (2000), Kohler et al. (1996)) this question should be comprehensively addressed in future with supplementary accessory and completing experiments to this study. However, current results indicated that the application of SCPs from titration and batch experiments is a promising and straightforward approach to predict transport processes which even though data and knowledge is scarce has already resulted in trustworthy verified predictions as shown in this study for Eu transport through quartz columns. More data will contribute to substantiate and verify the approach to transfer SCPs from static batch to steady state or dynamic transport experiments.

To ease the transferability of parameters from one experimental set-up to the other, in future batch experiments should be performed under conditions as close to transport experiments and as close to conditions predicted with RTMs as possible. Furthermore, column experiments should accompany batch experiments to offer a means to verify determined SCPs for selected systems. Nevertheless, batches still embody the less time consuming experimental set-up and might be preferably used where local equilibrium cannot be achieved in transport experiments, where adsorption and desorption are the governing retardation processes, and where K_d values are extremely large (Kohler et al., 1996).

One last word on the consistency of data and parametrization of different model approaches: This study used different mechanistic thermodynamic models to describe surface charge development, Eu surface complexation, and finally reactive transport of the trivalent lanthanide. Even though great attention was paid to consistent model approaches, data, and parametrization it was not possible to determine SCPs for muscovite in this study. Surface complexation models did not converge which was due to conditional cation exchange selectivity coefficients from literature that did not reflect the examined system of this study properly concerning collected experimental data and probably also the chosen model approach. This example shows that even though all remaining parameters were derived with the same model and mineral, and even though cation exchange coefficients were thoroughly evaluated and only taken from literature due to lack of data the definition of the cation exchange caused major model convergence problems and impeded SCP optimization for muscovite. This example illustrates that mixing of data from different sources can have major influence on model outcome which does not necessarily result in non-convergence but, even worse, might return nonobvious biased results leading to incorrect conclusions. Hence, it should be of greatest interest for any modelling study to secure the consistency of data and models and it should be refrained from substituting and mixing of parameter sets from one approach to another due to e.g. lack of data. Only conclusions drawn from consistent, comprehensive, transparent, and sound data as well as model approaches contribute to a sound system understanding based on scientific findings and knowledge rather than on lack of data, coincidence, and wild guesses.

Bibliography

- Adeleye, S. A., Clay, P. G., 1994. Sorption of caesium, strontium and europium ions on clay minerals. *Journal of Materials Science* 29, 954–958.
- Alessi, D. S., Fein, J. B., 2010. Cadmium adsorption to mixtures of soil components: Testing the component additivity approach. *Chemical Geology* 270, 186 – 195.
- Appelo, C. A. J., Postma, D., 2010. *Geochemistry, Groundwater and Pollution*, 2nd Edition. A. A. Balkema Publishers.
- Arnold, T., Zorn, T., Bernhard, G., Nitsche, H., 1999. Applying the DDLM to model the sorption of uranium onto quartz and muscovite. In: Bernhard, G. (Ed.), *Wissenschaftlich-technische Berichte*. No. FZR-285. Forschungszentrum Rossendorf e.V., Institute of Radiochemistry Town: Dresden (Germany), p. 17.
- Arnold, T., Zorn, T., Zänker, H., Bernhard, G., Nitsche, H., 2001. Sorption behavior of U(VI) on phyllite: experiments and modeling. *Journal of Contaminant Hydrology* 47, 219 – 231.
- Avena, M. J., De Pauli, C. P., 1998. Proton adsorption and electrokinetics of an Argentinean montmorillonite. *Journal of Colloid and Interface Science* 202 (1), 195 – 204.
- Baeyens, B., Bradbury, M., 2004. Cation exchange capacity measurements on illite using the sodium and cesium isotope dilution technique: Effects of the index cation, electrolyte concentration and competition: Modeling. *Clays and Clay Minerals* 52 (4), 421 – 431.
- Baeyens, B., Bradbury, M. H., 1997. A mechanistic description of Ni and Zn sorption on Na-montmorillonite. Part I: Titration and sorption measurements. *Journal of Contaminant Hydrology* 27, 199 – 222.

- Barrón, V., Torrent, J., 1996. Surface hydroxyl configuration of various crystal faces of hematite and goethite. *Journal of Colloid and Interface Science* 177 (2), 407 – 41.
- Bergaya, F., Lagaly, G., Vayer, M., 2006. Handbook of Clay Science - Developments in Clay Science. Vol. 1. Elsevier Ltd., Ch. 12.10, pp. 979–1001.
- BMUB, 2015. Joint convention on the safety of spent fuel management and on the safety of radioactive waste management. Federal Ministry for the Environment, Nature Conservation, Building and Nuclear Safety (BMUB), Division RS III 3 (Nuclear Waste Management, Nuclear Fuel Cycle).
- Bolt, G. H., 1957. Determination of the charge density of silica sols. *Journal of Physical Chemistry* 61, 1166–1169.
- Bolt, G. H., van Riemsdijk, W. H., 1979. Ion adsorption on inorganic variable charge constituents. In *Soil chemistry, Part B: Physico-chemical models (developments in soil science)*. Elsevier Science Publishing Company, Ch. 13, pp. 459 – 504.
- Bouby, M., Filby, A., Geckeis, H., Geyer, F., Götz, R., Hauser, W., Huber, F., Keesmann, S., Kienzler, B., Kunze, P., Küntzel, M., Lützenkirchen, J., Noseck, U., Panak, P., Plaschke, M., Pudewills, A., Schäfer, T., Seher, H., Walther, C., 2010a. Colloid/Nanoparticle formation and mobility in the context of deep geological nuclear waste disposal (Project KOLLORADO-1; Final report). Tech. rep., KIT INE and GRS mbH.
- Bouby, M., Lützenkirchen, J., Dardenne, K., Preocanin, T., Denecke, M. A., Klenze, R., Geckeis, H., 2010b. Sorption of Eu(III) onto Titanium dioxide: Measurements and modeling. *Journal of Colloid and Interface Science* 350, 551 – 561.
- Bradbury, M., Baeyens, B., June 2005a. Experimental and modelling investigations on Na-illite: Acide-base behavior and the sorption of strontium, nickel, europium and uranyl. Tech. Rep. 04-02, National Cooperative for the Disposal of Radioactive Waste, CH-5430 Wettingen/Switzerland.
- Bradbury, M., Baeyens, B., 2005b. Modelling the sorption of Mn(II), Co(II), Ni(II), Zn(II), Cd(II), Eu(III), Am(III), Sn(IV), Th(IV), Np(V) and U(VI) on montmorillonite: Linear free energy relationships and estimates of surface binding constants for some selected heavy metals and actinides. *Geochimica et Cosmochimica Acta* 69 (4), 875 – 892.

- Bradbury, M. H., Baeyens, B., 2000. A generalised sorption model for the concentration dependent uptake of caesium by argillaceous rocks. *Journal of Contaminant Hydrology* 42, 141 – 163.
- Bradbury, M. H., Baeyens, B., 2009. Sorption modelling on illite Part I: Titration measurements and the sorption of Ni, Co, Eu and Sn. *Geochimica et Cosmochimica Acta* 73, 990 – 1003.
- Bradbury, M. H., Baeyens, B., Geckeis, H., Rabung, T., 2005. Sorption of Eu(III)/Cm(III) on Ca-montmorillonite and Na-illite. Part 2: Surface complexation modelling. *Geochimica et Cosmochimica Acta* 69 (23), 5403 – 5412.
- Bragg, W. H., Bragg, W. L., 1913. The reflection of X-rays by crystals. *Proceedings of the Royal Society of London* 88 (605), 428 – 438.
- Brendler, V., Vahle, A., Arnold, T., Bernhard, G., Fanghänel, T., 2003. RES³T Rossendorf expert system for surface and sorption thermodynamics. *Journal of Contaminant Hydrology* 61 (1 - 4), 281 – 291.
- Britz, S., July 2011. Sorption studies of Eu³⁺ on muscovite and orthoclase. Diploma thesis, Technische Universität Carolo-Wilhelmina zu Braunschweig, available at: GRS gGmbH, Theodor-Heuss-Str. 4, 38122 Braunschweig, Germany.
- Bruggeman, C., Liu, D. J., Meas, N., 2010. Influence of Boom Clay organic matter on the adsorption of Eu³⁺ by illite - geochemical modelling using the component additivity approach. *Radiochimica Acta* 98, 597 – 605.
- Brunauer, S., Emmett, P., Teller, E., 1938. Adsorption of gases in multimolecular layers. *Journal of the American Chemical Society* 60, 309 – 319.
- Cases, J. M., Bérend, I., Besson, G., François, M., Uriot, J. P., Thomas, F., Poirier, J. E., 1992. Mechanism of adsorption and desorption of water vapor by homoionic montmorillonite. 1. The sodium-exchanged form. *Langmuir* 8, 2730 – 2739.
- Cho, Y., Korarneni, S., 2009. Cation exchange equilibria of cesium and strontium with K-depleted biotite and muscovite. *Applied Clay Science* 44, 15 – 20.
- Curtis, G. P., Davis, J. A., Kohler, M., Kent, D. B., 2001. Reactive transport modeling of uranium(VI) migration through quartz porous media under variable chemical conditions. In: Davis, J. A. (Ed.), *Surface complexation modeling of uranium(VI). Adsorption on*

- natural mineral assemblages. No. NUREG/CR-6708. U. S. Geological Survey, Ch. 18, pp. 181 – 191.
- Davis, J. A., Kent, D. B., 1990a. Mineral-water Interface Geochemistry. Mineralogical Society of America, Washington, DC, Ch. Surface complexation modeling in aqueous geochemistry, pp. 177 – 258.
- Davis, J. A., Kent, D. B., 1990b. Surface complexation modeling in aqueous geochemistry. *Reviews in Mineralogy and Geochemistry* 23 (1), 177 – 260.
- Davis, J. A., Kohler, M., Payne, T. E., Bargar, R., Reitmeyer, R., Waite, T. D., McBeath, M., Coston, J. A., Lumpkin, G., Joye, J. L., Fenton, B., Curtis, G. P., Kent, D. B., 2001. Surface complexation modeling of uranium(VI). Adsorption and natural mineral assemblages. In: Davis, J. A. (Ed.), Surface complexation modeling of uranium(VI). Adsorption and natural mineral assemblages. No. NUREG/CR-6708. U.S. Geological Survey, Washington, DC 20555-0001.
- Davis, J. A., Ochs, M., Olin, M., Payne, T. E., Tweed, C. J., 2005. Interpretation and prediction of radionuclide sorption onto substrates relevant for radioactive waste disposal using thermodynamic sorption models. NEA Sorption Project Phase II, OECD NEA.
- de Lange, M. F., Vlugt, T. H. H., Gascon, J., Kapteijn, F., 2014. Adsorptive characterization of porous solids: error analysis guides the way. *Microporous and Mesoporous Materials* 200, 199 – 215.
- DIN 19268, 2007. pH-Messung von wässrigen Lösungen mit pH-Messketten mit pH-Glaselektroden und Abschätzung der Messunsicherheit. Deutsches Institut für Normung e.V., 2007th Edition, Ersatz für DIN 19268:1985-02.
- DIN ISO 13536:1997-04, 1997. Bodenbeschaffenheit: Bestimmung der potentiellen Kationenaustauschkapazität und der austauschbaren Kationen unter Verwendung einer bei pH=8.1 gepufferten Bariumchloridlösung. Deutsches Institut für Normung e.V., Normausschuss Wasserwesen.
- Doherty, J., 2002. PEST Model-independent parameter estimation. Watermark Numerical Computing, 4th Edition.

- Duc, M., Gaboriaud, F., Thomas, F., 2005. Sensitivity of the acid-base properties of clays to the methods of preparation and measurement - 1. Literature review. *Journal of Colloid and Interface Science* 289, 139 – 147.
- Dzombak, D., Morel, F. M. M., 1987. Adsorption of inorganic pollutants in aquatic systems. *Journal of Hydraulic Engineering* 69, 430 – 475.
- Dzombak, D., Morel, F. M. M., 1990. Surface complexation modeling. John Wiley & Sons, Inc.
- Everett, D. H., Parfitt, G. D., Sing, K. S. W., 1974. The SCI/IUPAC/NPL project on surface area standards. *Journal of Applied Chemistry and Biotechnology* 24, 199 – 219.
- Fernandes, M. M., Scheinost, A. C., Baeyens, B., 2016. Sorption of trivalent lanthanides and actinides onto montmorillonite: Macroscopic, thermodynamic and structural evidence for ternary hydroxo and carbonato surface complexes on multiple sorption sites. *Water Research* 99, 74 – 82.
- Fischer-Appelt, K., Baltes, B., Buhmann, D., Larue, J., Mönig, J., 2013. Synthesebericht für die VSG. Research report GRS-290, GRS.
- Freundlich, H., 1922. *Kapillarchemie: Eine Darstellung der Chemie der Kolloide und verwandter Gebiete*. Akademische Verlagsgesellschaft Leipzig.
- Fricke, J., 2014. Sorption von Europium an Quarz - Batchversuche und geochemische Modellierung. Master thesis, Technical University Carolo-Wilhelmina zu Braunschweig.
- Geckeis, H., Lützenkirchen, J., Polly, R., Rabung, T., Schmidt, M., 2013. Mineral-water interface reactions of actinides. *Chemical Reviews* 113, 1016 – 1062.
- Giffaut, E., Grivé, M., Blanc, P., Vieillard, P., Colàs, E., Gailhanou, H., Gaboreau, S., Marty, N., Madé, B., Duro, L., 2014. Andra thermodynamic database for performance assessment: ThermoChimie. *Applied Geochemistry* 49, 225 – 236.
- Goldberg, S., Criscenti, L. J., Turner, D. R., Davis, J. A., Cantrell, K. J., 2007. Adsorption-desorption processes in subsurface reactive transport modeling. *Vadose Zone Journal* 6, 407 – 435.

- Guillaumont, R., Fanghänel, T., Neck, V., Fuger, J., Palmer, D. A., Grenthe, I., Rand, M. H., 2003. Update on the chemical thermodynamics of uranium, neptunium, plutonium, americium and technetium. Vol. 5 of Chemical Thermodynamics. Elsevier B. V.
- Hagemann, S., Bischofer, B., Scharge, T., Schönwiese, D. (Eds.), 2014. Entwicklung von Methoden und Modellen zur Bestimmung des Redoxpotentials salinarer Lösungen. No. 260. GRS gGmbH, Gesellschaft für Anlagen- und Reaktorsicherheit, Theodor-Heuss-Str. 4, 38122 Braunschweig, Germany.
- Hanna, K., Lassabatere, L., Bechet, B., 2009. Zinc and lead transfer in a contaminated roadside soil: Experimental study and modeling. *Journal of Hazardous Materials* 161, 1499 – 1505.
- Hanna, K., Martin, S., Quilès, F., Boily, J.-F., 2014. Sorption of phthalic acid at gothite surfaces under flow-through conditions. *Langmuir* 30, 6800 – 6807.
- Hanna, K., Rusch, B., Lassabatere, L., Hofmann, A., Humbert, B., 2010. Reactive transport of gentisic acid in a hematite-coated sand column: Experimental study and modeling. *Geochimica et Cosmochimica Acta* 74, 3351 – 3366.
- Hayes, K. F., 1987. Equilibrium, spectroscopic, and kinetic studies of ion adsorption at the oxide/aqueous interface. Ph.D. thesis, Stanford University, Stanford, C.A., USA.
- Hiemstra, T., 2010. Surface complexation at mineral interfaces: Multisite and charge distribution approach. Ph.D. thesis, Wageningen University.
- Hiemstra, T., de Wit, J. C. M., von Riemsdijk, W. H., 1989a. Multisite proton adsorption modeling at the solid / solution interface of (hydr)oxides: A new approach. II. Application to various important (hydr)oxides. *Journal of Colloid and Interface Science* 133 (1), 105 – 117.
- Hiemstra, T., van Riemsdijk, W. H., 1996. A surface structural approach to ion adsorption: The charge distribution (CD) model. *Journal of Colloid and Interface Science* 179, 488 – 508.
- Hiemstra, T., von Riemsdijk, W. H., Bolt, G. H., 1989b. Multisite proton adsorption modeling at the solid / solution interface of (hydr)oxides: A new approach. I. Model description and evaluation of intrinsic reaction constants. *Journal of Colloid and Interface Science* 133 (1), 91 – 104.

- Hill, M. C., 1998. Methods and guidelines for effective model calibration. Tech. Rep. Water-Resources investigation Report 98-4005, U. S. Geological Survey, revised version of 2001.
- Hodson, E. M., 2006. Searching for the perfect surface area normalizing term - a comparison of BET surface area-, geometric surface area- and mass normalized dissolution rates of anorthite and biotite. *Journal of Geochemical Exploration* 88, 288 – 291.
- Hodson, E. M., Martin, R. L., Parsons, I., 1997. Origins of the surface roughness of unweathered alkali feldspar grains. *Geochimica et Cosmochimica Acta* 61 (18), 3885 – 3896.
- Kallay, N., Kovačević, D., Žalec, S., 2006. Thermodynamics of the solid/liquid interface - its application to adsorption and colloid stability. In: Lützenkirchen, J. (Ed.), *Interface Science and Technology - Surface complexation modelling*, 1st Edition. Vol. 11. Elsevier AP, Ch. 6, pp. 133 – 170.
- Kar, A. S., Tomar, B. S., Godbole, S. V., Manchanda, V. K., 2011. Time resolved fluorescence spectroscopy and modeling of Eu(III) sorption by silica in presence and absence of alpha hydroxy isobutyric acid. *Colloids and Surfaces A: Physicochemical and Engineering Aspects* 378, 44 – 49.
- Kitamura, A., Fujiwara, K., Yamamoto, T., 1999. Analysis of adsorption behavior of cations onto quartz surface by electrical double-layer model. *Journal of Nuclear Science and Technology* 36 (12), 1167 – 1175.
- Klinge, H., Köthe, A., Ludwig, R.-R., Zwirner, R., 2002. Geologie und Hydrogeologie des Deckgebirges über dem Salzstock Gorleben. *Zeitschrift für Angewandte Geologie* 2, 7–15.
- Kohler, M., Curti, G. P., Kent, D. B., Davis, J. A., 1996. Experimental investigation and modeling of uranium(VI) transport under variable chemical conditions. *Water Resources Research* 32 (12), 3539 – 3551.
- Kosmulski, M., 2009. *Surface charging and points of zero charge*. Taylor and Francis Group, LLC.
- Kuan, W. H., Lo, S. L., Wang, M. K., 2004. Modeling and electrokinetic evidences on the processes of the Al(III) sorption continuum in SiO₂(s) suspension. *Journal of Colloid and Interface Science* 272, 489 – 497.

- Kumar, S., Aishwarya, S. K., Tomar, B. S., Bhattacharyya, D., 2012. X-ray absorption fine structure spectroscopy study of Eu(III) sorption products onto amorphous silica and γ -alumina: Effect of pH and substrate. *Polyhedron* 33, 33 – 40.
- Kumar, S., Pente, A. S., Bajpai, R. K., Kaushik, C. P., Tomar, B. S., 2013. Americium sorption on smectite-rich natural clay from granitic ground water. *Applied Geochemistry* 35, 28 – 34.
- Kuntze, H., Roeschmann, G., Schwerdtfeger, G., 1988. *Bodenkunde*, 4th Edition. Verlag Eugen Ulmer Stuttgart.
- Langmuir, I., 1918. The adsorption of gases on plane surfaces of glass, mica and platinum. *Journal of the American Chemical Society* 40, 1361 – 1403.
- Lee, S.-G., Lee, K. Y., Cho, S. Y., Yoon, Y. Y., Kim, Y., 2006. Sorption properties of ^{152}Eu and ^{241}Am in geological materials: Eu as an analogue for monitoring the Am behaviour in heterogeneous geological environments. *Geosciences Journal* 10 (2), 103 – 114.
- Lee, S. S., Schmidt, M., Laanait, N., Sturchio, N. C., Fenter, P., 2013. Investigation of structure, adsorption free energy, and overcharging behavior of trivalent Yttrium adsorbed at the muscovite (001)-water interface. *The Journal of Physical Chemistry* 117, 23738 – 23749.
- Lemire, R. J., Berner, U., Musikas, C., Palmer, D. A., Taylor, P., Tochiyama, O., 2013. *Chemical Thermodynamics of Iron, Part 1* (OECD Nuclear Energy Agency Data Bank). Tech. Rep. 13 a, OECD Nuclear Energy Agency, Issy-les-Moulineaux (France).
- Leonard, B. P., 1979. A stable and accurate convective modelling procedure based on quadratic upstream interpolation. *Computer methods in applied mechanics and engineering* 19, 59 – 98.
- Lindsay, W. L., 1980. *Chemical equilibria in soils*. John Wiley & Sons, Inc.
- Lützenkirchen, J., 1996. Description des interactions aux interfaces liquide - solide à l'aide des modèles de complexation et de précipitation de surface. Ph.D thesis, Université Louis Pasteur de Strasbourg.
- Lützenkirchen, J., 1998. Comparison of 1-pk and 2-pk version of surface complexation theory by the goodness of fit in describing surface charge data of (hydr)oxides. *Environmental Science and Technology* 32, 3149 – 3154.

- Lützenkirchen, J., 2002. Determination of points of zero charge of minerals, experimental and computational approaches. Vol. 5 of Current topics in colloid and interface science. Reserch Trends, Ch. 8, pp. 125 – 139.
- Lützenkirchen, J., Boily, J.-F., Lövgren, L., Sjöberg, S., 2002. Limitations of the potentiometric titration technique in determining the proton active site density of goethite surfaces. *Geochimica et Cosmochimica Acta* 66 (19), 3389 – 3396.
- Lützenkirchen, J., Kienzler, B., 2003. Modelling in natural science: Design, validation and case studies. Springer-Verlag Berlin Heidelberg, Ch. Modelling complexation Equilibria, pp. 378 – 412.
- Lützenkirchen, J., Preočanin, T., Bauer, A., Metz, V., Sjöberg, S., 2012 a. Net surface proton excess of smectites obtained from a combination of potentiometric acid-base, mass and electrolyte titrations. *Colloids and Surfaces A: Physicochemical and Engineering Aspects* 412, 11 – 19.
- Lützenkirchen, J., Prečanin, T., Kovačević, D., Tomišić, V., Lövgren, L., Kallay, N., 2012 b. Potentiometric titrations as a tool for surface charge determination. *Croatica Chemica Acta* 85 (4), 391 – 417.
- Macht, F., Eusterhues, K., Pronk, G. J., Totsche, K. U., 2011. Specific surface area of clay minerals: Comparison between atomic force microscopy measurements and bulk-gas (N₂) and -liquid (EGME) adsorption methods. *Applied Clay Science* 53, 20 – 26.
- Mantellato, S., Palacios, M., Flatt, R. J., 2015. Reliable specific surface area measurements on anhydrous cements. *Cement & Concrete Research* 67, 286 – 291.
- Maraqa, M. A., Zhao, X., Wallace, R. B., Voice, T. C., 1998. Retardation coefficients of nonionic organic compounds determined by batch and column techniques. *Soil Science Society of America Journal* 62, 142 – 152.
- Maslova, M. V., Gerasimova, L. G., Forsling, W., 2004. Surfae properties of cleaved mica. *Colloid Journal* 66 (3), 322 – 328.
- Matthes, S., 2001. Mineralogie - Eine Einführung in die spezielle Mineralogie, Petrologie und Lagerstättenkunde. Springer-Verlag Berlin Heidelberg New York Tokyo.
- Maček, M., Mauko, A., Mladenović, A., Majes, B., Petkovšek, A., 2013. A comparison of mehtods used to characterize the soil specific surface area of clays. *Applied Clay Science* 83 - 84, 144 – 152.

- Moog, H. C., 1997. Untersuchungen zum K/Ca-Austausch an den Tonminerale Montmorillonit und Vermiculit. Ph.D thesis, Technische Universität Carolo-Wilhelmina zu Braunschweig.
- Naderi, M., 2015. Progress in filtration and separation. Elsevier Ltd., Ch. 14, pp. 585 – 608.
- Noh, J. S., Schwarz, J. A., 1988. Estimation of the point of zero charge of simple oxides by mass titration. *Journal of Colloid and Interface Science* 130 (1), 157 – 164.
- Noseck, U., Brendler, V., Flügge, J., Stockmann, M., Britz, S., Lampe, M., Schikora, J., Schneider, A., 2012. Realistic integration of sorption processes in transport codes for long-term safety assessments. GRS report GRS - 297, Cooperation between Gesellschaft für Anlagen- und Reaktorsicherheit GRS gGmbH and Helmholtz-Zentrum Dresden-Rossendorf.
- Ohshima, H., 2006. Diffuse double layer equation for use in surface complexation models: Approximations and limits. In: Lützenkirchen, J. (Ed.), *Interface Science and Technology - Surface complexation modelling*, 1st Edition. Vol. 11. Elsevier AP, Ch. 3, pp. 67 – 87.
- Osman, M. A., Caseri, W. R., Suter, U. W., 1998. H^+/Li^+ and H^+/K^+ exchange on delaminated muscovite mica. *Journal of Colloid and Interface Science* 198, 157 – 163.
- Osman, M. A., Moor, C., Caseri, W. R., Suter, U. W., 1999. Alkali metals ion exchange on muscovite mica. *Journal of Colloid and Interface Science* 209, 232 – 239.
- Pan, D., Fan, F., Wang, Y., Li, P., Hu, P., Fan, Q., 2017. Retention of Eu(III) in muscovite environment: Batch and spectroscopic studies. *Chemical Engineering Journal* 330, 559 – 565.
- Parkhurst, D. L., Appelo, C. A. J., 1999. User's guide to PHREEQC (Version 2) - A computer program for speciation, batch-reaction, one-dimensional transport, and inverse geochemical calculations. U. S. Geological Survey, U. S. Department of the Interior.
- Parkhurst, D. L., Appelo, C. A. J., 2013. Description of input and examples for PHREEQC version 3—A computer program for speciation, batch-reaction, one-dimensional transport, and inverse geochemical calculations. *Techniques and Methods*, Chapter 43 of

- Section A, Ground Water Book 6, Modeling Techniques. U. S. Geological Survey, U. S. Department of the Interior.
- Pashley, R. M., 1981. DLVO and hydration force between mica surfaces in Li^+ , Na^+ , K^+ , and Cs^+ electrolyte solution: A correlation of double-layer and hydration forces with surface cation exchange properties. *Journal of Colloid and Interface Science* 83 (2), 531 – 546.
- Pashley, R. M., 1984. Forces between mica surfaces in La^{3+} and Cr^{3+} electrolyte solutions. *Journal of Colloid and Interface Science* 102 (1), 23 – 35.
- Poeter, E. P., Hill, M. C., Banta, E. R., Mehl, S., Christensen, S., 2005. UCODE_2005 and Six Other Computer Codes for Universal Sensitivity Analysis, Calibration, and Uncertainty Evaluation. Techniques and Methods, Chapter 11 of Section A, Ground Water Book 6, Modeling Techniques. U. S. Department of the Interior, U. S. Geological Survey, revised 2008 Edition.
- Poinssot, C., Baeyens, B., Bradbury, M. H., 1999. Experimental and modelling studies of caesium sorption on illite. *Geochimica et Cosmochimica Acta* 63 (19/20), 3217 – 3227.
- Polly, R., Schimmelpfennig, B., Flörsheimer, M., T., R., Kupcik, T., Klenze, R., Geckeis, H., 2013. Quantum chemical study of inner-sphere complexes of trivalent lanthanide and actinide ions on the corundum (001) surface. *Radiochimica Acta* 101, 561 – 570.
- Porro, I., Newman, M. E., Dunnivant, F. M., 2000. Comparison of batch and column methods for determining strontium distribution coefficients for unsaturated transport in basalt. *Environmental Science and Technology* 34, 1679 – 1686.
- Preočanin, T., Kallay, N., 1998. Application of "mass titration" to determination of surface charge of metal oxides. *Croatica Chemica Acta* 71 (4), 1117 – 1125.
- Preočanin, T., Kallay, N., 2006. Point of zero charge and surface charge density of TiO_2 in aqueous electrolyte solution as obtained by potentiometric mass titration. *Croatica Chemica Acta* 79 (1), 95 – 106.
- Rabung, T., Pierret, M. C., Bauer, A., Geckeis, H., Bradbury, M., Baeyens, B., 2005. Sorption of Eu(III) / Cm(III) on Ca-montmorillonite and Na-illite. Part I: Batch sorption and time-resolved laser fluorescence spectroscopy experiments. *Geochimica et Cosmochimica Acta* 69 (23), 5393 – 5402.

- Rard, J. A., 1987. Update of the europium data base. LLNL Internal Memo, Lawrence Livermore National Laboratory.
- Richter, C., 2015. Sorption of environmentally relevant radionuclides (U(VI), Np(V)) and lanthanides (Nd(III)) on feldspar and mica. Ph.D thesis, Technical University Dresden.
- Richter, C., Müller, K., Drobot, B., Steudtner, R., Großmann, K., Stockmann, M., Brendler, V., 2016. Macroscopic and spectroscopic characterization of uranium(VI) sorption onto orthoclase and muscovite and the influence of competing Ca^{2+} . *Geochimica et Cosmochimica Acta* 189, 143 – 157.
- Rouquerol, J., Llewellyn, P., Rouquerol, F., 2007. Is the BET equation applicable to microporous adsorbents? *Studies in Surface Science and Catalysis* 160, 49 – 56.
- Rusch, B., Hanna, K., Humbert, B., 2010. Sorption and transport of salicylate in a porous heterogeneous medium of silica quartz and goethite. *Environmental Science and Technology* 44, 2447 – 2453.
- Sächtling, H., 1995. Saechtling Kunststoff Taschenbuch, 31st Edition. Carl Hanser Verlag GmbH & Co.KG.
- Schwabe, K., 1967. Azidität konzentrierter Elektrolytlösungen. *Electrochimica Acta* 12, 67 – 93.
- Schwarz, J. A., Driscoll, C. T., Bhanot, A. K., 1983. The zero point of charge of silica-alumina oxide suspensions. *Journal of Colloid and Interface Science* 97 (1), 55 – 61.
- Shainberg, I., Alperovitch, N. I., Kern, R., 1987. Charge density and Na-K-Ca exchange on smectites. *Clay and Clay Minerals* 35 (1), 68 – 73.
- Simunek, J., van Genuchten, M. T., Sejna, M., Toride, N., Leij, F. J., 1999. The STANMOD computer software for evaluating solute transport in porous media using analytical solutions of convection-dispersion equation. U. S. Salinity Laboratory, Agricultural Research Service, U. S. Department of Agriculture, Riverside, CA, USA.
- Sing, K. S. W., Everett, D. H., Haul, R. A. W., Moscou, L., Pierotti, R. A., Rouquerol, J., Siemieniewska, T., 1985. Reporting physisorption data for gas/solid systems with special reference to the determination of surface area and porosity. *Pure and Applied Chemistry* 57 (4), 603 – 619.

- Spahiu, K., Bruno, J., 1995. A selected thermodynamic database for REE to be used in HLNW performance assessment exercises. Tech. Rep. 95-35, Svensk Kärnbränslehantering AB.
- Sposito, G., 1998. On points of zero charge. *Environmental Science and Technology* 32 (19), 2815 – 2819.
- StandAG, 2013. Gesetz zur Suche und Auswahl eines Standortes für ein Endlager für Wärme entwickelnde radioaktive Abfälle (Standortauswahlgesetz - StandAG), revised version from May 2017. Bundestag, BGBl. I S. 2553 Edition, renewed in May 2017.
- Stefánsson, A., Arnórsson, S., 2000. Feldspar saturation state in natural waters. *Geochimica et Cosmochimica Acta* 64, 2567 – 84.
- Steinbrecher, L., 2017. Sorption von Cs an Orthoklas und Muskovit - Batchversuche und geochemische Modellierung. Master thesis, Technical University Carolo-Wilhelmina zu Braunschweig.
- Stelljes, I., 2016a. Endlager Morsleben. <http://www.bfs.de/>, accessed January 2018.
URL http://www.endlager-morsleben.de/Morsleben/DE/service/Impressum/impressum_node.html
- Stelljes, I., 2016b. Endlager Morsleben. <http://www.bfs.de/>, accessed January 2018.
URL http://www.endlager-konrad.de/Konrad/EN/service/Imprint/imprint_node.html
- Stern, O., 1924. Zur Theorie der electrolytischen Doppelschicht. *Zeitschrift für Elektrochemie* 30 (21 - 22), 508 – 516.
- Stillings, L. L., Brantley, S. L., Michael, L. M., 1995. Proton adsorption at an adularia feldspar surface. *Geochimica et Cosmochimica Acta* 59 (8), 1473 – 1482.
- Stumpf, S., Stumpf, T., Lützenkirchen, J., Walther, C., Fanghänel, T., 2008. Immobilization of trivalent actinides by sorption onto quartz and incorporation into siliceous bulk: Investigations by TRLFS. *Journal of Colloid and Interface Science* 318, 5 – 14.
- Stumpf, S., Stumpf, T., Walther, C., Bosbach, D., Fanghänel, T., 2006. Sorption of Cm(III) onto different feldspar surfaces: a TRLFS study. *Radiochimica Acta* 94, 243–248.
- Tan, X., Fang, M., Wang, X., 2010. Sorption speciation of lanthanides/actinides on minerals by TRLFS, EXAFS and DFT studies: A review. *Molecules* 15, 8431 – 8468.

- Tertre, E., Berger, G., Simoni, E., Castet, S., Giffaut, E., Loubet, M., Catalette, H., 2006. Europium retention onto clay minerals from 25 to 150°C: Experimental measurements, spectroscopic features and sorption modelling. *Geochimica et Cosmochimica Acta* 70, 4563 – 4578.
- Thellier, C., Sposito, G., 1989. Influence of electrolyte concentration on quaternary cation exchange by Silver Hill Illite. *Soil Science Society of America Journal* 53, 705 – 711.
- Thoenen, T., Humel, W., Berner, U., Curti, E., 2014. The PSI/Nagra Chemical Thermodynamic Database 12/07, PSI Report 14-04. PSI Report 14 - 04, Cooperation between Paul Scherrer Institut (PSI) and the National Cooperative for the Disposal of Radioactive Waste (NAGRA).
- Toride, N., Leij, F. J., von Genuchten, M. T., 1998. The CXTFIT code for estimating transport parameter from laboratory or field tracer experiments, Version 2.1. U.S. Salinity Laboratory, Agricultural Research Service, U.S. Department of Agriculture, Riverside, CA, USA, report no. 137 Edition.
- Tournassat, C., Gailhanou, H., Crouzet, C., Braibant, G., Gautier, A., Gaucher, E. C., 2009. Cation exchange selectivity coefficient values on smectite and mixed-layer illite/smectite minerals. *Soil Science Society of America Journal* 73 (3), 928 – 942.
- Tournassat, C., Gailhanou, H., Crouzet, C., Braibant, G., Gautier, A., Lassin, A., Blanc, P., Gaucher, E. C., 2007. Two cation exchange models for direct and inverse modelling of solution major cation composition in equilibrium with illite surfaces. *Geochimica et Cosmochimica Acta* 71, 1098 – 1114.
- van Riemsdijk, W. H., Hiemstra, T., 2006. The CD-MUSIC model as a framework for interpreting ion adsorption on metal (hydr)oxide surfaces. In: Lützenkirchen, J. (Ed.), *Interface Science and Technology - Surface complexation modelling*, 1st Edition. Vol. 11. Elsevier AP, Ch. 8, pp. 251 – 268.
- Vicente, M. A., Suárez, M., de Dios López-González, J., Bañares-Munñoz, M. A., 1996. Characterization, surface area, and porosity analyses of the solids obtained by acid leaching of a saponite. *Langmuir* 12, 566 – 572.
- Voegelin, A., Vulava, V. M., Kretzschmar, R., 2001. Reaction-based model describing competitive sorption and transport of Cd, Zn, and Ni in an acidic soil. *Environmental Science and Technology* 35, 1651 – 1657.

- Voegelin, A., Vulava, V. M., Kuhnen, F., Kretzschmar, R., 2000. Multicomponent transport of major cations predicted from binary adsorption experiments. *Journal of Contaminant Hydrology* 46, 319 – 338.
- Voigt, W., Brendler, V., Marsh, K., Rarey, R., Wanner, H., Gaune-Escard, M., Cloke, P., Vercouter, E., Bastrakov, E., Hagemann, S., 2007. Quality assurance in thermodynamic databases for performance assessment studies in waste disposal. *Pure and Applied Chemistry* 79, 883 – 894.
- Wang, P., Anderko, A., 2001. Thermodynamic modeling of the adsorption of radionuclides on selected minerals. I: Cations. *Industrial & Engineering Chemistry Research* 40, 4428 – 4443.
- Westall, J., Hohl, H., 1980. A comparison of electrostatic models for the oxide/solution interface. *Advances in Colloid and Interface Science* 12, 265 – 294.
- Zorn, T., 2000. Untersuchungen der Sorption von Uran(VI) an das Gestein Phyllit zur Bestimmung von Oberflächenkomplexbildungskonstanten. Ph.d thesis, Technical University of Dresden.

Appendix A - Materials, methods, and additional information

Appendix A summarizes additional data and detailed information on data post processing, equipment, techniques, and models. Institutes that supported this study and that contributed to collected data sets are mentioned; relevant supplementary information of methods, calculations, and experimental set-up are provided.

A.1 Further information on the experimental procedure of titration experiments and reference pH values

In the following, background information to mass, electrolyte, and potentiometric acid-base titration experiments is given. Measurements are set into relation with different reference pH values e.g. pH_{mass} , pH_{pzse} , pH_{IEP} , pH_{ppzc} , pH_{pznpc} , etc.

A.1.1 Mass titration

Mass titrations involved suspensions with increasing *SLRs* in a low *IS* background electrolyte. At a mineral-specific *SLR* the obtained equilibrium pH of the suspension is independent of further addition of solid phase (pH_{mass}) and of the initial suspension H^+ concentration (pH_{ini}). For pristine oxide surfaces $\text{pH}_{mass} = \text{pH}_{ppzc}$. However, any contamination decreases (acidic impurities) or increases (basic impurities) pH_{mass} in relation to pH_{ppzc} (Sposito (1998), Davis and Kent (1990b), Lützenkirchen et al. (2012 a)).

A.1.2 Electrolyte titration

Electrolyte titrations evaluate pH_{mass} as a function of *IS*. The *SLR* of pH_{mass} is used to define the equilibrium pH that is independent of the electrolyte concentration (pH_{pzse}). At pH_{pzse} $(\delta p\text{H}/\delta IS)_{T,p} = 0$ applies (Tab. 2.1). The net surface proton charge is governed

by electrostatic forces at the solution-solid interface. Charging processes on a surface are controlled by electrostatic repulsion which is in turn depending on IS of the electrolyte. Increasing the electrolyte concentration reduces repulsive effects at the solid-solution interface. For suspensions of simple, symmetric 1:1 background electrolytes (e.g. $\text{Na}^+\text{ClO}_4^-$) with pristine metal oxides the pH_{pznpc} is independent of electrolyte concentration: $\text{pH}_{pznpc} = \text{pH}_{ppzc} = \text{pH}_{pzse}$. In case of preferential, asymmetric, counterion association affinities due to charged surface functional groups $\text{pH}_{nphc} \neq \text{pH}_{pznpc} \neq \text{pH}_{ppzc} \neq \text{pH}_{pzse}$. Preferential sorption processes of cations lead to $\text{pH}_{ppzc} > \text{pH}_{pzse}$ and vice versa regarding preferential sorption of anions, $\text{pH}_{ppzc} < \text{pH}_{pzse}$ (e.g. Preočanin and Kallay (2006), Lützenkirchen et al. (2012 a)).

A.1.3 Potentiometric acid-base titration

Potentiometric titration experiments are assumed to capture protonation and deprotonation reactions of surface functional groups (Si-OH, Al-OH) and exhibit a pH_{pznpc} as protonated and deprotonated surface functional groups are in equilibrium. For pristine or purified metal oxides $\text{pH}_{pznpc} = \text{pH}_{ppzc}$. In case of natural mineral surfaces or $\sigma_o \neq 0$, as for e.g. clay minerals where the prominent $\{001\}$ plane exhibits pH independent permanent negative surface charge due to isomorphic substitutions, $\text{pH}_{pznpc} \neq \text{pH}_{ppzc}$ and relative surface charge data is yielded from acid-base titration experiments. Discrimination between cation exchange processes, protolysis reactions, dissolution processes, or electrostatic repulsion processes is not explicitly possible via potentiometric titration experiments.

A.1.4 Isoelectric point

The pH_{IEP} is determined via zeta-potential measurements (Sec. 2.4). As a consequence of e.g. permanent negative surface charge, zeta-potential measurements result in very low isoelectric points (pH_{IEP}) due to very low electrokinetic potential over a wide pH range (Lützenkirchen et al., 2012 a). Hence, pH_{IEP} does not coincidence with pH_{mass} , pH_{pzse} , or pH_{pznpc} and, hence, $\text{pH}_{ppzc} \neq \text{pH}_{IEP}$.

A.2 Tools, equipment, and techniques used for the characterization of muscovite, orthoclase and quartz

Here, tools, equipment, and techniques used for mineral characterization of orthoclase, muscovite, and quartz are summarized. Supporting institutions are listed; if the institution is not mentioned measurements were performed at GRS gGmbH Braunschweig (Germany):

- Particle size analysis (Institut für Partikeltechnik, iPAT, Technical University of Braunschweig (iBMB), Braunschweig, Germany):
 - Parallel beam laser diffraction HELOS (Helium-Neon Laser Optisches System, Sympatec GmbH, Clausthal-Zellerfeld, Germany)
- Hydrofluoric acid digestion:
 - Inductively Coupled Plasma Mass Spectrometry (ICP MS, Thermo Electron GmbH, X Series II, SN 1001 C)
 - Optical Emission Spectrometry (ICP OES, Thermo Scientific, IRIS intrepid II XUV, 12262, Thermo Fisher Scientific Inc., Waltham, USA)
 - Atom Adsorption Spectrometry (Hitachi Z-2000 Zeeman-Tandem-AAS, 1707-013, Hitachi High-Technologies Corporation, Tokyo, Japan), Technical University Braunschweig, Germany.
- SSA after Brunauer, Emmet, and Teller (Brunauer et al., 1938):
 - Coulter SA3100, AE16018, Software Version 2.13 (Helmholtz-Zentrum Dresden-Rossendorf, Institute of Resource Ecology, Dresden, Germany)
 - Quantachrome Autosorb Automated Gas Sorption System, Autosorb for Windows®, Version 1.19 (Karlsruhe Institute of Technology, Institute for Nuclear Water Disposal (INE), Karlsruhe, Germany)
- Scanning Electron Microscopy (SEM) in combination with Energy Dispersive X-ray (EDX) spectroscopy (Concrete Construction and Fire Protection (iBMB), Technical University of Braunschweig, Braunschweig, Germany), cf. Appendix A.2.3:
 - SEM: JOEL Ltd, JSM-6700F, Tokyo, Japan (cold field emission gun)
 - EDX: EDAX SUTW Sapphire detector, Ametek GmbH, EDAX Business Unit AMETEK GmbH, Wiesbaden, Germany
 - Software: EDAX Genesis Spectrum V5.21 (2007), Institute of Building Material

- X-ray Diffraction analysis, also cf. Appendix A.2.2:
 - XRD, X'PertPRO, PANalytical
 - Database: Inorganic Crystal Structure Database (ICSD) for powder diffraction analysis (PW3213/p2, PAN-ICSD Database HS Plus, version 1.5.0, released December 2009)

A.2.1 Specific surface area

The *SSA* of a solid is typically assessed via the measurement of physical adsorption (physiosorption) of molecules onto the surface of a solid via non-specific van der Waals forces. To determine the *SSA* two main approaches have been developed: a) *SSA* calculations via physiosorption of a non-polar gas (N₂, Kr) and b) via physiosorption of polar liquids onto the solid's surface (Maček et al., 2013). In this study, *SSA* was obtained through physical adsorption of N₂ and Kr onto the minerals' surfaces. Data was evaluated after Brunauer et al. (1938). The so called BET model after Brunauer, Emmett, and Teller is most commonly applied whereby the *SSA* is calculated via the volumetric determination of the adsorbate under the assumption of a monomolecular layer coating on the adsorbent's surface.

A.2.2 Particle size separation

To obtain a particle size fraction of approximately 30 µm - 400 µm the feldspar was milled with an oscillating disk mill (FRITSCH GmbH, Germany) with wolfram carbide and zirconium oxide milling disks. A gap size of 150 µm was used. A standardised stainless steel Retsch sieve was used (wet-sieving) for further grain size separation. The PSD confirmed $d_{50} = 171 \mu\text{m}$, whereby 20 wt% exceeded a particle size of 242 µm. The milled, geochemically untreated orthoclase mineral is referred to as pristine mineral phase. Muscovite and orthoclase did not undergo this milling process and were used as supplied by the vendor for subsequent sieving processes.

For muscovite and orthoclase, desired particle fractions were separated via sieving (Retsch Analysesieb, DIN 4188/DIN-ISO 3310-1, D-42759 Haan, Germany). Muscovite was dry-sieved, whereas the milled orthoclase sample was separated via wet-sieving. Quartz was used as supplied by the vendor, no sieving took place. The PSD was determined via laser diffraction spectrometry (HELOS, Sympatec GmbH, Clausthal-Zellerfeld, Germany; conducted by Institut für Partikeltechnik, iPAT, Technical University of Braunschweig (iBMB), Braunschweig, Germany).

Muscovite

Discrimination between clay ($< 2\ \mu\text{m}$), silt ($2\ \mu\text{m} - 63\ \mu\text{m}$), and sand ($> 63\ \mu\text{m}$) fractions of the preliminary sieved $20\ \mu\text{m} - 400\ \mu\text{m}$ muscovite sample was achieved via the application of the Atterberg method. This technique was not applied for orthoclase, neither for quartz. Results yielded only $> 1\ \text{wt}\%$ clay fraction in the preliminary sieved powder mica which is in good correspondence with grain size analysis via laser diffraction. $10\ \text{wt}\%$ montmorillonite mineral was found in the separated clay fraction.

A.2.3 SEM, EDX measurements

The field emission electron microscope JSM-6700F (JOEL Ltd, Tokyo, Japan) with an integrated Energy Dispersive Spectrometry (Ametek GmbH, EDAX Business Unit AMETEK GmbH, Wiesbaden, Germany) was utilized to analyse quartz ($150 - 800\ \mu\text{m}$), muscovite ($20 - 400\ \mu\text{m}$), and orthoclase ($30 - 400\ \mu\text{m}$). Analysis were carried out under ultra high vacuum, mostly applying the COMPO mode at $20\ \text{kV}$, with varying working distances (WD), and different magnification factors. COMPO mode denotes the electron back-scattering mode which is sensitive to the average atomic number or density: The denser a particle, the lighter it appears. The EDX system provided quantitative area or point (few nanometers in diameter) elemental mappings as $\text{wt}\%$ or $\text{At}\%$.

A.2.4 Additional information on muscovite XRD measurements

Amongst others, XRD measurements offer information of swelling properties and the integrity of the mineral's structure that might change during preconditioning procedures. Sample preparation with diethyleneglycol allows to study a clay mineral's swelling potential. Diethyleneglycol preparation provided evidence for the presence of montmorillonite in the clay fraction of the muscovite sample (Fig. 2.3, cf. App. Sec. A.2.2). A shift of the $\{001\}$ XRD reflection at 6.2° $[2\theta]$ to 5.2° $[2\theta]$ is characteristic for spreading of clay lattice structure where the spreading of montmorillonite interlayers is caused due to incorporation of diethyleneglycol into the lattice (Fig. 2.3). This effect could be observed in this study and was more pronounced for the preconditioned muscovite sample (Fig. 2.3 B) in comparison to the untreated sample (Fig. 2.3 A).

Very briefly, X-ray reflection angles follow the Bragg formulation (Bragg and Bragg, 1913). Thus, provided that the change of crystal lattice distance is the only variable, collected X-ray reflection angles/Bragg angles $[\theta]$ decrease with increasing lattice distance. Diffraction angles are mineral specific. Montmorillonite swelling properties of

lattice structure are attributed to changes in the range of $0^\circ - 10^\circ$ [2Theta] depending on the degree of mineral layer distance alteration.

A.3 Tools, equipment, and techniques used for mineral titration experiments of muscovite, orthoclase, and quartz

Often minerals undergo purification procedures to remove basic or acidic impurities before conducting titration experiments (Noh and Schwarz, 1988). In the present study no prior preconditioning procedures were applied to reflect natural conditions in all examined systems (quartz, muscovite, orthoclase).

In the following, tools, equipment, and techniques relevant for mineral mass, electrolyte, and potentiometric titration measurements are summarized. Supporting institutions are mentioned separately; if the institution is not mentioned measurements were performed at GRS gGmbH Braunschweig (Germany):

- Ultrapure water
 - Sartorius arium[®] pro, H2OPRO-UV-D, 18.2 Mohm cm
- Sodim perchlorate hydrate salt (NaClO_4)
 - 99.99%, trace metal basis, 381225-500G, Aldrich, owned by Merck KGaA, Headquarter St. Louis, Missouri, U.S.A.
- Nitric acid (HNO_3) for background electrolyte pH adjustment
 - Certified nitric acid, 65% Suprapur[®], Merck, Millipore, Merck KGaA, Headquarter St. Louis, Missouri, U.S.A.
- Sodium hydroxide (NaOH) titrant solution
 - Titrisol[®], Merck (Sodium hydroxide solution for 1000 ml, Titrisol[®], 1 N), Merck KGaA, Headquarter St. Louis, Missouri, U.S.A.
- pH measurements of mass and electrolyte titration
 - Electrode: glass microelectrode, 125 mm, Metrohm
 - Temperature sensor: ALMEMO MA 10302, Za 9030-FS7, calibrated Pt 100 (0.001°C), AHLBORN, Mess- und Regelungstechnik GmbH, Holzkirchen, Germany, calibration mark: DKD-K-06701

- pH meter: 827 pH lab, 230 V, Metrohm
- Calibration: linear multipoint calibration of electrical potential in solution [mV]
- Merck standard buffer solutions pH 4, pH 7, pH 9, and pH 10: Merck, Certipur, NIST standard buffer solution (DIN 19266), Merck KGaA, Headquarter St. Louis, Missouri, U.S.A.
- Sample preparation (scale): Mettler TOLEDO XP205, DeltaRange®
- Magnetic stirrer: Heidolph magnetic stirrer, MR 1000 (Heidolph Instruments GmbH & Co. KG, Schwabach, Germany)
- pH measurements of potentiometric acid-base titration (Karlsruhe Institute of Technology, Institute for Nuclear Waste Disposal, Karlsruhe, Germany)
 - Electrode: glass electrode "iTrode", Pt 1000, 854 iConnect, Metrohm
 - Automatic titrator: Titrand 907, Metrohm
 - Automatic dosing system: DOSINO 800: 0.1 ml 2 min⁻¹ (software MaJo)
 - Magnetic stirrer: 801 stirrer, Metrohm
 - Calibration: A blank titration (so solid) of background electrolytes with defined amounts of H⁺ was carried out. With the specialized evaluation tool MaJo the pH was calculated from measured electrical potential difference U [mV]. Blank titrations were conducted with the combined glass electrode 854 iConnect (Metrohm) and repeated at least once before and after each mineral titration procedure. Each titration of the mica, feldspar, and quartz mineral followed the same procedure.
- Zeta-potential measurements (Helmholtz-Zentrum Dresden-Rossendorf, Institute of Resource Ecology, Dresden, Germany)
 - Laser Doppler velocimetry with a Zetasizer Nano ZS (Malvern Instruments, Malvern, U.K.) (Richter, 2015). Zeta-potential was measured via electrophoresis measurements using the Doppler shift in the laser beam (laser Doppler anemometry). Data was evaluated with the Smoluchowski approximation.

A.3.1 Correction of pH measurements in high IS conditions

For electrolyte titration experiments the pH was measured with electrodes that determined the electrical potential [mV] in a solution or suspension, which was then recalculated to

the pH (Eq. A.47).

$$E_{obs} = E_c + Nf \cdot \log a_{H^+} \quad (\text{A.47})$$

where E_{obs} corresponds to the measured electrical potential [mV], E_c to the reference electrode potential [mV], $\log a_{H^+}$ to the hydrogen ion activity (pH), and Nf to the Nernstian slope (≈ 59 mV/pH unit).

The measurement of the electrical potential of an electrolyte is dependent on the IS (Schwabe, 1967). To account for IS influences a correction (Δ_{pH}) as proposed by Hagemann et al. (2014) was determined where necessary (only for electrolyte titration experiments). Therefore, measurements once carried out by Schwabe (1967) were repeated; it was found that experimental data of both studies agreed well (Fig. A.22). Experimental data of both studies presented the basis to determine Δ_{pH} which was used to correct the IS influence for each pH measurement at elevated NaClO_4 concentrations (electrolyte titration experiments, Sec. 2.5.1). Corrected pH values are referred to as pH_c .

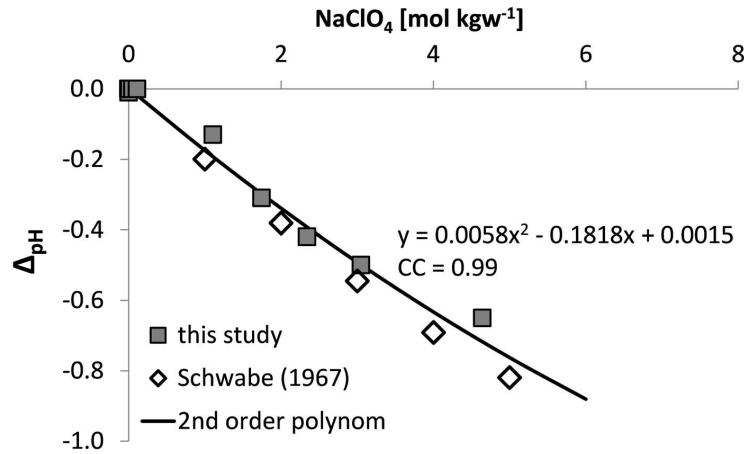


Fig. A.22: Δ_{pH} vs. NaClO_4 concentration [mol kgw⁻¹] after Schwabe (1967) and Hagemann et al. (2014). Δ_{pH} - correction term for pH measurements in high IS NaClO_4 environments, CC - correlation coefficient.

pH measurements of electrolyte titration experiments (Sec. 2.5.1) were corrected with according Δ_{pH} values: For example, Δ_{pH} for 1 mol L⁻¹ NaClO_4 electrolyte concentration corresponded to a decrease in pH of 0.2 pH units. A second order polynomial was used for regression analysis of measurements of this study in combination with data from Schwabe (1967) (Fig. A.22); individual Δ_{pH} values were calculated using this polynom. Additional information may be obtained from Hagemann et al. (2014) and Schwabe (1967).

A.3.2 Determination of pH uncertainties after DIN 19268 (2007)

Uncertainties of pH measurements for titration and batch experiments were derived following DIN 19268 (2007). From calibration data of pH measurements of suspensions containing muscovite (400 g L^{-1}), orthoclase (400 g L^{-1}), and quartz (1200 g L^{-1}) with pH values ranging between 3.5 - 10 a general estimation of pH uncertainties for mineral suspensions of this study was determined.

pH uncertainties amounted to a maximum of 0.16 pH units. The fairly high experimental error was due to the high *SLRs* which influenced pH measurements most according to DIN 19268 (2007). This uncertainty was assumed to be subject to all pH measurements; however, it can be considered a conservative estimation since *SLRs* varied significantly for acid-base titration and batch experiments.

A.3.3 Uncertainty of surface charge measurements

Baeyens and Bradbury (1997) estimated the experimental titration error to range between 10% and 30% for surface proton consumption measurements of Na-montmorillonite. They stated that limiting the lower end point of titration to pH 4 would reduce cation exchange influences on titration experiments to negligible levels. In contrast, mineral dissolution reactions were determined to also be relevant at $\text{pH} > 4.0$ (Baeyens and Bradbury, 1997). Generally, the estimated error range accounts for biasing effects such as mineral dissolution and e.g. potential cation exchange processes at the mineral water interface. Due to lack of more detailed data it was assumed that measurements of this study was subject to a similar error range.

A.4 Processing of relative raw data from potentiometric acid-base titration experiments to absolute values

A.4.1 Orthoclase: Linear relationship

Two different approaches were followed to determine absolute surface charge data for orthoclase:

- First, measurements were set into relation with $\text{pH}_{IEP} = 3.5$ with a shift of $\Delta\sigma = 0.047 \text{ C m}^{-2}$. A linear relationship with respect to pH_{IEP} had to be assumed in the absence of more detailed data sets. Unfortunately, the lower the pH, the

more prone to experimental error the measurements become, in particular with low surface area.

- Second, under the assumption of $K^+ - H^+$ exchange processes (Stillings et al., 1995) the orthoclase surface was treated like a clay mineral with permanent negative surface charges due to isomorphic substitution. Hence, potentiometric data was shifted in relation to $pH_{mass} \approx 8.0$ ($\Delta\sigma = 0.3 \text{ C m}^{-2}$) to transform relative raw data to absolute values.

Shifting measurements relative to $pH_{mass} \approx 8.0$ resulted in positive surface charge data for $pH < pH_{mass} \approx 8.0$ and negative surface charge for $pH_{mass} > 8.0$. Applying pH_{mass} as pH_{nphc} resulted in the hypothetical charge representation of surface functional edge sites of orthoclase.

A.4.2 Muscovite: Third order polynom

Since $pH_{pzse} \neq pH_{IEP} \neq pH_{mass}$ for muscovite, acid-base titration delivered relative surface charge measurements. To transform relative data into absolute values a third order polynomial relationship between pH_{IEP} and relative experimental data had to be assumed in the absence of more precise data. Figure A.23 depicts the third order polynomial illustrating a possible theoretical relationships between pH_{IEP} and relative titration measurements (grey symbols in Fig. A.23). The polynomial was used to derive absolute surface charge data (Fig. A.23 green symbols).

The application of the third order polynomial was related to a shift of relative raw data (measurements) equalling $\Delta\sigma = 0.005 \text{ C m}^{-2}$ and yielded a correlation coefficient (CC) = 0.998.

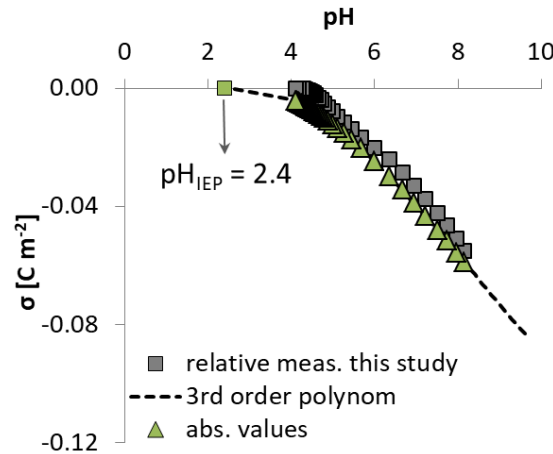


Fig. A.23: Shift of relative muscovite titration data (relative meas. this study) in relation to pH_{IEP} with $\Delta\sigma = 0.005 \text{ C m}^{-2}$. Third order polynomial regression yielded $\Delta\sigma = 0.005 \text{ C m}^{-2}$.

A.5 Goodness of fit (UCODE)

The following goodness of fit (gof) measures were used to assess surface charge and SCM performance; smallest values were preferred over larger ones (Hill, 1998). For detailed information on confidence interval (*CI*) and parameter standard deviation (*psd*) determination see Hill (1998).

- **Least squares objective function**

$$LSOF = \sum_{i=1}^{ND} \omega_i [y_i - y'_i]^2 \quad (\text{A.48})$$

with

LSOF weighted least squares objective function,

ND number of observations,

ω_i weight for *i*th observation (in this study: $\omega_i = 1$),

y_i *i*th observation being matched by regression,

y'_i simulated value corresponding to the *i*th observation.

- **Mean error**

$$ME = \frac{1}{ND} \sum_{i=1}^{ND} \omega_i (y_i - y'_i) \quad (\text{A.49})$$

with

ME mean error

- **Standard error**

$$SE = \sqrt{CEV} \quad (\text{A.50})$$

with

SE standard error

- **Calculated error variance**

$$CEV = \frac{LSOF}{ND - NP} \quad (\text{A.51})$$

with

NP number of estimated parameters

CEV calculated error variance

A.6 Additional information on surface charge models

PHREEQC uses the Davis equation for solution and surface speciation calculations by default which was not altered in the present study. Hence, geochemical conditions should not exceed $ISs > 0.5 \text{ mol L}^{-1}$ (e.g. Appelo and Postma (2010)). Weighting of experimental data was not included for any optimization procedure in UCODE (UCODE statistical means: $WT = 1$). This option ($WT = 1$) was defined in the UCODE observation file (.obs, cf. 2.7) and defined how weights were calculated for optimizations of the *LSOF* (equal weighing by unity of experimental data (weights = 1), Poeter et al. (2005)). Surface protolysis reactions were implemented as introduced in Section 2 (Eq. 2.6 - Eq. 2.8, Eq. 2.24 - Eq. 2.23). Equation 2.17 reduced the number of fitting parameters for the 2-pK approach. The *SSD* varied depending on the chosen pK approach: Application of the 1-pK approach needs twice as much sites to compensate mineral surface charge since only two species ($\text{S-O}^{-0.5}$, $\text{S-O}^{+0.5}$) are used. The 2-pK approach assumes S-O^- , S-OH_2^+ , and S-OH species to balance surface charge which covers two charge units. Zeta-potential measurements were included in BSM optimization procedures and were compared to the diffuse layer potential (ψ), when $\text{pH}_{IEP} = \text{pH}_{nphc}$. Zeta-potential measurements could not be considered for $\Delta\sigma = 0.30 \text{ C m}^{-2}$ and $\Delta\sigma = 0.51 \text{ C m}^{-2}$ for orthoclase and muscovite, respectively. PHREEQC standard state conditions applied: zero *IS*, activity coefficients of surface species were set unity, instant equilibrium of the evaluated systems was assumed.

A.6.1 Orthoclase surface charge models

Three approaches were followed to transform relative orthoclase surface charge data into absolute values (Sec. 2.5.1, Sec. 2.4.2, App. Sec. A.4.1):

- Relative measurements (raw data) were shifted with respect to pH_{mass}
- Relative measurements (raw data) were shifted with respect to pH_{IEP} .
- Relative data was shifted with respect to a fitted $\Delta\sigma$ as discussed in Section 2.5.2.

The *SSD* was calculated using Equation 2.33 and applied with *SSA_{BET}* (Tab. 2.2) to determine orthoclase protolysis constants (BSM, DDLM). Following results of electrolyte titration measurements (Sec. 2.5.1) symmetric counterion associations could be assumed since electrolyte influence became apparent only at $IS > 1 \text{ mol L}^{-1} \text{ NaClO}_4$. Equation 2.18 reduced the number of adjustable parameters and prevented correlations between $\log K_{a1}^{int}$ and $\log K_{a2}^{int}$.

Orthoclase was composed of microcline (66 wt%), albite (31 wt%), and minor weight percentages of quartz mineral phases (Sec. 2.3.2). Microcline and albite refer to K-Al silicate and Na-Al silicate mineral phases. To include Si-OH as well as Al-OH the 2-pK as well as the 1-pK approaches were applied. Zeta-potential measurements yielded a low pH_{IEP} and negative surface potentials for $\text{pH} > \text{pH}_{IEP}$ (Sec. 2.5.1). Negative surface potentials and a low pH_{IEP} in comparison to pH_{mass} may be due to isomorphic substitution of Si^{4+} against Al^{3+} in the crystal lattice. Stillings et al. (1995) suggested the application of cation exchange processes: Exchange of lattice K^+ against H^+ in solution. Mass and electrolyte titration results supported this recommendation and indicated influences of exchange processes (Sec. 2.5.1). However, in this study cation exchange reactions were neglected due to lack of data.

Orthoclase BSM

In this study, co- and counterion association coefficients $\log K_{Na^+}$ and $\log K_{ClO_4^-}$ were treated as fitting parameters and should be determined based on surface charge measurements at different IS s. In the present study, only one IS was available, so that final association coefficients only apply for $IS = 10 \text{ mM L}^{-1} \text{ NaClO}_4$. Equation 2.18 reduced the overall number of fitting parameters. Zeta-potential measurements were included and compared to the diffuse layer potential as experimental data (*SCP FS V, VI, VIII-X*, Fig. 2.17). Since the 1-plane and d-plane coincide (Stern (1924), Fig. 2.1), the electric surface potential of the 1-plane (ψ_1) determined by PHREEQC could be fitted to zeta-potential measurements. In the BSM C_1 is the only model inherent capacitance for the layer between the 0- and 1-planes. Hence, C_1 is a sensitive parameter (Eq. 2.3, Sec. 3.3) and was estimated as for muscovite BSMs (Tab. 2.3). Considering charge-potential relationships in Equations 2.3 and 2.4 $C_2 \rightarrow \infty$ (Kallay et al., 2006) the BSM is retrieved. Hence, C_2 was set to 30 F m^{-2} .

As C_1 was optimized it was subject to different model boundary conditions covering a range between 1.1 F m^{-2} and 2.8 F m^{-2} which was in agreement with literature estimates (RES³T, available at www.hzdr.de/res3t Brendler et al. (2003)). The capacitance is not a measurable value and therefore always an estimate.

A.6.2 Muscovite surface charge models and cation exchange

An offset of $\Delta\sigma = 0.051 \text{ C m}^{-2}$ and $\Delta\sigma = 5 \cdot 10^{-3}$ shifted relative data in relation to pH_{mass} and pH_{IEP} as pH_{nphc} , respectively (Sec. 2.5.1, App. Sec. A.4.2). Unfortunately, there is insufficient data available of muscovite *SSDs*, protolysis constants, layer capacitances,

etc.: Zorn (2000) calculated a SSD of 2.61 sites nm^{-2} from uranium nitrate sorption at pH 6.5 onto a muscovite surface. Maslova et al. (2004) used $SSD = 1.8$ sites nm^{-2} . They postulate a typical SSD for silicate oxides should range between 2 - 8 sites nm^{-2} . Since only little data is available, the SSD was optimized in this study but also used as fixed parameters with values following Maslova et al. (2004) and Zorn (2000). Initial parameter values for optimization procedures were manually adapted or values from Maslova et al. (2004) and Zorn (2000) were used.

Muscovite titration data could not be reliably used to calculate a specific muscovite SSD since saturation of surface functional groups was not reached in the examined pH-range. The lowest charge density value obtained at pH 8.2 equalled 0.06 C m^{-2} . Applying Equation 2.33 yielded $SSD = 0.34$ sites nm^{-2} for the 2-pK approach and accordingly $SSD = 0.69$ sites nm^{-2} for the 1-pK approach. These values range below typical SSD as proposed by Maslova et al. (2004) and were nevertheless used as initial SSD values in optimization procedures (*SCP M I, II, VI*, Tab. 2.3, Tab. 2.4).

The SSA_{BET} was used to describe the reactive surface area (Tab. 2.2). The 1-pK BSM and 1-pK DDLM were applied following Maslova et al. (2004). Where necessary the 2-pK approach was used (*SCP M I*). Zeta-potentials were included in the fitting procedure for the BSM with $\text{pH}_{IEP} = \text{pH}_{nphc}$. Equation 2.18 was used to prevent protolysis reactions to correlate and to reduce the number of adjustable parameters. For the BSM, C_1 was optimized. Counterion associations were fitted or $\log K_{Na^+}/\log K_{ClO_4^-}$ values were fixed below zero. Small $\log K_{Na^+}$ and $\log K_{ClO_4^-}$ parameter values electrostatically balance residual surface charge without posing strong competition on metal surface complexation processes. Since symmetrical co- and counterion association coefficients applied for $IS < 0.1$ mol L^{-1} (Sec. 2.5.1) $\log K_{Na^+} = \log K_{ClO_4^-}$ was assumed and supported by results of electrolyte titration experiments; IS influence became apparent at 10 mM NaClO_4 (Sec. 2.5.1).

Muscovite surface reactions are assumed to mainly take place at surface edge sites (Bradbury and Baeyens, 2000). The prominent {001}-plane only contributes insignificantly to surface protonation, deprotonation, and surface complexation processes. Phyllosilicates carry permanent negative surface charges and hence exhibit low IEPs which was verified with zeta-potential measurements. Permanent negative surface charges are partially balanced by incorporation of interlayer cations. Depending on the geochemical surrounding interlayer cations may be exchanged. With HF-analysis of this study minor contribution of Na and Mg could be detected which contributed to the muscovite composition. Both cations represent common interlayer cations (Tab. B.2). To include cation exchange

processes in SCMs cation exchange selectivity coefficients were defined that contributed to surface charge development. Since this study did not focus on the determination of selectivity coefficients literature data was used as a best estimate which is discussed in the following and in Section 3.3.3.

A vast amount of data is available regarding cation exchange selectivity coefficients of clay minerals (e.g. Shainberg et al. (1987), Tournassat et al. (2007), Bradbury et al. (2005)). For illite and montmorillonite Bradbury and Baeyens (2000), Bradbury et al. (2005), and e.g. Bradbury and Baeyens (2005b) conducted extensive investigations to define cation exchange processes and reactions (Tab. 3.2). Bradbury and Baeyens (2000) introduced cation exchange selectivity coefficients for Cs uptake for a "reference illite" that were validated by means of simulation of Cs sorption isotherms for various literature data sets. Unfortunately, no such data is available in literature for muscovite. Major cations that contributed to cation exchange processes in this study are typical interlayer cations such as Na^+ , K^+ , and H^+ (e.g. Bergaya et al. (2006)). Osman et al. (1998) and Osman et al. (1999) published homo-ionic Li- and K-muscovite selectivity coefficients for different geochemical conditions. Li^+ was exchanged for H^+ and Na^+ (Osman et al. (1998), Osman et al. (1999)), whereas K^+ was exchanged for H^+ (Osman et al., 1998). Maslova et al. (2004) examined two mica minerals (muscovite, phlogopite) and provide an optimized selectivity coefficient for the exchange of H^+ against K^+ of a preconditioned phlogopite. Since PHREEQC includes cation exchange processes via half reactions exchange reactions need to be included in relation to the same exchangeable cation (index cation). Therefore, Osman et al. (1998), Osman et al. (1999) and Maslova et al. (2004) did not provide coherent data for the present modeling study. However, Poinssot et al. (1999) published a sound data set for homo-ionic Na-illite. The Na-illite held a CEC of $12.7 \text{ cmol}^+ \text{ kg}^{-1}$, experiments were conducted in 10 mM NaClO_4 background electrolyte with pH values that ranged between pH 2 - 12. Derived cation exchange selectivity coefficients $\log K_c \text{Na}/\text{K}$ and $\log K_c \text{Na}/\text{H}$ were calculated from sorption experiments with Cs on Na-illite. Since geochemical conditions roughly related to this study and since the Na-illite's CEC did not differ by orders of magnitudes from muscovite (Tab. 3.1) the literature data set provided by Poinssot et al. (1999) was used for surface charge and surface complexation models in this study. Hence, $\log K_c \text{Na}/\text{Na} = 0$, $\log K_c \text{Na}/\text{H} = -1.75$, and $\log K_c \text{Na}/\text{K} = -2.25$ (Poinssot et al., 1999). Applying Poinssot et al. (1999) half reactions considered the index cation Na^+ which corresponded well to mineral preconditioning procedures of batch and column experiments (Sec. 3.2.1 and Sec. 4.2.1) and HF-analysis (Tab. B.2). Cation exchange selectivity coefficients were applied as fix parameter values for all mica optimization procedures and simulations.

A.7 Tools, equipment, and techniques used for batch experiments of muscovite, orthoclase and quartz

The following tools and equipment were used for the experimental set-up of batch experiments. Techniques and supporting institutions are summarized; if the institution is not mentioned measurements were performed at GRS gGmbH Braunschweig (Germany):

- Batch experiments
 - Sieve: Retsch Analysesieb, DIN 4188/DIN-ISO 3310-1, D-42759 Haan, Germany
 - Electrolyte: NaClO_4 hydrate salt, 99.99%, trace metal basis, Aldrich, owned by Merck KGaA, Headquarter St. Louis, Missouri, U.S.A.
 - Electrode: combined glass electrode, 6.0233.100 (Pt 1000), Metrohm
 - Bottles: 125 ml wide-mouth bottles, LDPE, NALGENE
 - Magnetic stirrer: Heidolph magnetic stirrer, MR 1000 (Heidolph Instruments GmbH & Co. KG, Schwabach, Germany)
 - Europium ICP Standard, 1000 mg L^{-1} , Merck KGaA, Headquarter St. Louis, Missouri, U.S.A.
 - Anotop syringe filter
 - Acidification: Certified nitric acid, 65% Suprapur[®], Merck, Millipore, Merck KGaA, Headquarter St. Louis, Missouri, U.S.A.
 - ICP MS: Thermo Electron GmbH, X Series II, SN 1001 C
 - Ultrapure water: Sartorius arium[®] pro, H2OPRO-UV-D, 18.2 Mohm cm
- Eu ICP MS analysis uncertainty estimation (long-term precision measurements)
 - ICP MS: Thermo Electron GmbH, X Series II, SN 1001 C
 - Europium ICP Standard, 1000 mg L^{-1} , Merck KGaA, Headquarter St. Louis, Missouri, U.S.A.
 - Acidification: Certified nitric acid, 65% Suprapur[®], Merck, Millipore, Merck KGaA, Headquarter St. Louis, Missouri, U.S.A.
 - Ultrapure water: Sartorius arium[®] pro, H2OPRO-UV-D, 18.2 Mohm cm

A.8 Estimation of Eu measurement uncertainties

Long-term precision measurements were carried out to assess Eu ICP MS analyses uncertainties. Therefore, Eu samples were prepared with Eu concentrations ranging between $C_{Eu} = 10^{-5} - 10^{-8} \text{ mol L}^{-1}$ in 5% HNO_3 background electrolyte. Samples were stored in chemically inert PFA vessels. ICP MS measurements of samples were conducted over eight months: Twice a week for the first four months, the last four months samples were analysed once a week.

From long-term precision measurements of Eu samples the relative standard deviation was calculated for each Eu concentration (C_{Eu}). A logarithmic function was fitted to the relative standard deviation as a function of Eu concentration in solution (C_{Eu}) and was used for the estimation of the ICP MS measuring error for each batch sample. The double relative standard deviation of C_{Eu} was used to calculate Eu uptake uncertainties given in [%Eu immobilized]. Error were used to illustrate measurement uncertainties in Figures 3.3 - 3.12 (error bars), error estimations were not used for parameter optimization procedures with UCODE.

A.9 Data processing of quartz batch measurements and supplementary information on quartz SCMs

The pH values of quartz batch experiments ranged between 3.5 - 7, Eu C_0 ranged between $10^{-5} - 10^{-8} \text{ mol L}^{-1}$. Two *SLRs* were used: 12.5 g L^{-1} and 50 g L^{-1} (Fig. 3.3). Experiments were conducted in doublets. Initial Eu concentrations (C_0) were defined to equal ideal C_0 concentrations ($10^{-8} \text{ mol L}^{-1}$, $10^{-7} \text{ mol L}^{-1}$, $10^{-6} \text{ mol L}^{-1}$, $10^{-5} \text{ mol L}^{-1}$) since no measurements of Eu C_0 were available. Data illustrated in Figure 3.3 was corrected for outliers. Since experiments were conducted in triplets measurements that violated the following relationships were declared outliers and excluded from data evaluation: Eu sorption isotherms on quartz surfaces are pH dependent (the larger the pH, the smaller Eu C_{equil}); and increasing *SLRs* result in higher Eu uptake due to sorption or other immobilization processes.

1-pK DDLM

A cation exchange site was included in 1-pK DDLMs to account for sorption processes at low pH conditions (*SCP I mono+EX*, *SCP I bi+EX*, *SCP I mono+bi+Ex*, Tab. 3.4)

where 1‰ surface sites were attributed to potential cation exchange processes. Since the pH of the suspensions was adjusted in 10 mM NaClO₄ Na⁺ was chosen as the index cation to be exchanged against Eu³⁺. The Eu³⁺ selectivity coefficient ($\log K_{cNa/Eu}$) as well as the surface complexation constant were fitted. The cation exchange was only exemplarily considered for DDLMS.

A.10 Data processing of orthoclase batch measurements and supplementary information on orthoclase SCMs

As for quartz, two SLRs, four initial Eu concentrations (C_0), and four pH_{ini} were used as geochemical boundary conditions for orthoclase batch experiments. Triplet experiments were conducted. For data processing purposes of the equilibrium concentration of Eu in the suspensions (C_{equil} , raw data, cf. Sec. 3.2.2), initial Eu concentrations ranging between 10⁻⁶ - 10⁻⁸ mol L⁻¹ were defined to equal ideal concentrations relating to $C_0 = 10^{-8}$ mol L⁻¹, 10⁻⁷ mol L⁻¹, 10⁻⁶ mol L⁻¹ since measurements of C_0 were not available. For the highest initial Eu concentration C_0 was specified to equal 1.07·10⁻⁵ mol L⁻¹ which corresponded to the highest measured C_{equil} at pH 3.6, SLR 12.5 g L⁻¹. Hence, it was assumed that no sorption processes occurred at pH ≤ 3.6.

Initial Eu concentrations C_0 were adjusted using Eu stock solutions that were prepared from Europium ICP Standard, 1000 mg L⁻¹. After the addition of appropriate amounts of Eu stock solution to samples pH_{ini} dropped up to 3.0 pH units (Britz, 2011). Since Eu hydrolysis effects were previously ruled out (Britz, 2011), this pH decrease was attributed to the 2% HNO₃ background solution of the Europium ICP Standard. Decreasing pH values due to Eu stock solution addition were observed for Eu $C_0 = 1.07 \cdot 10^{-5}$ mol L⁻¹ and $C_0 = 10^{-6}$ mol L⁻¹. Smaller Eu C_0 showed no pH drop since only small amounts of Eu stock solution had to be added. pH values in Figures 3.9 - 3.11 represent the pH after the addition stock solution. For quartz batch experiments the effect of decreasing pH due to stock solution addition was avoided by pH adjustment of the stock solutions prior to the addition to batch samples.

Equivalent to quartz fitting approaches, the DDLM, BSM, and the noEDLM were used and SCP sets from surface charge models were utilized as fix parameter values (Sec. 2, Tab. 2.4). As discussed in Section 2.5.2, only the 1-pK approach was considered. Cation exchange reactions were not included for orthoclase. Potential Eu(III) solid

phase precipitation reactions were allowed. The SSA_{BET} was used in orthoclase SCMs (Tab. 2.2). Following TRLFS measurements by Stumpf et al. (2006) bi- and tridentate surface complexes, as well as a hydrolysed monodentate surface complex were included in orthoclase Eu SCMs. Considering studies of Fernandes et al. (2016) and Polly et al. (2013) who studied montmorillonite and corundum surfaces a tetradentate surface complex was also considered. Tetradentate surface complexes were used to verify whether an increase of chemical bonds towards the mineral surface would result in an improvement of gof. Furthermore, combinations of Eu surface complexes (e.g. monodentate + bidentate, monodentate + hydrolysed monodentate surface complex), and a single monodentate surface complex were taken into account for inverse modeling procedures. However, the combination of two or more Eu surface complexes resulted in large parameter confidence intervals and/or in high parameter correlations and inverse modeling via UCODE did not result in unique parameter estimates (model approaches not provided). Therefore, only optimized results of single Eu surface complexes are illustrated and discussed.

A.11 Data processing of muscovite batch measurements

The experimental procedure of muscovite batch experiments followed orthoclase and quartz. For data processing purposes (Sec. 3.2.2) of the muscovite batch data Eu C_0 were expressed as ideal concentrations (10^{-5} mol L⁻¹, 10^{-6} mol L⁻¹, 10^{-7} mol L⁻¹, 10^{-8} mol L⁻¹).

As for orthoclase batch experiments, Europium ICP Standard (1000 mg L⁻¹, Merck KGaA, 64271 Darmstadt, Germany, Headquarter St. Louis, Missouri, U.S.A.) was used to prepare Eu stock solutions for muscovite batch experiments. Since the pH of stock solutions was not adjusted prior to the addition to batch samples, pH_{ini} dropped up to 3.3 pH units (Britz, 2011). For Eu $C_0 = 10^{-5}$ mol L⁻¹ and 10^{-6} mol L⁻¹ pH conditions were shifted towards lower pH values; for $C_0 = 10^{-7}$ mol L⁻¹ and $C_0 = 10^{-8}$ mol L⁻¹ no pH shift occurred due to small amounts of added stock solution (Britz, 2011). pH values in Figure 3.12 represent measurements after the addition of Eu stock solution.

A.12 Tools, equipment, and techniques used for the experimental set-up of transport experiments

In the following, tools, equipment, chemicals, and techniques used for the experimental set-up of column experiments (incl. preconditioning procedures) are summarized:

- Preconditioning (cf. App. A.12.1)

- Temperature: ALMEMO MA 10302, Pt 100, Ahlborn, Holzkirchen, Deutschland (ZA 9030-FS7, Norm E4) calibrated thermometer (German Calibration Service, DKD-K-06701)
- Electrolyte: NaClO_4 hydrate salt, 99.99%, trace metal basis, Aldrich, owned by Merck KGaA, Headquarter St. Louis, Missouri, U.S.A.
- pH meter and electrode: Metrohm 827 pH lab, 6.0234.100 and Metrohm glass microelectrode (178 mm) (Metrohm AG, Herisau, Switzerland)
- Syringe filter: Minisart, syringe filter, 0.2 μm , cellulose acetate membrane, Sartorius, Göttingen, Germany
- ICP MS, ICP OES: Specifications given in Appendix A.2
- pH adjustment: Certified nitric acid, 65% Suprapur[®], Millipore, Merck KGaA, Headquarter St. Louis, Missouri, U.S.A.
- N_2 -atmosphere: N_2 , nitrogen 4.8, ISO 14175-N1-N, 99.998 Vol% N_2
- Glove box: Plas Labs, model 815-PGB/EXP, no 22105, Lansing, MI 48606, USA
- Sterile pipettes: TPP, Tissue culture and laboratory inventory, 2 ml, sterile serological pipettes
- Drying chamber: Binder FED 115, 283.15 - 573.15 K, 60 Hz, No 990580, Binder GmbH, 78532 Tullingen, Germany
- Autoclave treatment of mineral samples and equipment for preconditioning of minerals were performed at the Helmholtz-Zentrum Dresden-Rossendorf e.V. (App. A.12.1).
- Column experiments
 - Background electrolytes:
 - * NaClO_4 : $\text{NaClO}_4 \times \text{H}_2\text{O}$, trace metal basis, 99.99%, Aldrich, owned by Merck KGaA, Headquarter St. Louis, Missouri, U.S.A.
 - * Na_2SO_4 : Sodium sulfate decahydrate, p.a., EMSURE[®], Merck KGaA, Headquarter St. Louis, Missouri, U.S.A.
 - * Artificial groundwater: See Table A.1.
 - pH adjustment:
 - * 65% HNO_3 : certified nitric acid, 65% Suprapur[®], Merck Millipore, Merck KGaA, Headquarters St. Louis, Missouri, U.S.A.

- * NaOH: Titrisol, NaOH for 1000 ml, 1 mol L⁻¹, Merck KGaA, Headquarters St. Louis, Missouri, U.S.A.
- pH meter and electrode: Metrohm 827 pH lab, 6.0234.100 and Metrohm glass microelectrode (178 mm) (Metrohm AG, Herisau, Switzerland)
- Eu: Europium ICP Standard, 1000 mg L⁻¹, Merck KGaA, Headquarters St. Louis, Missouri, U.S.A.
- NaBr: NaBr suprapure®, 99.995%, Merck KGaA, Headquarters St. Louis, Missouri, U.S.A.
- Peristaltic pump: IPC High Precision Multichannel Dispenser, ISM932D, ISMATEC, Cole-Parmer GmbH, Wertheim, Germany
- Peristaltic pump tubing: Fluran®Tubing, F5500-a (ISMATEC, IDEX Health & Science, Cole-Parmer GmbH, Wertheim, Germany).
- Fraction collector: Retriever 500 TELEDYNE ISCO, Lincoln, Nebraska, U.S.A.
- 65% HNO₃: Specifications given above (v.s.)
- Syringe filter: Specifications given above (v.s.)
- Scale: Excellence plus XP 205, Delta Range®, METTLER TOLEDO, Gießen, Germany

A.12.1 Preconditioning of mineral samples for column experiments

All mineral samples except for quartz underwent preconditioning procedures before transport experiments were initiated; quartz was used as provided by the supplier (Sec. 2.3.3). Muscovite and orthoclase underwent two different preconditioning treatments: In a first step (i), the muscovite and freshly milled orthoclase (App. A.2.2) were suspended in NaClO₄, pH 7 to equilibrate the mineral surfaces with the background electrolyte. In a second step (ii), equilibrated minerals were preconditioned with NaClO₄, pH 3.5 to reduce the equilibration time between the solids and the background electrolyte during column experiments (Sec. 4.2.1).

(i) Equilibration with NaClO₄ electrolyte, pH 7

Milling of orthoclase resulted in freshly cleaved grains and potentially highly reactive surfaces which are not typical for naturally equilibrated systems. Muscovite on the other hand was provided by the supplier without information of mining

conditions and pretreatment of the mineral. To create a sound basis for comparability 5 kg of each mineral were preconditioned in 20 L 0.05 mol L⁻¹ NaClO₄ background electrolyte over approximately three months. Equilibration took place under ambient conditions in lightproof containers at 294.7 K ± 0.6 K (± single standard deviation). On an every day basis samples were stirred and the pH was measured. In regular time intervals samples from the supernatant solution were taken, filtered, and analyzed for Ti, Mn, Sr, Ba, Co, Cu, Zn, Cd, Eu, Pb, U (ICP MS) and Al, Ca, Fe, K, Mg, Si (ICP OES). The systems were assumed to be equilibrated after element concentrations and pH reached a constant level.

(ii) **Preconditioning of mineral surfaces with NaClO₄, pH 3.5**

A prerequisite for column experiments was a chemical equilibrium between the minerals and the background electrolytes: Equilibration was attained after the effluent pH of the column (pH_{equil}) equalled pH_{ini} of the background electrolyte (Sec. 4.2.1). This second preconditioning procedure was necessary to decrease equilibration times of column experiments to feasible time frames since pretests had shown that equilibration of column systems exceeded six months when mineral samples from preconditioning step (i) (v.s.) were used (App. Fig. B.34).

For the second preconditioning procedure, mineral samples and equipment (glass bottles, NaClO₄ electrolytes, screw caps, etc.) were autoclaved at 394 K over 20 minutes. The autoclaved orthoclase and muscovite samples were subsequently suspended in 10 mmol L⁻¹ NaClO₄, pH 3.5 solution under N₂ atmosphere in a glove box over approximately six months. The glove box itself and all equipment that was transferred into the glove box were sterilized with 70% alcohol. The autoclaving and sterilization approach was necessary to minimize the possibility of algae growth during the second preconditioning step. Furthermore, influences caused by organic remains on the mineral surfaces were also eliminated. The adjustment of the suspension pH was achieved via the addition of appropriate amounts of 65% HNO₃ on a daily basis during the first weeks; time intervals were extended as buffer capacities of the minerals reduced over time. Samples were shaken on a daily basis. For pH measuring purposes sterile disposable pipettes were used to obtain approximately 2 ml aliquots from the suspensions. pH measurements were carried out outside the glove box under ambient conditions. After pH_{equil} = const. = 3.5, suspensions were decanted and solids dried at 303 K in a drying chamber.

Orthoclase and muscovite samples used for column experiments underwent preconditioning procedure (i) and (ii) and are referred to as "preconditioned mineral(s)".

A.12.2 Specification of the artificial groundwater after Klinge et al. (2002)

The artificial groundwater composition was used as suggested by Klinge et al. (2002) and Noseck et al. (2012) and represented a groundwater composition present at the Gorleben study site. The NaHCO_3 concentration was decreased in relation to the Klinge et al. (2002) composition which was necessary to prevent degassing of CO_2 at pH 3.5. The geochemical speciation calculations with PHREEQC provided the maximum possible HCO_3^- concentration without degassing of CO_2 at pH 3.5 (PHREEQC calculation not provided here). Ion balance was reached with adaptations of Na^+ concentrations. The exact composition of the artificial groundwater as used in this study is provided in Appendix A Table A.1 (v.i.).

Tab. A.1: Composition (Klinge et al. (2002), Noseck et al. (2012)) and specification of chemicals used for the artificial groundwater. NaHCO_3 concentration was decreased to prevent degassing of CO_2 at pH 3.5, ion balance was reached with adaptations of Na^+ . Salts and ICP standard from Merck KGaA, Darmstadt, Germany (Headquarters St. Louis, Missouri, U.S.A.).

Salt	Specification	Concentration [mol L ⁻¹]
$\text{CaSO}_4 \cdot 2\text{H}_2\text{O}$	2161.0500, p.a.	$2.84 \cdot 10^{-4}$
$\text{Ca}(\text{Cl})_2 \cdot \text{H}_2\text{O}$	1.42000.5000, p.a., EMPROVE®	$9.21 \cdot 10^{-4}$
NaHCO_3	1.6329.0500, p.a.	$1.50 \cdot 10^{-5}$
NaCl	1.06404.100, p.a., EMSURE®	$4.24 \cdot 10^{-4}$
KCl	1.04936.1000, p.a., EMSURE®	$5.40 \cdot 10^{-5}$
$\text{Mg}(\text{Cl})_2 \cdot 6\text{H}_2\text{O}$	1.05833.1000, p.a., EMSURE®	$1.67 \cdot 10^{-4}$
$\text{Al}(\text{NO}_3)_3$	Aluminium ICP Standard, 1000 mg L ⁻¹	$1.85 \cdot 10^{-6}$

A.12.3 Equations for the evaluation of transport data and determination of transport parameters

Listed below, calculations and equations were used to assess and evaluate experimental transport data and were applied to determine transport parameters for e.g. 1D Eu reactive transport simulations with PHREEQC. The following equations mainly comprise supplementary information on data and parameters provided in Table 4.2.

[1] Pore space of a mineral-filled (packed) column V_0 [cm³]

$$V_0 = \theta \cdot V_{tot} \quad (\text{A.52})$$

with

θ	$[-]$	Total column water content assumed to be equal to the porosity
----------	-------	--

V_{tot} [cm³] Empty column volume: 161.7 cm³, $L = 122.5$ mm, $id = 41$ mm

id [mm] Inner diameter

The water content of each column was gravimetrically determined (scale). The pore space of a column (V_0) was used to calculate the amount of applied background electrolyte (PV, pore volume) in relation to V_0 .

[2] Darcy velocity q [cm h⁻¹]

$$q = \frac{Q}{A} \quad (\text{A.53})$$

with

Q [cm³ h⁻¹] Water flux, flow rate

A [cm²] Cross section area of a column: 13.2 cm²

[3] Pore water velocity v [cm h⁻¹]

$$v = \frac{q}{\theta} \tag{A.54}$$

with

q [cm h⁻¹] Darcy velocity

θ	$[-]$	Total water content of a column; assumed to be equal to the porosity
----------	-------	---

[4] Péclet number Pe [-]

$$Pe = \frac{v \cdot L}{D} \quad (\text{A.55})$$

with

v	$[\text{cm h}^{-1}]$	Pore water velocity
-----	----------------------	---------------------

L [cm] Column length: 122.5 mm

D	$[\text{cm}^2 \text{ h}^{-1}]$	Dispersion coefficient
-----	--------------------------------	------------------------

[5] **Grid Péclet number Pe_{grid} [-]**

$$Pe_{\text{grid}} = \frac{L_{\text{cell}}}{\lambda} \quad (\text{A.56})$$

with

L_{cell} [m] Cell length (column grid discretization PHREEQC:
180 cells, $L_{\text{cell}} = 0.0007$ m)

λ [m] Dispersivity (cf. [6], Eq. A.57)

[6] **Dispersivity λ [cm]**

$$\lambda = \frac{D}{v} \quad (\text{A.57})$$

with

v [cm h⁻¹] Pore water velocity

D [cm² h⁻¹] Dispersion coefficient

The dispersivity λ was calculated with D from CXTFIT optimizations and used as a fixed transport parameter in PHREEQC reactive transport simulations.

[7] **Bulk density ρ_b [g cm⁻³]**

$$\rho_b = \frac{M}{V_{\text{tot}}} \quad (\text{A.58})$$

with

M [g] Solid mass (dried)

V_{tot} [cm³] Empty column volume: 161.7 cm³, $L = 122.5$ mm, $id = 41$ mm

id [mm] Inner diameter

Appendix B - Supplementary data

Appendix B provides supplementary data, additional figures, suppliers data, and further information/data/measurements to substantiate the findings of this research. Provided data complements informatoin given in Sections 2, 3, and 4.

B.1 Characterization of muscovite, orthoclase and quartz

In the following, additional, detailed information on the mineral characterization of muscovite, orthoclase, and quartz are offered. Data on hydrofluoric acid digestion, EDX, XRD, as well as an example of BET analysis are provided. Error sources of BET measurements are summarized; zeta-potential measurements of orthoclase, quartz, and muscovite are illustrated.

Table B.2 compares HF analysis carried out in this study with suppliers data and the ideal geochemical composition of the respective minerals.

Tab. B.2: Comparison of supplier’s data and HF digestion analysis of this study of muscovite^[1], quartz^[2], and orthoclase^[3]. Values given in [wt%], - no data available, limit of quantification (LOQ) regarding MgO and Na₂O < 0.02 wt%. If not specified analyses carried out with ICP MS and ICP-OES (cf. App. A.7, App. A.2), * AAS measurement: Na 589.6 nm, K 766.5 nm.

K ₂ O·3Al ₂ O ₃ ·6SiO ₂ ·2H ₂ O ^[1]		Normag GmbH	this study
SiO ₂	45.3	48.80 - 51.67	54.71
Al ₂ O ₃	38.5	29.37 - 31.05	28.42
K ₂ O*	11.8	-	9.40
Na ₂ O*		1.04 - 1.07	1.00
CaO		-	0.04
MgO		0.72 - 0.84	0.84

Continued on next page

Fe ₂ O ₃		2.00 - 4.16	4.93
TiO ₂		0.77 - 0.81	0.65
<hr/>			
	SiO₂^[2]	Schlingmeyer Quarzsand GmbH	this study
<hr/>			
SiO ₂	100.0	>99.7	98.65
Al ₂ O ₃		0.09	0.20
K ₂ O		<0.01	0.05
Na ₂ O		<0.01	< 0.02
CaO		<0.01	0.05
MgO		<0.01	< 0.02
Fe ₂ O ₃		0.0068	0.04
TiO ₂		0.0084	0.01
<hr/>			
	K₂O·Al₂O₃·6SiO₂^[3]	Sibelco GmbH	this study
<hr/>			
SiO ₂	64.7	66.2	62.80
Al ₂ O ₃	18.3	18.8	18.57
K ₂ O*	16.9	10.5	12.80
Na ₂ O*		3.6	5.12
CaO		0.8	0.52
MgO		-	< 0.02
Fe ₂ O ₃		0.11	0.17
TiO ₂		-	0.02
<hr/>			

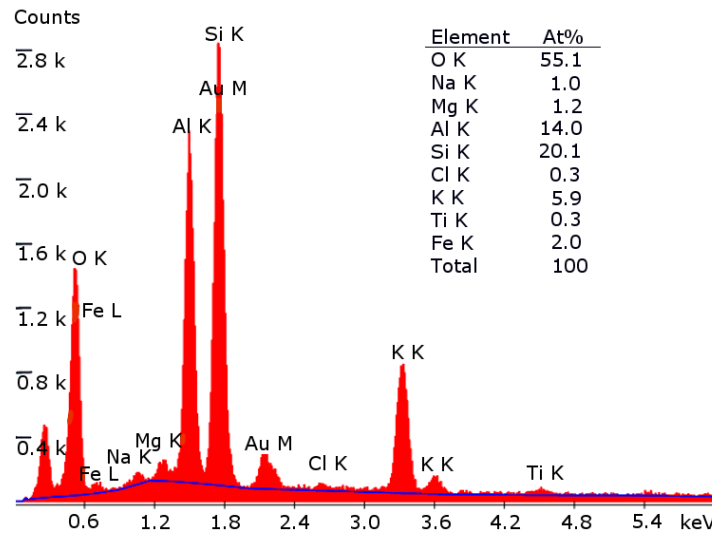


Fig. B.24: EDX analysis of muscovite (preconditioned sample) for batch experiments. Typical mineral composition of muscovite was detected including FeOX and MgO, Na₂O impurities. The insert shows element distributions [At%] which agreed well with HF digestion (App. Tab. B.2). Deficits in Al balanced with Mg and Fe impurities. Ideal structural formula muscovite: KAl₃Si₃O₁₀(OH)₂. Carbon was not analysed. Au diffraction pattern resulted from sample treatment. Blue line indicates background noise. K, L, M relate to the excitation energy of incident X-ray energy (shells of Bohr model).

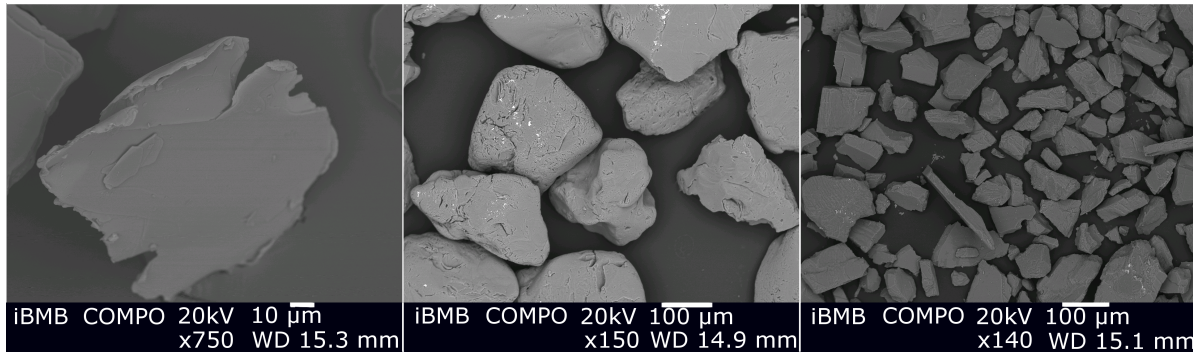


Fig. B.25: Comparison of SEM analysis of muscovite (left), quartz (middle), orthoclase (right). Measurements conducted at iBMB (Technical University Braunschweig, Germany). Figures depict characteristic shaping of minerals. *PSF*: muscovite 63 - 400 µm, quartz 150 - 800 µm, orthoclase 63 - 400 µm. Bright areas/patches on the quartz surface indicate Fe and Cr impurities which originate from sample preparation. WD - working distance, x - magnification factor. COMPO - measurement mode.

COULTER**SA3100**

Serial No.	AE16018	Software Version	2.13
------------	---------	------------------	------

Sample ID	MUSK01-1	Start Date	01/06/15
Customer	RICHTER-C	Start Time	09:34:41
Operator	ECKARDT	Elapsed Time	24 min
Sample Wt	1.28592 g	Outgas Time	480 min
Profile	BET	Outgas Temperature	100 C

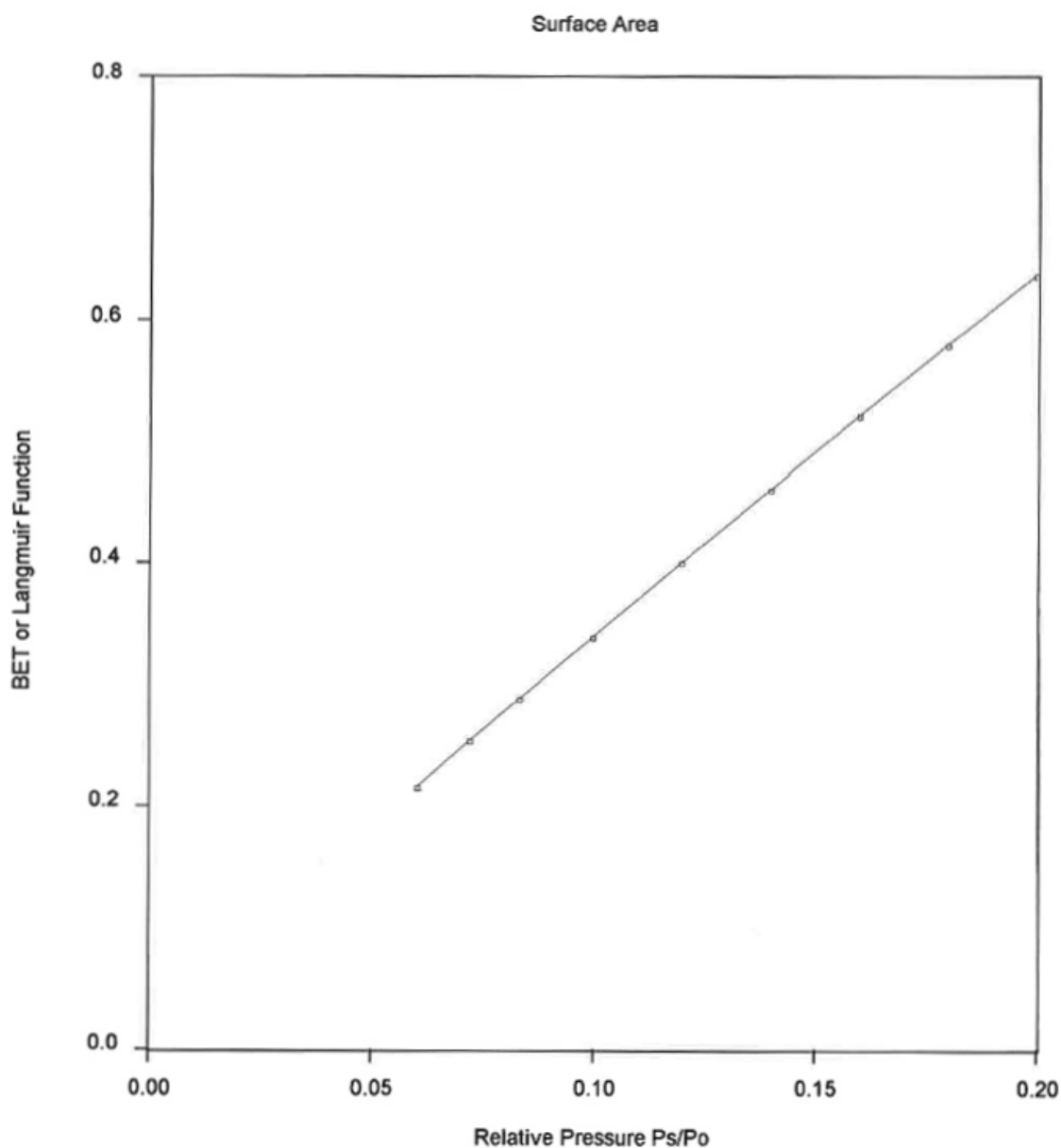


Fig. B.26: Example of BET isotherm for SSA determination after Brunauer et al. (1938) (SSA_{BET}). In the present study, the relative partial pressure range $p/p_0 = 0.05 - 0.2$ was used for BET isotherm regression. Linearity between $p/p_0 = 0.05 - 0.2$ was fulfilled for all analyses. Wt - weight.

Tab. B.3: Summary of BET (Brunauer et al., 1938) measuring conditions, error sources, and estimation of SSA_{BET} error ranges as provided in literature. clay - clay minerals, CEC - cation exchange capacity, RH - relative humidity, T - temperature [K], RSD - relative standard deviation, DF - degrees of freedom, nonlin. - non-linear, Ref. - reference, review - review/summary of various SSA studies after Brunauer et al. (1938), R^2 - coefficient of determination, p/p_0 - relative pressure, musc, ortho - muscovite, orthoclase, ^[1] adsorptive, ^[11] includes analyses of bentonite, kaolinite, limestone, soils, claystone. Listed references refer to [1] Maček et al. (2013), [2] Cases et al. (1992), [3] Hodson (2006), [4] Mantellato et al. (2015), [5] Macht et al. (2011), [6] Vicente et al. (1996), [7] this study, [8] de Lange et al. (2014), [9] Rouquerol et al. (2007), [10] Naderi (2015).

Ref.	Mineral	Error sources	Measurement conditions	Error estimation
[1]	clay ^[11]	→ Material properties: CEC, permability, swelling capacity, soil water content/soil suction	Multipoint analysis: 5 DF, $p/p_0 = 0.05 - 0.3$, N_2 ^[1] , degassing/dehydration at 373 K until vacuum of 2 Pa was reached, 1 h at 378 K, 5 g sample mass	BET method underestimates SSA: determination of external SSA
[2]	montmorillonite	→ Material properties: CEC, coagulation, sample texture, e.g. surface roughness, micropores → Measurement conditions: pressure, dehydration T (drying of sample)	Vacuum of $1.3 \cdot 10^{-2}$ Pa, 298 K over 16 h, N_2 ^[1] , 560 mg sample mass	Error estimation: 2% - 4%
[3]	anorthite, biotite	→ Material properties: shape of grain, particle size, dissolution processes, sample preparation (e.g. application of ultrasound) → Measurement conditions: adsorptive (N_2 radius/cross section)	Not provided.	Not possible to determine initial SSA only SSA at current moment in time, dissolution at reactive sites increases amount of unreactive SSA but does not alter SSA
Continued on next page				

Ref.	Mineral	Error sources	Measurement conditions	Error estimation
[4]	unhydrous cement, gypsum	→ Measurement conditions: degassing (T, pressure, time), dehydration T (sam- ple drying).	Multipoint analysis, $p/p_0 = 0.02$ - 0.3, 77.3 K, degassing/dehydration 313 - 423 K under vacuum over 16 h, $N_2^{[1]}$ flux $3 \cdot 10^{-3} \text{ m}^3 \text{ h}^{-1}$, $RH \equiv 0$	Increase in T degassing times causes in- crease of SSA by 35% and 25%, respecti- vely, SSA of gypsum varies by 17% if de- gassed under N_2 vs. vacuum application, error range under identical conditions: 3%
[5]	illite, bentonite	→ Material properties: sample preparation (e.g. application of ultrasound), removal of interlayer cations → Measurement conditions: degassing (T, pressure, time), dehydration T (sample drying), adsorptive (N_2 radius/cross section)	Multipoint analysis: 7 DF, $N_2^{[1]}$, degassing/dehydration at 113 K over 24 h, $p/p_0 = 0.05 - 0.2$	Increasing outgassing T results in decre- ase of illite SSA by 22%, micropores only partially N_2 accessible, error estimation: 3% - 7%, reliable analysis require at least 1 m^2 surface area
[6]	saponite	→ Material properties: sample preparation (e.g. activation treatments), removal of interlayer cations	Measurements at 77 K, $N_2^{[1]}$, degassing/dehydration at 383 K over 8h	Error estimation: 5%, SSA increases with time and intensity of activation treatment (acid leaching: SSA increase within 2 h - 6 h)
[7]	musc, ortho, quartz	→ Material properties: grain size, sam- ple preparation/preconditioning, e.g. ul- trasound application (Richter, 2015) → Measurement conditions: sample mass, adsorptive, pressure window, num- ber of repetitive measurements	Degassing/dehydration over 8 h vacuum at 373 K, $N_2^{[1]}$ (m), $Kr^{[1]}$ (ortho,quartz), equilibration time approx. 20 min, p/p_0 0.05 - 0.2, sample size mostly $< 1 \text{ m}^2$, $R^2 > 0.97$, multipoint analysis (> 6 DF)	Sufficient reproducibility of BET mea- surements: RSD 0.4% - 11.2%
Continued on next page				

Ref.	Mineral	Error sources	Measurement conditions	Error estimation
[8]	review	→ Measurement conditions: sample mass, fitting strategy (DF, pressure window), adsorption equilibration time, pressure variability, cell volume of sample slide, device calibration	16 h vacuum at 473 K, adsorption equilibration time 2 min, pressure varies less than 80 Pa in 2 min	High reproducibility of BET measurements, difference in SSA measurement variation determined from a single isotherm/no repetitive BET analysis: error 20 - 40% with > 10 DF, if < 10 DF error increases to 400%, error is lowest for direct fit of data (nonlin. parameter estimation) and highest for linear parameter estimation, at least 3 DF is recommended
[9]	review	→ Material properties: sample texture (surface roughness, micro-pores) → Measurement conditions: fitting strategy (DF, pressure window)		Microporous solids: $p/p_0 = 0.05 - 0.35$ exceeds linearity of BET-isotherm, general error estimation: up to 30%
[10]	review	→ Measurement conditions: degassing (T, pressure, time), dehydration T (sample drying), adsorption equilibration time,	Measurements at 77 K for N_2 ^[1] , 350 K - 400 K for most alkanes ^[1]	Recommendation: $p/p_0 = 0.05 - 0.35$, $R^2 > 0.995$, sample size 1 m ² or 1 g sample mass, SSA determined via N_2 or Kr may differ by factor 6, degassing/-drying T must not affect integrity of surface, RH and SSA directly correlated, limit of adsorptive uptake governed by accessibility of micropores, removal of tightly bond water at 383 K significantly increases SSA

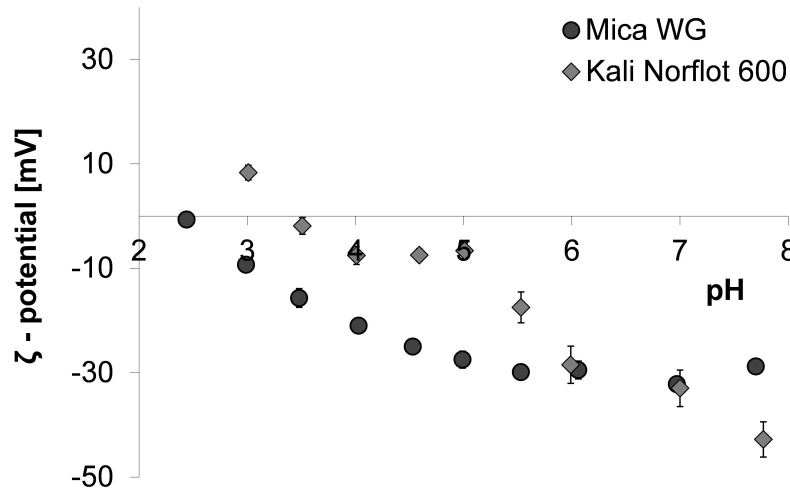


Fig. B.27: Zeta-potential measurements of muscovite and orthoclase. Data from Richter (2015). Details given in Sections 2.4.1 and 2.5. Mica WG refers to the muscovite sample, Kali Norflot 600 to the orthoclase sample of this study.

B.2 Comparison of potentiometric titration measurements of muscovite, orthoclase, and quartz

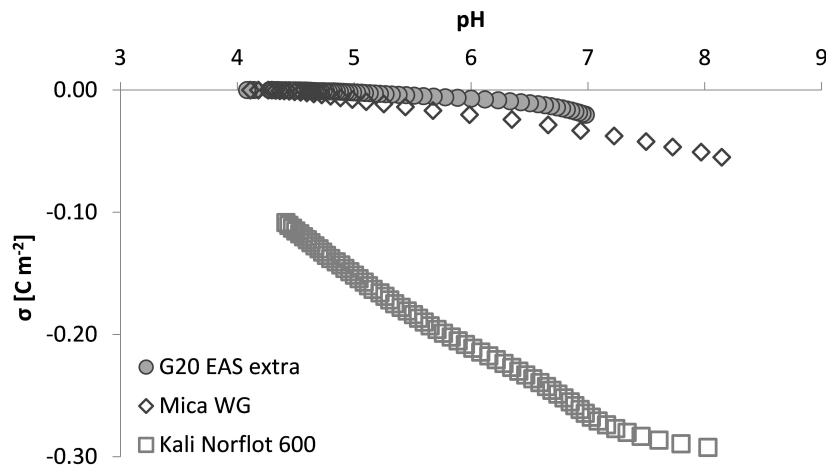


Fig. B.28: Comparison of relative titration data of muscovite (diamonds), orthoclase (squares), and quartz (solid circles). σ - surface charge density [C m^{-2}].

B.3 Supplementary data on Eu batch experiments

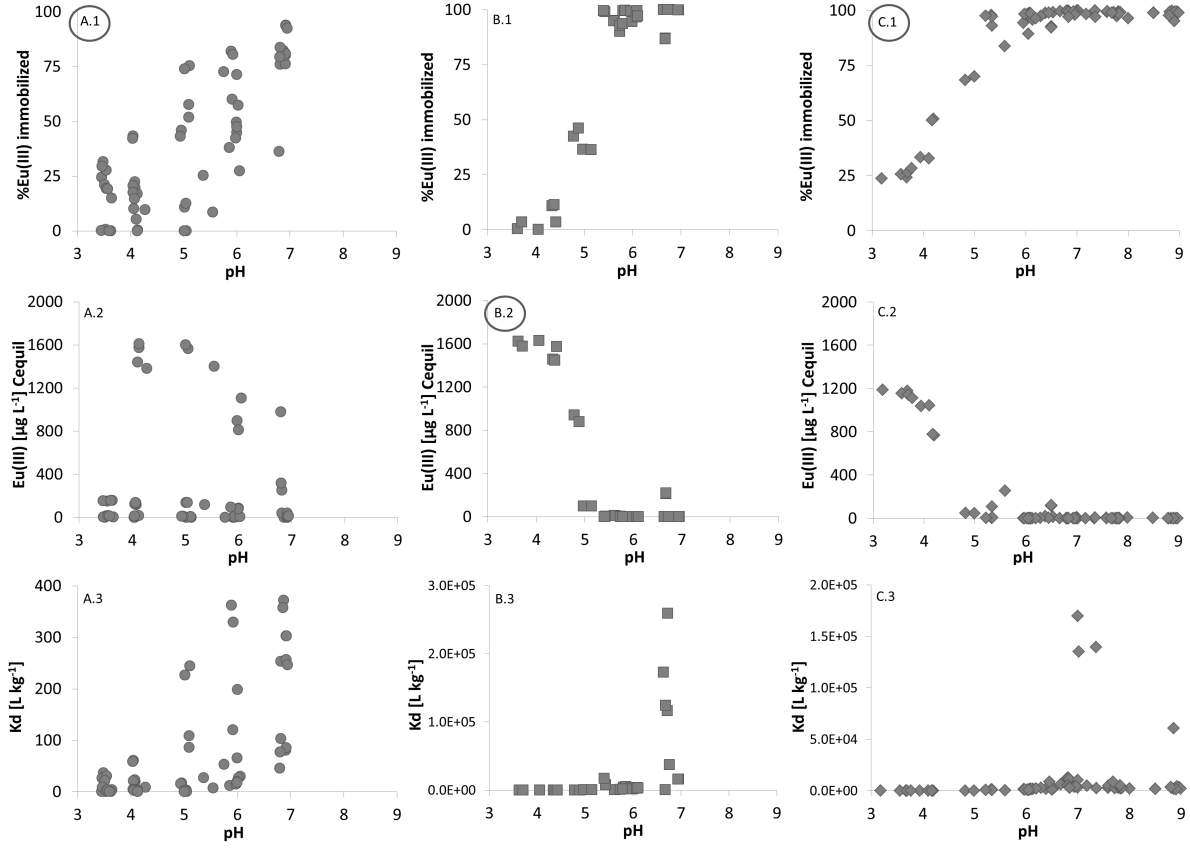


Fig. B.29: Batch data of quartz (A), orthoclase (B), muscovite (C) vs. pH. C_{equil} - Eu equilibrium concentration in solution, K_d - linear distribution coefficient (Eq. 3.38). A.1, B.2, C.1 data sets used for SCM optimization procedures.

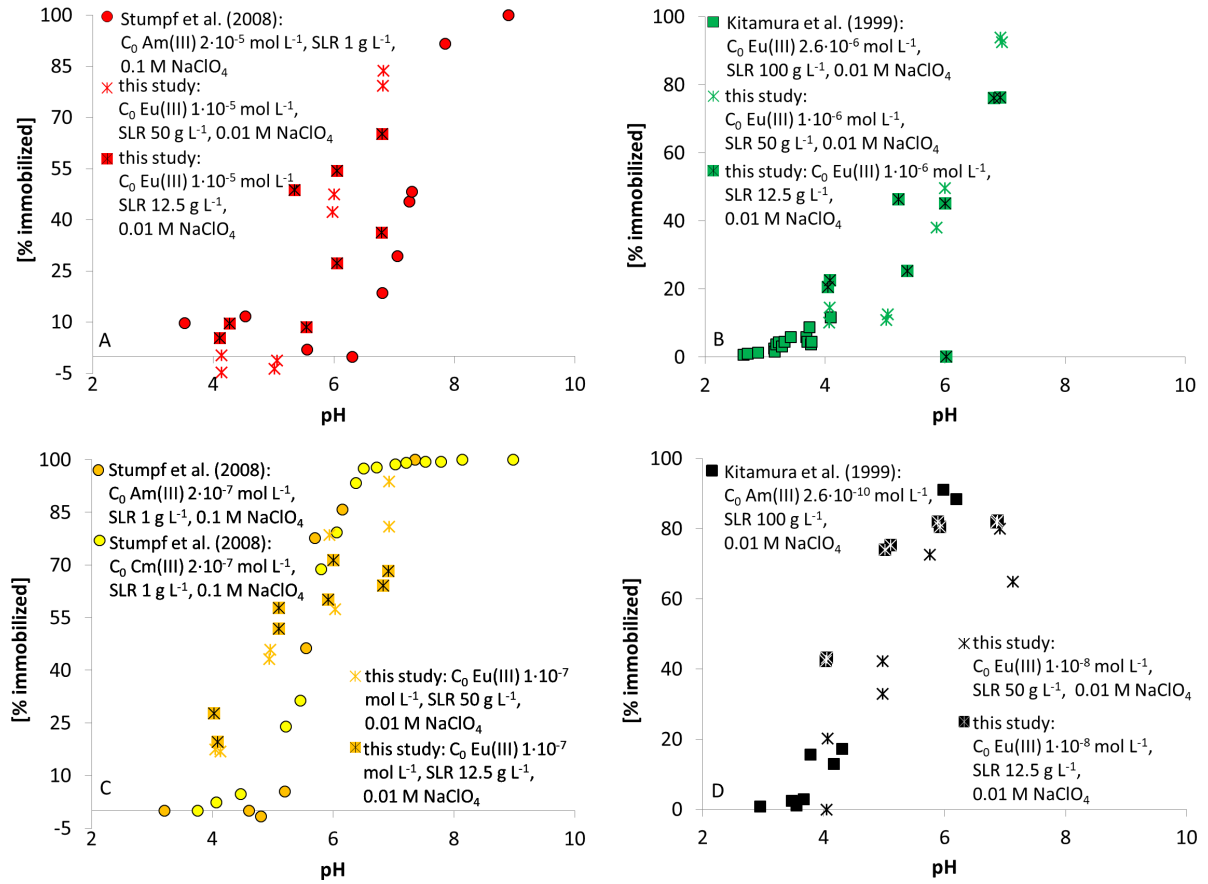


Fig. B.30: Comparison between batch experimental data of Eu, Am, Cm on quartz from literature and data collected in this study (after Fricke (2014)).

A: $C_0 \approx 10^{-5} \text{ mol L}^{-1}$, $\text{SLR } 1 - 50 \text{ g L}^{-1}$, $0.01 - 0.1 \text{ mol L}^{-1} \text{ NaClO}_4$.

B: $C_0 \approx 10^{-6} \text{ mol L}^{-1}$, $\text{SLR } 12.5 - 100 \text{ g L}^{-1}$, $0.01 \text{ mol L}^{-1} \text{ NaClO}_4$.

C: $C_0 \approx 10^{-7} \text{ mol L}^{-1}$, $\text{SLR } 1 - 50 \text{ g L}^{-1}$, $0.01 - 0.1 \text{ mol L}^{-1} \text{ NaClO}_4$.

D: $C_0 10^{-10} \text{ mol L}^{-1} - 10^{-8} \text{ mol L}^{-1}$, $\text{SLR } 12.5 - 100 \text{ g L}^{-1}$, $0.01 \text{ mol L}^{-1} \text{ NaClO}_4$.

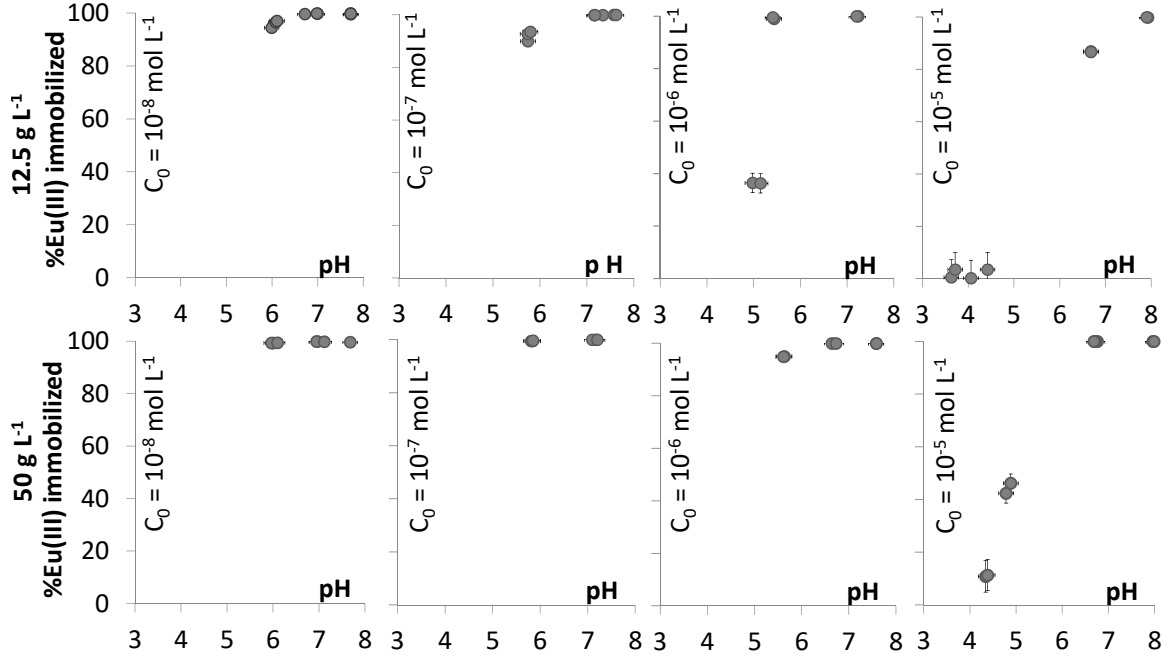


Fig. B.31: Batch sorption data of orthoclase (10 mM NaClO₄ electrolyte, laboratory conditions: ρCO_2 10^{-3.4} bar, $T = 298.15 \text{ K} \pm 2 \text{ K}$). C_0 - initial Eu concentration.

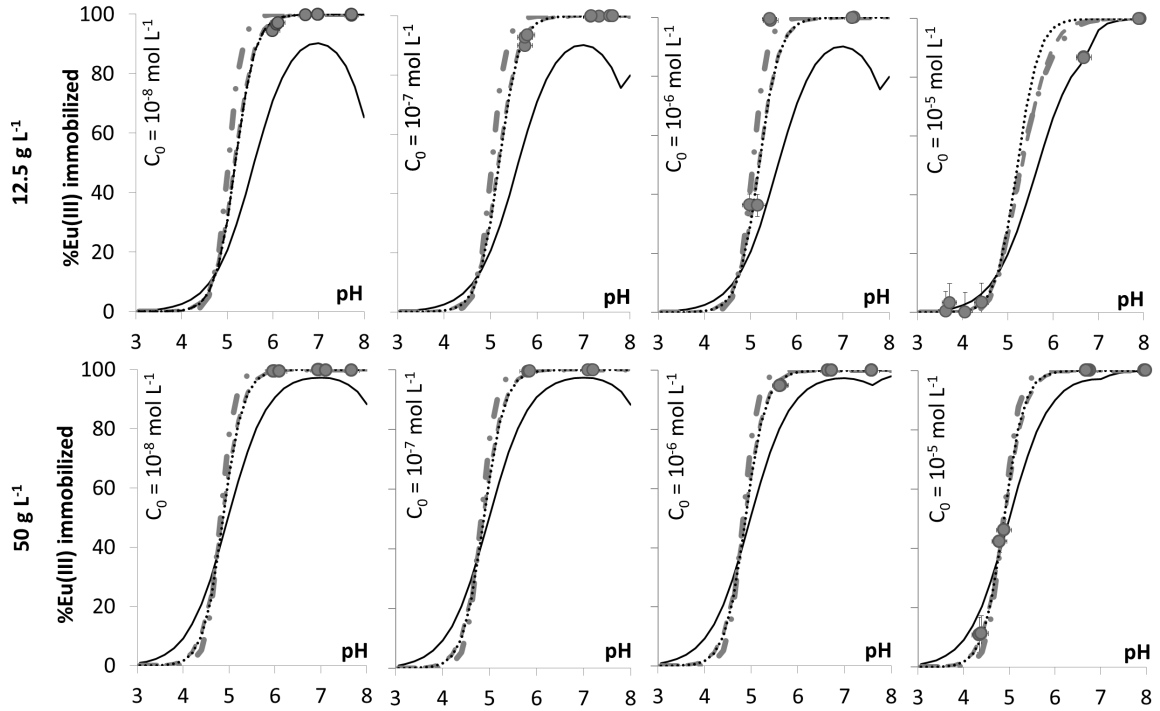


Fig. B.32: noEDLM fitting results of orthoclase batch data (10 mM NaClO₄ background electrolyte, laboratory conditions: ρCO_2 10^{-3.4} bar, $T = 296.0 \text{ K} \pm 2 \text{ K}$). C_0 - initial Eu concentration. Fitting results partially overlap. See Table 3.4 for final SCPs.

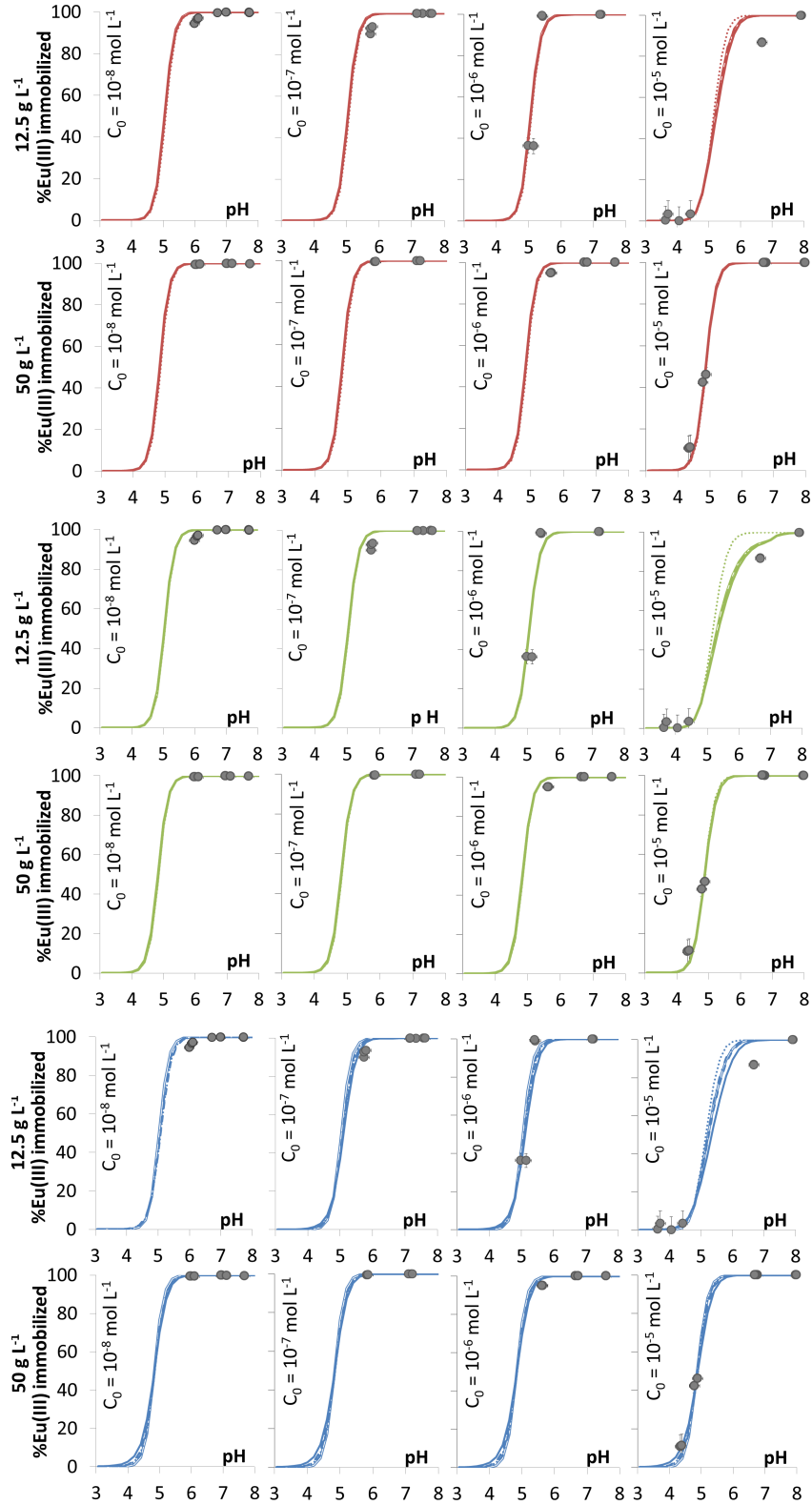


Fig. B.33: DDLM results of orthoclase batch data (10 mM NaClO_4 electrolyte, lab conditions: ρCO_2 $10^{-3.4}$ bar, $T = 296.0 \text{ K} \pm 2 \text{ K}$). C_0 - initial Eu concentration. $\Delta\sigma = 0.03 \text{ C m}^{-2}$ (DDLM, *SCP FS I*), $\Delta\sigma = 0.047 \text{ C m}^{-2}$ (DDLM, *SCP FS II*), $\Delta\sigma = 0.3 \text{ C m}^{-2}$ (DDLM, *SCP FS III*). Model results partially coincide, hence, lines overlap. For final SCPs cf. Table 3.4.

B.4 Supplementary data on Eu transport experiments

Following, additional information on preconditioning, experimental set-up, and relevant Eu speciation calculations are provided. Br tracer BTCs of muscovite and orthoclase are illustrated as well as supplementary data of Eu BTCs and SDs. Results of Br transport simulations with CXTFIT and Eu reactive transport simulations with PHREEQC are presented.

Figure B.42 provides additional data of Eu transport under close to nature geochemical boundary conditions (synthetic sediment, artificial groundwater, $\text{pH}_{ini} = 5.5$, SynSed-ii). Experiments were stopped after 35 d (Tab. 4.2); as Eu showed strong retardation under the chosen geochemical conditions the tailing of the Eu BTC (Fig. B.42 A) could not be entirely collected. Hence, the remaining Eu in the column is illustrated as a SD in Figure B.42 B.

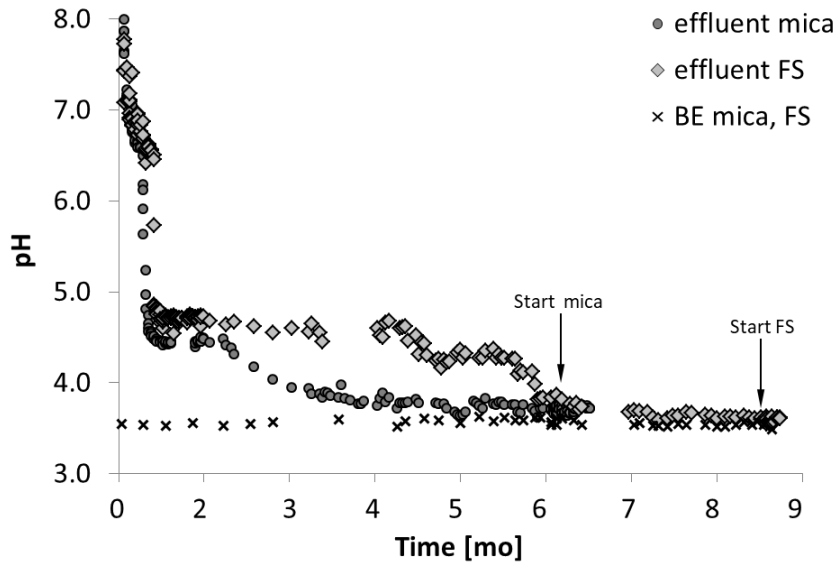


Fig. B.34: Pretests: Equilibration of muscovite (mica, circles) and orthoclase (FS, diamonds) columns for transport experiments (pretests) with $10 \text{ mmol L}^{-1} \text{ NaClO}_4$, pH 3.5 background electrolyte. x - pH of background electrolyte (BE), start of pretests indicated with arrows. Pulse solution of pretests composed of $10 \text{ mmol L}^{-1} \text{ NaClO}_4$, $10^{-5} \text{ mol L}^{-1} \text{ Eu}$, $10^{-5} \text{ mol L}^{-1} \text{ NaBr}$.

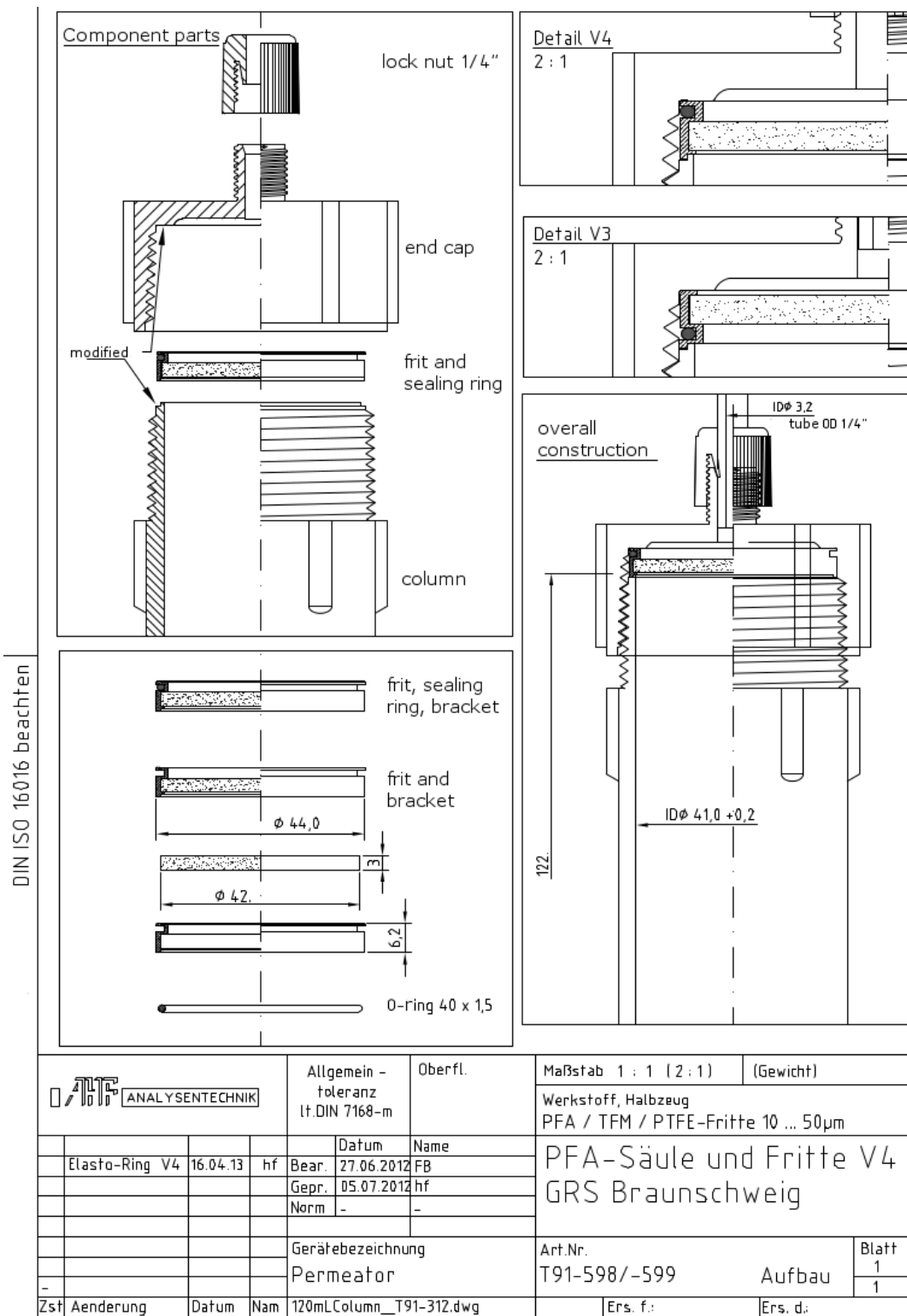


Fig. B.35: Technical drawing of PFA columns including PTFE frits, sealing ring, and bracket. Drawing provided by supplier (AHF Analysentechnik GmbH, Germany).

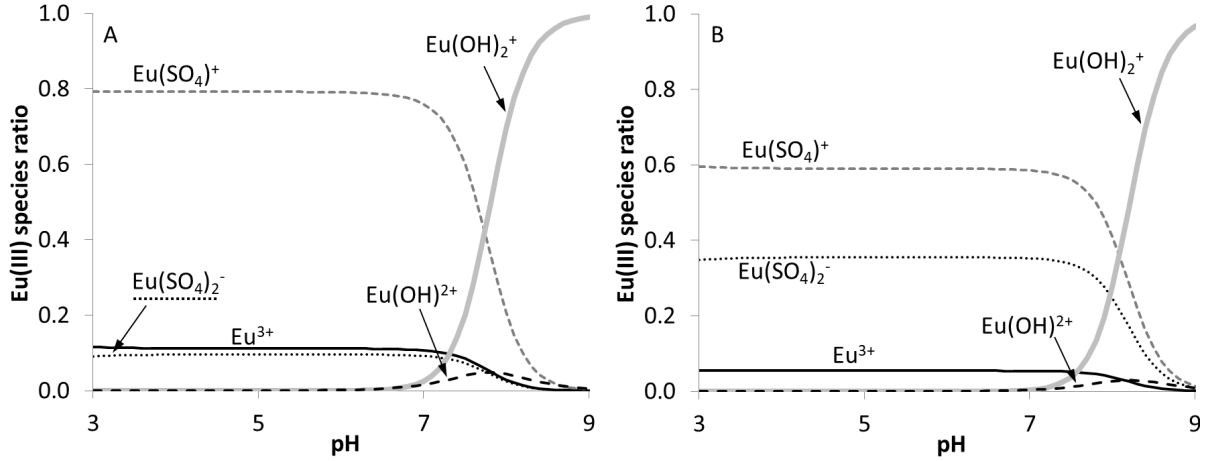


Fig. B.36: Eu speciation (10^{-5} mol L⁻¹ Eu) without atmospheric influence ($T = 298$ K) in 5 mmol L⁻¹ (A) and 50 mmol L⁻¹ (B) Na₂SO₄. Eu species ratio > 1% are depicted. PHREEQC, Version 3.1.2 was used (Parkhurst and Appelo, 2013), database as introduced in Sections 2.4.4 and 3.2.3. Atmospheric influence was excluded since reactive transport simulations were also calculated without CO₂ influence, cf. Section 4.2.5.

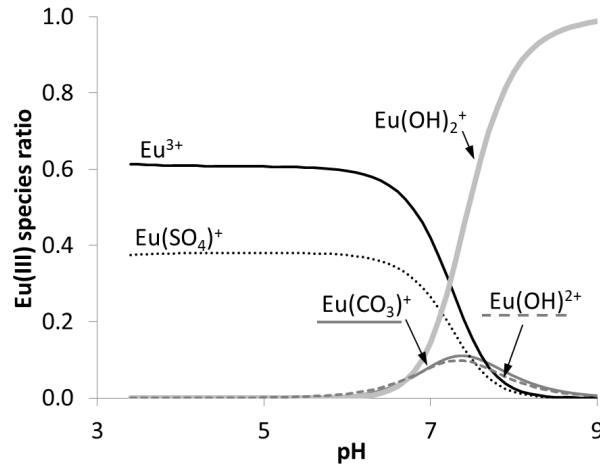


Fig. B.37: Eu speciation (10^{-5} mol L⁻¹ Eu) without atmospheric influence ($T = 298$ K) in artificial groundwater (App. Tab. A.1). Eu species ratio < 1% are depicted. PHREEQC, Version 3.1.2 was used (Parkhurst and Appelo, 2013), database as introduced in Sections 2.4.4 and 3.2.3. Atmospheric influence was excluded since reactive transport simulations were also calculated without CO₂ influence, cf. Section 4.2.5. Eu carbonato species are formed due to the composition of the artificial groundwater.

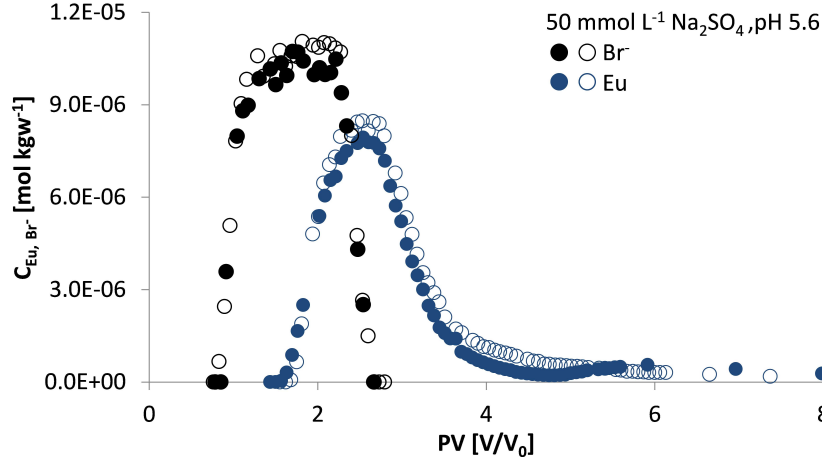


Fig. B.38: Comparison of Br (black) and Eu transport (blue) through quartz columns: $50 \text{ mmol L}^{-1} \text{ Na}_2\text{SO}_4$, $\text{pH}_{\text{ini}} = 5.6$. , C_{Eu} , C_{Br^-} denotes Eu and Br concentrations, PV – pore volume. Experiment was carried out in doublets (solid and empty characters).

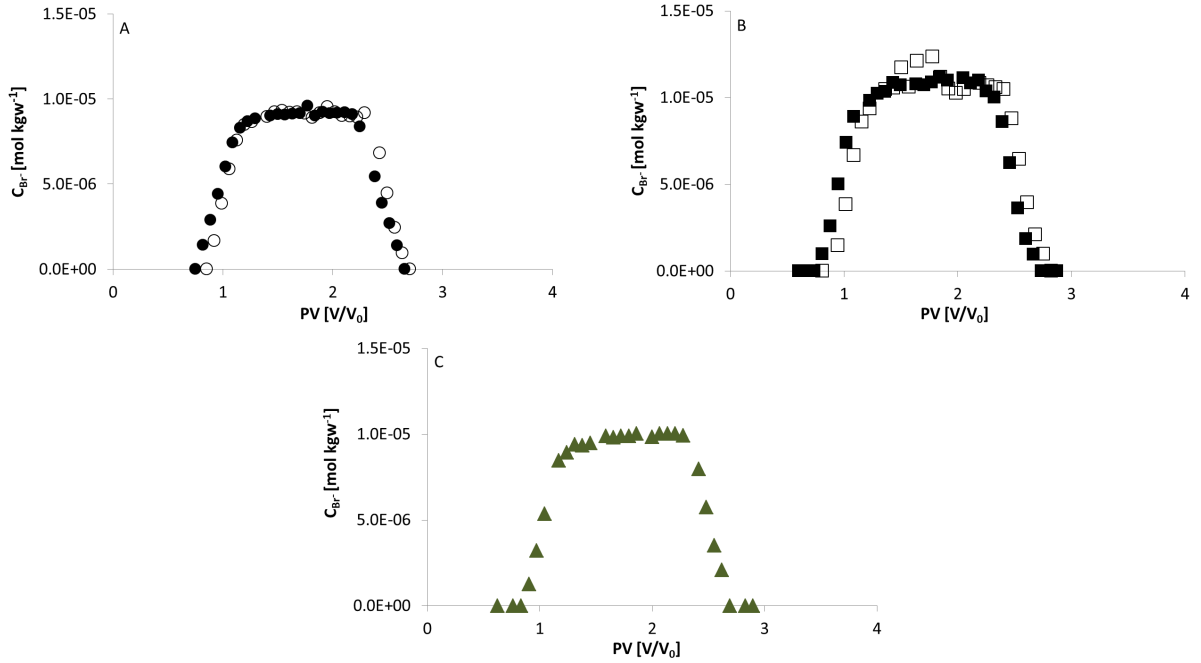


Fig. B.39: Br BTCs of orthoclase column experiments. A: FS-i $10 \text{ mmol L}^{-1} \text{ NaClO}_4$, pH 3.6, B: FS-ii $50 \text{ mmol L}^{-1} \text{ Na}_2\text{SO}_4$, pH 3.5, C: FS-iii $50 \text{ mmol L}^{-1} \text{ Na}_2\text{SO}_4$, pH 5.5. C_{Br^-} - Br concentrations, PV - pore volume. For experimental details cf. Tables 4.1 and 4.2.

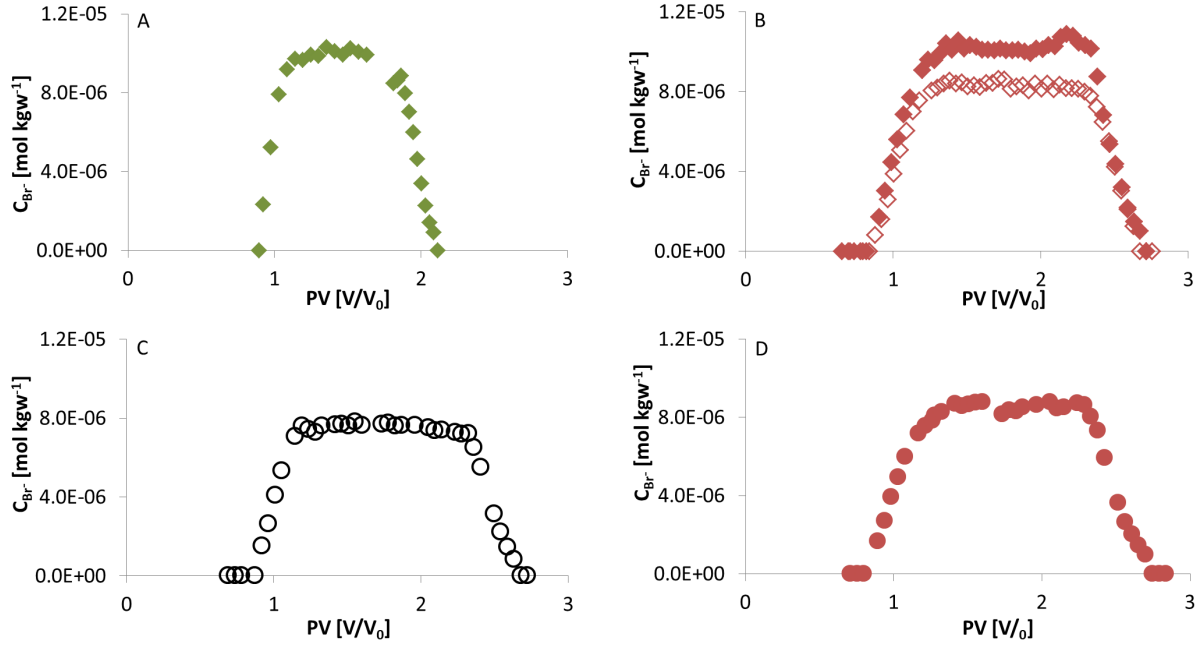


Fig. B.40: Br BTCs of muscovite column experiments. A: $10 \text{ mmol L}^{-1} \text{ NaClO}_4$, pH 3.6, B: $5 \text{ mmol L}^{-1} \text{ Na}_2\text{SO}_4$, pH 3.6, C: artificial groundwater (App. Tab. A.1), pH 5.5, D: $50 \text{ mmol L}^{-1} \text{ Na}_2\text{SO}_4$, pH 5.5. C_{Br^-} - Br concentrations, PV - pore volume. For experimental details cf. Tables 4.1 and 4.2.

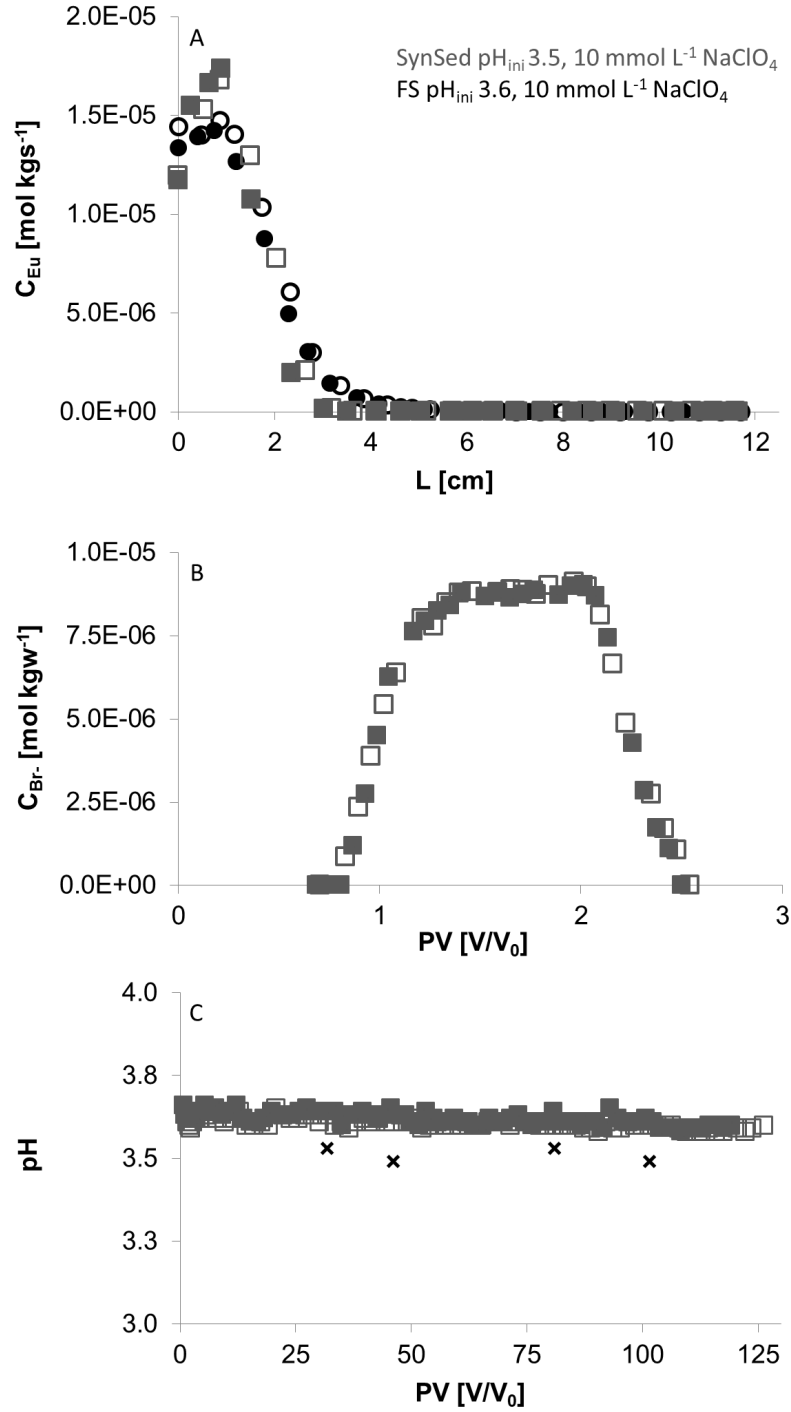


Fig. B.41: Eu transport through orthoclase (FS, black, $t = 136$ PV) and synthetic sediment (SynSed, grey, $t = 122$ PV) columns using 10 mmol L⁻¹ NaClO₄ background electrolyte, $pH_{ini} \approx 3.5$. A: Spatial distribution, B: Br breakthrough of the SynSed column, C: pH development of the SynSed column. Experiments carried out in doublets (solid and empty characters). The bottom of the column corresponds to $L = 0$ cm, the top to $L = 12.25$ cm. x denotes pH_{ini} , C_{Eu} , C_{Br} - Eu, Br concentrations, PV - pore volume. For experimental details cf. Tables 4.1 and 4.2.

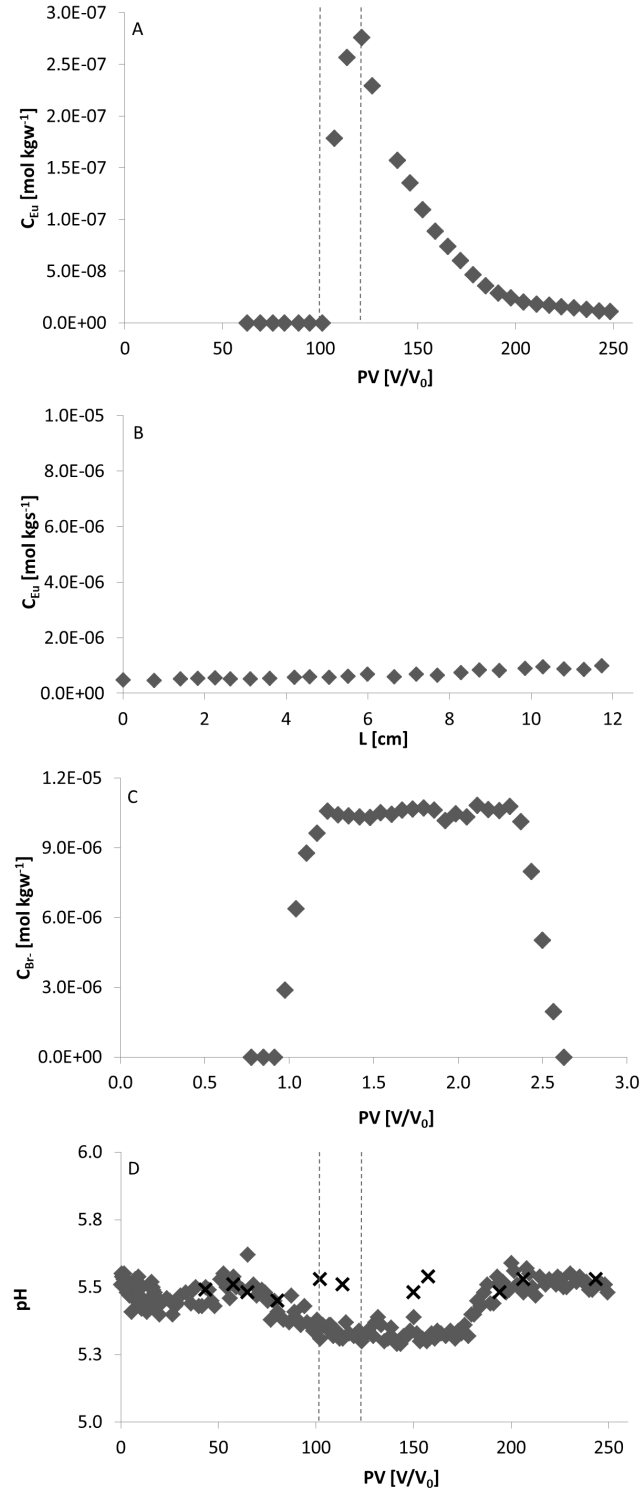


Fig. B.42: Eu transport through synthetic sediment columns using the artificial ground-water after Klinge et al. (2002) as a background electrolyte, $pH_{ini} = 5.5$. A: Eu BTC, B: Eu SD, C: Br BTC, D: pH development of the SynSed column. The bottom of the column corresponds to $L = 0$ cm, the top to $L = 12.25$ cm. x denotes pH_{ini} , C_{Eu} , C_{Br} - Eu, Br concentrations, PV - pore volume. For experimental details cf. Tables 4.1 and 4.2.

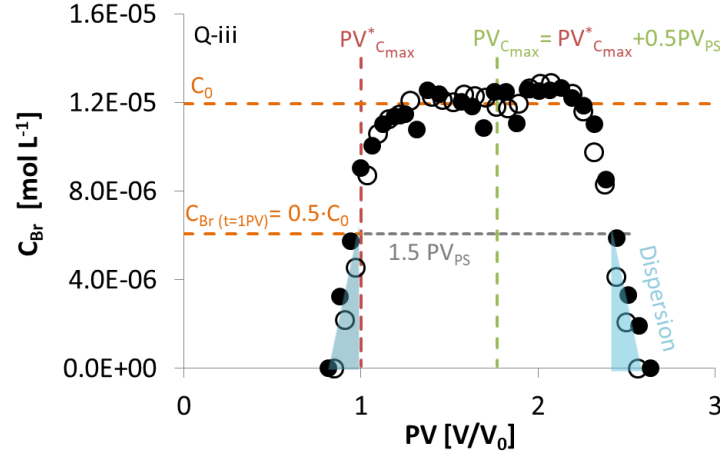


Fig. B.43: Illustration of ideal Br tracer BTC characterization with quartz column experiment Q-iii, $\text{pH}_{ini} \approx 5.5$, $5 \text{ mmol L}^{-1} \text{ Na}_2\text{SO}_4$ background electrolyte. $C_{Br} = 0.5 \cdot C_0$ applied for $t = 1 \text{ PV}$. $PV_{C_{max}}^*$ - pore volume of first concentration breakthrough of an ideal conservative tracer function (Dirac impulse), C_{Br} - Br concentration in solution, C_0 - initial concentration, PV - pore volume, PS - pulse solution, $PV_{C_{max}}$ - peak/plateau concentration at $t = 0.5PV_{PS}$, PV_{PS} - pore volume of pulse solution application $[V/V_0]$.

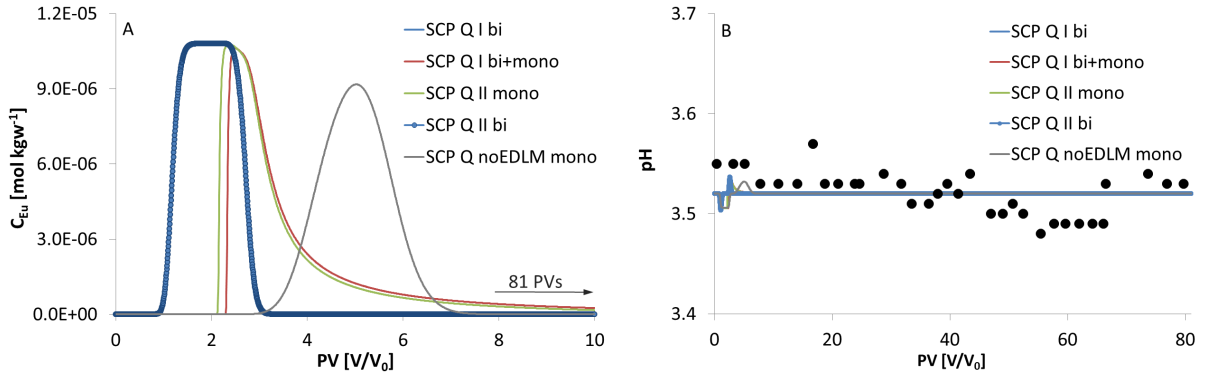


Fig. B.44: Eu transport simulations of column experiment Q-i. A: Predicted Eu BTCs; experimental results returned a Eu SD in contrast to RTMs that exclusively yielded Eu BTCs. B: Predicted and measured (solid characters) pH development. Simulation results of *SCP Q I bi* and *SCP Q II bi* overlap. For experimental details cf. Tables 4.1 and 4.2. PV - pore volume, C_{Eu} - Eu concentration $[\text{mol kgw}^{-1}]$.

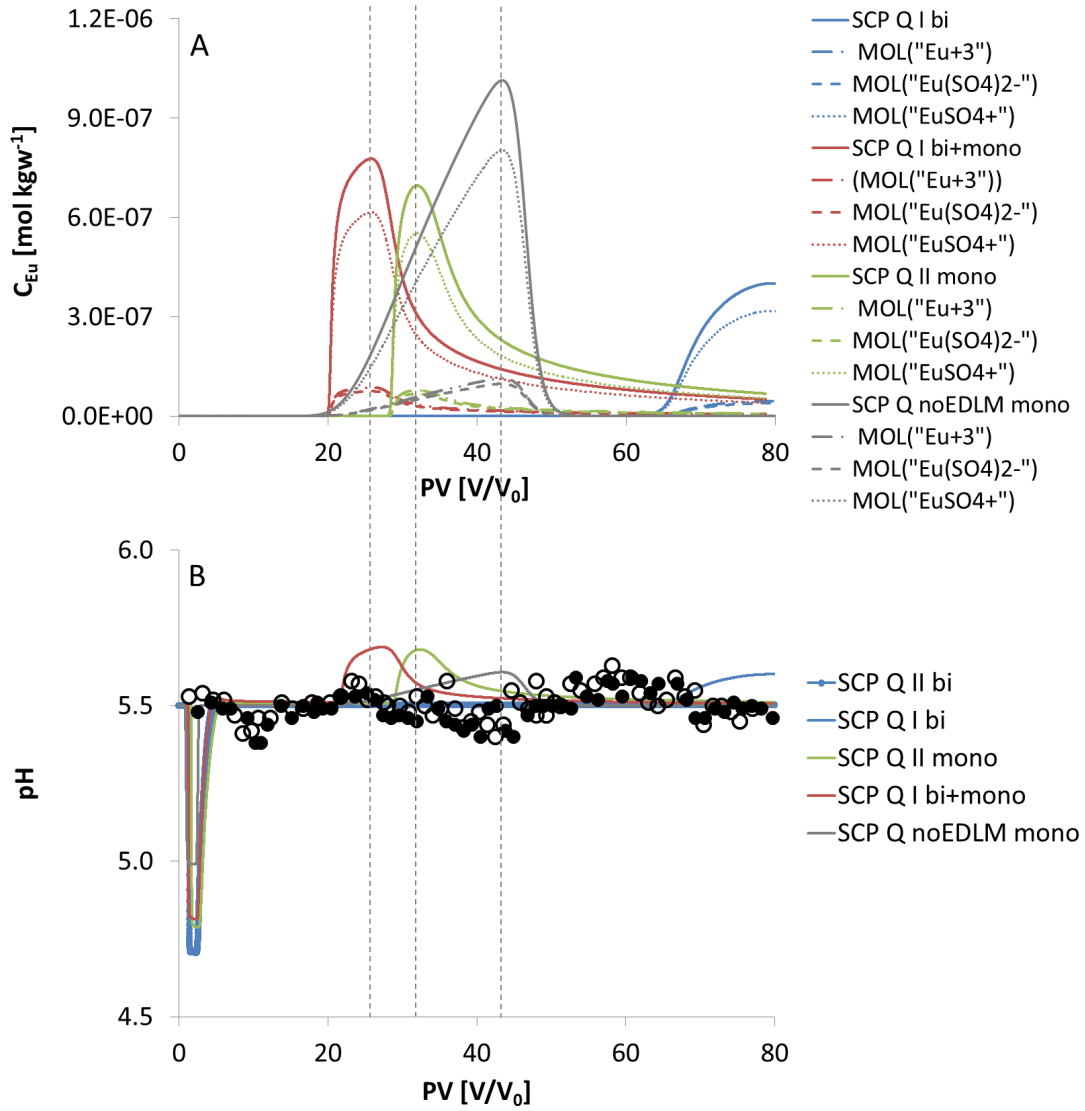


Fig. B.45: Eu transport simulations of column experiment Q-iii. A: Predicted Eu BTCs; experimental results returned a Eu SD in contrast to RTMs *SCP Q I mono+bi*, *SCP Q noEDLM mono*, *SCP Q II mono*. B: pH development of Q-iii; comparison between measurements (solid, empty symbols) and predictions (solid lines). Q-iii was carried out in double (solid, empty symbols). For experimental details cf. Tables 4.1 and 4.2. PV - pore volume, C_{Eu} - Eu concentration $[\text{mol kgw}^{-1}]$.

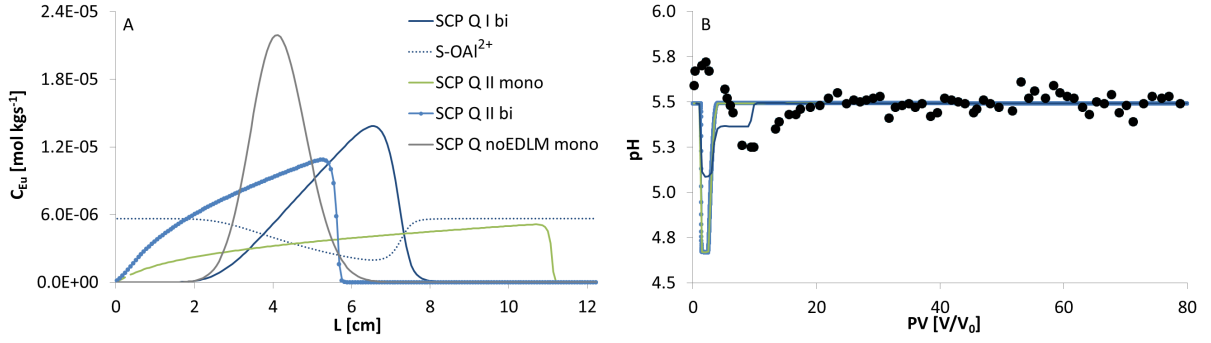


Fig. B.46: Eu transport simulations of column experiment Q-v. A: Predicted Eu SDs for $t = 80$ PV; experimental results returned Eu BTCs in contrast to RTMs that returned a Eu BTC only for *SCP Q I bi+mono*. B: Predicted (solid line) and measured (solid characters) pH development. For experimental details cf. Tables 4.1 and 4.2. PV - pore volume, C_{Eu} - Eu concentration [mol kgs⁻¹], L - column length [cm].

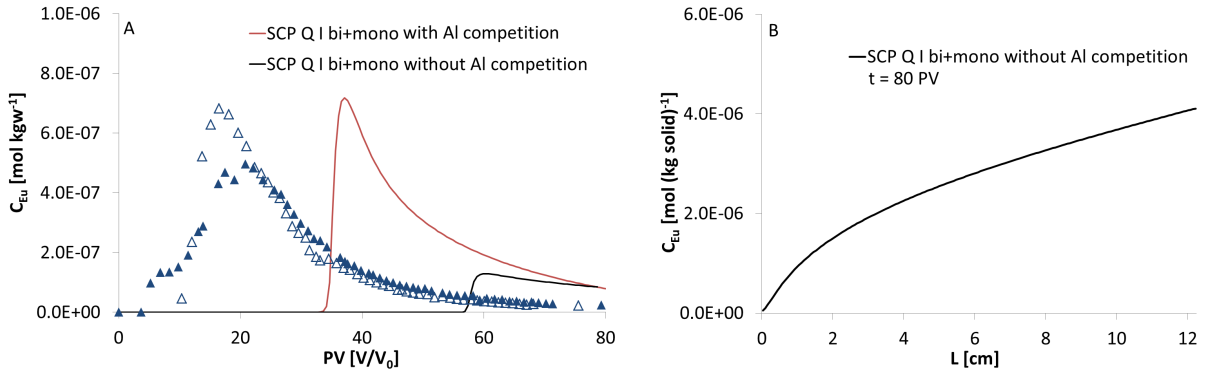


Fig. B.47: Eu transport simulations (*SCP Q I bi+mono*) of column experiment Q-v: Influence of Al³⁺ as a potential competing cation. A: Predicted Eu BTCs with (red) and without (black) the influence of the competing cation Al³⁺. B: Predicted Eu SD for *SCP Q I bi+mono* (without competing cation influence) at $t = 80$ PV. For experimental details cf. Tables 4.1 and 4.2. PV - pore volume, C_{Eu} - Eu concentration, L - column length [cm].

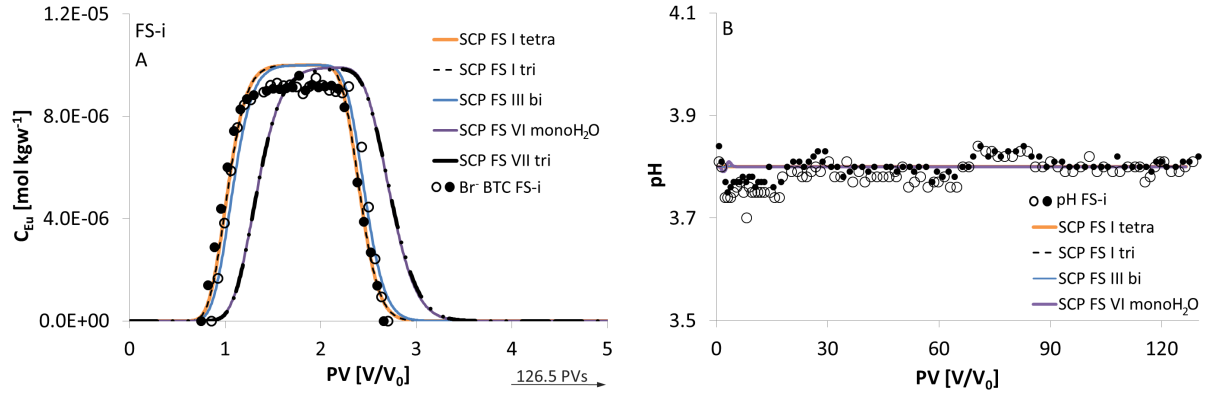


Fig. B.48: Eu transport simulations of column experiment FS-i. A: Comparison between experimental Br BTCs (solid, empty symbols) and predicted Eu BTCs (solid, dashed lines). Transport experiment FS-i resulted in a SD (Fig. 4.8); RTMs exclusively yielded Eu BTCs. B: Predicted and measured pH development. Simulation results of RTMs overlap. Labelling corresponds to Figure 4.8. For experimental details cf. Tables 4.1 and 4.2.

